Scholars' Mine

Summer 2016

Characterization of fracture initiation in non-cylindrical buckle folds using 3D finite element analysis

Eli Jacob Steinbeck

Recommended Citation

CHARACTERIZATION OF FRACTURE INITIATION IN NON-CYLINDRICAL
BUCKLE FOLDS USING 3D FINITE ELEMENT ANALYSIS

by

ELI JACOB STEINBECK

A THESIS

Presented to the Faculty of the Graduate School of the

MISSOURI UNIVERSITY OF SCIENCE AND TECHNOLOGY

In Partial Fulfillment of the Requirements for the Degree

MASTER OF SCIENCE IN PETROLEUM ENGINEERING

2016

Approved by

Dr. Andreas Eckert, Advisor
Dr. John Hogan
Dr. Runar Nygaard

ABSTRACT

The spatial distribution of fracture sets associated with buckle folds has been well documented in field studies. There are difficulties, however, in placing accurate constraints on the timing of the initiation of individual fracture sets during the deformation history of the fold under in-situ conditions. This study investigates specific conditions that give rise to the initiation of various fracture sets in the hinge and limb of a pericline, based on an analysis of the effective stress evolution during the processes of buckling and erosional unloading. A 3D finite element modeling approach is used to simulate the effective stress evolution in single-layer folds with a Maxwell viscoelastic rheology, while including the influence of overburden stress, pore pressure, and a geologic strain rate. Several material properties and geometric features are varied to test their influence on fracture initiation. The modeling results show that fracturing is most heavily influenced by permeability, initial overburden thickness, and erosional unloading. Further analysis reveals that six fracture sets, which are observed in natural buckle folds, are also observed in the modeling results: outer arc tensile fractures, outer arc normal faults, and inner arc thrusts, all of which strike parallel to the fold axis, are determined to be common fracture sets; outer arc tensile fractures that strike perpendicular to the fold axis, and thrusts in the limb that strike roughly parallel to the fold axis are determined to be less common fracture sets that require low permeability ($< 10^{-21}$ m^2) folding layers in order to initiate; vertical conjugate shear fractures in the outer arc, where the fold axis bisects the acute angle between fracture planes, are determined to be a rare fracture set. Most importantly, the timing of initiation is determined for each set, thus providing the most difficult information to obtain from a field study on fold related fractures.

ACKNOWLEDGMENTS

I would like to thank my advisor, Dr. Andreas Eckert, for accepting me into the geomechanical modeling group. During my time as an undergraduate he was very influential in my decision to pursue a master's degree, and throughout my last two years as a graduate student he has been a supportive and encouraging mentor and friend. His theoretical knowledge and technical guidance have proven to be invaluable tools that have helped guide me through my research and on to the completion of this thesis.

I would also like to thank Dr. John Hogan and Dr. Runar Nygaard for the time and effort they have put forth as members of my graduate committee. Your advice regarding this thesis, my current academic career, and my future career in the petroleum industry has been very much appreciated.

My thanks also go to my friends and colleagues that are, or have been a part of the geomechanical modeling group: Xiaolong Liu, Weicheng Zhang, Davi Rodrigues Damasceno, Huining Zhang, Zhe Yuan, and Mengke Li. Thank you all for all your help and support during my time as a master's student; and most importantly, thank you for your friendship, and for keeping me sane during all those hours spent in B21 McNutt.

Lastly I would like to thank my family: my parents, my sister Hannah, and my fiancée Erika Miller. Thank you for your unwavering love, and endless support and encouragement in all of my endeavors. You will always be my primary motivator to strive for success in everything that I do.

TABLE OF CONTENTS

LIST OF ILLUSTRATIONS

LIST OF TABLES

NOMENCLATURE

Symbol	Description
λ_d	Dominant Wavelength
σ_1	Maximum Principal Stress
σ_2	Intermediate Principal Stress
σ_3	Minimum Principal Stress
h	Folding Layer Thickness
μ_L	Folding Layer Viscosity
μ_M	Matrix Viscosity
E	Young's Modulus
ν	Poisson's Ratio
P	Layer-parallel Stress
G	Shear Modulus
A_0	Initial Fold Amplitude
σ'_1	Effective Maximum Principal Stress
σ'_2	Effective Intermediate Principal Stress
σ'_3	Effective Minimum Principal Stress
τ	Shear Stress on a Surface
σ_n	Normal Stress on a Surface
C_0	Rock Cohesion
μ	Coefficient of Friction
ψ	Angle of Internal Friction
θ	Failure Angle
T	Tensile Strength
σ_d	Differential Stress
$\sigma_{d,crit}$	Critical Differential Stress at Failure
σ_m	Mean Stress
q^e	Nodal Forces
K^e	Element Stiffness Matrix
u^e	Nodal Displacements

f^e	Nodal Forces Required to Balance Distributed Loads
N_a	Shape Function
$\tilde{u}_a$	Approximate Nodal Displacements
σ_{ij}	Stress Tensor
P_p	Pore Pressure
ρ_m	Material Density
g	Gravitational Acceleration
K	Bulk Modulus
$\dot{\varepsilon}$	Strain Rate
α	Biot (Effective Stress) Coefficient
v	Material Velocity
μ_f	Fluid Viscosity
k	Permeability
$\dot{\sigma}_{ij}$	Time Derivative of the Stress Tensor
ϕ	Porosity
z	Depth
ρ_b	Bulk Density
ρ_s	Density of Solid Grains
ρ_f	Fluid Density
ρ_{db}	Dry Bulk Density
ρ_w	Density of Water
G_s	Specific Gravity of Solid Grains
λ	1st Lamé Parameter
E_f	Young's Modulus of the Folding Layer
E_m	Young's Modulus of the Matrix
R_μ	Viscosity Contrast

1. INTRODUCTION

1.1. OVERVIEW

For over half a century, folded rocks have been studied from a theoretical standpoint for the insight they provide in regards to the deformation history of rock structures. There are also practical incentives in the petroleum industry that can be gained from studies on the geometry and mechanics of folding. Large scale anticline structures provide some of the most common structural traps for conventional hydrocarbon reservoirs (Davis et al., 2012). Although there are many factors that influence the ultimate recovery from these reservoirs, one of the most important is the presence of natural fractures. Open fracture clusters are typically zones of elevated permeability that aid in the flow of hydrocarbons through a relatively impermeable rock matrix (Odling el al., 1999). Closed fractures and filled fractures can greatly reduce the relative permeability to hydrocarbons (Nelson, 2001), but they may require relatively little stimulation to reactivate or re-open (Sibson, 2003).

Fracture patterns that develop in folded rocks are complex, and they reflect the complex nature of the stress and strain evolution during the initiation and growth of the folds (Price and Cosgrove, 1990; Nelson, 2001). This becomes apparent for large scale anticline structures, once buried at depth, that are now visible at the surface as a result of erosion and exhumation. Many of these structures have been the focus of field studies to help build conceptual fold-fracture models that can be related to similar subsurface anticlines (e.g., Stearns, 1964; Bergbauer and Pollard, 2004; Bellahsen et al., 2006; Cooper et al. 2006; Stephenson et al. 2007; Al-Mahmoud et al. 2009). A common takeaway from surface field studies is that there is more than one fracture pattern associated with folds, each with its own characteristic fracture types and orientations, indicating that each pattern formed under a different state of stress and at different times. While surface studies are effective in determining the relative timing of fracture initiation, based on cross-cutting relationships, they are less effective in determining the absolute timing of fracture initiation or even if the fractures initiated pre-folding, during folding, or post folding (Twiss and Moores, 2007).

There are also geophysical tools and techniques that help determine the location, and orientation of fractures in the subsurface. These include the use of special seismic wave interpretation techniques to characterize subsurface fractures on a regional scale (e.g., Schoenberg and Sayers, 1995; Gray et al., 2003; Far et al., 2013), and the use of acoustic and electrical borehole image logs to characterize fractures on a much more localized scale (e.g., Zemanek et al., 1970; Barton and Zoback, 2002). While still useful for delineating subsurface fractures, as well as aiding in the exploration and exploitation of subsurface natural resources, these methods are still unable to place any accurate constraints on the timing of fracture initiation within a fold.

A technique that has been commonly used to predict fracture occurrence in developed fold shapes, is fold curvature analysis (e.g., Lisle, 1994; Fischer and Wilkerson, 2000; Bergbauer and Pollard, 2004; Frehner, 2011). This technique uses the neutral surface concept (Price and Cosgrove, 1990; Twiss and Moores, 2007) to distinguish between regions of tensile and compressional failure within a fold (Figure 1.1). Above the neutral surface lies a region of layer parallel extensional strain, and below lies a region of layer parallel compressional strain. Thus, the location of tensile failure is limited to the region above the neutral surface, and the location of compressional failure is limited to the region below the neutral surface (Davis et al., 2012). When used as a tool for field studies, however, fold curvature analysis is still unable to predict the timing of fracture initiation (Smart et al., 2009). Furthermore, since fold curvature calculations are made based on fold geometry, this technique can only be used to quantify strain. Fold curvature analysis provides no quantification of stress magnitudes at any point during the folding history.

In order to better understand the relationship between folding and fracturing, it is necessary to simulate the principal stress evolution during the initiation and structural development of a fold. Mechanical Earth Modeling, using numerical approaches such as the finite element method, allows for the simulation of subsurface folding over a reasonable geologic deformation period, while using realistic material properties of rocks, and including the influence of fluids in the subsurface (e.g., Eckert et al., 2014; Eckert et al., 2015) .
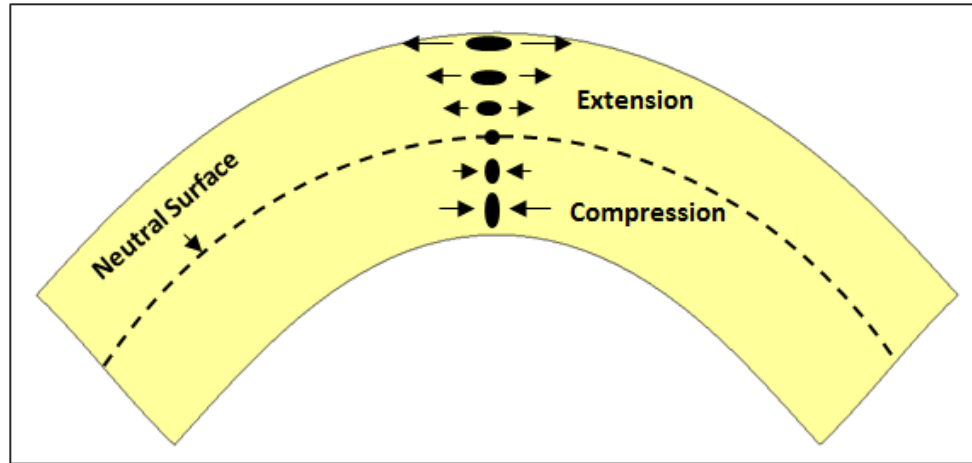
Figure 1.1. Strain distribution above and below the neutral surface of a fold.

As a result of field studies, theoretical analyses, and experimental tests, several different processes have been proposed to account for the flexural folding of layers of rock. These include the passive folding of layers, the bending of layers to produce forced folds, and the buckling of layers to produce buckle folds (Price and Cosgrove, 1990). In regards to the mechanical analysis of folding, buckle folding has been the most extensively studied (Davis et al., 2012). Buckle folds form when a mechanically competent horizontal layer embedded in a less competent matrix is subjected to layer parallel compression (Figure 1.2). If the layer parallel compressive stresses become large enough, a mechanical instability will develop causing the competent layer to "buckle" (Twiss and Moores, 2007). These buckle folds can be further subdivided into two groups: those that are cylindrical and maintain a constant geometry along their fold hinge (Davis et al., 2012), and those that depart from a cylindrical geometry and begin to form more irregular fold shapes (Figure 1.3). Non-cylindrical folds in nature have the tendency to take the form of an elongated dome or basin, which is also called a pericline (Cosgrove and Ameen, 1999).

This study utilizes the finite element method to construct a 3D Mechanical Earth Model [MEM] capable of simulating the principal stress evolution during the initiation and growth of a single-layer, periclinal buckle fold, and predicting the following characteristics related to fracture initiation: timing of initiation, location, type, and orientation. The methodology presented in this study, for predicting fracture initiation,
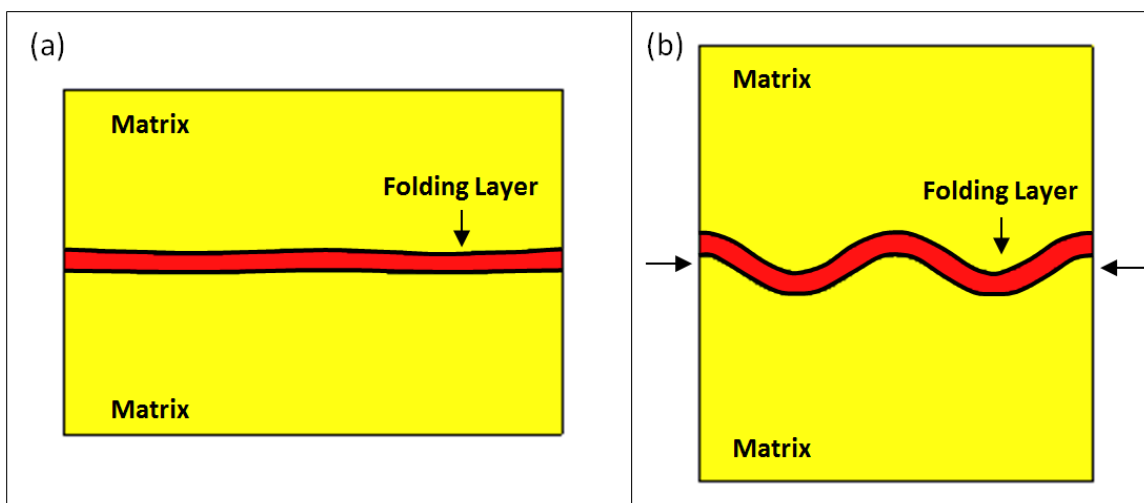
Figure 1.2. Buckling of a competent layer in a less competent matrix. (a) Isolated competent layer with initial sinusoidal perturbation prior to shortening. (b) Sinusoidal wave train produced as a result of buckling.
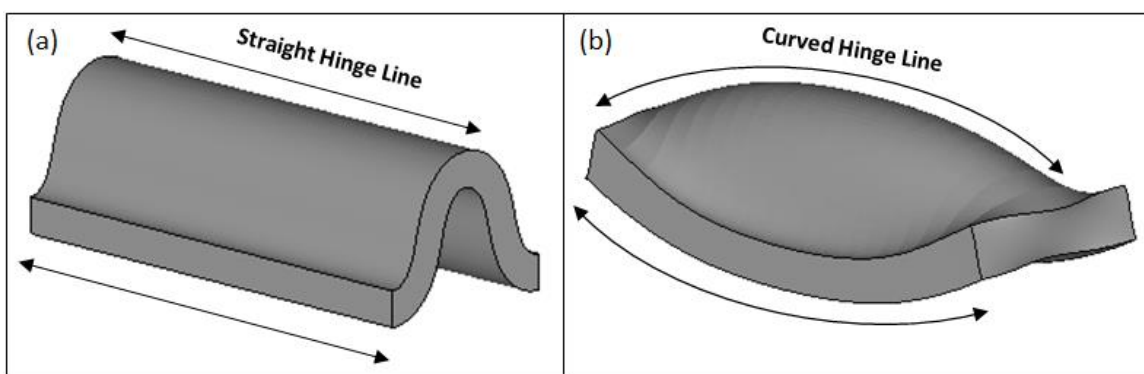
Figure 1.3. Cylindrical vs. non-cylindrical fold geometries. (a) Cylindrical fold with a constant geometry along the fold hinge. (b) Pericline with a changing geometry along the fold hinge.

closely follows the procedure presented by Eckert et al. (2014), while introducing an additional dimensional component, which allows for the generation of more complex fold geometries. Fracture occurrence can be predicted by combining the complete effective stress tensor obtained from the finite element model [FEM], with a particular failure criterion at any point in the fold. The timing of fracture initiation is of critical importance in understanding permeability and porosity changes, fluid flow patterns, and fluid accumulation potential within a folded rock structure. This methodology provides a

means of distinguishing between the fractures that formed during folding, and the fractures that formed post-folding; information that cannot be readily determined from surface field studies or subsurface geophysical investigations.

1.2. LITERATURE REVIEW

Of the vast literature that exists on the subject of buckle folding, most studies are based on the foundation of classical single-layer fold theory presented in the classic works of Biot (e.g., 1957, 1959, 1961), and Ramberg (e.g., 1959, 1961, 1963). This theory concerns the buckling of an isolated and competent viscous, elastic, or viscoelastic layer embedded in a less competent matrix. If the competent layer is given small sinusoidal perturbations of different wavelengths, it is predicted that one of the perturbations will amplify at a greater rate than all the others. The wavelength of this particular perturbation is termed the dominant wavelength (λ_d).

One common assumption in most studies on buckle folding is that buckle folds are cylindrical and maintain a constant geometry along the fold hinge. For this reason a 2D analysis of buckle folding is deemed sufficient for most applications. However, field studies of natural folds, as well as experimentally produced folds, have shown that while buckle folds may maintain a cylindrical shape over much of their length, but they do eventually die out (sometimes very abruptly) along their hinges (Price and Cosgrove, 1990). This knowledge calls to attention, the need for a 3D analysis of buckle folds in order to obtain a complete picture of the geometric and mechanical changes that occur during the folding process.

1.2.1. Non-cylindrical Folding in Three Dimensions. The majority of studies on folding in 3D have focused on analysis of experimentally produced folds using rock analogue materials such as modeling clay or paraffin wax. Experimentally generated buckle folds have proven to be a useful tool for investigating 3D fold geometries created after a single deformation event (e.g., Dubey and Cobbold, 1977; Ghosh et al., 1995; Zulauf and Zulauf, 2005), two successive deformation events (e.g., Odonne and Vialon, 1987; Grujic, 1993; Johns and Mosher, 1996), and as a result of gravity gliding (e.g., Blay et al., 1977; Guterman, 1980). These studies produced folds bearing a close

geometric resemblance to many natural folds, and primarily focused on the geometries and fold interference patterns that arise for each study's respective mode of deformation. Ghosh and Ramberg (1968) and Skjernaa (1975) went beyond studying a single mode of deformation, and made direct comparisons between fold geometries that develop as a result of a single period of compression in one direction, a single period of compression in two directions (constriction), and two successive periods of compression in two directions (superimposed folding). Both studies showed that the resulting structures produced from shortening in two directions were highly complex and diversely oriented, with simplistic dome and basin structures only appearing in the early stages of constriction. It has also been shown for both of these studies that buckle folds generated from compression in a single direction often deviate from a cylindrical geometry, and moreover, that non-cylindrical folds are not necessarily indicative of shortening in two directions.

The geometric complexity of non-cylindrical folding in 3D has also given incentive to the study of tools that aid in the geometric description of folds, such as fold interference pattern classification and the use of differential geometry on folded surfaces. Theissen and Means (1980) proposed a modification to the traditional Ramsay (1967) classification of interference patterns by introducing a new parameter that avoids several ambiguities associated with Ramsay's classification scheme (Figure 1.4). This modification provides a superior means of determining the geometry of complicated 3D refold structures, produced by two separate episodes of folding, based solely on the 2D interference patterns that appeared on a cut section through the refold structure. Graseman et al. (2004) also built on the traditional Ramsay classification scheme by introducing three new end members of refold structures to supplement the classical types 1, 2, and 3 refold structures. The application of differential geometry to fold studies has proven to be useful in providing a detailed geometric description of folds at the surface and in the subsurface, especially with the increased availability of 3D data sets from GPS, LiDAR, and seismic surveys (Mynatt et al., 2007). Lisle and Toimil (2007) presented a method for describing the geometry of folded surfaces by calculating Gaussian curvature and mean curvature at points along the folded surfaces. They point out that the use of differential geometry combined with the 3D data sets mentioned above have provided
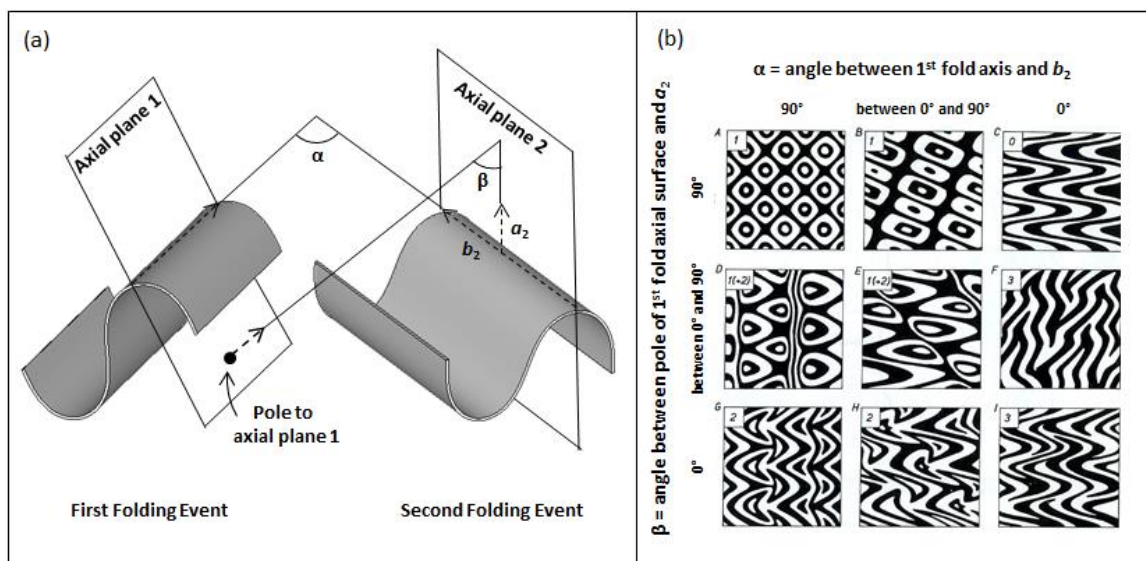
Figure 1.4. Relationship between interfering folds, and fold interference patterns. (a) Geometric relationship between two folding events. (b) Fold interference patterns that can develop for different combinations of α and β. (After Ramsay, 1967)

confirmation that natural folds often depart significantly from a cylindrical geometry and exhibit changes in amplitude, curvature, and wavelength both parallel and perpendicular to their hinges.

Only few selected studies focus on the theoretical modeling of 3D buckle folds. Ghosh (1970) performed a mathematical study on "intersecting folds of the first kind," formed during constriction. The findings show that the ratio of wavelengths of non-cylindrical folds is dependent on the ratio of the rates of compression in the two shortening directions. Fletcher (1991) derived a "thick plate" growth rate equation for an embedded viscous layer in pure shear and concluded that a cylindrical fold form, with the fold's axial plane normal to the maximum shortening directions, amplifies faster than any other form. Fletcher (1995) extended his theoretical analysis of three dimensional folding to include the folding of power-law layers, and found that buckle folds in power-law layers tend to be more cylindrical than in Newtonian viscous layers. Mulhaus et al. (1998) also performed a mathematical analysis of buckle folding for non-Newtonian layers and concluded that at least two dominant wavelengths within the plane of a folded layer are present in 3D systems.

In addition to theoretical studies of 3D buckle folding, there have also been several studies that utilized the finite element method to perform a 3D analysis of buckle folding. Kaus and Schmalholz (2006) used 3D finite element analysis [FEA] to conclude that axial planes of folds tend to form perpendicular to the maximum shortening direction, that 3D folding patterns are relatively insensitive to any shortening applied orthogonal to the maximum shortening direction, and that a 3D folding instability causes a reduction of the average differential stress in the folding layer. Using a similar approach, Schmid et al. (2008) were able to demonstrate that 3D buckle folds that form as a result of constriction, are curved and randomly oriented and do not match the theoretically predicted dome and basin structures that should arise from constriction. Both of these studies, along with the work of Schmalholz (2008), were also able to show that non-cylindrical fold shapes can form during a single, unidirectional shortening event.

1.2.2. Periclines. The results of analogue modeling and numerical simulations show that the geometry of buckle folds becomes very complicated in 3D systems. It is therefore very difficult to pinpoint a single fold form that is representative of all natural folds. However, field observations as well as experimental folding have shown that buckle folds have a tendency to form a periclinal (elongated dome or basin with a doubly plunging hinge line) geometry (e.g., Blay et al., 1977; Dubey and Cobbold, 1977; Guterman, 1980; Price and Cosgrove; 1990). Some of the best exposed periclines can be observed in the Zagros Mountains, Iran (Figures 1.5a and 1.5b).
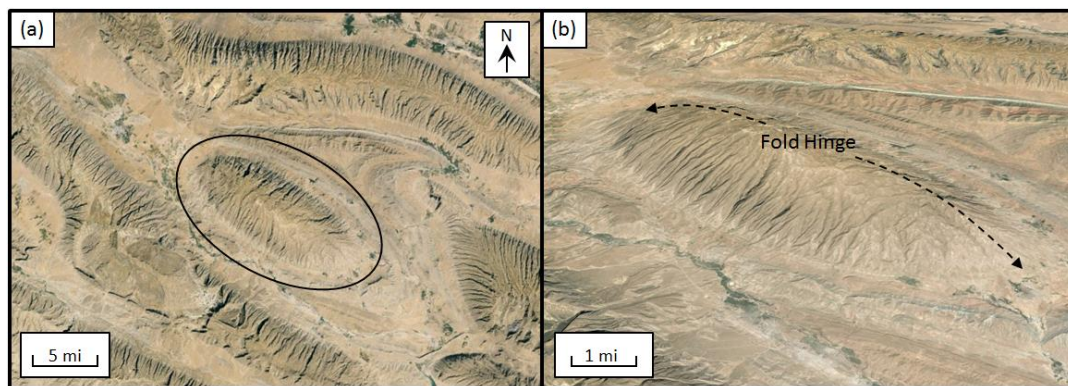
Figure 1.5. Natural pericline in the Zagros Mountains, Iran (Google Earth). (a) Plan view of the pericline (central structure outlined in black). (b) Oblique view of the pericline showing the doubly plunging hinge line (black dashed line).

A detailed description of periclines can be found in Price and Cosgrove (1990) and Cosgrove and Ameen (1999). A summary of their description of periclines is as follows:

(1) The pericline geometry is described by giving the ratio of half wavelength $(\frac{\lambda}{2})$ to hinge length (HL), also known as the aspect ratio. Most natural periclines in the upper levels of the crust have aspect ratios between 1:5 and 1:10 (Figure 1.6).

(2) Periclines initiate at their center and progressively develop outwards.

(3) The central part of a pericline typically has a chevron-like profile shape while the ends are more rounded.

(4) Due to strain softening and decreasing compressive stress adjacent to periclines they typically form in an en-echelon arrangement.

(5) Depending on the length of the separation of their hinges, periclines can either link up with other periclines to form larger periclines, or they can lock up and cease to grow.

(6) Natural periclines have been observed over a wide range of scales, from wavelengths of a few centimeters, to wavelengths of 2km or more in the periclinal folds of the Jura Mountains, and wavelengths as large as 10-20 km in the periclinal folds of the Zagros Mountains (e.g., Colman-Sadd, 1978; Blanc et al., 2003; Stephenson et al., 2007, Casciello et al., 2009).

Several studies on buckle folding using analogue materials have directly referenced a periclinal geometry for the folds that develop during the experiments. Dubey and Cobbold (1977) were able to produce non-cylindrical folds using plasticline that bore a close resemblance to the "whale-back" pericline at Bude Haven, North Cornwall, England. This recreation was achieved with a single shortening event perpendicular to the axial surface of the fold. They go on to state that the periclinal geometry is believed to be a result of the initial layer perturbations as well as a slow lengthening of the fold hinge relative to the fold amplification. Similar fold geometries have also been achieved in the works of Ghosh and Ramberg (1968), Skjernaa (1975), Blay et al. (1977), Guterman (1980), and Johns and Mosher (1996). In each of these studies the periclinal geometry was achieved with a single shortening event perpendicular
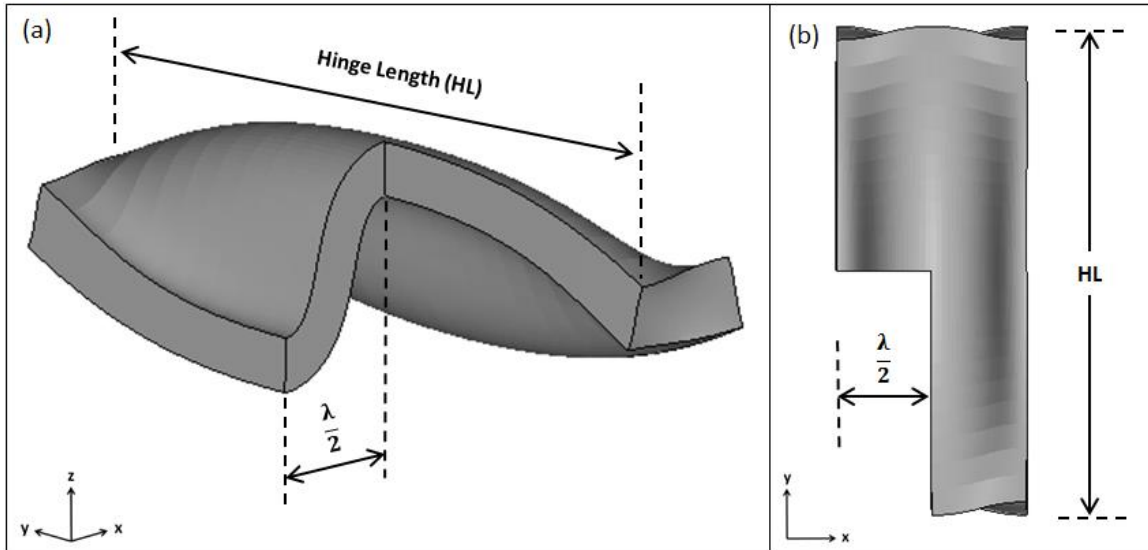
Figure 1.6. Aspect ratio ($\lambda/2$:HL) of a pericline. (a) Oblique view of the half wavelength and hinge length of a pericline. (b) Plan view of the half wavelength and hinge length of a pericline.

to the fold's axial surface, and was only prominent in the early stages of deformation. Progressive deformation led to a more cylindrical geometry.

Theoretical works provide little to no reference of periclinal geometries in buckle folding, however Treagus and Treagus (1981) provide a scenario in which periclines are the favored geometry. In their model for folding, which occurs oblique to the finite strain ellipsoid, it is suggested that for generally oblique layers, en-echelon periclines with aspect ratios between 1:6 and 1:12 will form in slight constriction, as well as in some cases for plane strain. They also suggest that in oblique layers, the axial migration of the periclines prevents the folds from ever becoming cylindrical, as opposed to a perfectly horizontal layer where the folds grow more cylindrical with progressive deformation.

1.2.3. Fracture Patterns Associated With Buckle Folding. When conducting a geomechanical analysis of folding, the timing and location of fracture initiation becomes of critical importance. The vast literature that exists on fold related fractures has primarily focused on either the mapping of fractures on surface folds (e.g., Stearns, 1964; McQuillan, 1974; Engelder et al. 1997, Wennberg et al. 2006) or the use of FEA to predict likelihood of fracture occurrence based on the state of stress (e.g., Casey and

Butler, 2004; Eckert et al., 2014; Eckert et al., 2015), and the state of strain (e.g., Dieterich, 1970; Sanz et al. 2008, Frehner, 2011).

A compilation of numerous field studies on the fracture patterns present on exposed folds has given rise to several widely accepted conceptual models of common fold related fracture patterns. Among these is Stearns' (1964; 1967) conceptual model of macrofracture patterns on the Teton Anticline, in Northwestern Montana. In this first comprehensive study on fractures related to a pericline, Stearns identifies five major fracture patterns associated with the Teton Anticline, with two of the patterns appearing far more often than the rest (Figure 1.7). Both fracture patterns consist of two conjugate shear fractures and an extension fracture with the intermediate principal stress (σ_2) always oriented perpendicular to the bedding. For the first pattern the maximum principal stress (σ_1) is oriented parallel to the strike of the bedding and the minimum principal stress (σ_3) is oriented in the dip direction. For the second pattern σ_3 is oriented parallel to the strike of the bedding and σ_1 is oriented in the dip direction. Stearns and Friedman (1972) also conclude that these two fracture patterns initiate as a result of folding itself, since the fractures maintain a consistent relationship with the bedding even when the orientation of the bedding changes rapidly.
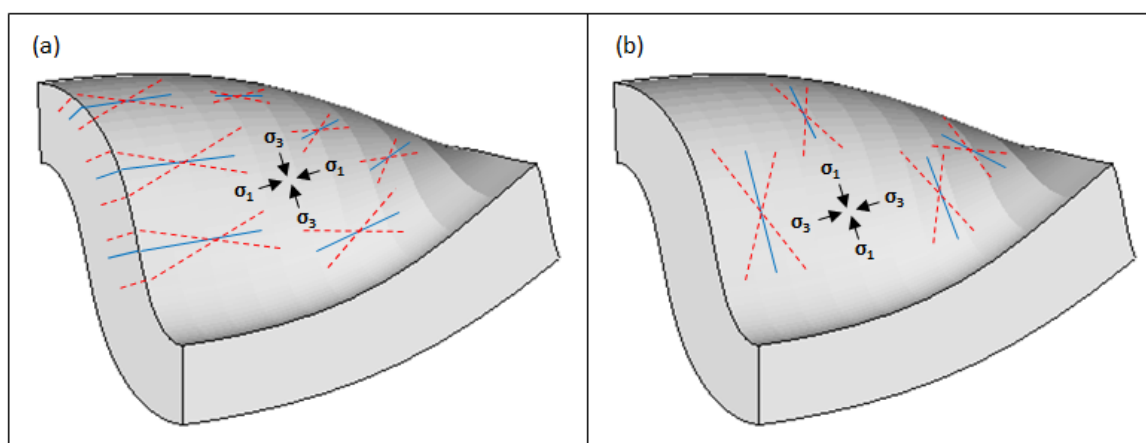
Figure 1.7. Two most common fracture patterns associated with Teton Anticline, northwestern Montana. (a) Pattern 1. (b) Pattern 2. Red dashed lines and blue lines represent conjugate shears and extension fractures, respectively. (After Stearns and Friedman, 1972)

One of the major drawbacks to using natural folds as an indicator for fracture occurrence in similar structures is the uniqueness of each fold. Folds not only vary geometrically speaking, but also by the means in which they formed. Conceptual fold fracture models such as those presented by Bergbauer and Pollard (2004), Cooper et al. (2006), and even Stearns (1964) cannot be inherently tied to buckle folding because the anticlines in each study are fault cored and were not created strictly by buckling.

Cosgrove and Ameen (1999) present one of the few conceptual fold/fracture models that can be specifically applied to buckle folds (Figure 1.8). This model is based on information obtained from previous literature as well as numerous field studies, and it includes the orientations of σ_1 and σ_3 associated with each fracture set based on the Navier-Coulomb criterion of failure. Fracture Sets 1-3 are extensional fractures with σ_3 oriented perpendicular to the failure plane (Figure 1.8a). Eckert et al. (2014) determined that Fracture Set, 1 which occurs in the outer arc of the hinge, normal to the bedding and parallel to the fold axis, can initiate for folds with a low permeability ($<10^{-19}$ m^2), and/or high viscosity ($>10^{21}$ Pa s), and/or low overburden thickness (<500m). It was also determined that Fracture Set 2 which occurs in the fold limb, normal to the bedding and parallel to the fold axis, can initiate for high permeability folds ($>10^{-16}$ m^2) after erosional unloading. Fracture Set 3, which opens normal to the bedding and the fold axis could not be explained by the modeling results as the out of plane principal stress remained compressive throughout the simulations.

Fracture Sets 4-9 (Figures 1.8b and 1.8c) are shear fractures, normal faults, and thrusts that are commonly observed on buckle folds. Normal faults at the top of the fold hinge (Set 7) and thrusts at the base of the hinge (Set 8) have been well documented in the literature and are commonly classified as strain accommodation features (Price and Cosgrove, 1990; Lemiszki et al., 1994; Frehner, 2011). Fracture Set 4 has been documented by Cosgrove and Ameen (1999) as a common fracture set occurring in the limb of buckle folds, while Sets 5 and 6 have been rarely observed. Cosgrove and Ameen (1999) also point out that the inferred orientation of the principal stresses for each fracture set suggests that the fractures did not develop at the same time, and that not all the individual fracture sets shown in Figure 1.8 are likely to develop in a single fold.
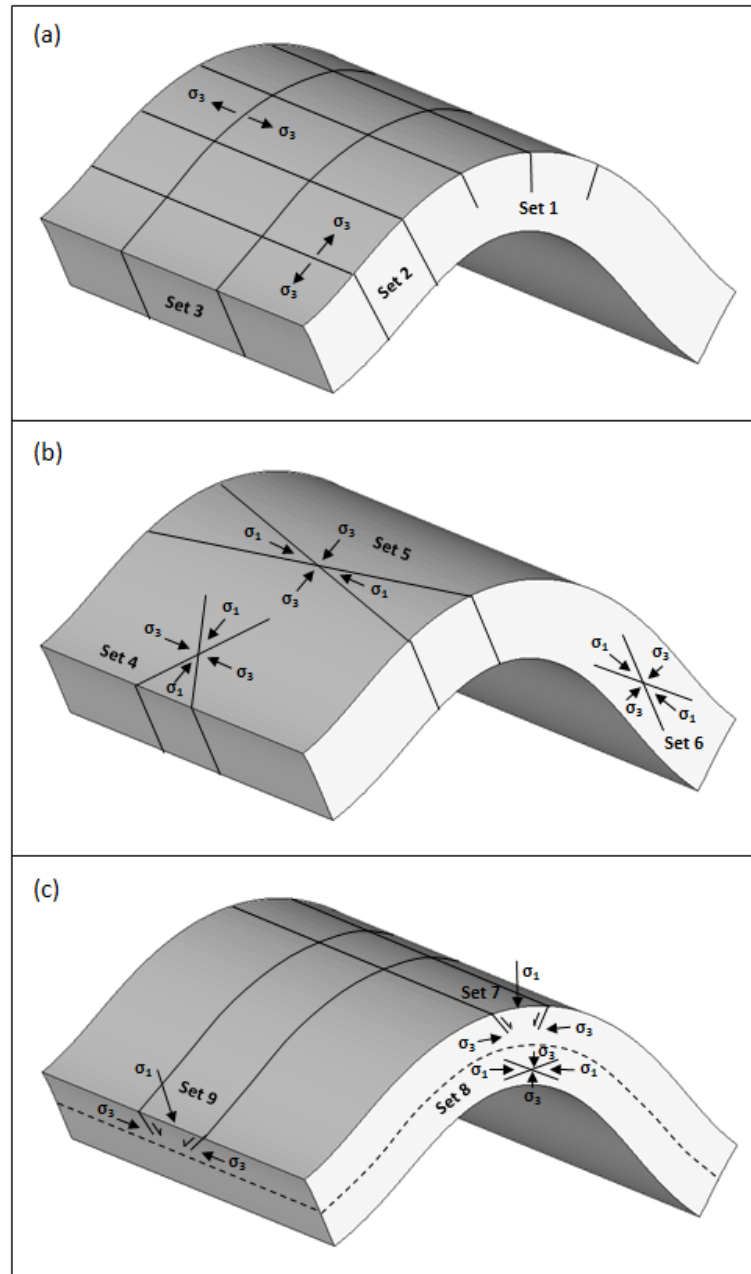
Figure 1.8. Fracture sets associated with buckle folding. (a) Extensional fractures with inferred orientations of σ_3. (b & c) Shear fractures, normal faults, and thrusts with inferred orientations of σ_1 and σ_3 (After Cosgrove and Ameen, 1999).

1.2.4. Limitations of Existing Literature. While a great amount of knowledge has been gained from studies on the structural and mechanical evolution of buckle folds, many assumptions and simplifications are made. The influence of gravity on folding is only taken into consideration for a few studies on analogue modeling (e.g., Guterman,

1980; Dixon and Tirrul, 1991), analytical solutions (e.g., Schmalholz et al., 2002), and FEA (e.g., Eckert et al., 2014; Eckert et al., 2015). In addition, Eckert et al. (2014; 2015) represent the only two studies to date that include the influence of pore pressure and permeability.

It can clearly be seen from existing literature that timing and location of fracture initiation in folded rocks is still not fully understood. Few analogue modeling studies attempt to characterize fold related fractures (Cloos, 1955) and field studies of natural folds have difficulties constraining the timing of fracture initiation. Curvature analysis studies have attempted to predict fracture occurrence based on extensional or compressional strain within the fold, but the fracturing of rocks is dependent on the state of stress (Jaeger et al., 2009), and stress and strain do not always have the same relationship (Davis et al., 2012). In order to truly understand how and when fractures initiate in folded rocks a more thorough study of the stress evolution during folding, which includes the influence of overburden stress, pore pressure, and a geologic strain rate, is necessary.

To the author's knowledge, Eckert et al., (2014) is the only study that focuses primarily on conditions that give rise to the onset of fracture initiation in folds, while including the influence of overburden stress, pore pressure, and a geologic strain rate. Their study focuses on the specific conditions that give rise to the initiation of tensile fractures in cylindrical buckle folds using 2D FEA. As it has been previously stated though, most buckle folds are not cylindrical and have a tendency to form a periclinal geometry. For this reason, a 3D FEA approach is necessary in order to include the influence of 3D fold geometries.

1.3. RESEARCH OBJECTIVES AND QUESTIONS

The main objective of this study is to use 3D FEA to simulate 3D single-layer periclinal buckle folding under in-situ stress magnitudes while including the influence of pore pressure. The FEM used in this study is capable of simulating the stress evolution over the entire buckling period as well as during erosional unloading, which occurs as a post-buckling process. By applying a specific failure criterion to the stress results from

the 3D FEM, the timing of initiation, and location of individual fracture sets can be determined and directly compared to the conceptual model for fractures associated with buckle folds presented by Cosgrove and Ameen (1999). Specific objectives of this study include the following:

(1) Setup a 3D FEM that can simulate the initiation and growth of a single-layer pericline with a single, unidirectional shortening event.

(2) Perform a sensitivity analysis of various parameters (e.g., fold shape, permeability, overburden stress, and competence contrast) to study their influence on the location and type of fractures that can develop in the hinge and limb of a pericline.

(3) Use stress results from the FEM to identify individual fracture sets based on fracture orientations relative to the folding layer and bedding planes.

These objectives will be used to address the following questions:

(1) Can periclines (i.e., non-cylindrical folds) be produced by a single, unidirectional shortening event?

(2) At what times during the folding process do shear and tensile failure occur in the hinge and limb of a pericline?

(3) What is the influence of geometric properties (aspect ratio, amplitude) and material parameters (permeability, viscosity contrast) on shear and tensile fracture initiation?

(4) Can the results from this study help determine the timing of initiation and the spatial distribution of the fracture sets presented in Cosgrove and Ameen's (1999) conceptual model?

2. THEORETICAL BACKGROUND

2.1. ROCK PROPERTIES AND ROCK MECHANICS

Any study that seeks to simulate a physical process occurring below the Earth's surface requires a thorough understanding of the materials that are present in the subsurface, and how those materials interact with one another. For a study concerning geologic folding, the materials of interest include the rocks that are being folded, as well as any fluids that are present. Rocks are complex materials consisting of a solid granular matrix and a system of interconnected pores that can store and transmit fluids. The matrix portion of rocks is an aggregate of minerals with varying compositions, grain sizes, and physical and chemical properties. The pore system within rocks is a function of the size of the individual mineral grains, and their spatial arrangement. For this reason, the total pore volume within a rock and the degree of connectivity between individual pores is constantly changing with time, and is dependent not only on a rock's composition, but also on its location in the subsurface.

The complex nature of rocks subsequently makes the prediction of their behavior, when subjected to applied loads, very complicated. The discipline of rock mechanics seeks to explain how rocks interact with one another, how fluids will move through rocks, and how rocks will fail under the influence of applied loads. In regards to rock mechanics, this study is concerned with the failure of rocks over thousands of years of continuous deformation.

In order to fully understand the methodology and results presented in this thesis, the reader must have a good comprehension of the following properties related to rocks and subsurface fluids: rock density (bulk and dry bulk), fluid density, porosity, permeability, elastic parameters (specifically Young's modulus and Poisson's ratio), and rheological behavior. In addition the reader should have a basic knowledge of the stress tensor, principal stresses, effective stresses, differential stress, mean stress, pore pressure, shear failure, tensile failure, and Mohr circles. Going forward, the author assumes these concepts to be common knowledge, and therefore a description of each concept is not included in this thesis. A detailed description of rock properties and rock mechanics can

be found in standard geology and rock mechanics text books (e.g., Fjar et al., 2008, Jaeger et al., 2009; Turcotte and Schubert, 2014).

2.2. BUCKLE FOLDING THEORY

2.2.1. Single Layer Fold Theory. Single layer fold theory centers on the buckling of an isolated competent folding layer, embedded in a less competent matrix, when subjected to layer parallel compression. The theory predicts that for a layer with numerous sinusoidal perturbations with different wavelengths, one perturbation will amplify faster than all the rest. This perturbation has a characteristic wavelength, which is termed the dominant wavelength (λ_d). Biot (1961) and Ramberg (1961) derived a mathematical relationship that predicts λ_d for a Newtonian viscous layer and matrix in plane strain, with the maximum shortening direction parallel to the folding layer. Using this relationship, λ_d is given as:

$$\lambda_d = 2\pi h \sqrt[3]{\frac{\mu_L}{6\mu_M}} \tag{1}$$

where h is the layer thickness, μ_L is the viscosity of the folding layer, and μ_M is the viscosity of the matrix. Biot (1961) also derived a mathematical relationship that predicts λ_d for the case of a competent elastic folding layer embedded in a less competent viscous matrix. This relationship is given as:

$$\lambda_d = \pi h \sqrt{\frac{E_L}{P(1 - v_L^2)}} \tag{2}$$

Where E_L is the Young's Modulus of the folding layer, P is the layer-parallel stress in the folding layer, and v_L is the Poisson's ratio of the folding layer.

Schmalholz and Podladchikov (1999) later derived a dominant wavelength solution for the buckling of a competent viscoelastic layer embedded in a less competent viscous matrix. Their primary motivation in deriving this solution was to resolve some of

the problems associated with equations (1) and (2). Among these problems was the assumption that buckle folding could be approximated as a purely viscous or a purely elastic deformation mode without any true knowledge of which deformation mode is dominant. They present a parameter, termed the dominant wavelength ratio (R), which predicts, whether buckling is dominated by viscous or elastic behavior. R is defined as the ratio of the viscous dominant wavelength (λ_{dv}) over the elastic dominant wavelength (λ_{de}):

$$R = \frac{\lambda_{dv}}{\lambda_{de}} = \sqrt[3]{\frac{\mu_L}{6\mu_M}} \sqrt{\frac{P}{G}} \tag{3}$$

where G is the shear modulus of the folding layer. If $R < 1$ then λ_d is approximated by equation (1), and if $R > 1$ then λ_d is approximated by equation (2). Solutions to the approach by Schmalholz and Podladchikov are applicable to layers that exhibit a Maxwell viscoelastic rheological behavior (Jaeger et al., 2009), which can be represented as a spring and a dashpot in series (Figure 2.1). In this setup the spring acts as the elastic (instantaneous) response of a material to an applied load while the dashpot acts as the Newtonian viscous (time-dependent) response.
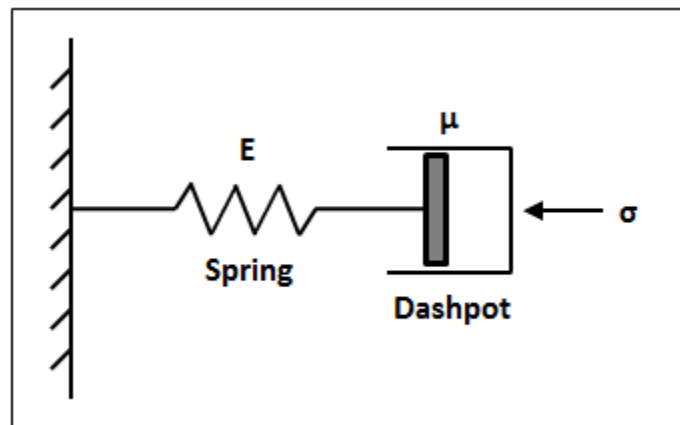
Figure 2.1. Mechanical model of a spring and a dashpot in series to represent Maxwell viscoelastic behavior. Under a continuous applied load (σ) the spring will rapidly deform elastically and then gradually return to its initial undeformed state as the dashpot begins to deform viscously.

2.2.2. Stress Distribution and Evolution in Buckle Folds. Fracture orientation in rocks is dependent on the orientation of the principals stresses at the time of failure. The dynamic nature of folding gives rise to continuously changing principal stress orientations within the folding layer. Dietrich and Carter (1969) analyzed stress distributions in a high amplitude 2D viscous fold, embedded in a less competent viscous matrix, using a modified version of the finite element method. Figure 2.2 shows the orientations of σ_1 at various stages of shortening for a fold with a viscosity contrast $(\frac{\mu_L}{\mu_M})$ of 42, a wavelength over thickness ratio $(\frac{\lambda}{h})$ of 12, and an initial fold amplitude (A_0) of 0.1h. In the early stages of shortening, σ_1 is oriented parallel to the folding layer and is highly compressive. In the later stages of shortening, fold amplitude increases, and σ_1 magnitudes and orientations change in both the limb and hinge of the fold. Along the limb, σ_1 begins to decrease in magnitude, and also begins to rotate to increasingly higher inclinations to the folding layer. In the outer arc of the fold hinge, σ_1 becomes oriented perpendicular to the folding layer, and decreases rapidly in magnitude as a result of layer parallel extension. In the inner arc of the fold hinge, σ_1 remains parallel to the folding layer, and increases in magnitude as a result of layer parallel compression. The results from the simulations by Dieterich and Carter also show that low magnitude layer-parallel tensile stresses are expected to develop in the outer arc of the fold hinge.
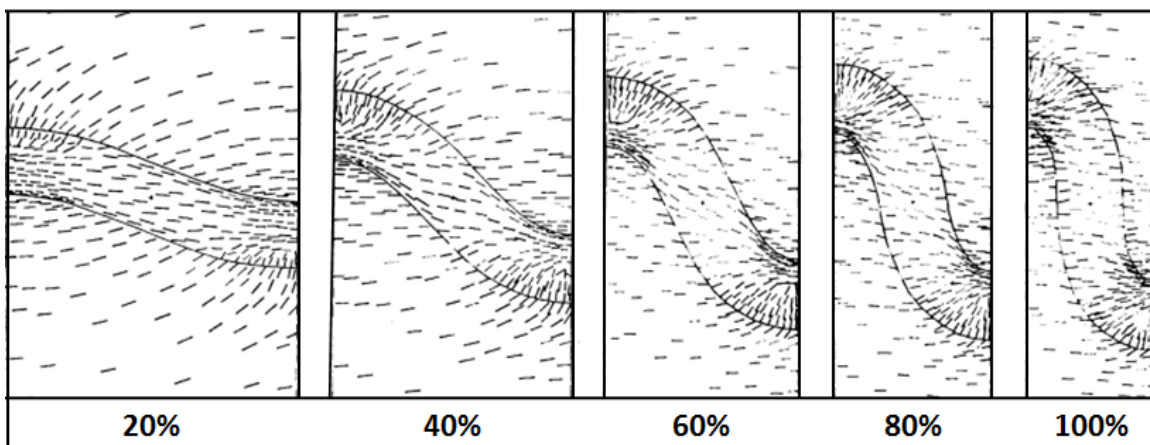
Figure 2.2. Orientations of σ_1 within a buckle fold for various stages of shortening (After Dieterich and Carter, 1969).

While fracture orientation depends on the orientation of the principal stresses, a rocks true ability to fracture depends on the magnitudes of the effective principal stresses. Eckert et al. (2014) document the temporal evolution of the minimum effective principal stress (σ'_3) magnitude as part of their study on the initiation of tensile fractures during the buckling of a 2D viscoelastic fold embedded in a less competent viscoelastic matrix. In the hinge of the fold (Figure 2.3), σ'_3 can be observed to evolve differently for the outer arc and inner arc. In the outer arc of the hinge (Figure 2.3b), σ'_3 initially increases up to a certain point. At this point σ'_3 decreases rapidly and then steadily increases again. For the case of Element 1 this rapid decrease occurs at ~16% shortening and the lowest magnitude of σ'_3 is reached at ~26% shortening. This rapid drop in σ'_3 indicates that for Element 1, tensile fractures will be most likely to initiate during the 16-26% shortening window. The temporal evolution of σ'_3 in the inner arc of the hinge (Figure 2.3c) follows a trend very similar to that of the fold limb (Figures 2.4b and c). For both cases σ'_3 steadily increases with only some minor drops in σ'_3 for select elements. These trends indicate that tensile failure is unlikely to occur in the inner arc of the fold hinge or in the fold limbs unless σ'_3 is tensile at the start of the shortening period.
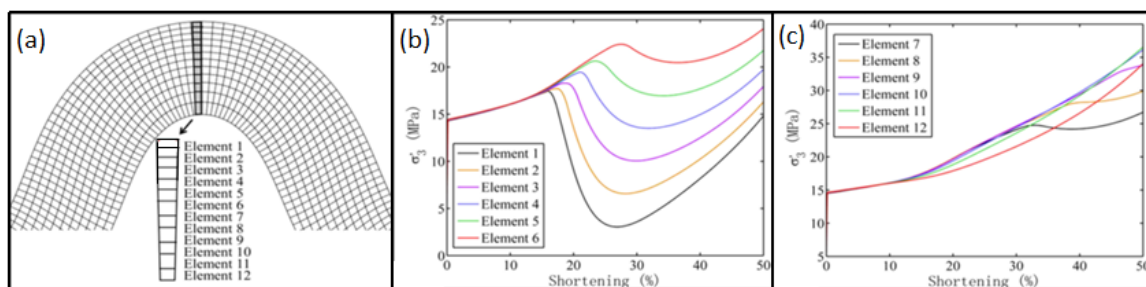
Figure 2.3. Temporal evolution of σ'_3 magnitudes in the fold hinge. (a) Illustration of elements 1-12 in the fold hinge. Plot of σ'_3 vs percent shortening included for elements 1-6 (b) and 7-12 (c) (After Eckert et al., 2014).

2.2.3. Strain Distribution in Buckle Folds. Strain within a folding layer can be accommodated in a number of different ways depending on the material properties of the layer, as well as the fold geometry (Ramsay, 1967). Many studies using finite element analysis (e.g., Dieterich and Carter, 1969; Parrish, 1973; Frehner, 2011) have shown that
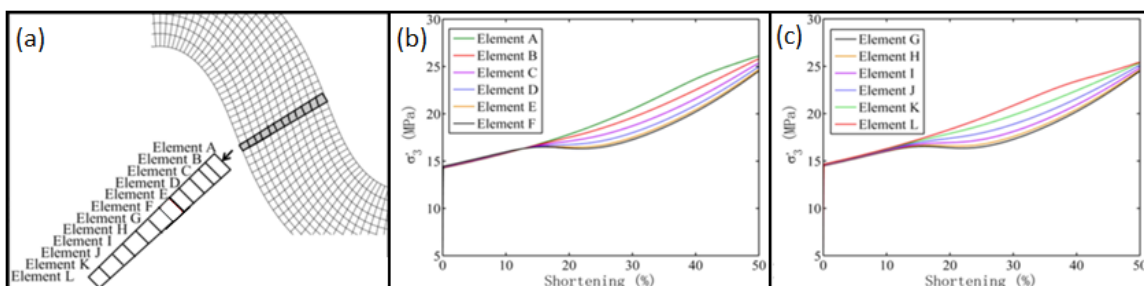
Figure 2.4. Temporal evolution of σ'₃ magnitudes in the fold limb. (a) Illustration of elements A-L in the fold limb. Plot of σ'₃ vs percent shortening included for elements A-F (b) and G-L (c) (After Eckert et al., 2014).

single layer buckling of a competent layer embedded in a less competent matrix will produce parallel folds (folds that retain a constant orthogonal thickness). There are two well-known end members of internal deformation associated with parallel folding: tangential longitudinal strain [TLS] and flexural flow [FF] (Ramsay, 1967).

TLS is characterized by principal strain axes that are oriented either parallel or perpendicular to the folding layer and by strain concentration in the fold hinges (Figure 2.5a). Within TLS folds lies a surface where the strain is zero. This surface, called the neutral surface, separates regions of layer parallel extension from layer parallel compression in the hinge of the fold. TLS folding is typically associated with homogenous, isotropic materials (Price and Cosgrove, 1990).

FF is characterized by simple shear strain that is concentrated in the limb of the fold (Figure 2.5b), and zero strain in the fold hinges. This type of folding is analogous to the bending of a stack of papers where the individual sheets slide past one another. FF folding is typically associated with materials that exhibit a high degree of mechanical anisotropy (Price and Cosgrove, 1990).

Shimamoto and Hara (1976), Lan and Hudleston, (1995), and Huddleston et al. (1996) all use finite element analysis to show that TLS appears to be the dominant mechanism for viscous folding models. It should be noted however that studies of natural folds have shown that most folds exhibit strain patterns that represent some combination of TLS and FF. (Ramsay, 1967).
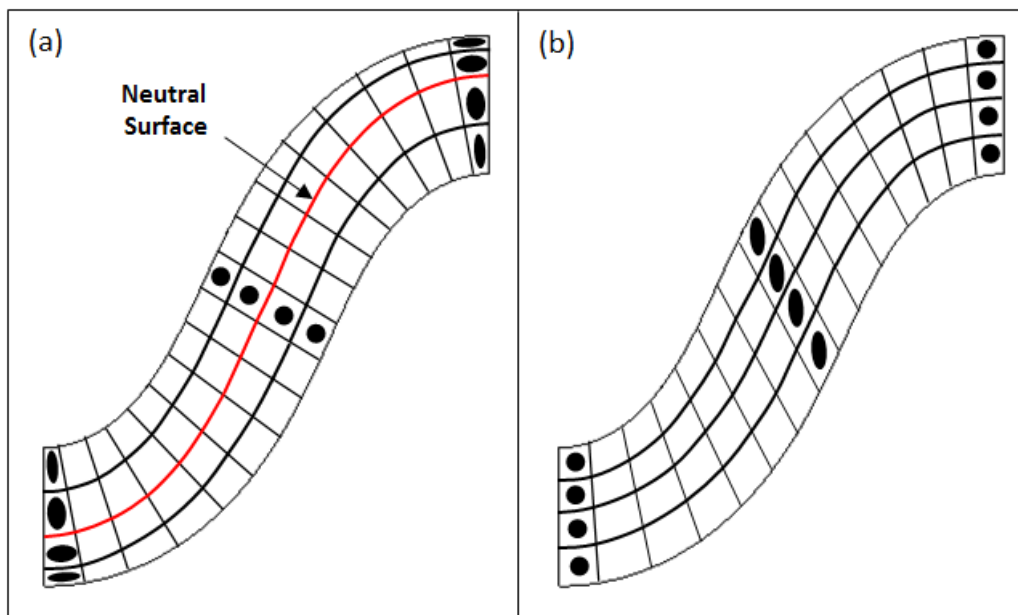
Figure 2.5. Strain distribution in a fold developed by tangential longitudinal strain (a) and flexural flow (b). Strain ellipses show that strain is concentrated in the hinges for a TLS fold and in the limbs for a FF fold (after Hudleston et al., 1996).

2.3. FRACTURE PREDICTION

The following paragraph is a brief summary of brittle failure of rocks. A more thorough description of the deformation and failure of rocks can be found in Jaeger et al. (2009).

Rocks can behave in a number of ways when subjected to applied loads. In some cases the rock can deform, and subsequently return to the original undeformed state when the applied load is removed (elastic deformation). In other cases the rock can experience permanent deformation while still being able to sustain increasing applied loads (ductile deformation). When applied loads become too large though, and stresses can no longer be accommodated by elastic or ductile deformation, the rock will fail abruptly; termed brittle failure. The two basic types of brittle failure include shear fractures, which are characterized by shear displacement along the fracture surface, and tensile fractures, which are characterized by an opening of the fracture and no shear displacement. Rock failure can be analyzed by combining the state of stress, with rock strength, and a particular failure criterion (e.g., Mohr-Coulomb, Von Mises, Hoek-Brown, Griffith).

This analysis can determine whether a rock will fail, how it will fail (i.e., shear or tensile fractures), and the fracture orientation.

2.3.1. Combined Griffith/Navier-Coulomb Failure Criterion. Experimental deformation of rocks under triaxial compression have yielded two common relationships between principal stresses at failure: linear and non-linear (Figure 2.6). The Navier-Coulomb and Griffith criteria of brittle failure have been examined to explain both of these relationships (Price and Cosgrove, 1990).
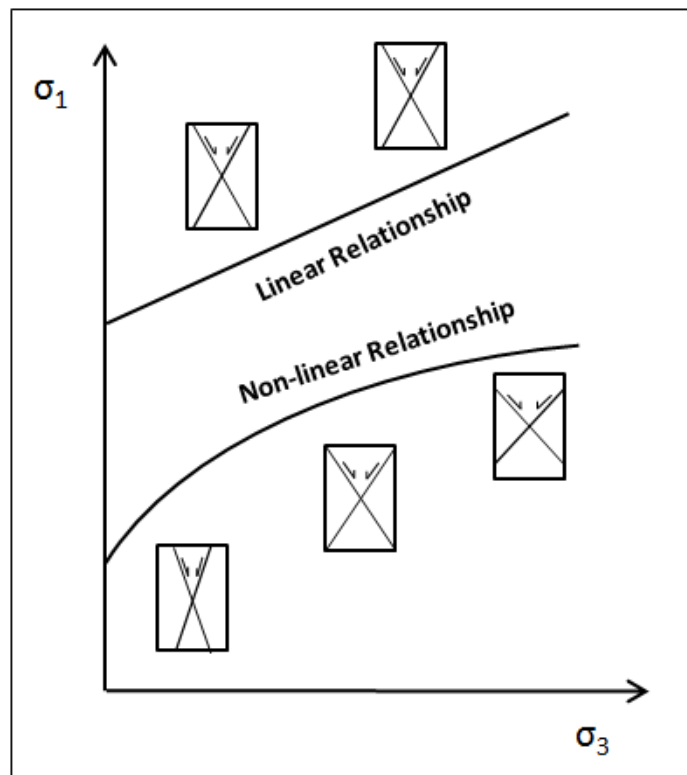
Figure 2.6. Linear and non-linear relationships between principal stresses at failure. Note that for a linear relationship the acute angle between fracture planes remains the same with an increase in σ_3. For a non-linear relationship, the acute angle between fracture planes increases with an increase in σ_3 (After Price and Cosgrove, 1990).

The Navier-Coulomb criterion of brittle failure predicts that shear failure will occur on a surface if the shear stresses become high enough to overcome the cohesive strength of a rock, and the frictional resistance to sliding (Price and Cosgrove, 1990).

This criterion can be plotted as a failure envelope on a Mohr stress diagram (Figure 2.7a) using the following equations:

$$\tau = C_0 + \sigma_n \mu \tag{4}$$

$$\mu = \tan\psi \tag{5}$$

where τ and σ_n are the shear and normal stresses, respectively, which are acting on the surface, C_0 is the cohesion of the rock, μ is the coefficient of friction, and ψ is the angle of internal friction. The linear geometry of the failure envelope for the Navier-Coulomb failure criterion allows for the prediction of the acute angle between σ_1 and the shear plane. This angle, termed the failure angle (θ), is given by:

$$\theta = 45 - \frac{\psi}{2} \tag{6}$$

On a Mohr stress diagram, the acute angle between the normal stress axis and the normal to the failure envelope is equivalent to 2θ (Figure 2.7a). Since the sign of θ does not influence the shear stress, two conjugate shear planes of failure are possible at angles of $\pm\theta$ to σ_1 (Figure 2.7b).
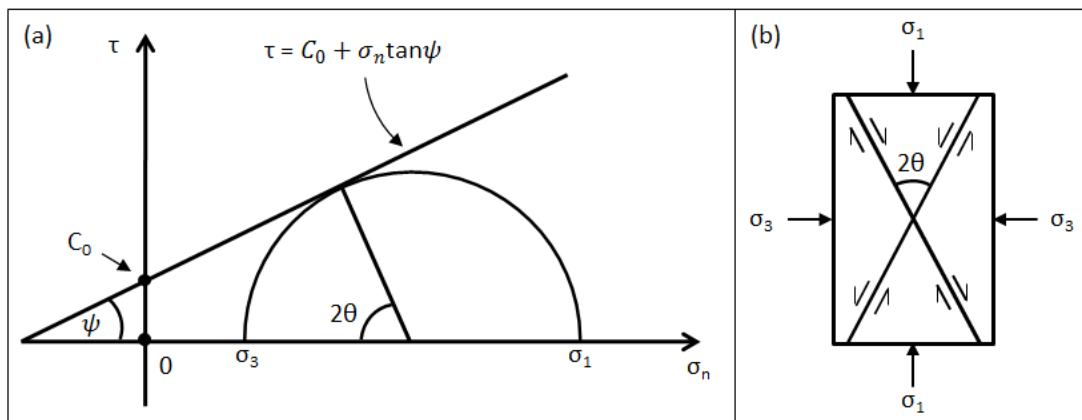
Figure 2.7. Navier-Coulomb brittle failure criterion. (a) Navier-Coulomb failure envelope on a Mohr stress diagram. (b) Conjugate shear fractures that can initiate based on the Navier-Coulomb criterion. σ_1 bisects the acute angle (2θ) between the two failure planes.

The Griffith criterion of brittle failure was developed based on the assumption that rocks contain numerous elliptical shaped micro-cracks (Price and Cosgrove, 1990). Griffith (1925) suggested that stress concentrations around the tips of these cracks could explain the vast differences observed between theoretical and experimental values of a materials tensile strength. Griffith ultimately developed a non-linear relationship between principal stresses at the time of failure, which, when expressed as a failure envelope on a Mohr's stress diagram, takes the form:

$$\tau^2 + 4T\sigma_n - 4T^2 = 0 \tag{7}$$

where T is the tensile strength of the rock. It can be seen from this equation that the cohesion (τ when $\sigma_n = 0$) of the Griffith failure criterion is twice the tensile strength of the rock.

Using the concept that a compressive stress field will cause the Griffith micro-cracks to close, and subsequently allow shear stresses to be generated along the surfaces of the cracks, a hybrid failure criterion can be implemented which includes the Griffith failure criterion and the Navier-Coulomb failure criterion (McClintock and Walsh, 1962). The shape of the failure envelope for the combined Griffith/Navier-Coulomb failure criterion can be determined by combining the two envelopes from each respective individual failure criterion. The failure envelope in tension is determined using equation (7). In compression, the failure envelope takes the following form:

$$\tau = 2T + \sigma_n\mu \tag{8}$$

which is identical to equation (4), except C_0 has now been replaced with 2T. A benefit of using the combined Griffith/Navier-Coulomb failure criterion is that a distinction can be made between whether tensile failure or shear failure will occur based on the differential stress (σ_d). If $\sigma_d > 4T$ (shear regime), the Mohr circle will touch the shear failure envelope before $\sigma_3 = -T$, and thus only shear failure is possible (red circle in Figure 2.8). Shear failure can be separated into two categories: extensional shear failure, which
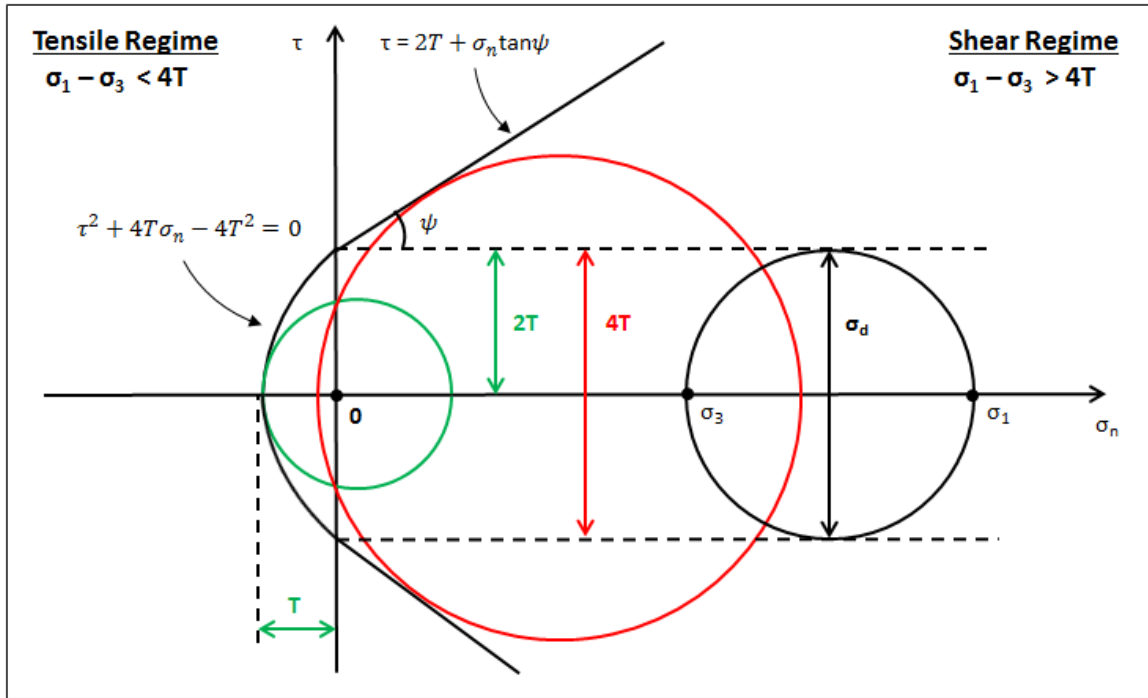
Figure 2.8. Combined Griffith/Navier-Coulomb failure criterion. In the tensile regime only tensile failure is possible (green circle). In the shear regime only shear failure is possible (red circle).

requires $4T < \sigma_d < 5.66T$; and compressional shear failure, which requires $\sigma_d > 5.66T$ (Sibson, 2003). For the purpose of this study, however, shear failure is only considered as a whole, and no distinctions are made between extensional shear failure and compressional shear failure. If $\sigma_d < 4T$ (tensile regime), the radius of the Mohr circle never becomes large enough to touch the shear failure envelope, and due to the shape of the Griffith parabola, failure can only occur when $\sigma_3 = -T$ (green circle in Figure 2.8).

2.3.2. Fracture Potential. When trying to predict fracture occurrence in a geologic structure by means of stress analysis, three issues must be addressed. First it must be determined if fractures will actually be initiated. Second, if fractures are initiated, a distinction must be made between shear fractures and tensile fractures. Third, how do fractures evolve once they initiate? As will be seen in later sections, the methodology presented in this study is not capable of accounting for fracture propagation after initiation, and thus the third issue is beyond the scope of this investigation. Connolly and Cosgrove (1999), and Eckert and Connolly (2004) utilize a concept called

the fracture potential method [FP], based on the combined Griffith/Navier-Coulomb failure criterion, which addresses the first two issues. In addition, the geometric relationship between the principal stresses and the failure planes for the combined Griffith/Navier-Coulomb failure criterion allows for the orientations of the failure planes to be calculated using the complete stress tensor.

Fracture potential can be further subdivided into two categories: fracture potential in the shear regime [sFP], and fracture potential in the tensile regime [tFP]. Since failure in the shear regime can only occur if the Mohr circle touches the shear failure envelope, sFP can be defined by the relationship between the actual differential stress and the critical differential stress at failure ($\sigma_{d,crit}$), for the same value of mean stress (σ_m). This relationship can be expressed using the following ratio:

$$sFP = \frac{\sigma_d/2}{\sigma_{d,crit}/2} \tag{9}$$

If this ratio reaches 1 it indicates that the Mohr circle has touched the shear failure envelope, and shear failure occurs (Figure 2.9a). From Figure 2.9a it can be seen that $\sigma_{d,crit}$ can be determined using the following equations:

$$\frac{\sigma_{d,crit}}{2} = (x + \sigma_m)\sin\psi \tag{10}$$

$$x = \frac{C_0}{\tan\psi} \tag{11}$$

where $C_0 = 2T$. Substituting equations (10) and (11) into equation (9) gives sFP as:

$$sFP = \frac{\sigma_d}{2(C_0\cos\psi + \sigma_m\sin\psi)} \tag{12}$$

In addition it should be noted that if $\sigma_d < 4T$, shear failure is not possible, and sFP is assigned a value of 0.
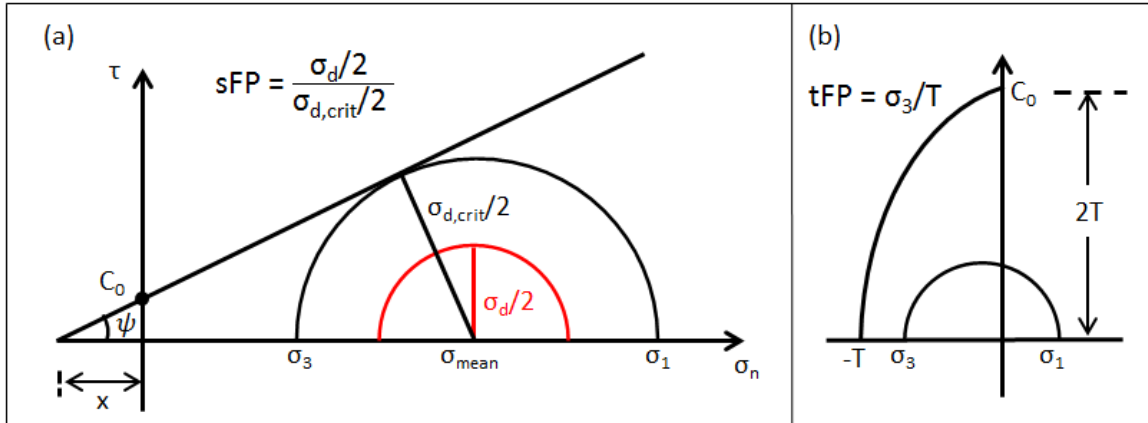
Figure 2.9. Illustration of the fracture potential concept using Mohr stress diagrams. (a) sFP is determined by taking the ratio of the actual differential stress (σ_d for red semicircle) over the critical differential stress at failure (σ_d for black semicircle). Failure occurs when sFP = 1. (b) tFP is determined by taking the ratio of the minimum principal stress over the tensile strength of the rock. Failure occurs when tFP = -1.

In the tensile regime, shear failure is not possible, and tensile failure can only occur when σ_3 = -T. Thus, tFP can be defined by the ratio of σ_3 over T:

$$\text{tFP} = \frac{\sigma_3}{T} \qquad (13)$$

If this ratio reaches -1 it indicates that σ_3 = -T, and tensile failure occurs (Figure 2.9b). Since the Mohr circle is unable to reach the Griffith parabola in the shear regime, tFP is assigned a value of 0 when $\sigma_d > 4T$. tFP is also assigned a value of 0 for an additional case when $\sigma_d < 4T$ and $\sigma_3 > 0$. For this case the Mohr circle lies in the tensile regime, however, since $\sigma_3 > 0$ stresses never become tensile, tensile failure will not occur.

2.4. STEREOGRAPHIC PROJECTIONS AND STEREONETS

In the world of geology, stereographic projections are a useful method for visualizing the 3D orientations of lines and planes using a 2D surface. If the lines and planes are thought of as passing through the center of a sphere (Figure 2.10a), their intersection with the lower hemisphere is the projection (Figure 2.10b). The Schmidt equal-area stereonet is one of the most versatile tools for plotting stereographic

projections (Davis et al., 2012). To plot the orientations of lines and planes on a stereonet only two measurements are necessary; azimuth and inclination. Azimuth is measured clockwise from north with values that range from $0°$-$360°$. Inclination is measured from a horizontal plane with values that range from $0°$-$90°$. For the purpose of this study only a basic knowledge of how lines and planes are plotted on a stereonet is necessary. Additional details regarding relationships between lines and planes on a stereonet can be found in standard structural geology textbooks (e.g., Ragan, 1973; Davis et al., 2012).
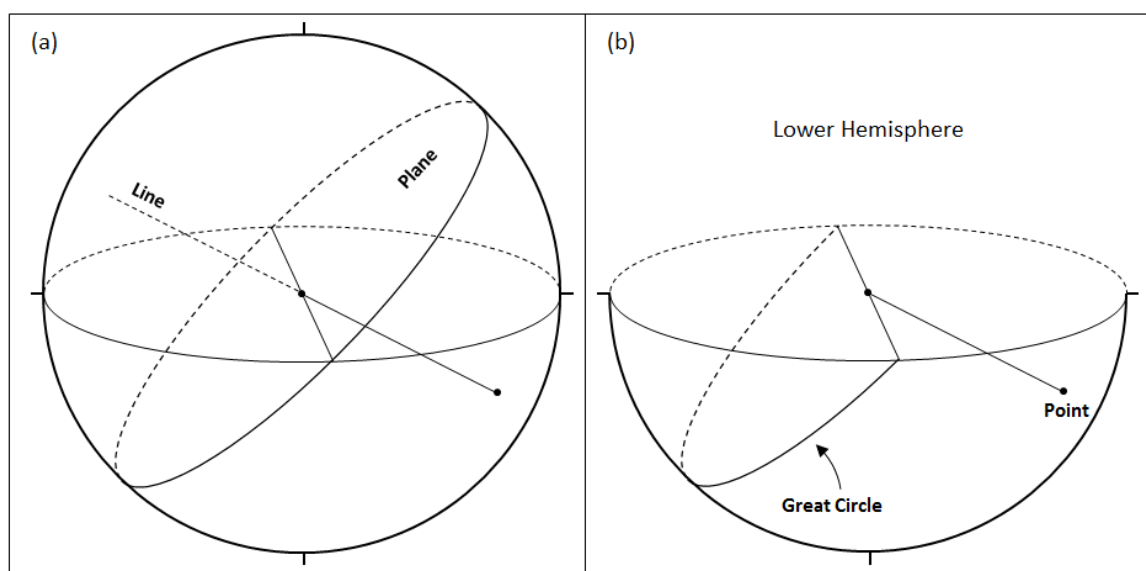
Figure 2.10. Stereographic projection of a line and a plane. Lines and planes passing through the center of a sphere (a) project as points and great circles, respectively, in the lower hemisphere (b).

2.4.1. Plotting Lines on a Stereonet. The azimuth and inclination of a linear feature are referred to as the trend and plunge, respectively. For a line with a trend of $30°$ and a plunge of $60°$ the procedure for plotting the trend and plunge on a stereonet is as follows:

(1) Place a tracing paper overlay on the stereonet, being sure that north (N) corresponds to an azimuth of $0°$ (Figure 2.11a).

(2) Locate the azimuth marker of 30 °on the outer perimeter of the stereonet and mark it as point x (Figure 2.11a).

(3) Rotate the overlay until the point x is at the top end of the north-south line of the stereonet (Figure 2.11b).

(4) Plot the plunge as point y by counting in 60 °from the perimeter of the stereonet (Figure 2.11b).

(5) Rotate the overlay back so that point x is once again at the 30 °azimuth marker. The resulting point y represents the stereographic projection of a line with a trend of 30 °and a plunge of 60 °(Figure 2.11c).
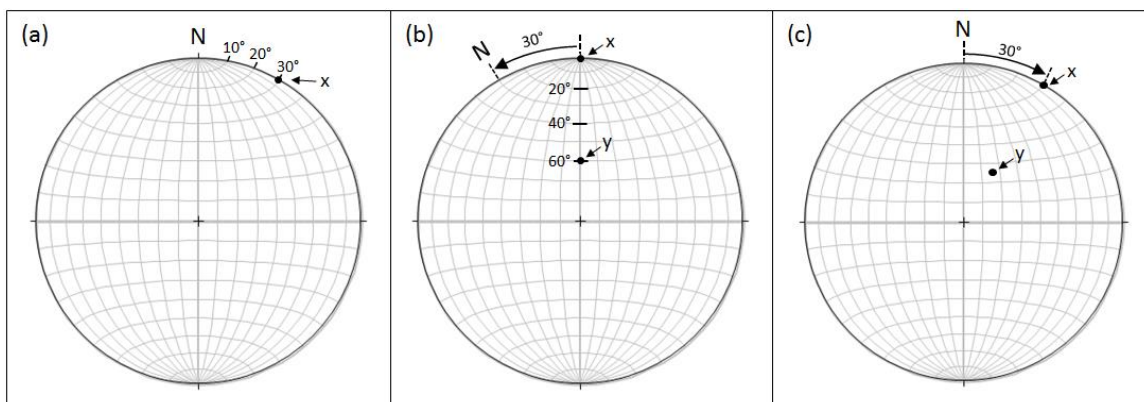
Figure 2.11. Procedure for plotting the projection of a line with a trend of 30 °and a plunge of 60 °on a stereonet. (a) Mark the trend of the line along the perimeter of the stereonet with the point x. (b) Rotate overlay until x is at the top of the north-south line. Plot the plunge of the line as point y by counting in 60 °from the stereonet perimeter. (c) Rotate overlay back to original position. Point y represents the projection of a line with a trend of 30 °and a plunge of 60 °.

2.4.2. Plotting Planes on a Stereonet. The azimuth and inclination of a planar feature are referred to as the strike and dip, respectively. For a plane with a strike of 30 ° and a dip of 30 °the procedure for plotting the strike and dip on a stereonet is as follows:

(1) Place a tracing paper overlay on the stereonet, being sure that north (N) corresponds to an azimuth of 0 °(Figure 2.12a).

(2) Locate the azimuth marker of 30 °on the outer perimeter of the stereonet and mark it as point x (Figure 2.12a).

(3) Rotate the overlay until the point x is at the top end of the north-south line of the stereonet (Figure 2.12b).

(4) Plot the dip as a great circle by counting in 30° from the right perimeter of the stereonet. The dip direction follows the right-hand rule where the thumb points in the strike direction and the rest of the fingers point in the dip direction (Figure 2.12b).

(5) Rotate the overlay back so that the point x is once again at the 30° azimuth marker. The resulting great circle represents the stereographic projection of a plane with a strike of 30° and a dip of 30° (Figure 2.12c).
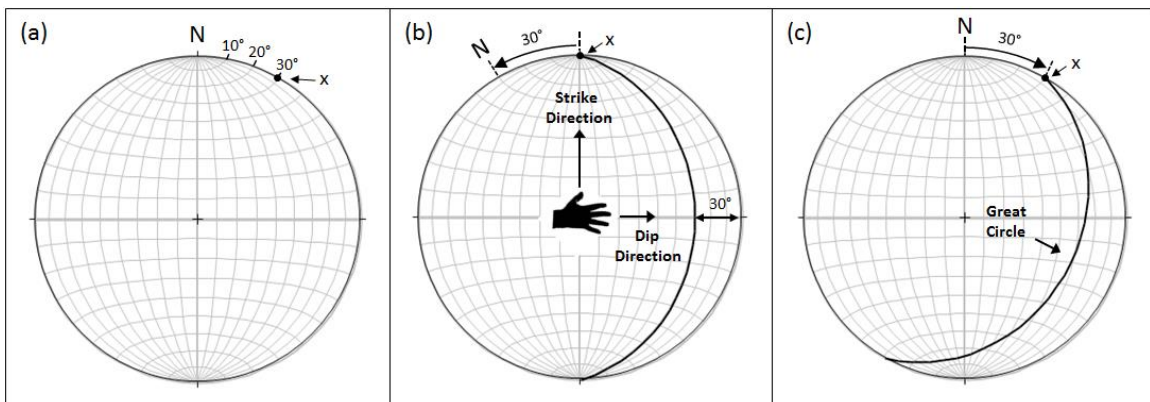
Figure 2.12. Procedure for plotting the projection of a plane with a strike of 30° and a dip of 30° on a stereonet. (a) Mark the strike of the line along the perimeter of the stereonet with the point x. (b) Rotate overlay until x is at the top of the north-south line. Plot the dip of the plane as a great circle by counting in 30° from the right side of the stereonet perimeter (use right hand rule to determine dip direction). (c) Rotate overlay back to original position. Great circle represents the projection of a plane with a strike of 30° and a dip of 30°.

2.5. FINITE ELEMENT METHOD

Many physical phenomena in nature can be mathematically described as a continuous process using partial differential equations [PDE], where a dependent variable is a function of more than one independent variable. These PDE's can be solved analytically to obtain unique solutions of the unknown dependent variable at various times and locations within a physical body. In some cases, however, the geometry of the

physical body and/or the boundary conditions associated with the PDE's are too complex, and an analytical solution does not exist. When analytical solutions cannot be determined, numerical methods such as the finite element method may be used to give an approximate solution of the unknown variable.

What follows in this section is a basic summary of two approaches to the finite element method: the standard discrete system, and the generalized finite element method. A complete mathematical description of the finite element method is beyond the scope of this study. A more detailed investigation of the finite element method is given in Zienkiewicz et al. (2005).

2.5.1. The Standard Discrete System. The finite element method is built on the fundamental concept that the solution to a continuous problem (continuum) can be more easily determined if that continuum is divided (discretized) into a finite number of individual components. In engineering, this concept is analogous to discretizing a physical domain, over which a continuous physical process is acting, into a finite number of sub-domains (elements). These elements are interconnected at a number of discrete points (nodes) along the element's boundaries (Figure 2.13). The displacements of these nodes are the unknown values for the problem of interest. Assuming linear elasticity, the relationship between nodal forces and displacements for an individual element takes the following form:

$$q^e = K^e u^e + f^e \qquad (14)$$

where q^e represents the nodal forces, K^e is the element stiffness matrix, u^e represents the nodal displacements, f^e represents the nodal forces required to balance any distributed loads acting on the element, and $K^e u^e$ represents the forces induced by displacement of the nodes. If the two conditions of

    (a) displacement compatibility

       and

    (b) nodal force equilibrium

are satisfied throughout the domain, equation (14) for each individual element can be combined to give a global set of equations which can be represented as:

$$Ku + f = 0 \qquad (15)$$

where K is the global stiffness matrix.
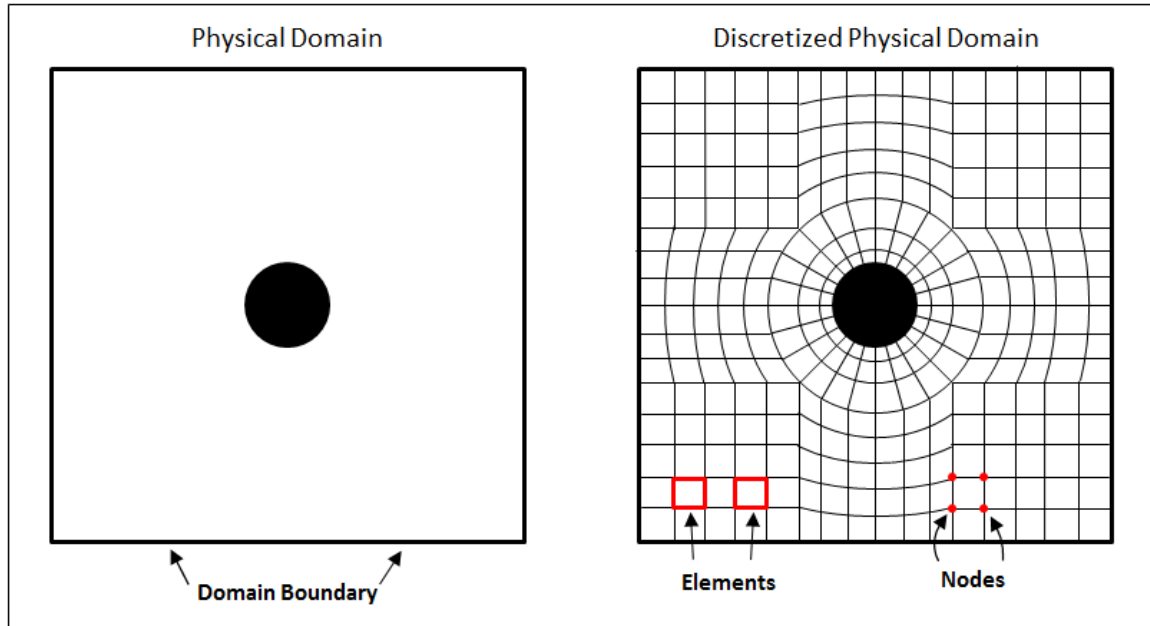
Figure 2.13. Discretization of the cross section of a borehole (physical domain) using finite elements with interconnecting nodes.

2.5.2. The General Finite Element Method. The method described in Section 2.5.1 is known as the standard discrete system, which is capable of solving for solutions of the unknown parameter (u) at the nodes of an element, while assuming linear elasticity. If a problem arises (that may or may not assume linear elasticity) which is posed in the form of a PDE with a set of boundary conditions, another method can be utilized to solve for approximations of the unknown parameter. This method, stated as the generalized finite element method, seeks approximate solutions of the unknown parameter (u) in the form:

$$u \approx \sum_{a=1}^{n} N_a \tilde{u}_a \qquad (16)$$

where N_a are shape functions given in terms of independent variables (such as spatial coordinates), and $\tilde{u}_a$ are the approximate solutions of the unknown parameter. For problems that take the form:

$$A(u) + B(u) = 0 \qquad (17)$$

where $A(u)$ represents a differential equation acting on a domain (Ω), and $B(u)$ represents boundary conditions acting on the domain boundary (Γ). $A(u)$ and $B(u)$ can be multiplied by an arbitrary function (v) and integrated to give:

$$\int_\Omega vA(u)d\Omega + \int_\Gamma vB(u)d\Gamma = 0 \qquad (18)$$

An approximation to equation (18) can be made by inserting two approximate functions; the approximate function presented in equation (16), and an additional approximate function (w) to be used in place of the arbitrary function (v):

$$v \approx \sum_{b=1}^{n} w_b \delta\tilde{u}_b \qquad (19)$$

where $\delta\tilde{u}_b$ is an arbitrary parameter. Inserting the approximations from equations (16) and (19) into equation (18) gives:

$$\delta\tilde{u}_b \left[\int_\Omega w_b A(N_a \tilde{u}_a)d\Omega + \int_\Gamma w_b B(N_a \tilde{u}_a)d\Gamma \right] = 0 \qquad (20)$$

Since $\delta\tilde{u}_b$ is arbitrary, it can be divided on both sides of the equation to give:

$$\int_\Omega w_b A(N_a \tilde{u}_a)d\Omega + \int_\Gamma w_b B(N_a \tilde{u}_a)d\Gamma = 0 \qquad (21)$$

By using a procedure known as "the Galerkin method," the approximate function (w_b) is set equal to the shape function (N_b); which results in the equation:

$$\int_{\Omega} N_b A(N_a \tilde{u}_a) d\Omega + \int_{\Gamma} N_b B(N_a \tilde{u}_a) d\Gamma = 0 \qquad (22)$$

Equation (22) is now an integral equation of the form $Ku + f = 0$, and can be used to solve for $\tilde{u}_a$, not only at the nodes of an element, but within the element and at any location along the element boundary.

3. METHODOLOGY

3.1. NUMERICAL MODELING APPROACH

Because the finite element method solves for approximate solutions of an unknown parameter, a general rule of thumb is that the more elements there are in a given domain, the lower the magnitude of any errors associated with the approximation will be, and the closer the results will be to the analytical solution (Zienkiewicz et al., 2005). The downside to introducing a large number of elements is that the resulting system of equations can become very large, making hand calculations tedious and impractical. Fortunately, the finite element method can be readily incorporated into the numerical algorithms of computer software programs; capable of handling very large element numbers, and solving very large equation systems in a matter of minutes. In order to successfully employ a computer software program that uses the finite element method to simulate a physical process, both an understanding of the equations that govern the physical process, and the ability of the software to solve those equations is necessary.

3.1.1. Governing Equations for 3D Viscoelastic Folding. This study simulates the buckling of a competent viscoelastic folding layer embedded in a less competent viscoelastic matrix. The viscoelastic rheology is incorporated by following a Maxwell model approach (e.g., Mancktelow, 1999; Schmalholz et al., 2001; Eckert et al., 2014), which allows for instantaneous linear elastic behavior for fast strain rates, and Newtonian viscous behavior for slower strain rates. For this study it is assumed that buckle folds have a constantly changing geometry along the fold axis, and thus a 3D equation system is introduced to allow for x, y, and z components of displacement during folding. The influence of pore pressure is also taken into consideration for this study by utilizing effective stress analysis.

Assuming that the material for this study consists of a compressible rock with an incompressible pore fluid (water), and that mass is conserved everywhere, the following must be satisfied: the equations of equilibrium, conservation of mass, equations of pore fluid flow, and constitutive equations for a compressible Maxwell body. Unknown parameters for the problem include: all six stress tensor components (σ_{xx}, σ_{yy}, σ_{zz}, σ_{xy}, σ_{xz},

and σ_{yz}), the pore pressure (P_p), the material velocities in the x, y, and z directions (v_x, v_y, and v_z), and the material density (ρ_m). 11 unknowns require 11 governing equations.

For a 3D body, the equations of equilibrium using effective stresses are given by (Jaeger et al., 2009):

$$\frac{\partial \sigma_{xx}}{\partial x} - \frac{\partial(\alpha P_p)}{\partial x} + \frac{\partial \sigma_{xy}}{\partial y} + \frac{\partial \sigma_{xz}}{\partial z} = 0 \tag{23}$$

$$\frac{\partial \sigma_{yy}}{\partial y} - \frac{\partial(\alpha P_p)}{\partial y} + \frac{\partial \sigma_{xy}}{\partial x} + \frac{\partial \sigma_{yz}}{\partial z} = 0 \tag{24}$$

$$\frac{\partial \sigma_{zz}}{\partial z} - \frac{\partial(\alpha P_p)}{\partial z} + \frac{\partial \sigma_{xz}}{\partial x} + \frac{\partial \sigma_{yz}}{\partial y} + \rho_m g_z = 0 \tag{25}$$

where g_z is the gravitational acceleration in the z-direction and α is the Biot coefficient. The constitutive relationships for a compressible 3D Maxwell body are:

$$\dot{\varepsilon}_{xx} = \frac{1}{3K}\frac{\partial \sigma_{xx}^{iso}}{\partial t} - \frac{\alpha}{3K}\frac{\partial P_p}{\partial t} + \frac{1}{2G}\frac{\partial \sigma_{xx}^{dev}}{\partial t} + \frac{\sigma_{xx}^{dev}}{2\mu} \tag{26}$$

$$\dot{\varepsilon}_{yy} = \frac{1}{3K}\frac{\partial \sigma_{yy}^{iso}}{\partial t} - \frac{\alpha}{3K}\frac{\partial P_p}{\partial t} + \frac{1}{2G}\frac{\partial \sigma_{yy}^{dev}}{\partial t} + \frac{\sigma_{yy}^{dev}}{2\mu} \tag{27}$$

$$\dot{\varepsilon}_{zz} = \frac{1}{3K}\frac{\partial \sigma_{zz}^{iso}}{\partial t} - \frac{\alpha}{3K}\frac{\partial P_p}{\partial t} + \frac{1}{2G}\frac{\partial \sigma_{zz}^{dev}}{\partial t} + \frac{\sigma_{zz}^{dev}}{2\mu} \tag{28}$$

$$\dot{\varepsilon}_{xy} = \frac{1}{2G}\frac{\partial \sigma_{xy}^{dev}}{\partial t} + \frac{\sigma_{xy}^{dev}}{2\mu} \tag{29}$$

$$\dot{\varepsilon}_{xz} = \frac{1}{2G}\frac{\partial \sigma_{xz}^{dev}}{\partial t} + \frac{\sigma_{xz}^{dev}}{2\mu} \tag{30}$$

$$\dot{\varepsilon}_{yz} = \frac{1}{2G}\frac{\partial \sigma_{yz}^{dev}}{\partial t} + \frac{\sigma_{yz}^{dev}}{2\mu} \tag{31}$$

where $\dot{\varepsilon}$ is the strain rate, K the bulk modulus, G the shear modulus, and μ the viscosity. The superscript "iso" denotes the isotropic component of the stress tensor and the

superscript "dev" denotes the deviatoric component of the stress tensor. Since density is changing as a function of depth, and depth is changing as a function of time, the conservation of mass is given by:

$$\frac{\partial \rho_m}{\partial t} + \rho_m \left(\frac{\partial v_x}{\partial x} + \frac{\partial v_y}{\partial y} + \frac{\partial v_z}{\partial z} \right) = 0 \qquad (32)$$

Finally, using the conservation of fluid mass, Darcy's law in 3D (Jaeger et al., 2009), and assuming an incompressible pore fluid, the governing equation for fluid flow is represented as:

$$\frac{Kk_x}{\mu_f} \frac{\partial^2 P_p}{\partial x^2} + \frac{Kk_y}{\mu_f} \frac{\partial^2 P_p}{\partial y^2} + \frac{Kk_z}{\mu_f} \frac{\partial^2 P_p}{\partial z^2} - \frac{\partial P_p}{\partial t} + \dot{\sigma}^{iso} = 0 \qquad (33)$$

where k_x, k_y, and k_z are the permeabilities in the x, y, and z directions, respectively, and μ_f is the viscosity of the pore fluid. Equations (23-33) represent the 11 governing equations used to solve for the 11 unknowns of the problem. A detailed derivation of the equation system can be found in Appendix 1.

3.1.2. The ABAQUS^{TM} Solver. For this study, the commercial FEA software package ABAQUS^{TM} (Abaqus, 2014) is employed to solve the governing equations presented in the previous section. This software is capable of simulating static or dynamic processes using 2D and 3D models, and has been used to address a number of problems related to earth sciences (e.g., Dyksterhuis et al., 2005; Vidal-Gilbert et al., 2009; Smart et al., 2012, Mitani et al., 2013). ABAQUS^{TM} includes constitutive material relationships which can be modified to combine linear elastic and Newtonian viscous behavior (i.e., Maxwell Model), while simultaneously accounting for the influence of gravity and pore pressure. Additionally, ABAQUS^{TM} is able to define constant or parameter dependent material properties (density, porosity, permeability, etc.) for individual element sets, specify time dependent creep behavior to initiate a viscoelastic response analysis, and export result sets for post-processing purposes. In regards to single layer buckle folding, ABAQUS^{TM} has proven successful in simulating effective

stress evolution, and pore pressure evolution, for the case of a 2D Maxwell viscoelastic folding layer and matrix (Eckert et al., 2014; 2015).

3.2. MODEL SETUP

One of the objectives of this study is to perform a sensitivity analysis, which tests how various parameters (e.g., fold shape, permeability, overburden stress, and competence contrast) influence the location and type of fractures that can initiate in a pericline. In order to perform this sensitivity analysis, a base model must be established that serves as a reference point for comparisons. The base model is assigned characteristic geometric and material properties which are varied for each individual parametric study.

3.2.1. Material Properties. In order to simulate in-situ stress magnitudes using FEA, material properties must be appropriately assigned to all components in the model. ABAQUS^{TM} requires that the following material properties be defined for a consolidation analysis of a fluid filled, viscoelastic porous media: porosity, permeability, dry bulk density, fluid density, fluid saturation, Young's modulus, Poisson's ratio, and dynamic viscosity.

The magnitude of porosity and permeability of a rock is directly related to the degree of cementation, amount of compaction, and the method of grain packing (Selley and Sonnenberg, 2014). Each of these factors is heavily influenced by the depth of burial and amount of overburden stress. Greater burial depths and higher overburden stresses typically correspond to higher degrees of cementation, increased amounts of compaction, and tighter grain packing; this in turn leads to lower magnitudes of porosity and permeability (Tiab and Donaldson, 2015). Since this study includes the influence of gravity and increasing overburden loads over time, the following relationships are applied to model porosity and permeability changes with depth (Medina et al., 2011):

$$\phi(z) = 16.39e^{-0.00039z} \tag{34}$$

$$k(z) = 7.583 \cdot 10^{-17} e^{0.283\phi} \tag{35}$$

where ϕ is the porosity (%), z is the depth in meters, and k is the permeability in m^2. The permeability for the base model is considered to be isotropic.

As a result of increasing overburden stresses at greater burial depths, the fluids in a rock are forced from the pore spaces, allowing the rock matrix to compact. Thus, so long as the surrounding matrix is denser than the pore fluid, any reduction in the rock's pore volume (i.e., porosity) is met with a simultaneous increase in bulk density (ρ_b). For a coupled pore fluid flow/stress analysis, ABAQUS^{TM} defines ρ_b in terms of the dry bulk density (ρ_{db}) of the rock, and the fluid density (ρ_f). This relationship can be expressed as (Jaeger et al., 2009):

$$\rho_b = \rho_s(1 - \phi) + \rho_f\phi = \rho_{db} + \rho_f\phi \tag{36}$$

where ρ_s is the density of the solid grains. By introducing the specific gravity of the solid grains (G_s):

$$G_s = \frac{\rho_s}{\rho_w} \tag{37}$$

where ρ_w is the density of water (1000 kg/m^3), and including the depth dependent porosity given in equation (34), the dry bulk density component of equation (36) can be rewritten as:

$$\rho_{db} = G_s\rho_w(1 - \phi) = G_s\rho_w(1 - 16.39e^{-0.00039z}) \tag{38}$$

Since water is the only fluid being considered in this study, ρ_f in equation (36) is set equal to ρ_w, and relationship for ρ_b becomes:

$$\rho_b = G_s\rho_w(1 - 16.39e^{-0.00039z}) + \rho_w(16.39e^{-0.00039z}) \tag{39}$$

For the relationship in equation (39) to hold true, the pore volume must be 100% saturated with water. G_s is assigned a value of 2.75 for all the models in this study. This value is a representative average of the specific gravities of sedimentary rocks composed predominantly of quartz, calcite, dolomite, and clay minerals (Dietrich and Skinner, 1979).

Constitutive relationships between stress and strain for materials that exhibit linear elasticity can be described using various combinations of the five elastic parameters: Young's modulus (E), Poisson's ratio (ν), shear modulus (G), bulk modulus (K), and the 1st Lamé parameter (λ). While each parameter has a unique physical meaning all five are mutually related, and because of these mutual relationships, only two parameters must be independently defined for a constitutive relationship to be established (Fjar et al., 2008). ABAQUS[TM] establishes linear elastic constitutive relationships using Young's modulus and Poisson's ratio. For the models used in this study, E is defined as a depth dependent parameter using the relationship presented by Eckert et al. (2014):

$$E_f = 10 \cdot E_m = 33.7(1 - 0.1639e^{-0.00039z}) \tag{40}$$

where E_f and E_m are the Young's moduli of the folding layer and matrix, respectively, in GPa. All the models in this study are assigned a constant Poisson's ratio of 0.25; a value which is typical for most rocks (Fjar et al., 2008).

Lastly, the dynamic viscosity (μ) must be defined to establish a constitutive relationship between the stress and the strain rate for a Newtonian viscous material. As described in Section 2.2, the dominant wavelength equations have been developed for the cases of a competent folding layer embedded in a less competent matrix. The degree to which the folding layer is more or less competent than the matrix can be quantified by a viscosity (or competence) contrast (R_μ), which is defined as:

$$R_\mu = \frac{\mu_f}{\mu_m} \tag{41}$$

The folding layer is assigned a constant viscosity of 1.2×10^{21} Pa · s which falls in the range of viscosities tested by previous viscoelastic folding studies (e.g., Zhang et al., 1996; Mancktelow, 1999; Eckert et al., 2014). The viscosity of the matrix is dependent on the value of R_μ. For the base model a R_μ value of 50 is chosen, giving a μ_m of 2.4×10^{19} Pa · s.

A list of the material properties for the base model, comprised of a folding layer, matrix, overburden, and base, is given in Table 3.1.

Table 3.1. Material properties for the base model

Properties	Folding Layer	Matrix/Overburden/Base
Porosity (ϕ) at 1000m	11.1 (%)	11.1 (%)
Permeability (k) at 1000m	1.75×10^{-15} (m^2)	1.75×10^{-15} (m^2)
Specific Gravity of Solid Grains (G$_s$)	2.75	2.75
Fluid Density (ρ_f)	1000 (kg/m^3)	1000 (kg/m^3)
Fluid Saturation	100 (%)	100 (%)
Young's Modulus (E) at 1000m	30 (GPa)	3 (GPa)
Poisson's Ratio (v)	0.25	0.25
Viscosity (μ)	1.2×10^{21} (Pa·s)	2.4×10^{19} (Pa·s)

3.2.2. Model Geometry. The geometry of the base model is comprised of a 30 m thick folding layer embedded in a 500 m thick matrix, a 280 m thick base layer underlying the matrix, and a 250 m thick overburden layer above the matrix (Figure 3.1a). The folding layer is characterized by sinusoidal perturbations in the x and y-directions with initial amplitudes of 2.5 m. As previously mentioned in Section 1.2.2, the geometry of a pericline is described by giving the folds aspect ratio (ratio of half wavelength to hinge length), with most periclines in the upper levels of the crust exhibiting an aspect ratio in the range of 1:5 to 1:10. For this study, initial perturbations are assigned in such a way that there will always be four half-wavelengths in the x-direction, two hinge lengths in the y-direction, and a doubly plunging anticline (pericline) located in the central portion of the model (Figure 3.1b). Thus, the aspect ratio of the
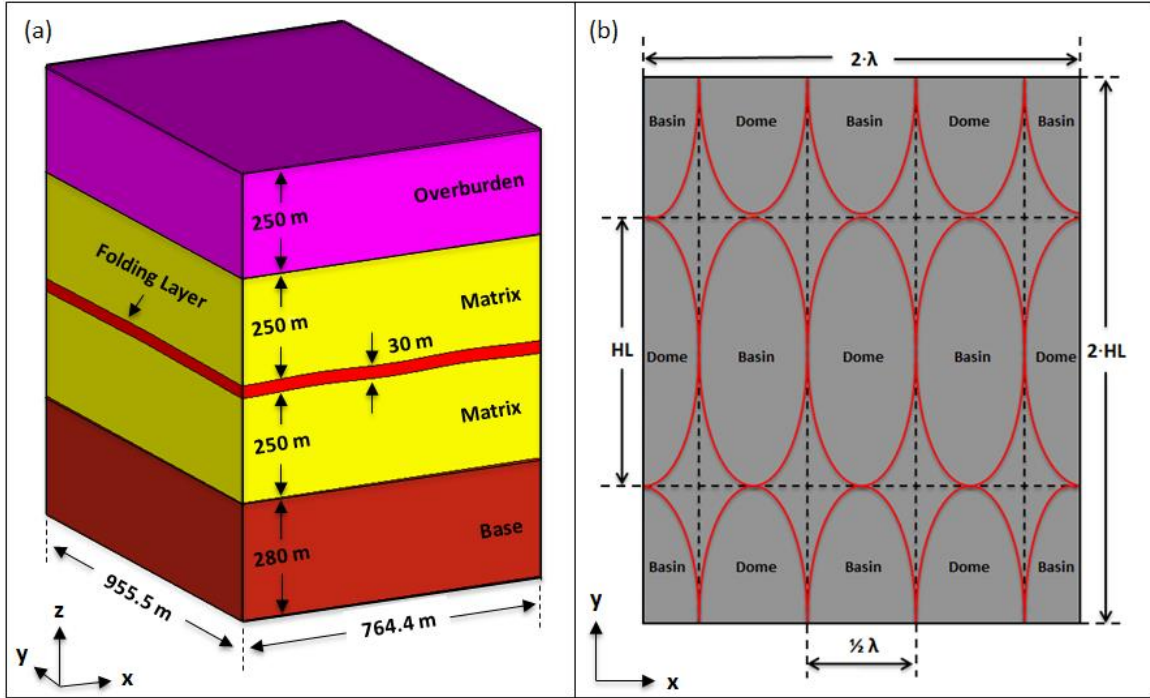
Figure 3.1. Geometry of the base model. (a) Oblique view of the base model with overall dimensions in the x, y, and z-directions. (b) Plan view showing the distribution of domes and basins in the folding layer. It should be noted that while the model length in the x-direction will change during the folding process, the model will always be characterized by two wavelengths in the x-direction and 2 hinge lengths in the y-direction.

central pericline can be determined at any time during buckling based on the model dimensions in the x and y-directions.

The perturbations in the x-direction are assigned initial wavelengths equivalent to the dominant wavelength. Since the models in this study are viscoelastic, the dominant wavelength ratio (R) must be calculated using equation (3) to determine whether the model is controlled largely by elastic or viscous properties. The layer parallel stress in equation (3) can be estimated using the following relationship (Schmalholz and Podladchikov, 1999):

$$P = 4\mu_l\dot{\varepsilon} \qquad\qquad (42)$$

where $\dot{\varepsilon}$ is the background strain rate. Using a strain rate of 10^{-14}s^{-1}, which is representative of a reasonable geologic deformation rate (Twiss and Moores, 2007), and a

folding layer viscosity of 1.2 x 10^{21} Pa·s gives a layer parallel stress of 40 MPa. This value remains fixed for all models since $\dot{\varepsilon}$ and μ_l are held constant for this study. The other two parameters besides P which influence the value of R, viscosity contrast (R_μ) and shear modulus (G), are varied in certain cases during this study. For the different viscosity ratios considered (R_μ = 25, 50, 75, 100), R is in the range of 0.094 - 0.150 (Table 3.2), which corresponds to dominantly viscous behavior (i.e., R<1). The magnitude of the shear modulus changes with depth in a similar manner as the Young's modulus, and thus models with different initial overburden thicknesses will have different magnitudes of shear modulus for their respective folding layers. For the different overburden thicknesses considered (500 m, 1000 m, 1500 m, 2000 m) with a constant R_μ of 50, R is in the range of 0.115 – 0.119 (Table 3.2), which also corresponds to dominantly viscous behavior. All of the models in this study exhibit dominantly viscous behavior; therefore, choosing to express the dominant wavelength as the viscous dominant wavelength from equation (1) is deemed appropriate. The dominant wavelength for the base model, with a viscosity contrast of 50, is 382.2 m, making the initial length of the model in the x-direction 764.4 m.

Table 3.2. Calculated values of R used to verify dominant wavelength selection.

R_μ	Overburden Thickness (m)	P (MPa)	G (GPa)	R
25	500	40	11.67	0.094
50	500	40	11.67	0.119
75	500	40	11.67	0.136
100	500	40	11.67	0.150
50	1000	40	11.99	0.117
50	1500	40	12.26	0.116
50	2000	40	12.47	0.115

No lateral strains are applied parallel to the y-axis during this study, which keeps the model length in the y-direction fixed during buckling. The initial length of the model in the y-direction depends on the final desired aspect ratio of the pericline and the relative amount of lateral shortening the model experiences parallel to the x-axis. The base

model is set up so a pericline with an aspect ratio of 1:5 is generated after 50%
shortening. At the end of the 50% shortening period, the initial perturbations in the x-
direction with dominant wavelengths of 382.2 m are shortened to 191.1 m. At this point
the half-wavelength of the pericline is 95.55 m. Following the definition of the aspect
ratio, the half wavelength is multiplied by five to give a hinge length of 477.75 m,
subsequently making the initial length of the model in the y-direction 955.5 m.

     3.2.3. Loading Procedures. In natural subsurface settings absent of a current
state of rapid deformation (e.g., fault rupture, karst collapse, landslide), rock formations
are in a state of stress equilibrium (Twiss and Moores, 2007). The model presented in
Section 3.2.2 represents an undeformed volume lacking an initial state of stress
equilibrium. In order to introduce an initial state of stress equilibrium to the model that is
representative of natural subsurface settings, a stress initialization procedure known as
pre-stressing is utilized (Buchman and Connolly, 2007; Eckert and Liu, 2014). This
procedure begins with the introduction of gravity, which subsequently causes the model
to compact, and ends when the resultant stresses reach a state of equilibrium. The
resultant stress state represents the initial stress conditions for the model prior to the onset
of buckling.

     The loading procedures used in this study to simulate in-situ stress magnitudes
during buckle folding are adopted after the works of Eckert et al. (2014; 2015) and
include the following:

(1) Pre-stressing step where gravity is applied to the model. Boundary conditions are
applied to constrain the model in such a way that only vertical displacements are
allowed (Figure 3.2a). Pre-stressing concludes when the modeled stresses reach a
state of equilibrium.

(2) Horizontal compression parallel to the x-direction at a constant strain rate ($10^{-14}s^{-1}$) to simulate a unidirectional tectonic shortening event necessary to induce
buckling (Figure 3.2b). Horizontal compression concludes when the pericline
reaches the final desired aspect ratio (Figure 3.2c). It should also be noted that
this study only considers horizontal shortening parallel to the x-axis. For this
reason, the model boundaries perpendicular to the y-axis are always assigned
boundary conditions that only allow for displacements in the x and z-directions.
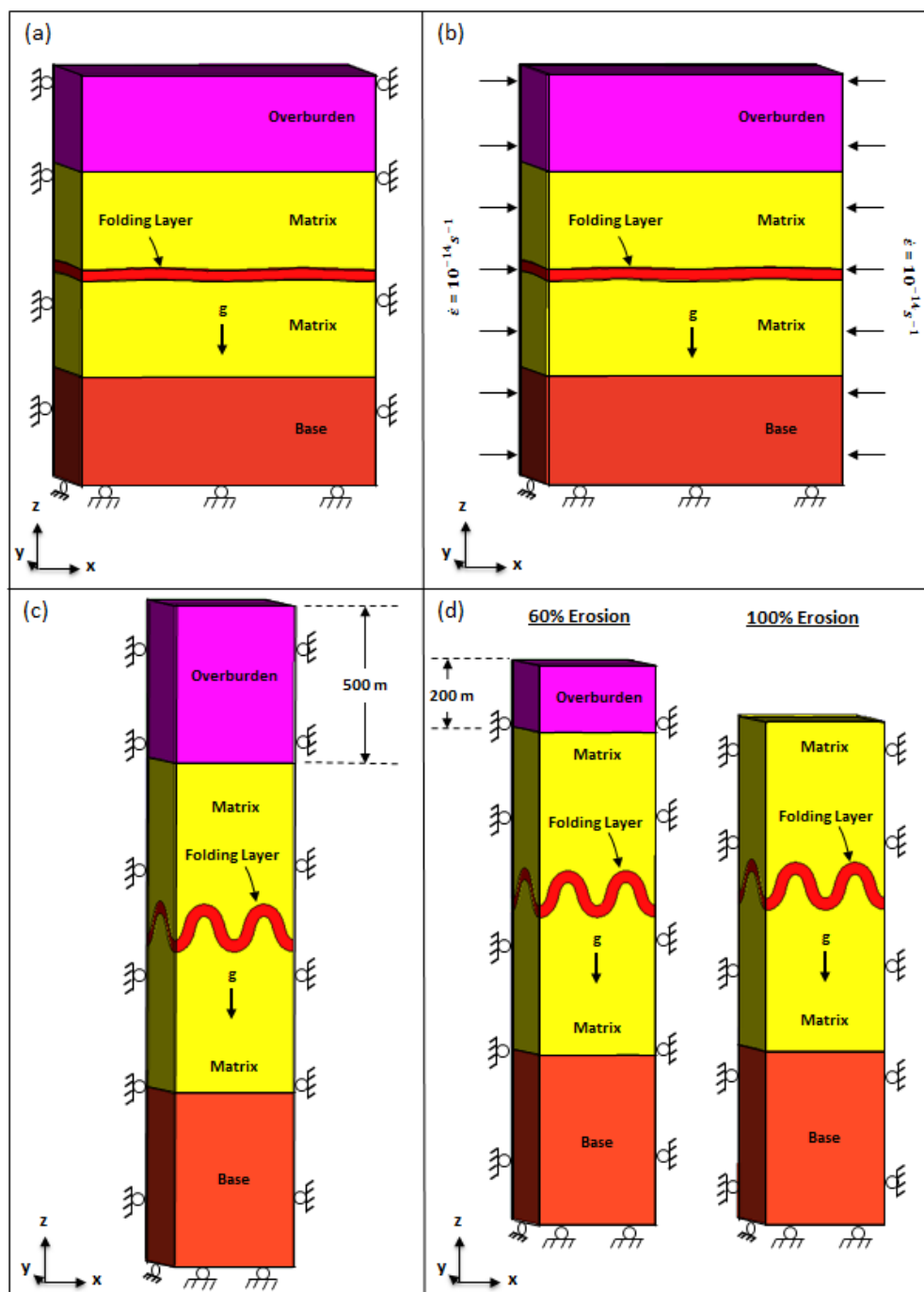
Figure 3.2. Loading procedures used during buckle fold simulations. (a) Gravitational pre-stressing step is used to simulate in-situ stress magnitudes. Boundary conditions are applied that only allow for vertical displacements (rollers). (b) Horizontal shortening in the x-direction applied after gravitational equilibrium is reached. Shortening continues until the desired pericline aspect ratio is achieved (c). Note that the horizontal shortening has caused the overburden thickness to increase to 500m. (d) Erosional unloading step where the gravitational acceleration and pore pressure are gradually decreased in the overburden layer. Roller boundary conditions are applied at the y-boundaries in each loading step.

(3) Erosional unloading step where the pore pressure and gravitational acceleration of the overburden layer are gradually reduced at a rate consistent with an erosion/exhumation rate of 1 mm/yr (Burbank, 2002). The erosional unloading step concludes when the gravitational acceleration of the overburden layer reaches zero (i.e., complete erosion of the overburden layer). The boundary conditions for the erosional unloading step are the same as those used during pre-stressing so that the final fold shape at the end of shortening may be preserved during erosional unloading (Figure 3.2d).

Lastly, the initial pore pressure condition for each model is hydrostatic, and can be calculated for any depth using the following equation:

$$P_p = \int_0^z \rho_f(z)gdz \qquad (43)$$

where $\rho_f(z) = \rho_w$.

4. RESULTS

In order to predict the timing and location of fracture initiation within a fold, a thorough analysis of the principal stress evolution during the initiation and growth of the fold is necessary. This series of simulations employs the fracture potential method (see Section 2.3.2) to simultaneously combine the principal stress evolution obtained from the 3D FEM with a particular set of rock strength parameters, and ultimately determine fracture characteristics (e.g., timing of initiation, location, type, orientation) for an individual fold.

The results presented in this study can be divided into two sections. The first section examines the stress evolution for the base model pericline, and introduces the analysis procedure used throughout the remainder of the study. The second section highlights the findings from a series of parametric studies designed to pinpoint which subsurface conditions have the greatest influence on fracture initiation. The parameters included in this study are permeability magnitude, degree of permeability anisotropy, viscosity contrast, pericline aspect ratio, shortening percentage, overburden stress, and erosional unloading.

4.1.   BASE MODEL RESULTS ANALYSIS

After 50% shortening at a constant strain rate of $10^{-14} \, s^{-1}$, the folding layer of the base model has evolved into a series of alternating domes and basins with a centrally located pericline (Figure 4.1). This pericline will serve as the focal point of stress analysis for each model in this study. The geometric evolution of the pericline can be seen in Figure 4.2, where the initial dominant wavelength perturbation with an amplitude of 2.5 m gradually develops into a pericline with steeply dipping limbs ($\sim 70°$) and a final fold amplitude of 56.5 m.

In order to reduce the quantity of finite elements to be analyzed, two simplifications are made for the stress analysis procedure: first, due to the pericline being symmetric about its axial plane and central profile plane, the analysis can be restricted to a quarter section of the pericline (Figure 4.3a); second, within the quarter section of the
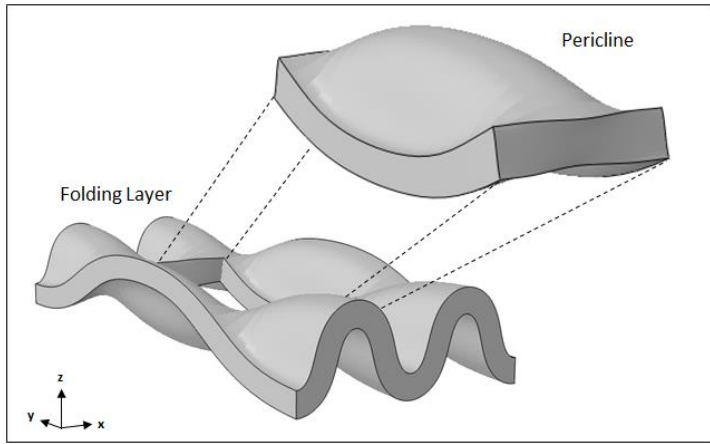
Figure 4.1. Folding layer with a centrally located pericline after 50% shortening.
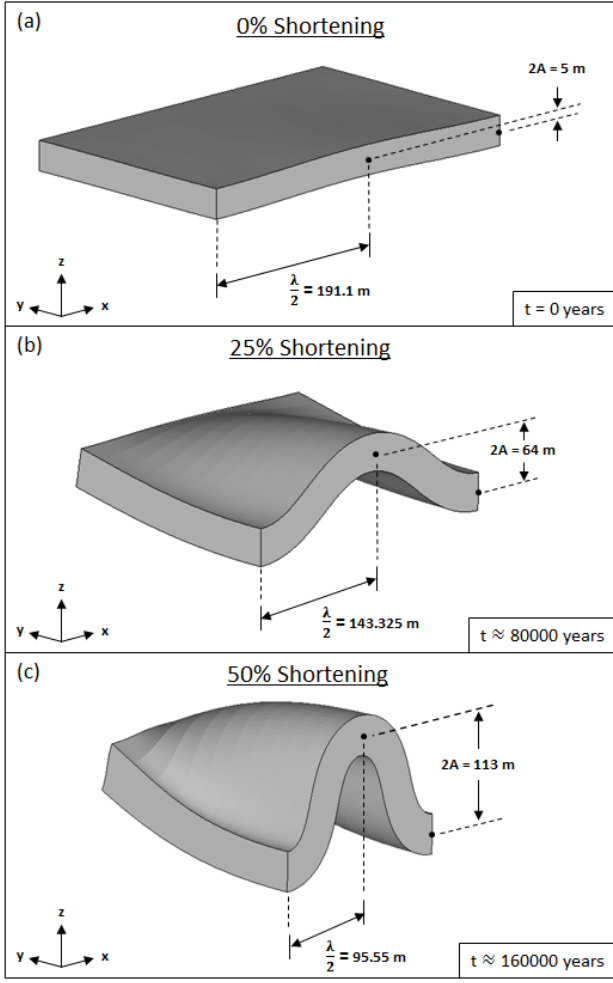
Figure 4.2. Pericline shape prior to shortening (a), after 25% shortening (b), and after 50% shortening (c). Pericline hinge length remains fixed at 477.75 m resulting in a final aspect ratio of 1:5 after 50% shortening.

pericline, the analysis is further restricted to a section of finite elements along the hinge and a section of finite elements along the limb (Figure 4.3b-d). Simplification two is deemed appropriate since the primary motivation for this study is to help explain the timing and likelihood of occurrence for conceptual fracture sets that are located in the hinges and limbs of buckle folds (i.e., Cosgrove and Ameen, 1990), and not to provide a comprehensive fracture analysis for the entire fold structure. The specific locations of the hinge and limb elements are along the crest (top of the hinge) and inflection surface (where the fold changes from an anticline to a syncline) of the periclne, respectively.
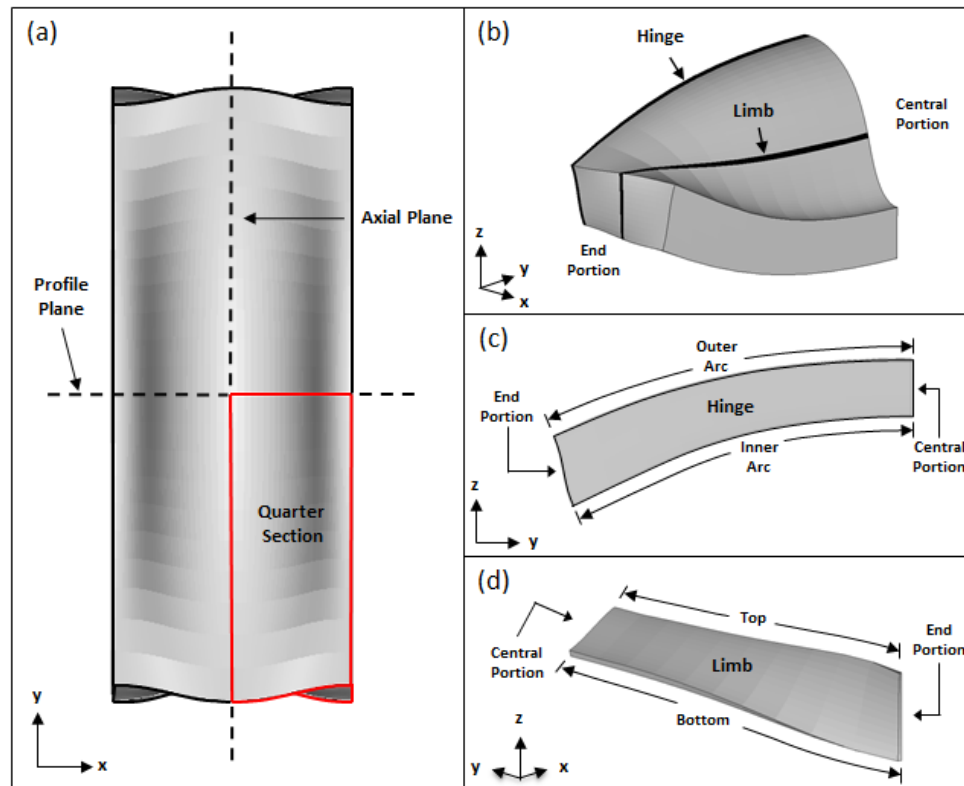
Figure 4.3. Locations for stress analysis and fracture prediction. (a) Plan view of the periclne showing fold symmetry about the central profile plane and axial plane. (b) Quarter section of the periclne highlighting the hinge (c) and limb (d) sections to be analyzed. Limb elements in (d) have been rotated for optimal viewing purposes.

4.1.1. Stress Analysis. The principal stress evolution becomes of importance for pinpointing the timing of stress conditions that are most likely to cause fracture initiation. The minimum principal stress (σ'_3) and the differential stress ($\sigma_d = \sigma'_1 - \sigma'_3$) are the main indicators used to determine the likelihood of fracture initiation. Tensile fractures initiate, when σ'_3 equals the tensile strength (T) of the rock, and thus the point when σ'_3 becomes tensile ($\sigma'_3 < 0$) is identified as the start of a period when tensile failure is possible. The indicator for potential shear fracture initiation is not as clear cut as that for tensile fractures, but in general, shear fracture initiation is most likely to occur for higher magnitudes of differential stresses and/or lower magnitudes of σ'_3.

For the hinge of the pericline, six elements are examined to see how the principal stress evolution changes at different locations along the hinge line. Elements 1, 3, and 5 are located at the outer arc of the hinge where extensional strains will be highest, and elements 2, 4, and 6 are located in the inner arc where compressional strains will be highest (Figure 4.4a). It can be seen that the principal stress evolution for elements 1 (Figure 4.4b) and 3 (Figure 4.4d) follow similar trajectories. σ'_3 magnitudes initially increase before steeply decreasing in the early stages of shortening (~13-15%) and then gradually increase again. σ'_1 magnitudes sharply decrease in the early stages of shortening until reaching a pronounced minimum at ~13-15% shortening, at which point the magnitudes steadily increase during the remainder of shortening. σ'_3 magnitudes become tensile for elements 1 and 3 at ~18% and ~24% shortening, respectively, and reach respective minimums at ~27% and ~33% shortening, indicating that tensile fracture initiation is most likely to occur during these shortening windows. The largest magnitudes of differential stress for elements 1 and 3 are present during the earliest stages of shortening ($< 5\%$) and during later stages of shortening when σ'_3 minimums are reached (~27% and ~33%); however, shear fracture initiation is unlikely during the earliest stages of shortening considering that σ'_3 magnitudes are also the highest during this period. Element 5 (Figure 4.4f) exhibits markedly different principal stress trajectories than elements 1 and 3. The magnitude of σ'_1 decreases gradually from ~7% shortening on while the magnitude of σ'_3 steadily increases until ~22% shortening, at which point it gradually decreases for the remainder of shortening. It can be seen that σ'_3 only becomes tensile at the end of shortening (50%), indicating that tensile fracture

Figure 4.4. Principal stress history of select elements in the hinge of the pericline. Elements 1 (b), 3 (d), and 5 (f) are selected to see how σ'$_1$ and σ'$_3$ evolution changes in the outer arc of the hinge at different locations along the pericline. Elements 2 (c), 4 (e), and 6 (g) are selected to see how σ'$_1$ and σ'$_3$ evolution changes in the inner arc of the hinge at different locations along the pericline.

initiation is possible, but unlikely for element 5. Differential stress magnitudes are again highest at the start of shortening ($<7\%$), but shear fracture initiation becomes more likely during later stages of shortening ($>22\%$) when the magnitude of σ'_3 decreases. Elements 2 (Figure 4.4c), 4 (Figure 4.4e), and 6 (Figure 4.4g), in the inner arc of the hinge, are characterized by large magnitudes of σ'_1, and σ'_3 magnitudes that never become tensile during buckling. The highly compressive nature of σ'_1, combined with the lowest magnitudes of σ'_3 during the early stages of shortening ($\sim$10-20%), indicate that shear fracture initiation is most likely to occur in elements 2 and 4 during this time period. Element 6 reaches the same conditions that condone shear fracture initiation during late stages of shortening ($\sim$40-50%). An additional phenomenon of interest can be observed at $\sim$14% shortening in element 1 (Figure 4.4b), where σ'_1 and σ'_3 have approximately the same magnitudes. This point represents a complete rotation of the principal stresses in Element 1, whereby the vertical stress changes from σ'_3 to σ'_1, and the horizontal stress changes from σ'_1 to σ'_3.

In a similar fashion as for the fold hinge, six elements are selected in the limb of the pericline to see how the principal stress evolution changes at different locations along the limb (Figure 4.5a). One result of interest from the principal stress evolution that can immediately be noted is that σ'_3 magnitudes never become tensile in the limb of the pericline. Also, due to the layer parallel strain distribution within a single layer buckle fold (Ramsay, 1967), the principal stress evolution is nearly identical for elements 1 and 2 (Figures 4.5b and c), elements 3 and 4 (Figures 4.5d and e), and elements 5 and 6 (Figures 4.5f and g). It can clearly be seen that the highest differential stress magnitudes appear during the early stages of shortening ($<15\%$) for elements 1-4; however, the early, relatively large magnitudes of σ'_3, make fracture initiation during this time period unlikely. Elements 5 and 6 can be characterized by much higher magnitudes of σ'_1 and σ'_3 than elements 1-4, but are still unlikely to experience shear fracture initiation given that σ'_3 magnitudes increase in a similar fashion as σ'_1, and the resulting differential stress does not change much.

The qualitative analysis of the principal stress evolution indicates that fracture initiation will be more likely to occur in the hinge of a pericline than the limb during the buckling process. Initial results also indicate that within the hinge, fractures will first
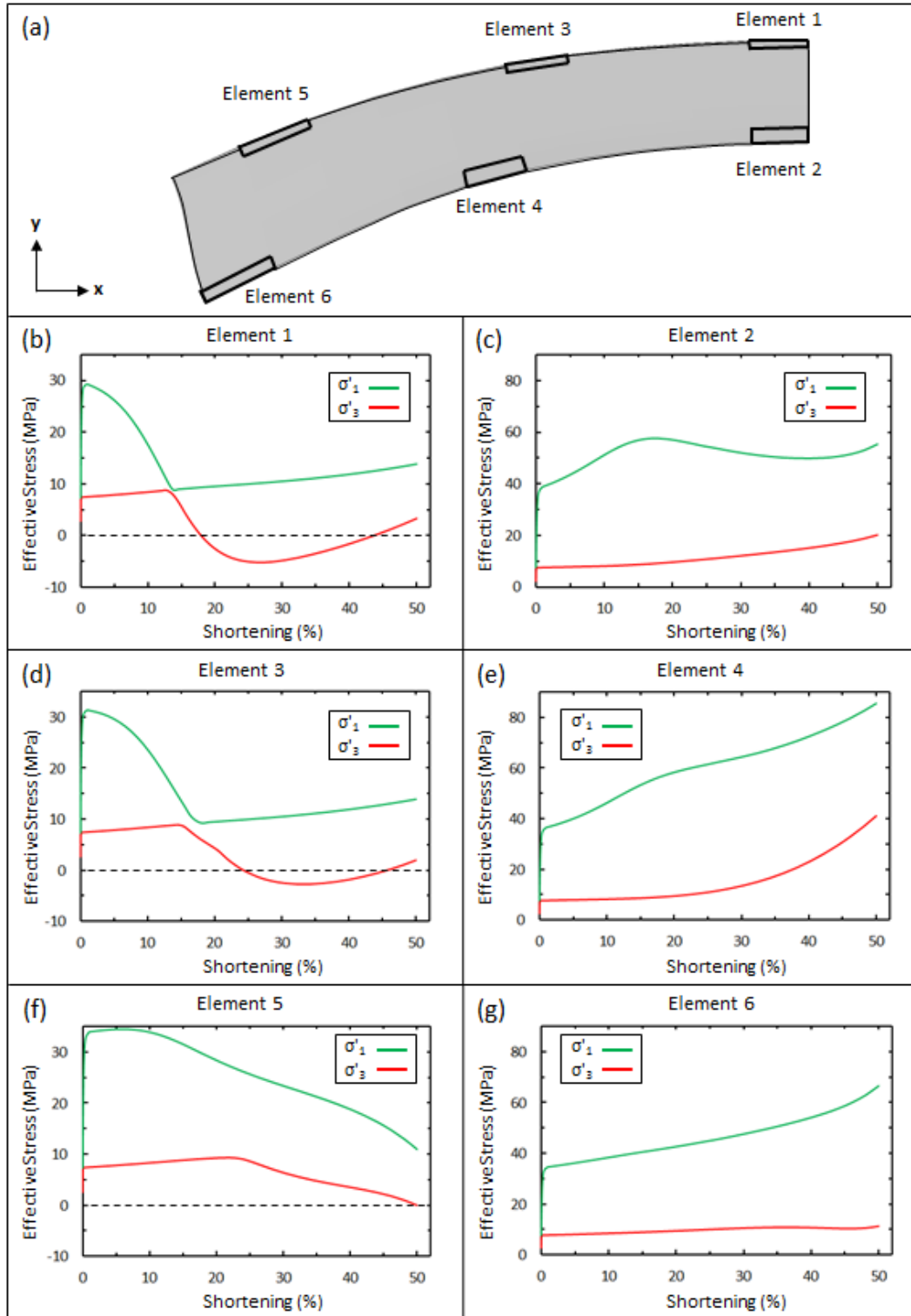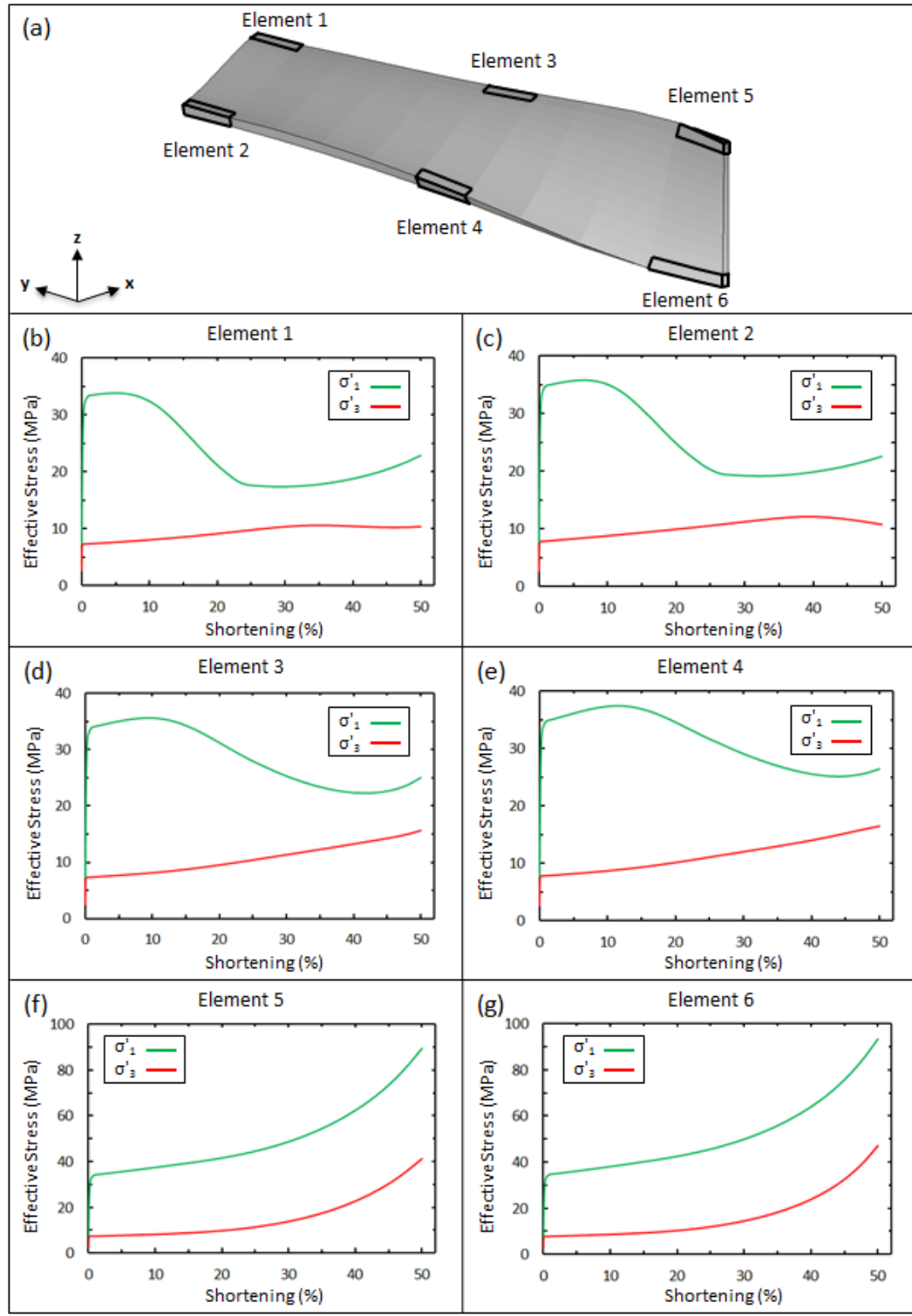
Figure 4.5. Principal stress history of select elements in the limb of the pericline. Elements 1 (b), 3 (d), and 5 (f) are selected to see how σ'_1 and σ'_3 evolution changes in the outer edge of the limb at different locations along the pericline. Elements 2 (c), 4 (e), and 6 (g) are selected to see how σ'_1 and σ'_3 evolution changes in the inner edge of the hinge at different locations along the pericline.

initiate at the central portion of the pericline where the amplitude is the highest, and will progressively initiate along the hinge line towards the end portion of the pericline, where the amplitude is the lowest. From this point forward it becomes necessary to utilize an approach that can effectively quantify whether fractures will initiate for each element within the hinge and limb of the pericline.

4.1.2. Fracture Potential Results. The fracture potential method presented in Section 2.3.2 is utilized to provide a quantitative means for predicting fracture initiation, and to avoid the necessity of performing a thorough qualitative analysis of the stress evolution for thousands of finite elements. Since this study seeks to characterize the actual initiation of fractures, only fracture potential values of -1 (tensile) and 1 (shear) are considered; the fracture potential is assumed to be 0 for all other cases.

Because the constitutive material model used for this study does not include plasticity, and permits the continuous growth of viscoelastic stresses even when failure conditions are met, two assumptions must be made before the fracture potential method can be applied. First, the element boundaries are assumed to be fracture propagation boundaries, simultaneously ensuring that fracture initiation is confined to an individual element and that the stress evolution in adjacent elements remains undisrupted (Figure 4.6a). Second, because the FEM does not simulate the stress changes associated with fracture initiation, the stress evolution after a fracture potential of -1 or 1 has been reached is assumed to be invalid, thus permitting only a single fracturing event within an individual element (Figure 4.6b).

The basis for these assumptions comes from a description of fracture sizes observed in periclines by Stearns and Friedman (1972). A large number of the observed fractures exhibit lengths in the range of a few inches to a few feet. Since the shortest dimension of the finite elements in this study is approximately six feet, it is reasonable to state that fractures of similar size to the ones just described can be initiated within an element, without propagating beyond the element boundaries. Bearing that in mind, it is important to mention that this cannot be stated for all cases. There are many fractures observed by Stearns and Friedman (1972) that exhibit lengths in the range of tens of feet to hundreds of feet. Clearly the assumptions made would fall short in these situations, since fractures of these lengths could easily propagate beyond the element boundaries,
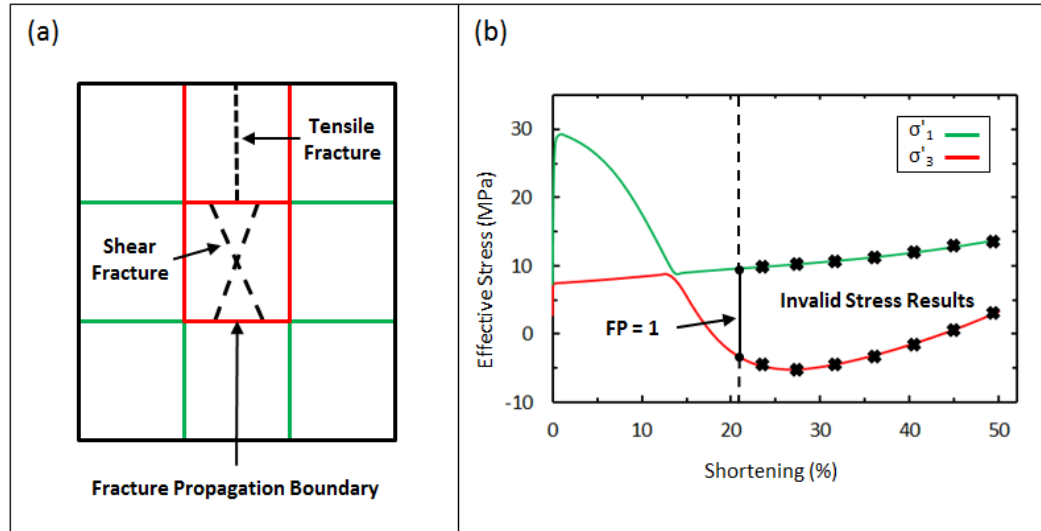
Figure 4.6. Necessary assumptions for the fracture potential approach. (a) Element boundaries are assumed to restrict fracture propagation once fractures have initiated within an individual element. (b) The stress evolution after a fracture has been initiated within an individual element is assumed to be invalid since the FEM does not simulate plastic failure or the stress changes that accompany plastic failure.

and subsequently influence the state of stress in adjacent elements. Even so, the assumptions are deemed appropriate based on the abundance of smaller size fractures observed in folds (Stearns and Friedman, 1972).

For the fracture potential analysis, the angle of internal friction (ψ) is assumed to be 30° (Jaeger et al., 2009), and three combinations of rock cohesion (C_0) and tensile (T) strength are selected to represent a weak rock ($C_0 = 6$MPa, $T = 3$MPa), an intermediate strength rock ($C_0 = 9$MPa, $T = 4.5$MPa), and a strong rock ($C_0 = 12$MPa, $T = 6$MPa). These rock strength parameters are selected based on experimental data from Bieniawski (1984), Pollard and Fletcher (2005), and Fossen (2010).

Figure 4.7 shows the fracture potential results for the hinge of the base model, with the fold shape representing the final fold shape that is generated after 50% shortening. In order to characterize the timing of fracture initiation the buckling process is divided into three stages: early-stage (0-15% shortening), mid-stage (15-30% shortening), and late stage (>30% shortening). Fracture sets can subsequently be classified according to the shortening period in which they were initiated. For a weak rock, shear fractures are initiated along the entire length of the inner arc of the hinge, with
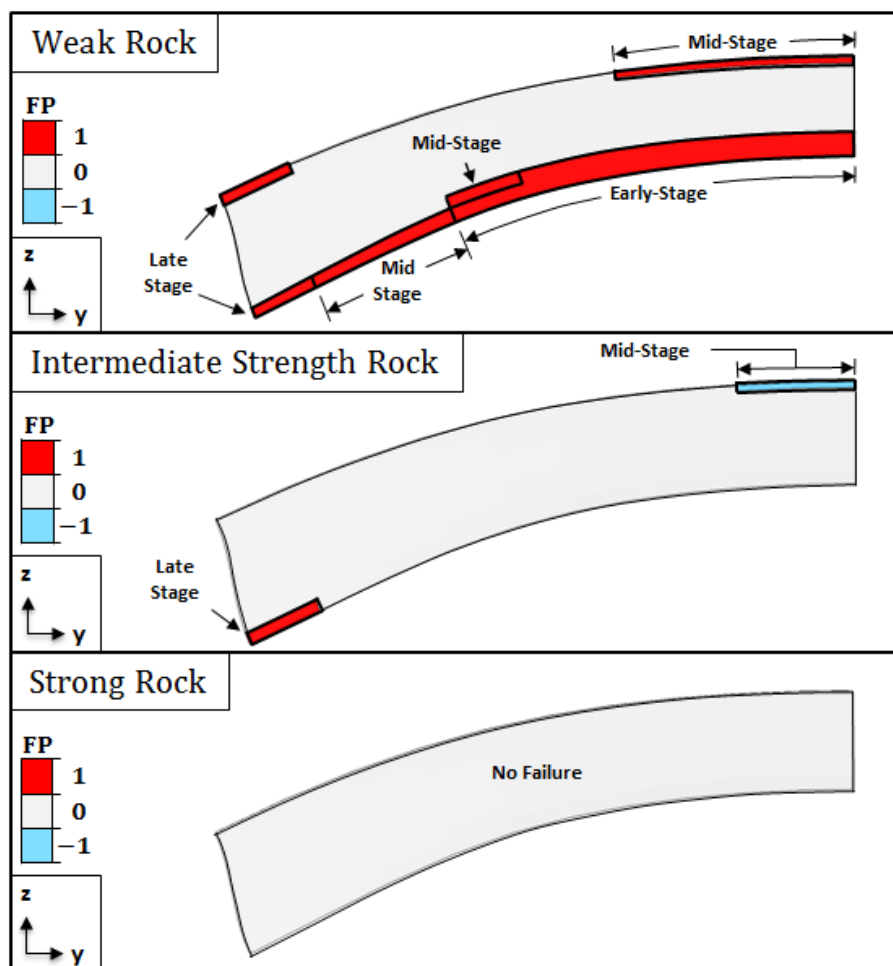
Figure 4.7. Fracture potential results in the hinge of the base model. Results are shown for the final fold shape that develops after 50% shortening.

early stage fractures initiating closer to the central portion, eventually giving way to the initiation of mid and late stage fractures towards the end portion. The outer arc is characterized by mid-stage shear fractures that initiate near the central portion, and late stage shear fractures near the end portion. For intermediate strength rocks, mid-stage tensile fractures initiate near the central portion of the outer arc, and late-stage shear fractures initiate near the end portion of the inner arc. Fractures are not observed in the hinge of strong rocks, and are not observed for any case in the limb.

4.2. PARAMETRIC ANALYSIS

This series of parametric studies present the fracture potential plots generated for each analysis. For the sake of saving space only the fracture potential plots for the weak rock are presented in this section. The fracture potential plots for the intermediate strength rocks and the strong rocks can be found in Appendices B-G.

4.2.1. Influence of Permeability Magnitude. Variations in the permeability magnitude are assigned for different models to investigate how higher and lower permeability formations can influence fracture initiation. Permeabilities are varied from $10^{-13} \, m^2 - 10^{-21} \, m^2$ (Table 4.1), reflecting a wide range for sedimentary rocks (Jaeger et al., 2009), where the folding layer, matrix, overburden, and base are assigned permeabilities of the same order of magnitude for each respective model; all other material properties in Table 3.1 remain fixed. The different permeability magnitudes can be accounted for by using a modified version of equation (35). In addition, the permeability for this particular analysis is considered to be isotropic. The initial geometric properties for each model are the same as the base model, which results in a centrally located pericline with a final aspect ratio of 1:5 after 50% shortening. Table 4.1 shows some of the final geometric properties at the central portion of the pericline for each model. It can be seen that the permeability magnitude has only a minor influence on the final fold geometry, with lower permeabilities leading to slightly higher fold amplitudes, slightly steeper limb dips, and slightly thinner folding layers.

Table 4.1. Geometric properties for the permeability magnitude models (base model is shaded gray). Measurements are representative of the central portion of the pericline.

Model (k)	Final Half Wavelength (m)	Final Hinge Length (m)	Final Amplitude (m)	Final Folding Layer Thickness (m)	Final Limb Dip (°)
$10^{-13} \, m^2$	95.55	477.52	56.24	39.15	75.3
$10^{-15} \, m^2$	95.55	477.52	56.64	39	75.5
$10^{-17} \, m^2$	95.55	477.52	57.45	38.65	75.8
$10^{-19} \, m^2$	95.55	477.52	58.56	38.17	76.1
$10^{-21} \, m^2$	95.55	477.52	58.88	38.06	76.2

Figure 4.8 shows the fracture potential results for the hinge of a weak rock, where a permeability of 10^{-15} m^2 represents the base model. It can be seen that the fracture distribution for permeabilities of 10^{-13} m^2, 10^{-17} m^2, and 10^{-19} m^2 all approximate the distribution for the base model, with only minor variations observed for the locations of early and mid-stage shear fractures along the inner arc. The fracture distribution is much more extensive for the lowest permeability case (10^{-21} m^2). Early-stage shear fracturing is observed along the entire length of the inner arc, and extend well into the interior of the fold. Mid-stage shear fracturing spans nearly the entire thickness of the fold in the end portion, and extends slightly inwards at the interior of the folding layer. The outer arc can be characterized by mid-stage shear and tensile fractures near the central portion, that give way to late-stage shear and tensile fractures almost halfway along the hinge line.

Figure B.1 shows the fracture potential results for the hinge of an intermediate strength rock. As with the weak rock, the fracture distribution for permeabilities of 10^{-13} m^2, 10^{-17} m^2, and 10^{-19} m^2 is approximately the same as the base model. An exception exists for a permeability of 10^{-19} m^2 where late stage shear fractures are observed near the end portion of the outer arc. The lowest permeability model exhibits early-stage shear fracturing that extends from the central portion of the inner arc, along a majority of the hinge line, to the end portion which contains mid-stage and late-stage shear fractures. The outer arc is dominated by mid-stage and late-stage tensile fractures, with late-stage shear fractures only initiating near the end portion.

Figure B.2 shows the fracture potential results for the hinge of a strong rock. Only the lowest permeability model is capable of initiating fractures in a strong rock. Mid-stage tensile fracturing is observed in the outer arc, extending from the central portion to nearly halfway along the hinge line. The late-stage fractures include tensile fractures near the halfway point of the hinge line in the outer arc, tensile and shear fractures near the end portion of the outer arc, and shear fractures near the end portion of the inner arc.

No scenario gives rise to the initiation of fractures in the limb during the permeability magnitude analysis.
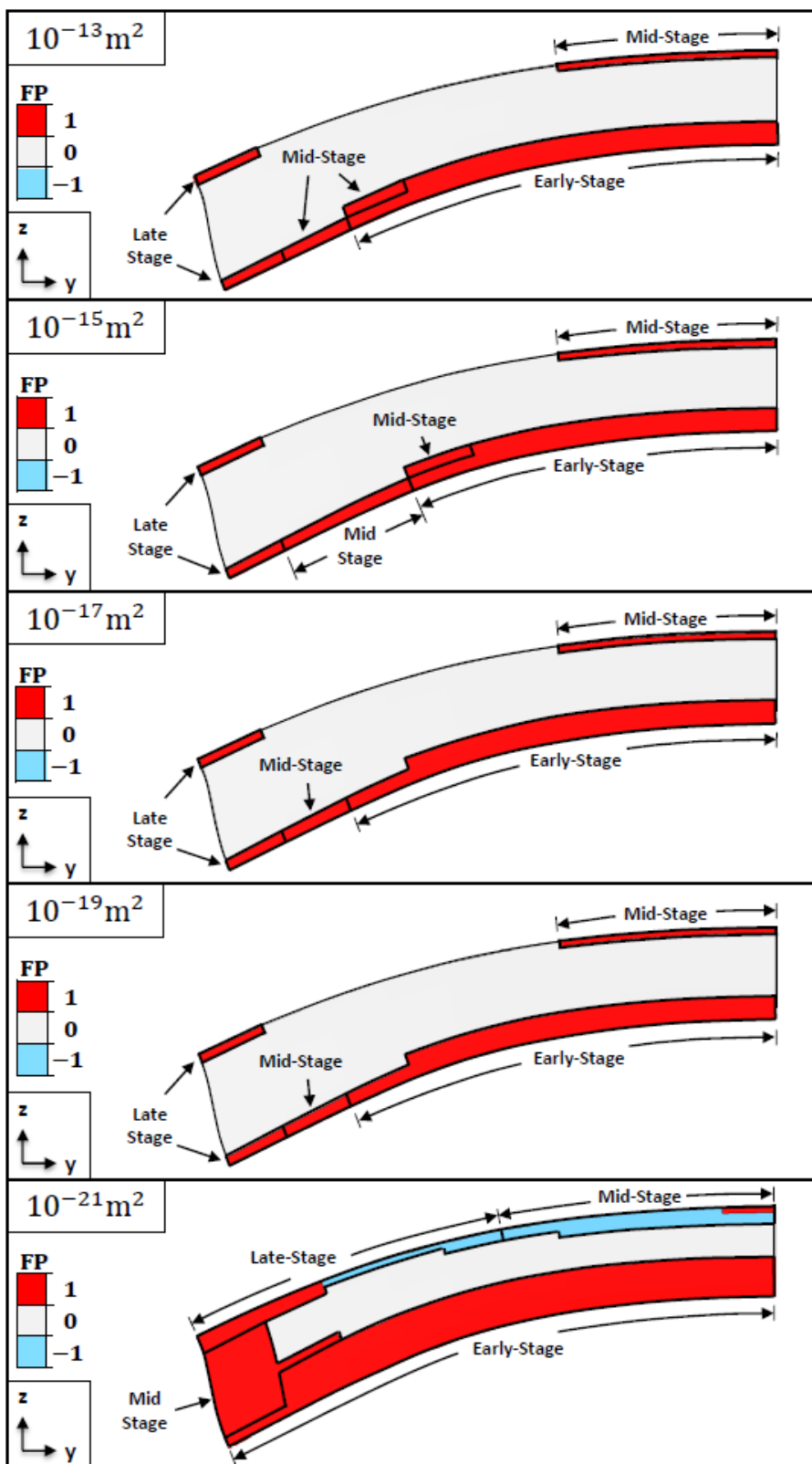
Figure 4.8. Fracture potential results in the hinge for a weak rock with varying permeability magnitudes. The final fold shape is approximately the same for each model.

4.2.2. Influence of Anisotropic Permeability. Because rock formations typically exhibit noticeable differences in vertical and horizontal permeabilities (Tiab and Donaldson, 2015), a set of models is established to test the influence of the degree of permeability anisotropy on fracture initiation. These models are set up to where the ratio of horizontal permeability to vertical permeability is 5:1, 10:1, and 20:1, which can be representative of highly cemented sandstones (Chapman, 2000) or laminated shale layers (Tiab and Donaldson, 2015). To accomplish this, the horizontal permeability is set equivalent to the permeability calculated for Table 3.1, and the vertical permeability is decreased accordingly while all other material properties remain fixed. The varying permeability anisotropy ratios are applied to three separate cases: buckling for high permeability models (10^{-15} m^2), buckling for low permeability models (10^{-21} m^2), and erosional unloading for high permeability models. Initial geometric properties remain the same as the base model, and 50% shortening is once again applied resulting in a centrally located pericline with a final aspect ratio of 1:5. The final geometric properties for high permeability models are given in Table 4.2. These properties indicate that the degree of permeability anisotropy has little to no influence on the final fold shape.

Table 4.2. Geometric properties for the anisotropic, high permeability models (base model is shaded gray). Measurements are representative of the central portion of the pericline.

Model (k_h to k_v)	Final Half Wavelength (m)	Final Hinge Length (m)	Final Amplitude (m)	Final Folding Layer Thickness (m)	Final Limb Dip (°)
Isotropic	95.55	477.52	56.64	39	75.5
5 to 1	95.55	477.52	56.51	39.06	75.5
10 to 1	95.55	477.52	56.45	39.07	75.4
20 to 1	95.55	477.52	56.51	39.06	75.5

4.2.2.1 High permeability buckling. Figure 4.9 shows the fracture potential results for the hinge of a weak rock, where the isotropic case represents the base model. It becomes immediately apparent that the fracture distributions for the anisotropic permeability models deviate very little from the base model. The only difference can be

Figure 4.9. Fracture potential results in the hinge for a high permeability (10^{-15} m^2) weak rock, with varying degrees of permeability anisotropy. The final fold shape is approximately the same for each model.

observed in the inner arc, close to the end portion, where shear fracturing extends slightly farther into the folding layer for the anisotropic permeability models. It is also observed that the fracture distributions for all the anisotropic permeability models are identical.

Figure C.1 shows the fracture potential results for the hinge of an intermediate strength rock. The fracture distribution for the anisotropic permeability models are nearly the same as the base model, with mid-stage tensile fractures initiating near the central portion of the outer arc, and late stage shear fractures initiating near the end portion of the inner arc. A minor deviation from the base model distribution can be observed for an anisotropic permeability ratio of 10:1 where tensile fracturing extends slightly farther along the hinge line of the outer arc.

Fractures are not observed in the hinge for strong rocks, and are not observed in the limb for any scenario during the anisotropic permeability analysis for high permeability folds.

4.2.2.2 Low permeability buckling. Figures 4.10 and 4.11 show the fracture potential results for the hinge and limb, respectively, of a weak rock. Initial observations at the fold hinge clearly show that the permeability magnitude plays a role in determining how much of an impact anisotropic permeability has on fracture initiation. The extensive fracturing for each model in Figure 4.10 is reflective of the low permeability magnitudes, as seen in Section 4.2.1, but there are noticeable changes in fracture distribution for the low permeability models that are not observed in the high permeability models. In contrast to high permeability models, where anisotropic permeability had very little influence on fracture initiation, low permeability models show more extensive fracturing for increasing anisotropic permeability ratios. Further inspection reveals that higher anisotropic permeability ratios lead to more widespread early-stage fracturing in the inner arc, and more widespread mid-stage fracturing in the outer arc, replacing what would have respectively been mid-stage and late-stage fractures for models with lower anisotropic permeability ratios. Fracturing in the models is too extensive to provide a detailed description of the timing and location of fractures, but the general distribution of shear and tensile fractures is similar for each model. The inner arc consists of early-stage shear fracturing that extends well into the interior of the fold. The outer arc exhibits varying combinations of mid-stage and late-stage tensile fracturing beginning at the central portion and extending along a majority of hinge line, eventually giving way to late-stage shear fractures near the end portion. The end portion is characterized by shear
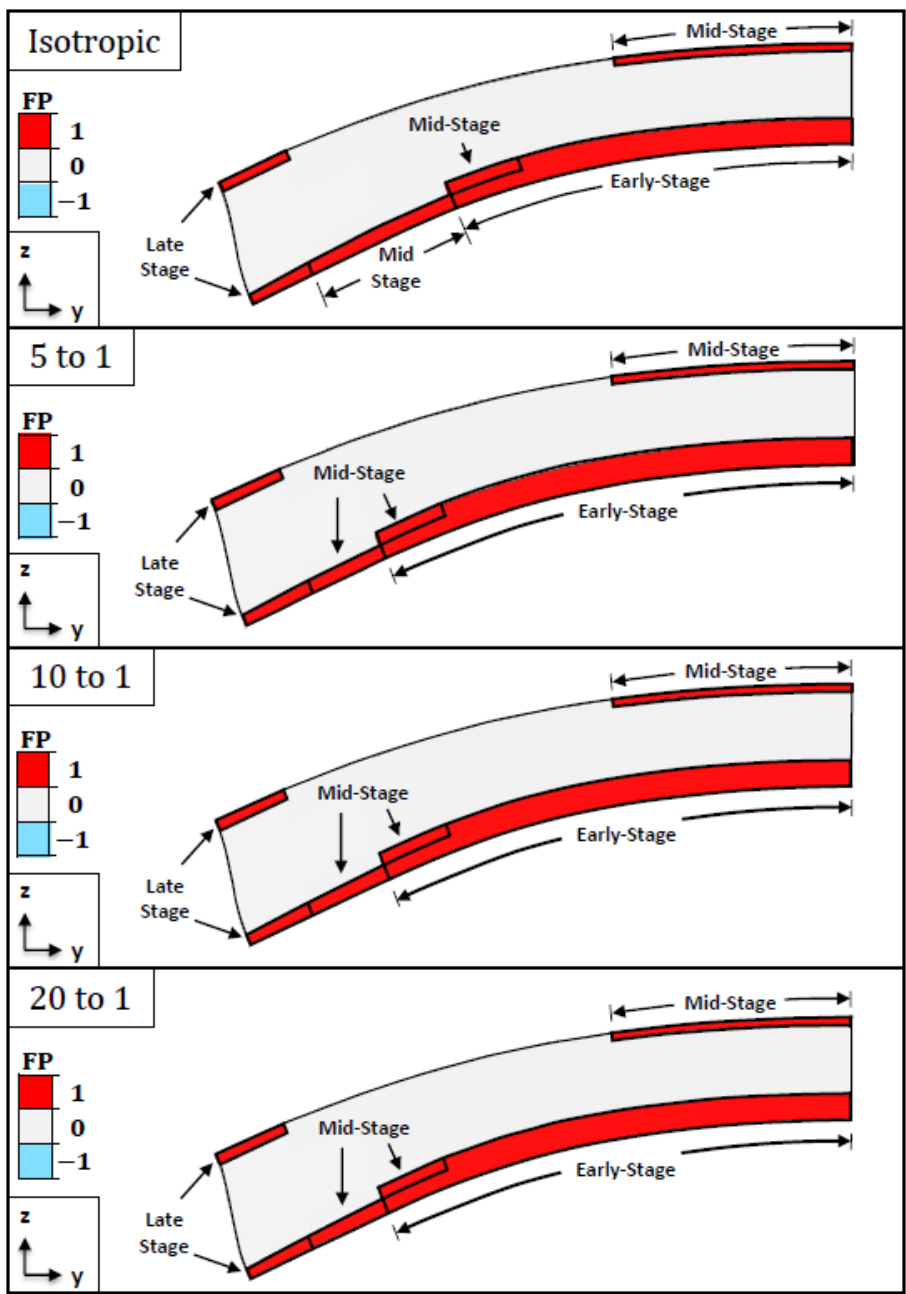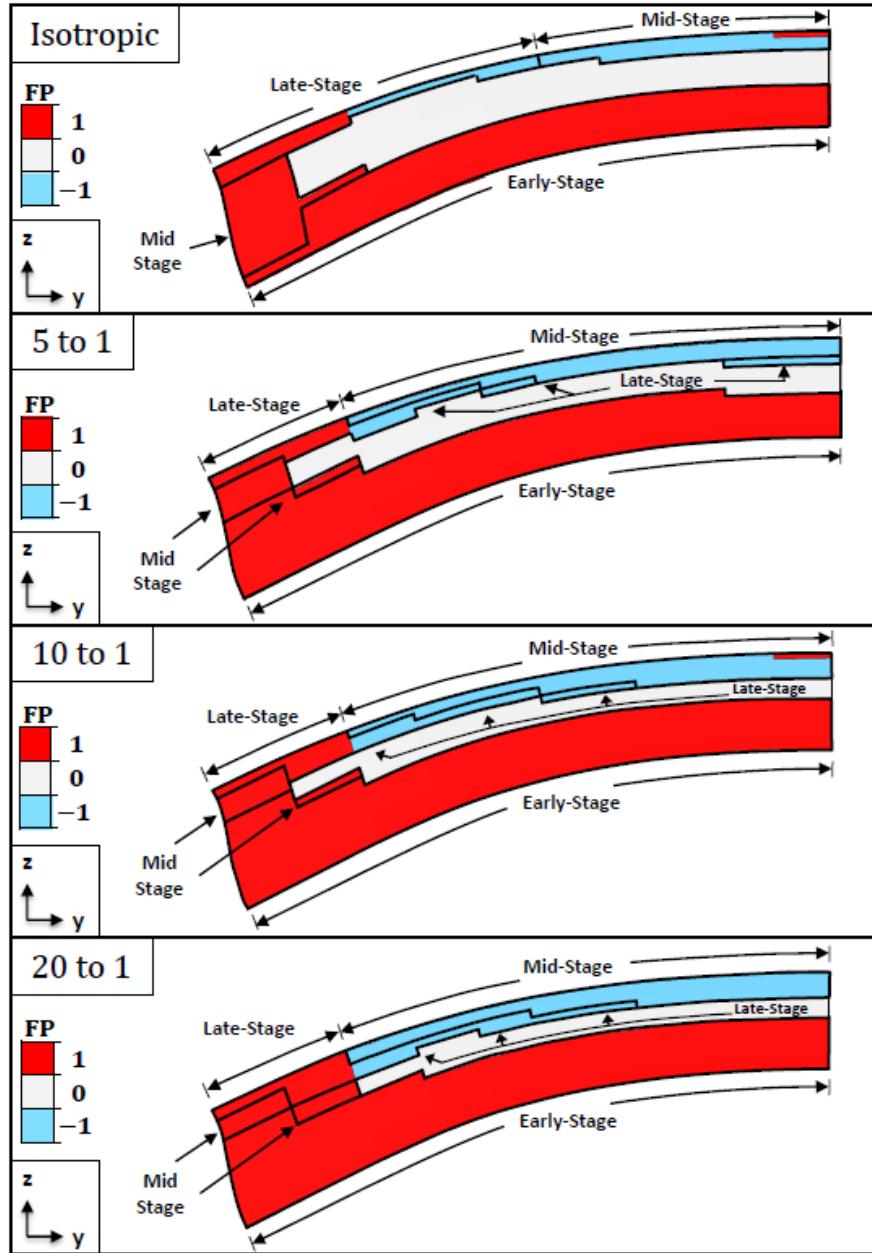
Figure 4.10. Fracture potential results in the hinge for a low permeability (10^{-21} m^2) weak rock, with varying degrees of permeability anisotropy. The final fold shape is approximately the same for each model.

fractures that grade from early-stage in the inner arc, to mid and late-stage in the outer arc. Early stage shear fractures are also initiated in the limb for the anisotropic permeability models. Figure 4.11 shows that the fractures initiate in the top and bottom of the limb near the end portion, and fracturing extends both along the length of the limb
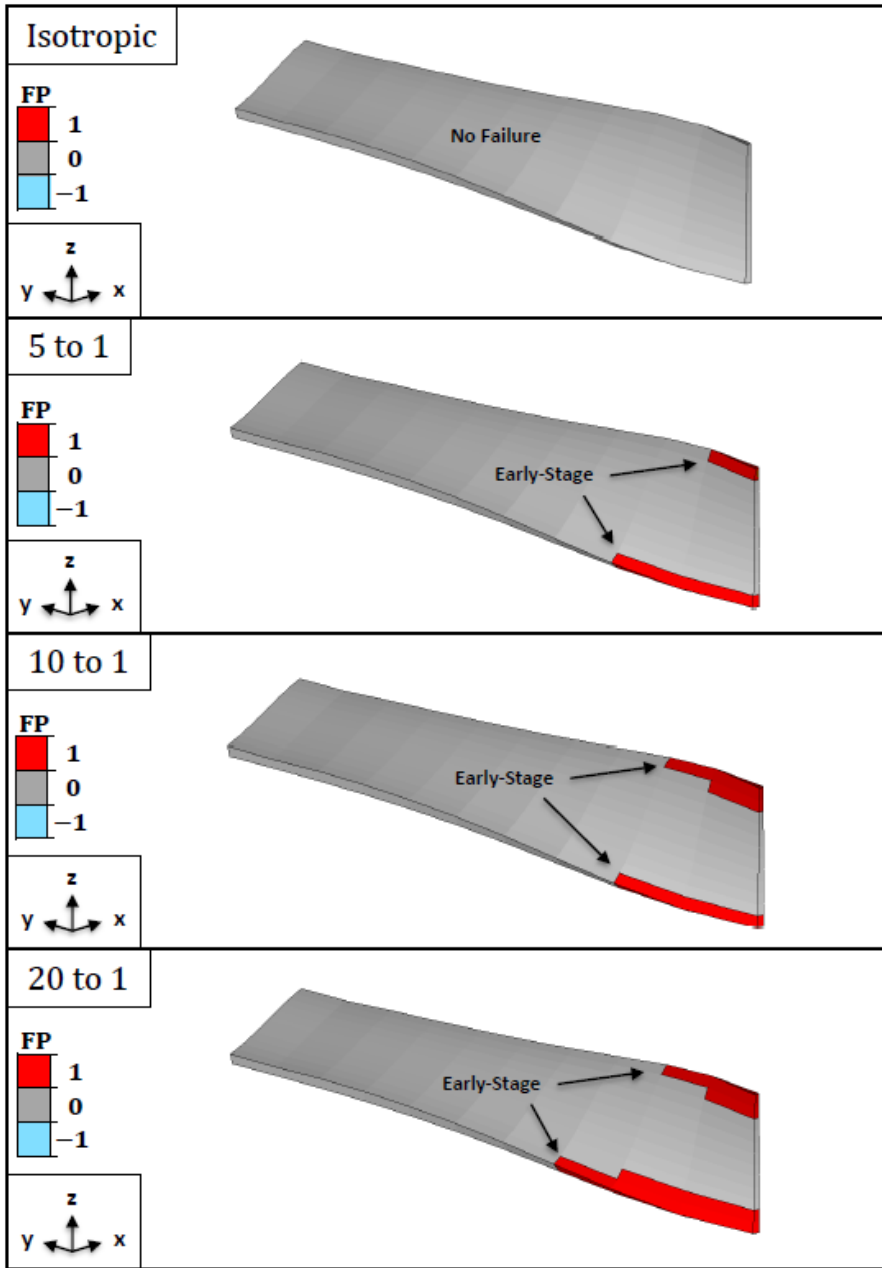
Figure 4.11. Fracture potential results in the limb for a low permeability (10^{-21} m^2) weak rock, with varying degrees of permeability anisotropy. The final fold shape is approximately the same for each model.

and inwards toward the interior of the fold as the anisotropic permeability ratio is increased.

Figures C.2 and C.3 show the fracture potential results for the hinge of an intermediate strength rock and strong rock, respectively. While not as noticeable as it is

for a weak rock, anisotropic permeability still exhibits the same influence for intermediate strength rocks and strong rocks, where fracturing is more widely distributed for higher anisotropic permeability ratios. Mid to late-stage tensile fractures and shear fractures still persist along the outer arc for both intermediate strength rocks and strong rocks, but the extent of inner arc shear fracturing decreases a great deal for intermediate strength rocks, and all but disappears for strong rocks. Fracture initiation is not observed in the limb for intermediate strength rocks or strong rocks.

4.2.2.3 Erosion. The erosional unloading step from Section 3.2.3 is applied to high permeability models to test the influence on fracture initiation in folds with anisotropic permeability. Erosional unloading for low permeability models is not examined in this study following observations by Eckert et al. (2014), which show that the pore pressure evolution for low permeability folds during erosional unloading gives rise to a state of effective stress that is unlikely to cause fracture initiation. It is important to note that the overburden thickness increases significantly during the lateral shortening step. Thus, the amount of overburden to be eroded, and the duration of the erosional unloading step are dependent on both the initial thickness of the overburden, and the amount of lateral shortening. The overburden thickness prior to erosion, and duration of erosion for the anisotropic, high permeability models are given in Table 4.3. Since the initial geometric properties are the same for each model, and the same amount of shortening is applied, the pre-erosion overburden thickness and the duration of erosion are also the same for each model.

Table 4.3. Erosion characteristics for the anisotropic, high permeability models.

Model (k_h to k_v)	Pre-Erosion Overburden Thickness (m)	Duration of Erosion (Ma)
Isotropic	498.7	0.5
5 to 1	498.7	0.5
10 to 1	498.7	0.5
20 to 1	498.7	0.5

It is recalled that the assumptions for this study permit only one fracturing event for an individual element. This assumption also applies during erosional unloading such that an element, which is fractured during buckling, will not fracture during erosion. Because the exact timing of fracture initiation during erosional unloading is beyond the scope of this study, fracture potential plots for erosion only consider two scenarios for the timing of fracture initiation: fractures that initiate prior to erosion (i.e., during buckling), and fractures that initiate during erosion.

Figures 4.12 and 4.13 show the fracture potential results for the hinge and limb, respectively, of a weak rock. The fracture potential plots reveal that erosional unloading leads to the initiation of new fractures in the hinge and limb, but these fractures appear to be independent of the degree of permeability anisotropy since they initiate in the exact same manner for each model. Erosional fractures in the hinge include shear fractures that initiate in the end portion near the outer arc, and tensile fractures that initiate along the outer arc. In the limb, erosional shear fracturing extends across the entire thickness of the fold near the central portion, and extends towards the end portion at select locations within the folding layer.

Figures C.4 and C.5 show the fracture potential results for the hinge of an intermediate strength rock and strong rock, respectively. The results for the intermediate strength rock and strong rock show less extensive fracturing than for a weak rock, but present the same general observation; new fractures are initiated during erosional unloading but they are independent of the degree of permeability anisotropy. Fracture initiation is not observed in the limb for intermediate strength rocks or strong rocks.

4.2.3. Influence of Viscosity Contrast. Using a constant folding layer viscosity of 1.2×10^{21} Pa · s, the viscosity for the matrix, overburden, and base is varied so that fracture initiation can be observed and compared for models with different viscosity contrasts (R_μ = 25, 50, 75, 100). All other material properties in Table 3.1 remain fixed, and the permeability is considered to be isotropic. The vertical dimensions of the initial model geometry remain unchanged for each model, but horizontal dimensions must be altered to ensure that a pericline with a final aspect ratio of 1:5 still develops after 50% shortening. It is recalled that R_μ governs the dominant wavelength selection. The wavelength of the initial perturbations in the x-direction for each model varies according

Figure 4.12. Fracture potential results in the hinge for a high permeability (10^{-15} m^2) weak rock, with varying degrees of permeability anisotropy, after erosional unloading. The final fold shape is approximately the same for each model.

to the Biot dominant wavelength relationship given in equation (1). Initial perturbations in the y-direction are adjusted for each model to ensure the desired final aspect ratio is achieved. The resulting final geometries for the viscosity contrast models are given in Table 4.4. Aside from the larger wavelengths and hinge lengths needed to satisfy initial

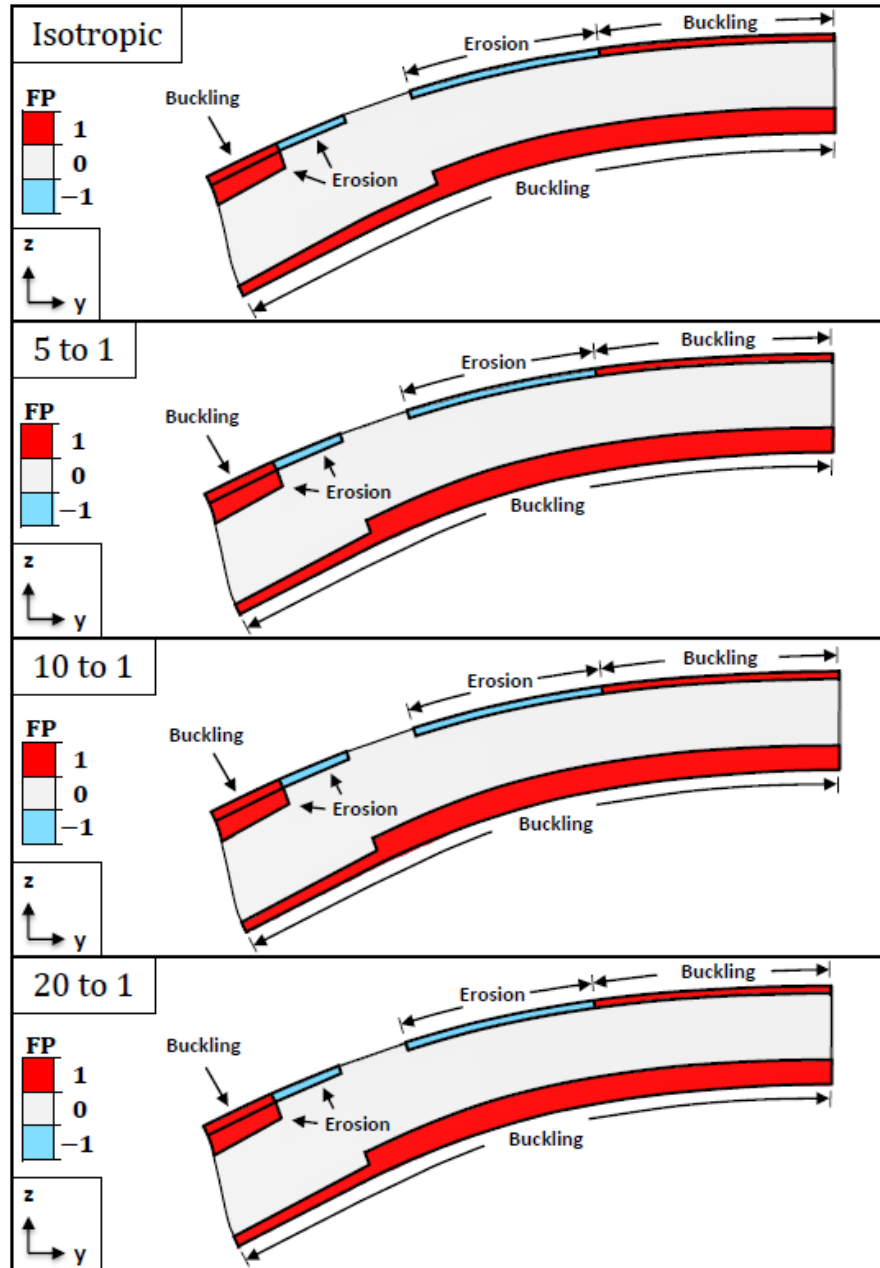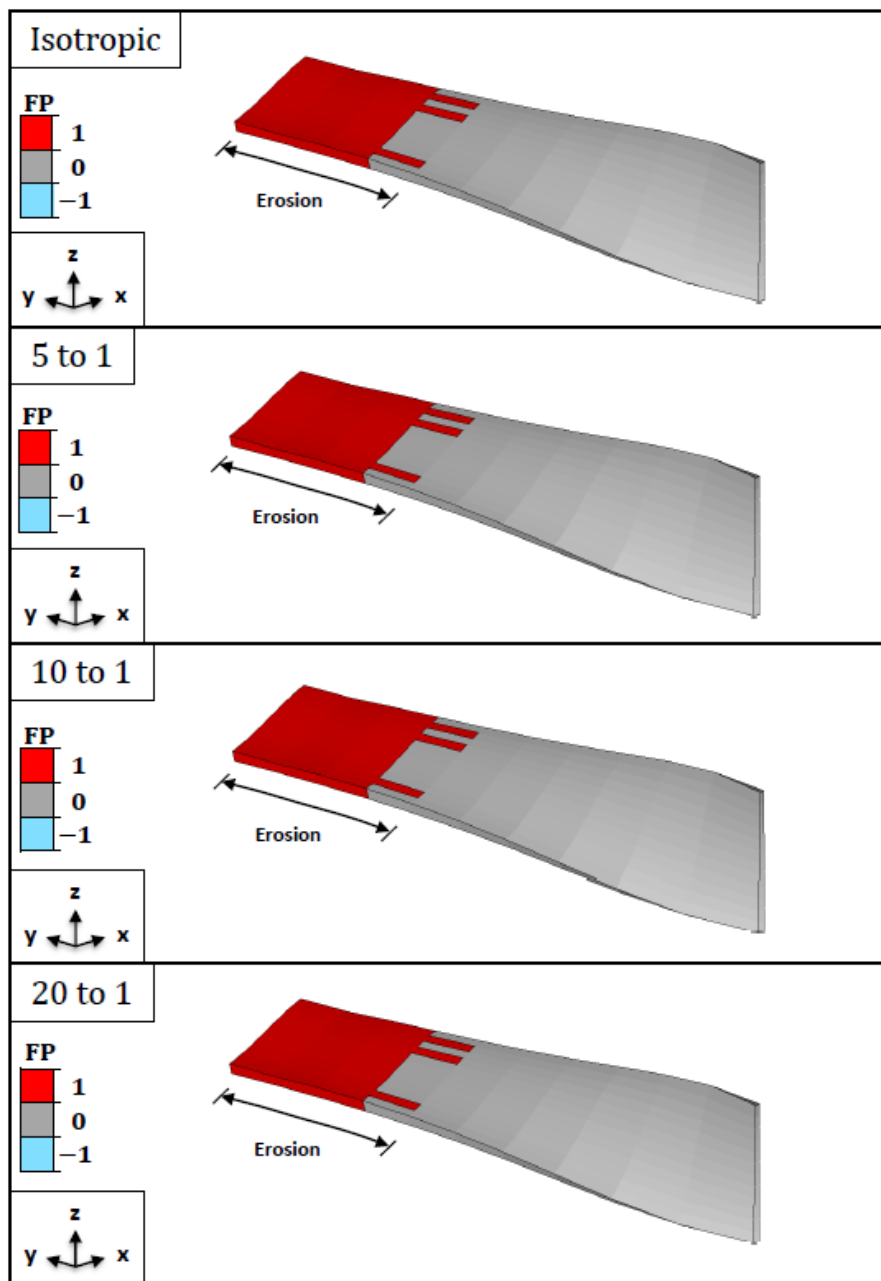Figure 4.13. Fracture potential results in the limb for a high permeability (10^{-15} m^2) weak rock, with varying degrees of permeability anisotropy, after erosional unloading. The final fold shape is approximately the same for each model.

geometry requirements, higher viscosity contrasts also result in noticeably higher fold amplitudes, slightly thinner folding layers, and moderately steeper limb dips.

Table 4.4. Geometric properties for the viscosity contrast models (base model is shaded in gray). Measurements are representative of the central portion of the pericline.

Model (R_μ)	Final Half Wavelength (m)	Final Hinge Length (m)	Final Amplitude (m)	Final Folding Layer Thickness (m)	Final Limb Dip (°)
25	75.83	379.14	36.82	43.49	68
50	95.55	477.52	56.64	39	75.5
75	109.36	546.83	68.68	37.71	77.1
100	120.37	601.87	77.83	37.13	77.5

Figures 4.14 and 4.15 show the fracture potential results for the hinge and limb, respectively, of a weak rock, with the viscosity contrast of 50 representing the base model. In the hinge, each model demonstrates noticeable deviations from the fracture distribution in the base model. For the model with the lowest viscosity contrast ($R_\mu =$ 25), mid-stage shear fracturing extends farther into the interior of the fold along the inner arc, but is not observed near the central portion of the outer arc. The model with a viscosity contrast of 75 is characterized by the disappearance of mid-stage shear fractures in the inner arc, and a decrease in the extent of mid-stage shear fracturing near central portion of the outer arc. The model with the highest viscosity contrast ($R_\mu = 100$) exhibits the same disappearance of mid-stage shear fractures in the inner arc, as well as the additional disappearance of mid-stage shear fractures near the central portion of the outer arc. Furthermore, the model with a viscosity contrast of 100 features the initiation of mid-stage tensile fractures near the central portion of the outer arc, and late-stage tensile fractures near the end portion of the outer arc. Shear fracturing is only observed in the limb for the lowest viscosity contrast model. Figure 4.15 shows that the shear fracturing initiates during the late stage of buckling in the folds interior, but does not extend to the central or end portions.

Figures D.1 and D.2 show the fracture potential results for the hinge of an intermediate strength rock and a strong rock, respectively. For intermediate strength rocks, the lowest viscosity contrast model exhibits mid and late-stage shear fracturing along the entire length of the inner arc, and late stage shear fracturing near the end

Figure 4.14. Fracture potential results in the hinge for a weak rock with varying values of R_μ. Increasing the viscosity contrast will result in folds with larger wavelengths and hinge lengths, higher amplitudes, thinner folding layers, and steeper limb dips.

portion of the outer arc. Once R_μ increases to values greater than 50, fracture initiation all but ceases for intermediate strength rocks, with only late-stage shear fractures initiating near the end portion of the inner arc for the model with a viscosity contrast of 100. The only fractures initiated in strong rocks are late-stage shear fractures near the end portion
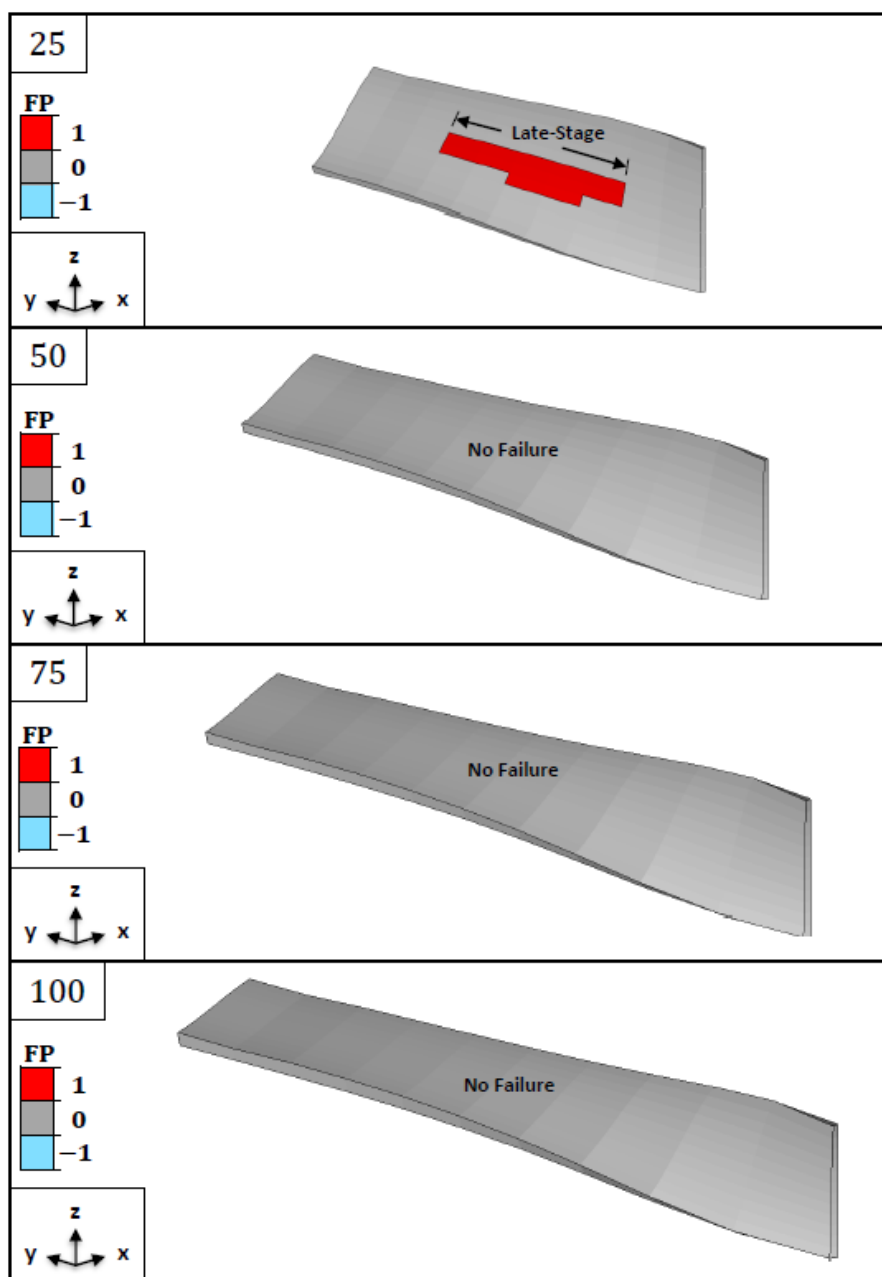
Figure 4.15. Fracture potential results in the limb for a weak rock with varying values of R_μ. Increasing the viscosity contrast will result in folds with larger wavelengths and hinge lengths, higher amplitudes, thinner folding layers, and steeper limb dips.

of the inner arc for the lowest viscosity contrast model. Fracture initiation is not observed in the limb for intermediate strength rocks or strong rocks.

Viscosity contrast models that include erosion are excluded from this study due to asymmetric fold shapes that develop during the erosional unloading procedure.

4.2.4. Influence of Pericline Aspect Ratio. Because periclines in nature exhibit a range of different aspect ratios, a set of models is established to test the influence of the pericline aspect ratio on fracture initiation. These models are set up such that periclines with aspect ratios of 1:3, 1:5, and 1:7 are generated after 50% shortening. Fracture initiation is investigated during both buckling and erosional unloading for the pericline aspect ratio analysis. To ensure that the pericline aspect ratio is the only parameter that is varied, all models are assigned material properties and initial model dimensions in the x and z-directions that are identical to the base model (refer to Figure 3.1). Only the initial perturbation length in the y-direction is modified to achieve the final desired aspect ratio for each respective model. Final fold geometries for the aspect ratio models are given in Table 4.5. As expected, the most significant geometric change is the considerable increase in hinge length that accompanies an increase in the aspect ratio. Increasing the final aspect ratio also results in slightly higher fold amplitudes, and slightly steeper limb dips; the largest increase for both cases is observed during the jump from an aspect ratio of 1:3 to an aspect ratio of 1:5. The final aspect ratio appears to have very little influence on the thickness of the folding layer.

Table 4.5. Geometric properties for the aspect ratio models (base model is shaded in gray). Measurements are representative of the central portion of the pericline.

Model (AR)	Final Half Wavelength (m)	Final Hinge Length (m)	Final Amplitude (m)	Final Folding Layer Thickness (m)	Final Limb Dip (°)
1 to 3	95.55	286.65	53.79	38.98	73.8
1 to 5	95.55	477.52	56.64	39	75.5
1 to 7	95.55	668.85	56.76	39.14	75.7

4.2.4.1 Buckling. Figure 4.16 shows the fracture potential results for the hinge of a weak rock, with an aspect ratio of 1:5 representing the base model. Overall fracture distributions are similar for each model, although there are two noteworthy deviations from the base model distribution. First, the lowest aspect ratio model (1:3) contains mid and late-stage shear fractures that span nearly the entire thickness of the fold at the end
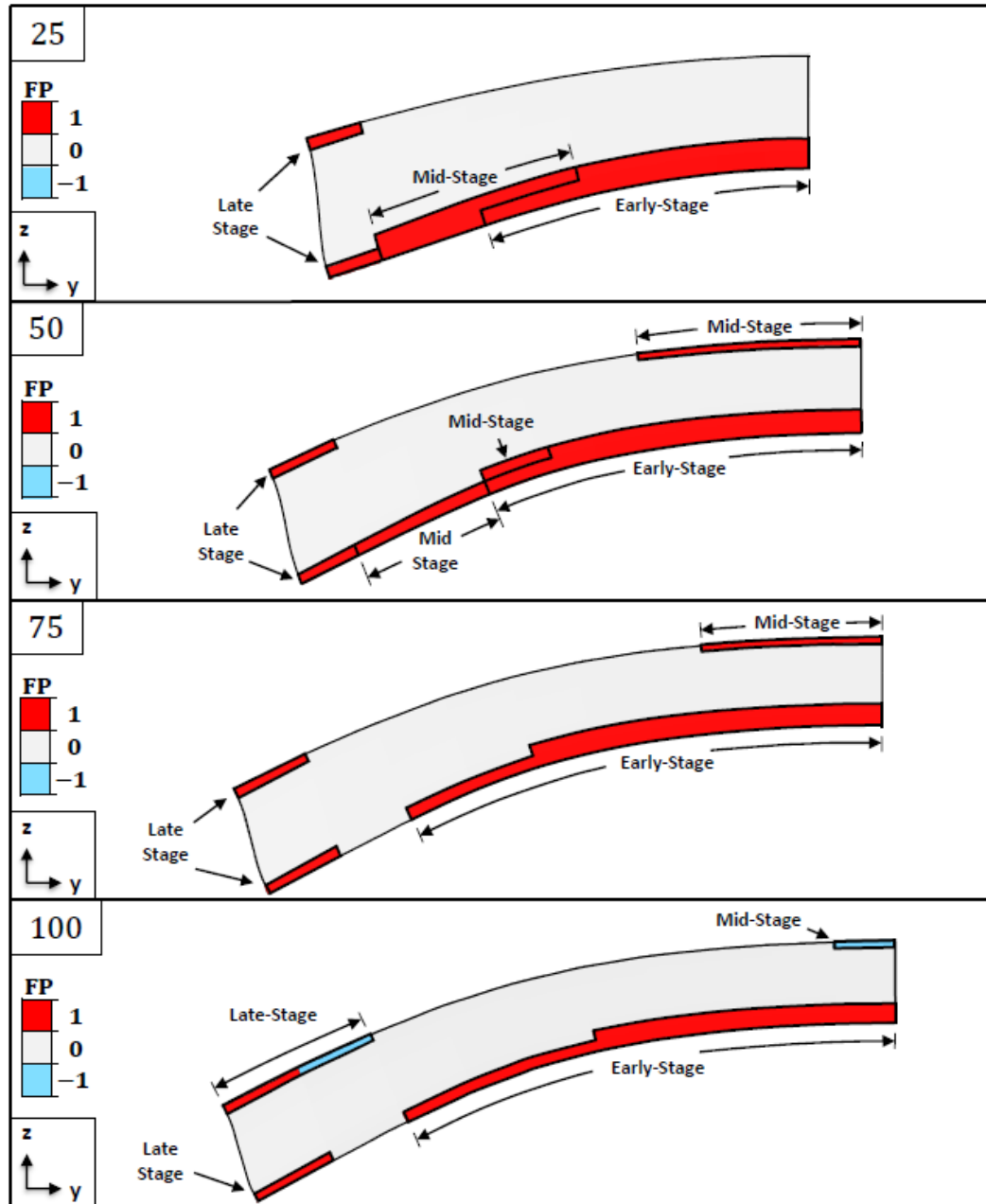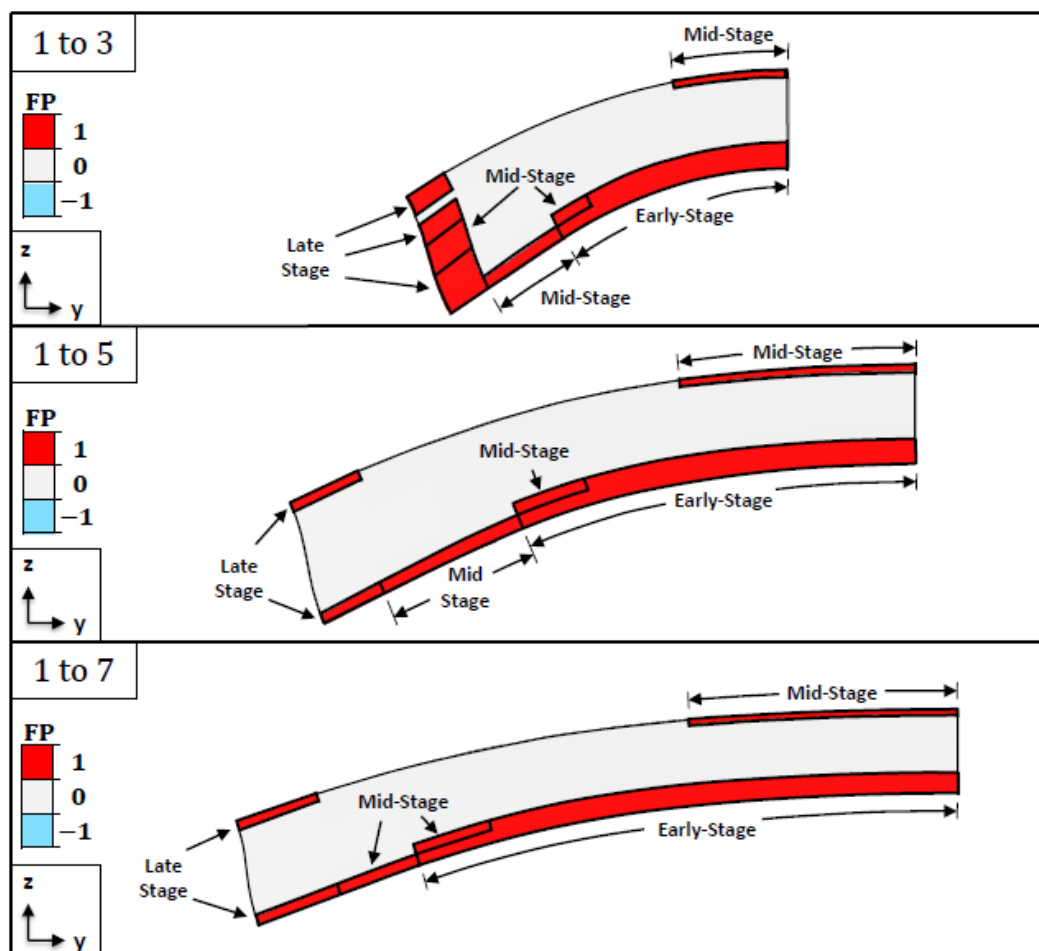
Figure 4.16. Fracture potential results in the hinge for a weak rock with varying final aspect ratios. Increasing the aspect ratio will result in folds with longer hinge lengths.

portion. Second, the highest aspect ratio model (1:7) exhibits mid-stage shear fracturing that extends slightly farther into the interior of the fold near the end portion of the outer arc.

Figure E.1 shows the fracture potential results for the hinge of an intermediate strength rock. The intermediate strength rock exhibits identical mid-stage tensile fracturing near the central portion of the outer arc for each model, but the locations of shear fracturing vary for different aspect ratios. Along the inner arc, shear fracturing is observed near the central portion and end portion for the lowest aspect ratio model, but is not observed at all in the highest aspect ratio model. Outer arc shear fractures are only

initiated in the highest aspect ratio model; these fractures initiate during the late stages of buckling near the end portion.

Fractures are not observed in hinge of a strong rock, and are not observed in the limb for any scenario during the buckling process.

4.2.4.2 Erosion. The erosion characteristics for the aspect ratio models are given in Table 4.6. Overburden thickness prior to the onset of erosion shows slight thinning as aspect ratios increase, but the changes are relatively insignificant, and the duration of the erosion remains approximately the same for each model.

Table 4.6. Erosion characteristics for the aspect ratio models.

Model (AR)	Pre-Erosion Overburden Thickness (m)	Duration of Erosion (Ma)
1 to 3	499.2	0.5
1 to 5	498.7	0.5
1 to 7	497.8	0.5

Figures 4.17 and 4.18 show the fracture potential results for the hinge and limb, respectively, of a weak rock. The hinge exhibits erosional fracturing of various combinations of type and location in the outer arc for each model. In general, outer arc erosional fractures appear to become slightly more dispersed as the aspect ratio increases. For instance, the highest aspect ratio model (1:7) shows patchy tensile fracturing along the outer arc, while the lowest aspect ratio model (1:3) displays localized tensile fracturing halfway along the hinge line and localized shear fracturing near the end portion. The limb of each model contains erosional shear fractures near the central portion. A clear relationship between shear fracturing in the limb and the aspect ratio is observed. As the aspect ratio increases, shear fracturing disappears in the fold interior and the distribution becomes increasingly thin at the top and bottom of the limb.

Figures E.2 and E.3 show the fracture potential results for the hinge and limb, respectively, of an intermediate strength rock. The lowest aspect ratio model exhibits

Figure 4.17. Fracture potential results in the hinge for a weak rock, with varying final aspect ratios, after erosional unloading. Differences in the final fold shape are a result of the different aspect ratios considered and not due to erosional unloading.

erosional shear fracturing near the end portions of the inner and outer arcs. In the highest aspect ratio model, shear fractures initiate near the end portions of the inner and outer arcs, and tensile fractures initiate at two separate locations closer to the end portion. In the limb, the only erosional fractures that initiate are shear fractures near the top and bottom of the central portion for the lowest aspect ratio model.

Figure E.4 shows the fracture potential results for the hinge of a strong rock. The lowest aspect ratio model only shows erosional shear fracturing near the end portions of the inner and outer arcs. The erosional fracture distribution in the highest aspect ratio model is identical to the distribution for the base model. Fracture initiation is not observed in the limb of a strong rock for any model.
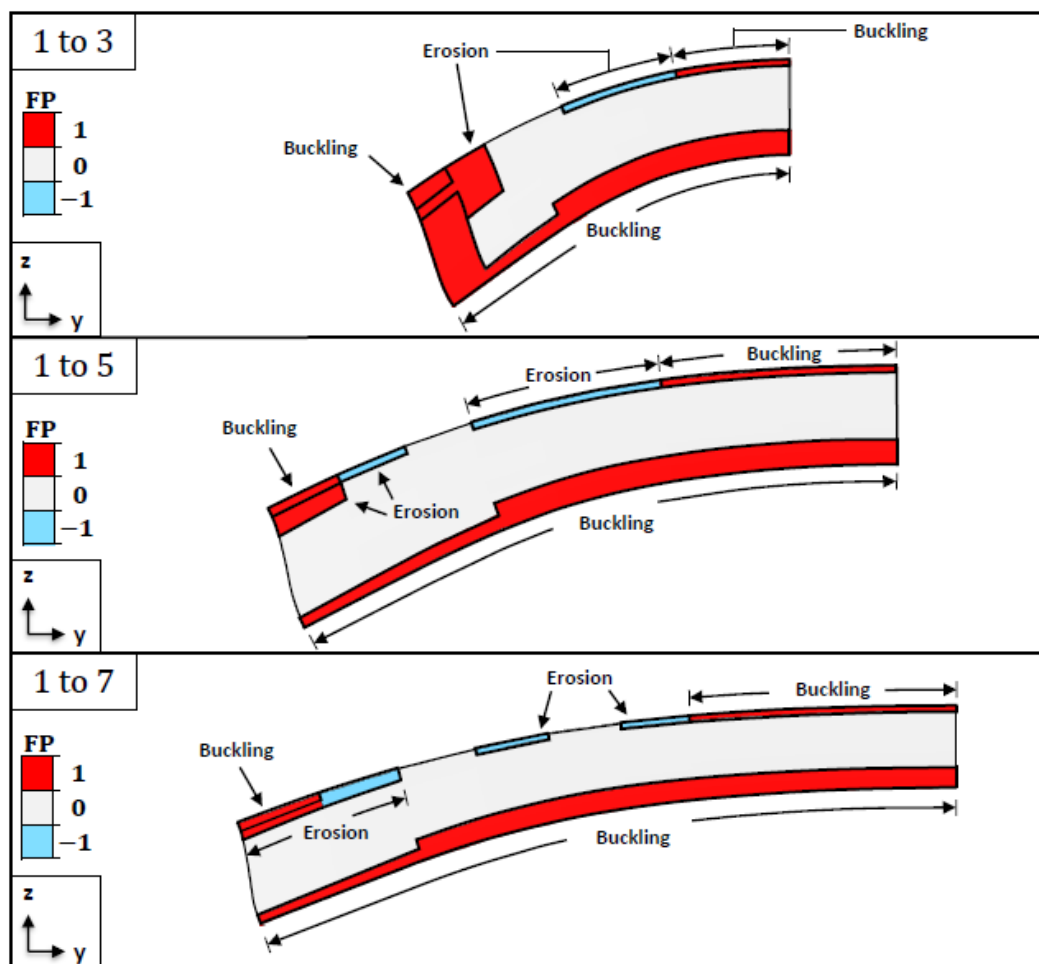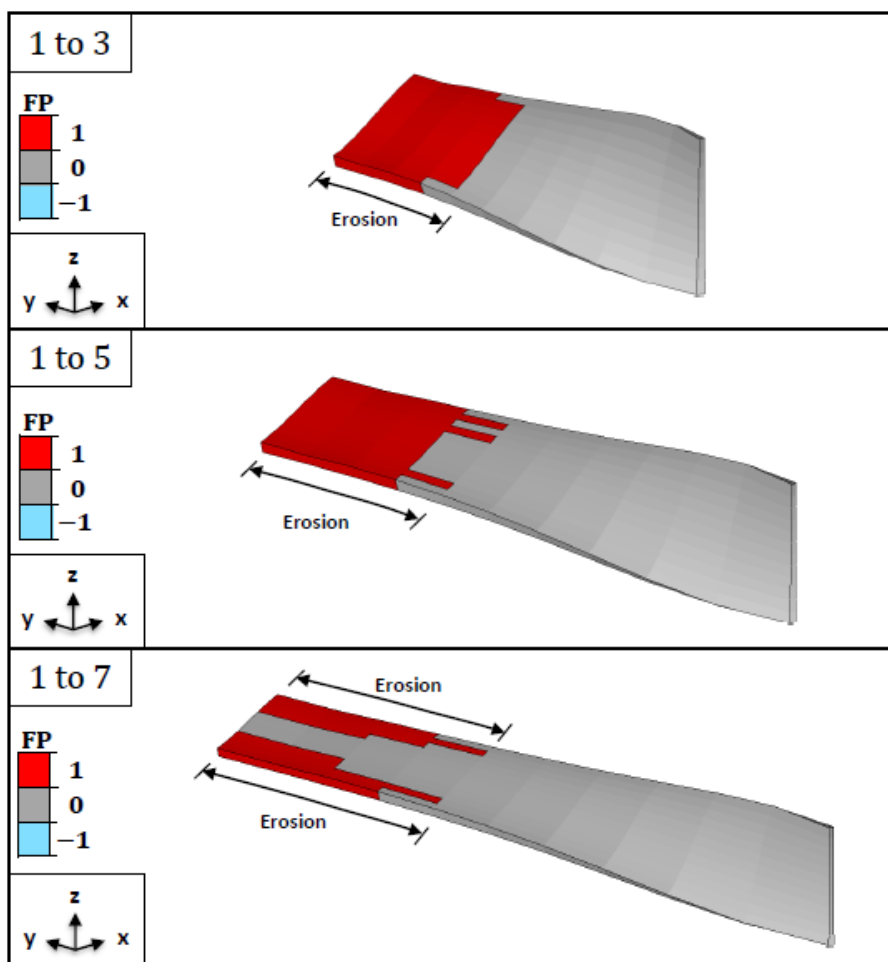
Figure 4.18. Fracture potential results in the limb for a weak rock, with varying final aspect ratios, after erosional unloading. Differences in the final fold shape are a result of the different aspect ratios considered and not due to erosional unloading.

4.2.5. Influence of Shortening Percentage. Each analysis up to this point has assumed that the final desired aspect ratio is achieved after 50% shortening, resulting in folds with relatively high amplitudes and steep limb dips. Keeping a constant final aspect ratio of 1:5, models are set up with various percentages of lateral shortening (10, 20, 30, 40, 50) to see how fracture initiation changes for lower amplitude folds with gentler limb dips. Fracture initiation in these models is tested for both buckling and erosional unloading. Each model is assigned material properties and initial geometric dimensions in the x and z-direction that are identical to the base model. To ensure that a final aspect ratio of 1:5 develops for each model, the length of the initial perturbation in the y-

direction is varied accordingly. Final geometric properties for the centrally located periclines in each respective model are given in Table 4.7. Models with lower shortening percentages result in folds with larger final wavelengths, and therefore require longer hinge lengths to achieve the desired aspect ratio. In addition, increasing the shortening percentage leads to higher amplitudes, thicker folding layers, and steeper limb dips.

Table 4.7. Geometric properties for the shortening percentage models (base model is shaded in gray). Measurements are representative of the central portion of the pericline.

Model	Final Half Wavelength (m)	Final Hinge Length (m)	Final Amplitude (m)	Final Folding Layer Thickness (m)	Final Limb Dip (°)
10%	171.98	860.61	9.97	33.1	11.6
20%	152.86	764.98	25.02	35.62	29.8
30%	133.77	668.71	38.31	37.08	47.9
40%	114.63	573.02	48.39	38.11	63.1
50%	95.55	477.52	56.64	39	75.5

4.2.5.1 Buckling. Figure 4.19 shows the fracture potential results at the hinge of a weak rock, with the 50% shortening model representing the base case. It should be noted that the timing of fracture initiation for the buckling analysis is not very meaningful since lower shortening percentages are considered (i.e., based on the definition of early, mid, and late-stage fractures only early stage fractures are initiated for the 10% shortening model). What becomes of primary interest is how the distribution and extent of fracturing changes with the increasing amplitudes and limb dips that accompany higher shortening percentages. Shear fracturing along the inner arc is observed for all models, but the extent of fracturing changes with shortening percentage. Shear fracturing in the inner arc of the 10% shortening model extends from the central portion to a point approximately halfway along the hinge line. Shear fracturing in the 20 and 30 % models nearly spans the entire length of the inner arc, only ceasing near the end portion. The 40% model and the base model both display shear fracturing along the entire length of the inner arc, but near the end portion the fracturing does not extend as far into the fold
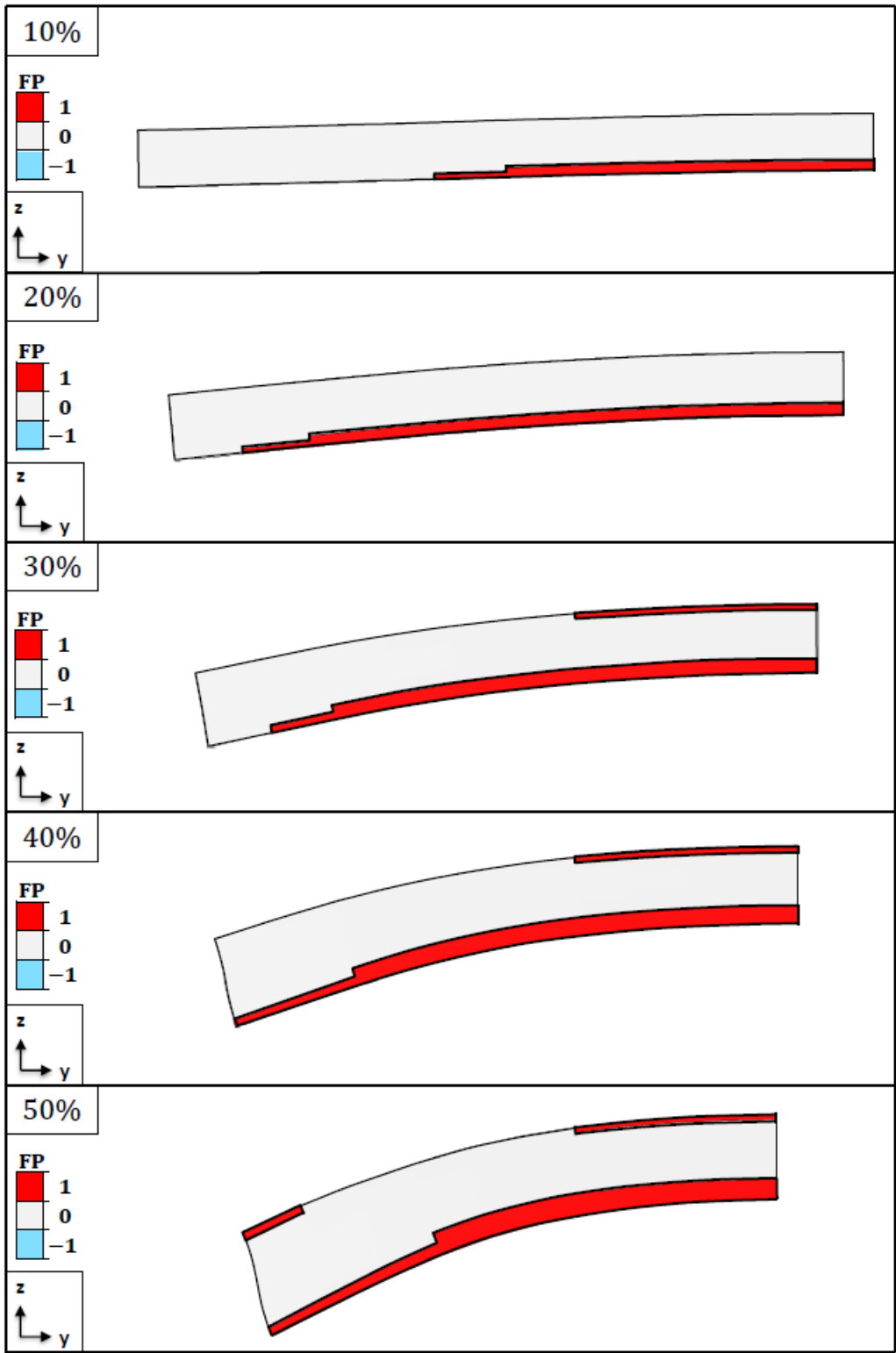
Figure 4.19. Fracture potential results in the hinge for a weak rock with varying amounts of lateral shortening. Increasing the shortening percentage will result in folds with smaller wavelengths and hinge lengths, higher amplitudes, thicker folding layers, and steeper limb dips.

interior for the base model. Shear fracture initiation is only observed in the outer arc for models that experience greater than 20% shortening. These include fractures near the central portion that appear for 30, 40, and 50% shortening, and fractures near the end portion that only initiate for the base model.

Figure F.1 shows the fracture potential results at the hinge for an intermediate strength rock. Tensile fractures in the central portion of the outer arc initiate for all models with shortening percentages greater than 20%. The only other fractures observed for intermediate strength rocks are shear fractures that initiate near the end portion of the inner arc for the base model.

Fracturing is neither observed in the hinge of strong rocks, nor in the limb for any combination of rock strength and shortening percentage.

4.2.5.2 Erosion. The erosion characteristics for the shortening percentage models are given in Table 4.8. Initial overburden thickness is the same for each model, but increasing the shortening percentage results in more significant thickening of the overburden during buckling, and therefore longer periods of erosion.

Table 4.8. Erosion characteristics for the shortening percentage models.

Model	Pre-Erosion Overburden Thickness (m)	Duration of Erosion (Ma)
10%	277.6	0.28
20%	312	0.31
30%	356.2	0.36
40%	415.7	0.42
50%	498.7	0.5

Figures 4.20 and 4.21 show the fracture potential results for the hinge and limb, respectively, of a weak rock. The most obvious relationship that can be observed is the regression of erosional shear fracture distributions along the inner arc as final fold amplitude and limb dip increase. For the 10% shortening model, which exhibits the lowest amplitude and gentlest limb dips, erosional shear fracturing spans the entire

Figure 4.20. Fracture potential results in the hinge for a weak rock, with varying amounts of lateral shortening, after erosional unloading. Differences in the final fold shape are a result of the differences in lateral shortening percentage and not due to erosional unloading.
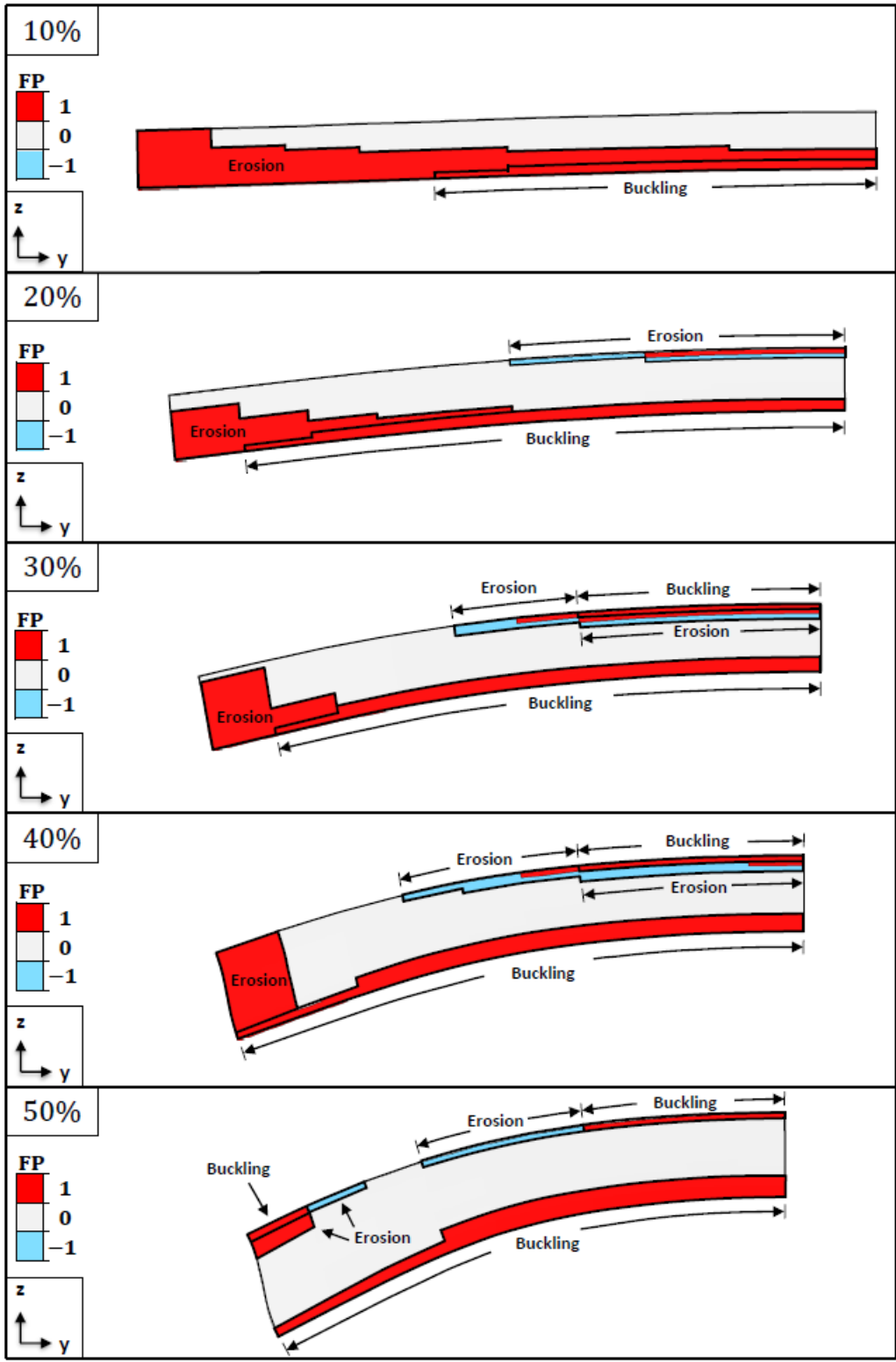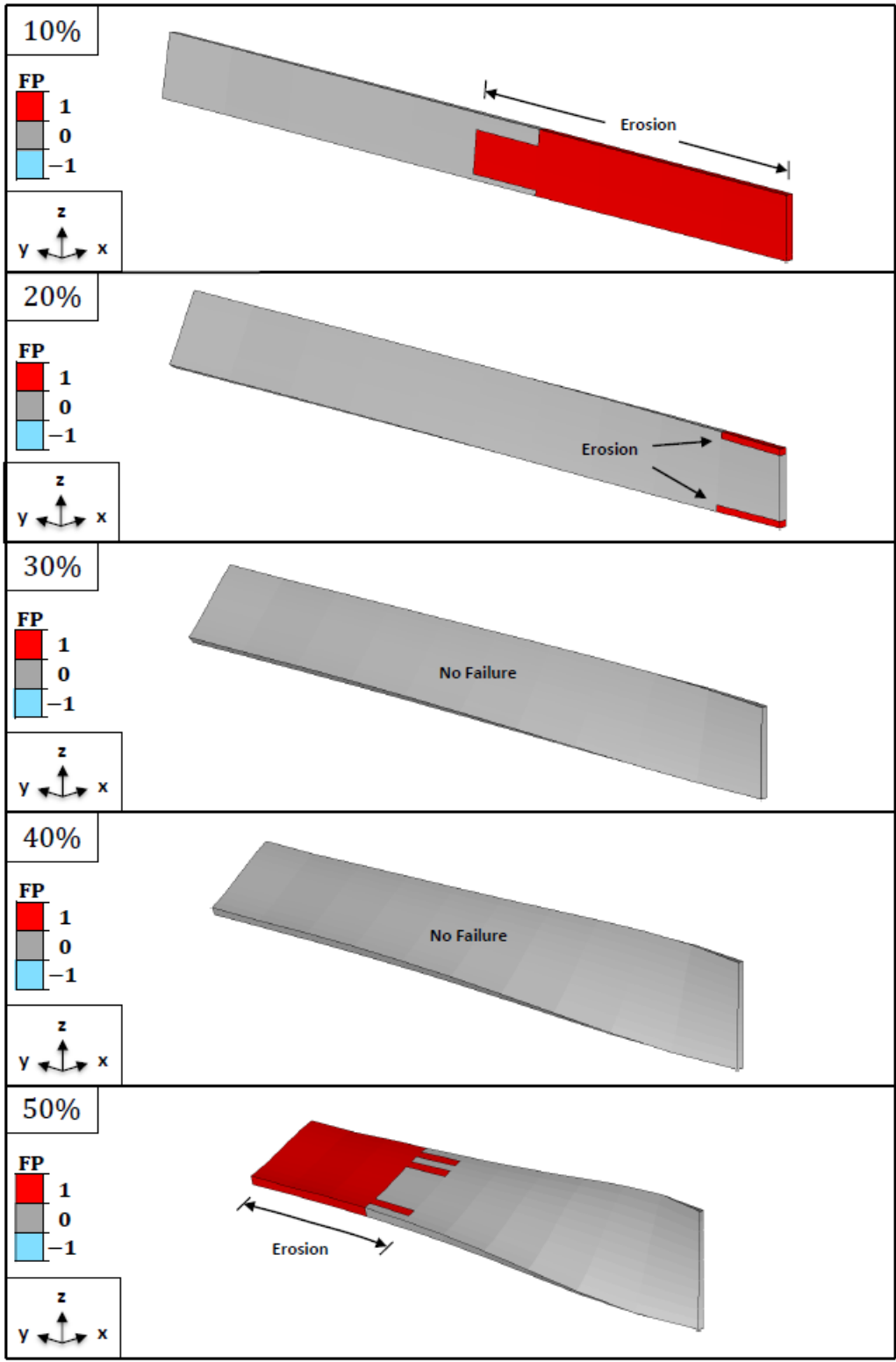
Figure 4.21. Fracture potential results in the limb for a weak rock, with varying amounts of lateral shortening, after erosional unloading. Differences in the final fold shape are a result of the differences in lateral shortening percentage and not due to erosional unloading.

thickness of the fold near the end portion, and extends along the entire length of the inner arc. A similar, but less extensive distribution can be observed in the 20% shortening model, with erosional fracturing only extending from the end portion to a point approximately halfway along the hinge line of the inner arc. The inner arc erosional fracturing becomes even less extensive for the 30 and 40% shortening models, and completely disappears for the base model. No erosional fracturing is observed near the central portion of the outer arc for the 10% model, but shear and tensile fracturing can be observed along the outer arc towards the central portion for the remainder of the models. The maximum extent of these outer arc fractures, both inwards and towards the end portion, are observed for the 40% shortening model. Pervasive, erosional shear fracturing is observed in the limb of the 10% shortening model and the base model. Fracturing in the 10% shortening model spans the entire thickness of the limb near the end portion, as opposed to the base model where shear fracturing spans the entire thickness of the limb near the central portion. The only other erosional fractures in the limb are shear fractures that appear in the top and bottom of the end portion for the 20% shortening model.

Figure F.2 shows the fracture potential results at the hinge of an intermediate strength rock. Inner arc erosional shear fractures are initiated for the 10, 20, and 30% shortening models. In the 10% shortening model these fractures extend from the central portion to slightly over halfway along the hinge line. For the 20% shortening model, inner arc shear fracturing extends along nearly the entire hinge length, disappearing only near the end portion. The inner arc erosional shear fractures for the 30% model are concentrated near the end portion. Erosional tensile fracturing is observed in the outer arc for shortening percentages of 20, 30, and 40%. In all cases, fracturing extends from the central portion towards the end portion, with the 40% shortening model showing fracturing that extends the farthest. No erosional fractures are observed in the limb for intermediate strength rocks.

Figure F.3 shows the fracture potential results at the hinge of a strong rock. Excluding the base model, the only fractures that are initiated during erosional unloading for strong rocks are found along the outer arc for shortening percentages of 20, 30, and

40%. These fractures are tensile, and are concentrated more towards the central portion. No erosional fractures are observed in the limb for strong rocks.

4.2.6. Influence of Overburden Stress. The final parameter that is varied for the parametric analysis is the overburden thickness. Overburden thickness for this particular analysis is the total thickness of the portion of the model that overlies the folding layer, and should not be confused with the thickness of the overburden layer. Models with initial overburden thicknesses of 500, 1000, 1500, and 2000 meters are set up to test the influence of overburden stress on fracture initiation. For all models, fracture initiation is analyzed during buckling and erosional unloading. The material properties and initial geometric dimensions in the x and y-directions for each model are identical to the base model. The only parameter that changes is initial thickness of the overburden layer. A final aspect ratio of 1:5 is once again achieved after 50% shortening. Final geometric properties for the overburden stress models are given in Table 4.9. These properties clearly show that initial overburden thickness has very little influence on the final fold geometry.

Table 4.9. Geometric properties for the overburden stress models (base model is shaded in gray). Measurements are representative of the central portion of the pericline.

Model	Final Half Wavelength (m)	Final Hinge Length (m)	Final Amplitude (m)	Final Folding Layer Thickness (m)	Final Limb Dip (°)
500m	95.55	477.52	56.64	39	75.5
1000m	95.55	477.52	56.63	39	75.5
1500m	95.55	477.52	56.66	39	75.4
2000m	95.55	477.52	56.93	38.86	75.5

4.2.6.1 Buckling. Figures 4.22 and G.1 show the fracture potential result for the hinge of a weak rock and intermediate strength rock, respectively, with an overburden thickness of 500 meters representing the base model. For both weak rocks and intermediate strength rocks fracturing is only initiated during buckling for the base
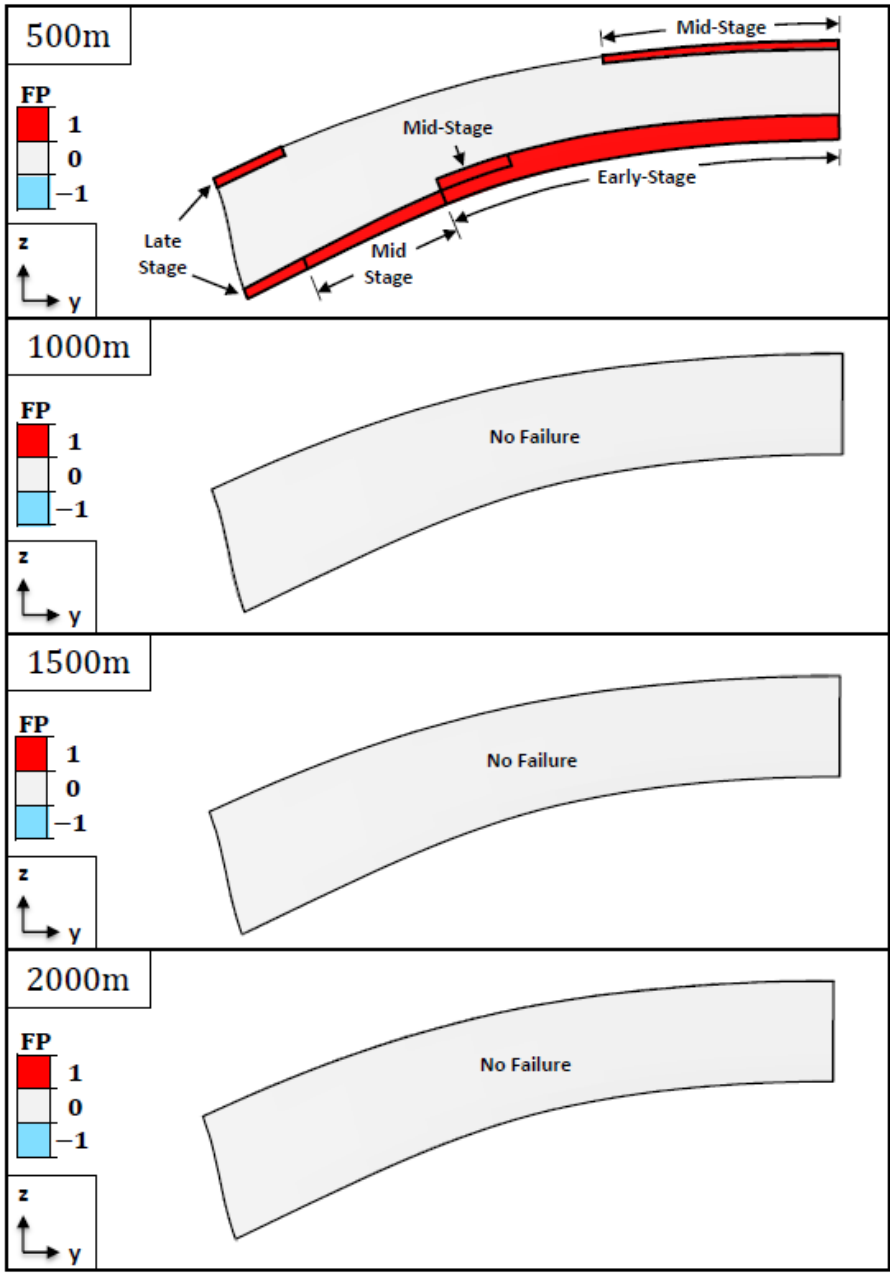
Figure 4.22. Fracture potential results in the hinge for a weak rock with varying amounts of overburden thickness. The final fold shape is approximately the same for each model.

model. Fracturing during buckling is not observed in the hinge of strong rocks and is not observed in the limb for any scenario.

4.2.6.2 Erosion. Erosional characteristics for the overburden stress models are given in Table 4.10. Since 50% shortening is applied to all models during buckling, the pre-erosion overburden thickness is only a function of the initial overburden thickness, and thus a steady increase in the duration of erosion is observed as initial overburden thickness increases.

Table 4.10. Erosion characteristics for the overburden stress models.

Model	Pre-Erosion Overburden Thickness (m)	Duration of Erosion (Ma)
500m	498.7	0.5
1000m	1493.1	1.49
1500m	2482.4	2.48
2000m	3466.2	3.47

Figures 4.23 and 4.24 show the fracture potential results in the hinge and limb, respectively, of a weak rock. Immediately it can be noted that erosional tensile fracturing is not initiated for initial overburden thicknesses greater than 500 meters. Erosional shear fractures are initiated for all models, and the extent of these fractures appears to be heavily influenced by overburden thickness and the duration of the erosion period. In the 1000m overburden model, erosional shear fracturing is predominantly concentrated near the end portion of the outer arc but also appears near the end portion of the inner arc. The fracturing becomes much more extensive for the 1500 and 2000 meter overburden models, spanning the entire length of the outer arc for both models and the entire thickness of the end portion of the fold for the 2000 meter overburden model. Highly pervasive erosional shear fracturing is observed in the limb for all models, beginning in the central portion and extending closer to the end portion as the initial overburden thickness increases.

Figures G.2 and G.3 show the fracture potential results in the hinge and limb, respectively, of an intermediate strength rock. In the hinge, erosional shear fracturing
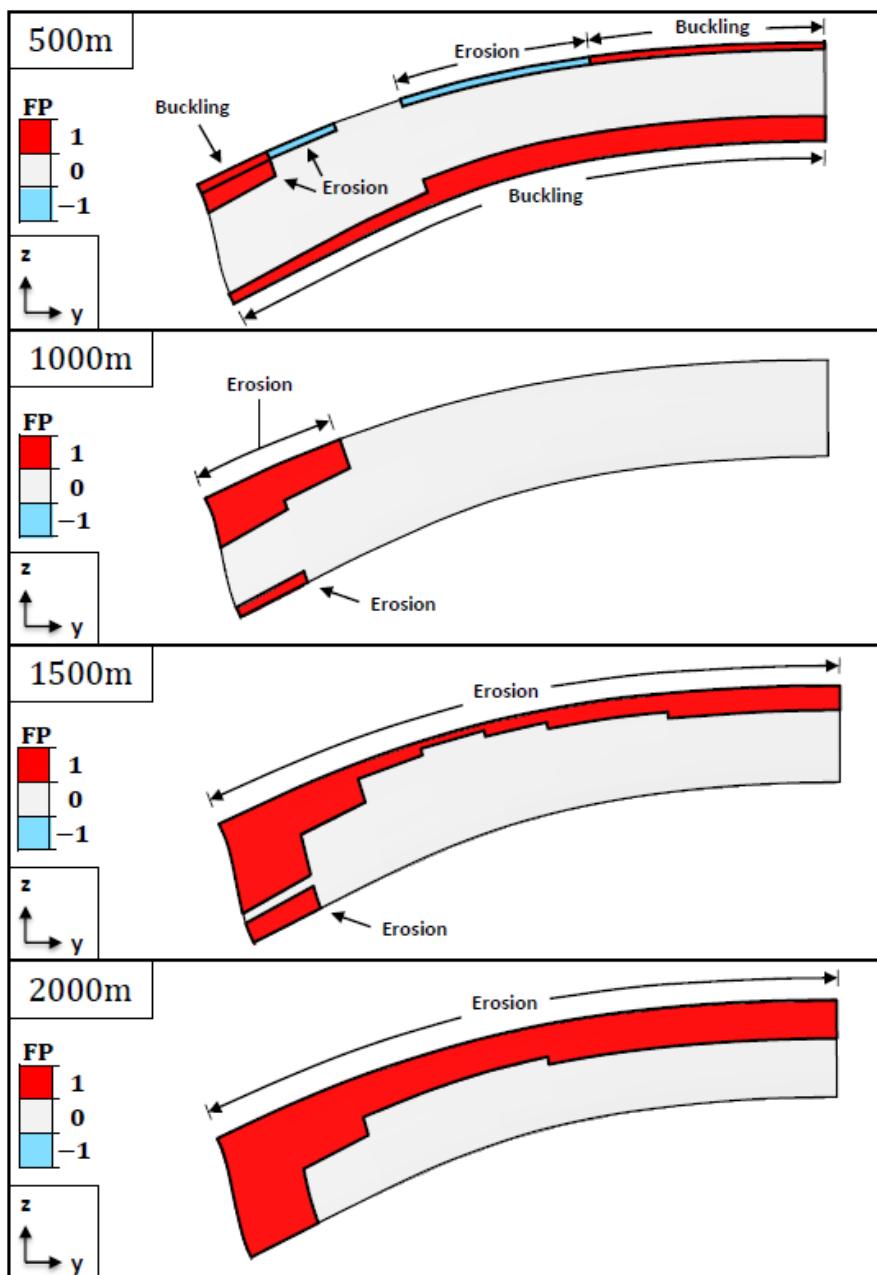
Figure 4.23. Fracture potential results in the hinge for a weak rock, with varying amounts of overburden thickness, after erosional unloading. The final fold shape is approximately the same for each model.

exhibits the same pattern that is observed for the weak rock. Fracturing is initially concentrated near the end portions of the outer and inner arc for the 1000 meter overburden model, and becomes more extensive through the end portion and along the outer arc as initial overburden thickness increases. With the exception of the base model,
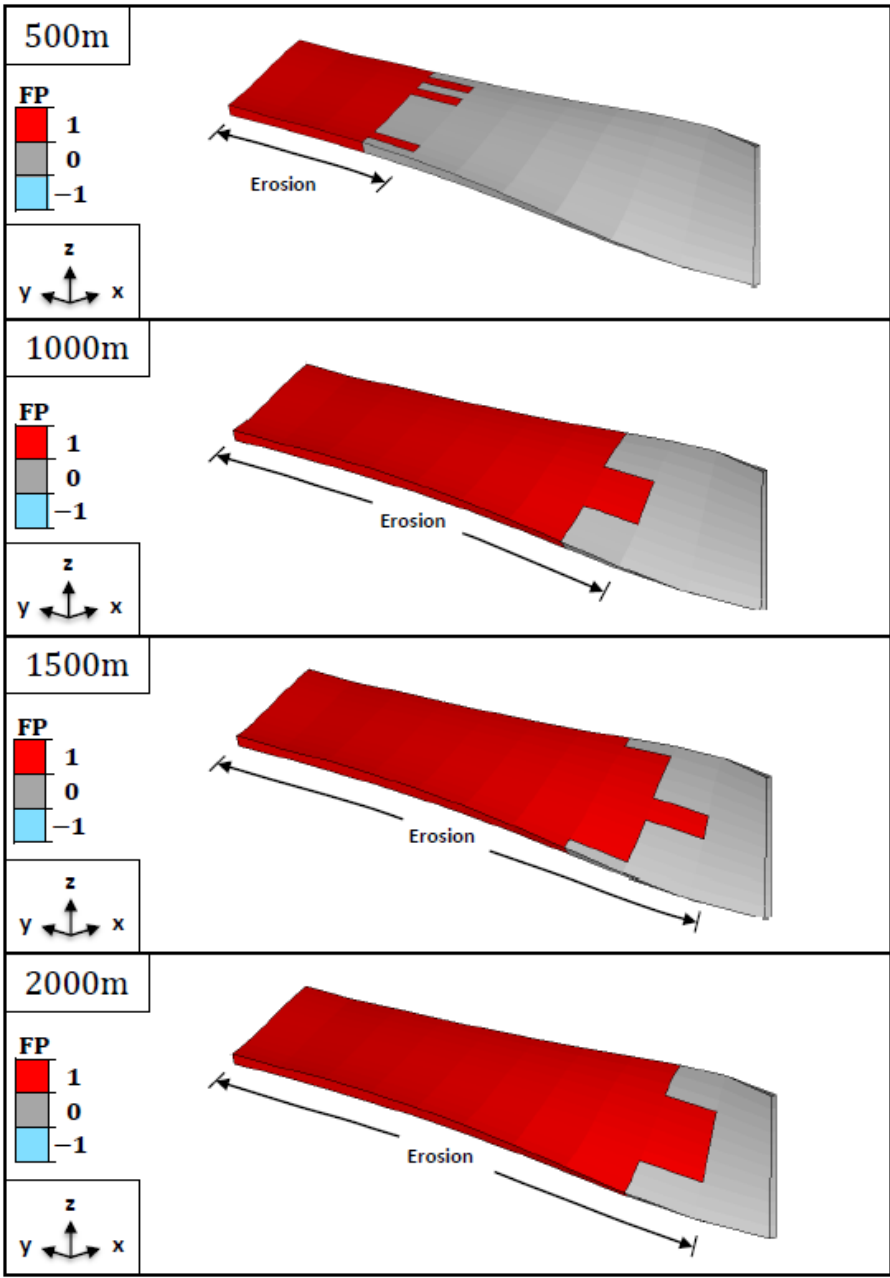
Figure 4.24. Fracture potential results in the limb for a weak rock, with varying amounts of overburden thickness, after erosional unloading. The final fold shape is approximately the same for each model.

erosional tensile fractures are only initiated near the end portion of the outer arc for the 1000 meter overburden model. Fracturing in the limb is slightly less extensive towards the end portion than for a weak rock, but the general distribution remains the same. No shear fractures are observed in the limb of the base model.

Figures G.4 and G.5 show the fracture potential results for the hinge and limb, respectively, of a strong rock. Erosional shear fracturing appears near the end portions of the inner and outer arcs of each model, and only initiates along the outer arc for the 2000 meter overburden model. With the exception of the base model, erosional tensile fractures are only initiated near the end portion of the outer arc for the 1500 meter overburden model. Once again, fracturing in the limb is distributed in the same manner as it is for weak rocks and intermediate strength rocks, just to a slightly lesser extent in the direction of the end portion. No shear fractures are observed in the limb of the base model.

5. DISCUSSION

The 3D modeling approach presented in this study shows that a non-cylindrical fold geometry can be generated for a single-layer buckle fold with a single unidirectional shortening event, which is in agreement with experimental studies by Dubey and Cobbold (1977), and Blay et al. (1977); and is also in agreement with numerical modeling studies by Kaus and Schmalholz (2006), and Schmid et al. (2008). Moreover, the effective stress evolution can be effectively simulated during the processes of buckling and erosional unloading. Furthermore, given the assumptions made regarding fracture initiation and propagation, the effective stresses from the numerical simulations can be extracted and applied to the combined Griffith/Navier-Coulomb failure criterion to document fracture characteristics (e.g., location, type, timing of initiation) within the fold. These fracture characteristics can help provide a better understanding of the occurrence of various fracture sets observed in folds that are partially or fully exposed at the surface (e.g., Stearns, 1964; Bergbauer and Pollard, 2004; Bellahsen et al., 2006; Cooper et al. 2006; Stephenson et al. 2007; Al-Mahmoud et al. 2009). When considering these natural fracture sets, two primary points of interest arise that cannot readily be explained by surface field studies or subsurface geophysical investigations: what conditions promote the initiation of each fracture set, and when do the fracture sets initiate (i.e., are they associated with buckling, erosional unloading, or another process)? A variety of studies have attempted to link fracture initiation to the state of strain in a folded layer using curvature analysis (e.g., Lisle, 1994; Hennings and Olson, 1997; Fischer and Wilkerson, 2000), or the neutral surface concept (e.g., Lisle et al., 2009; Frehner, 2011). An important shortcoming of such studies is that the results are based on strain distributions within the fold, and the in-situ stress magnitudes are not taken into account. While folds may exhibit extensional or compressional states of strain at any given instance, the in-situ state of stress may not promote the initiation of fractures, and thus a thorough understanding of the stress evolution is necessary to effectively predict fracture initiation. Eckert et al. (2014) presents one of the few studies that simulates the stress evolution during single-layer buckling, while including the influence of gravity and pore pressure. Their modeling approach successfully demonstrates that the stress

evolution can help provide a better understanding of tensile fracture initiation and occurrence in 2D cylindrical folds. This study follows a similar approach to that presented by Eckert et al. (2014), but introduces an additional dimensional component, therefore allowing for the generation of non-cylindrical fold geometries. The results presented thus far have demonstrated the influence of various parameters on the location, type, and extent of fracturing in the hinge and limb of a pericline, as well as the general timing of fracture initiation. In order to relate the fractures observed during the numerical simulations to the those presented in Cosgrove and Ameen's (1999) conceptual model for fractures associated with buckle folds (see Figure 5.1), as well as those observed in other conceptual models and field studies, an examination of the fracture orientation relative to the folding layer is still necessary.

Fracture orientations are presented in the form of stereographic projections, which show the strike and dip of the expected fracture planes, and the average poles to the bedding planes. A stereographic representation of fracture orientation within the periclines in this study can be accomplished by substituting the x and y-axes for the cardinal directions (i.e., north, south, east, west) that are used for traditional stereographic projections, where the y-direction is equivalent to the north/south line (+ y is north and − y is south), and the x-direction is equivalent to the east/west line (+ x is east and − x is west; Figure 5.2a). Given the relationship between the principal stresses and the fracture planes defined for the combined Griffith/Navier-Coulomb failure criterion, only the orientations of the principal stresses at the time of failure are necessary to calculate the strike and dip of the fractures. Figures 5.2b and 5.2c demonstrate how the orientations of two of the principal stresses (σ'_1 and σ'_3) are extracted at a specific time (50% shortening in this case), and plotted as lines on a stereonet for 9 element sets along the top of the folding layer. Similarly, the principal stress orientations can be extracted for an individual element in the hinge or limb the moment a fracture potential of -1 or +1 is reached, and the strikes and dips of the fracture planes can be subsequently calculated.

Combining the fracture orientation with the fracture location and timing of initiation allows for a complete discussion of the different types fracture sets that initiate, where and when they initiate, and whether or not they are observed in conceptual fold/fracture models or field studies. The fracture sets observed in this study are divided
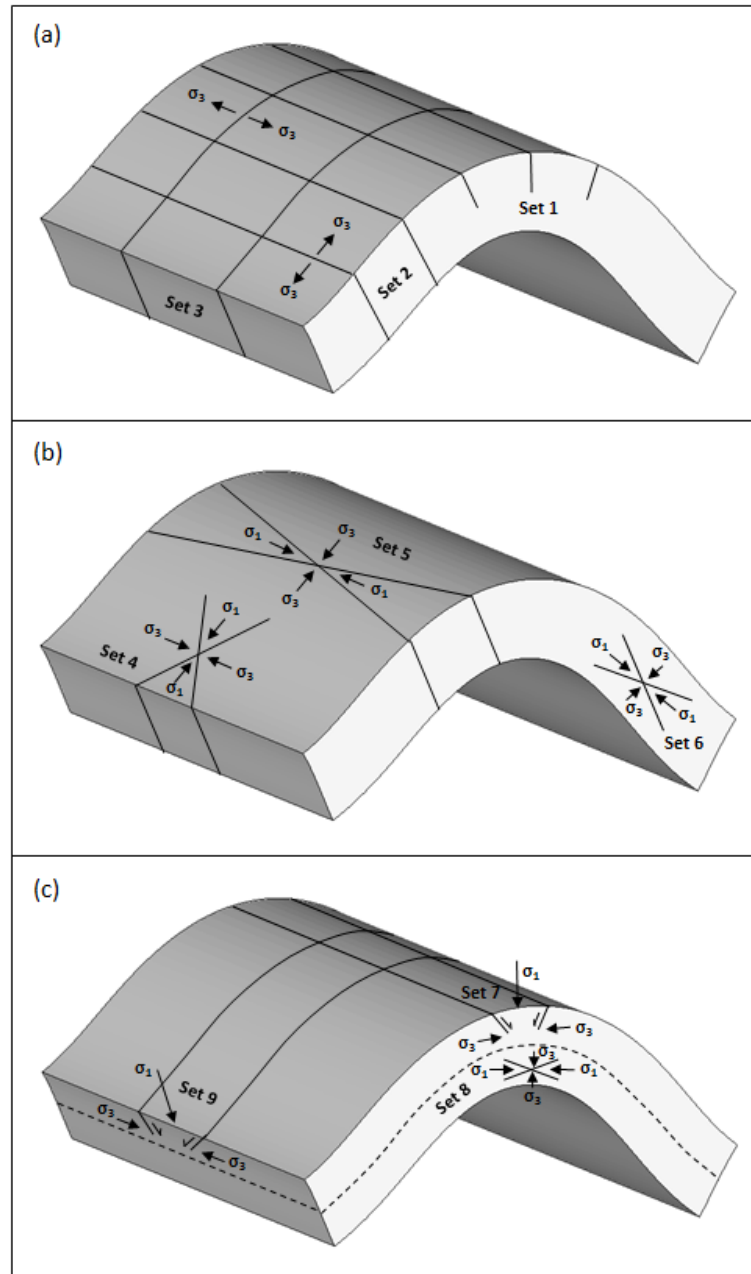
Figure 5.1. Fracture sets associated with buckle folding. (a) Extensional fractures with inferred orientations of σ_3. (b & c) Shear fractures, normal faults, and thrusts with inferred orientations of σ_1 and σ_3 (After Cosgrove and Ameen, 1999).

into two classes: fractures associated with buckling, and fractures associated with erosional unloading; the possible existence of pre-existing fractures is discussed later on.
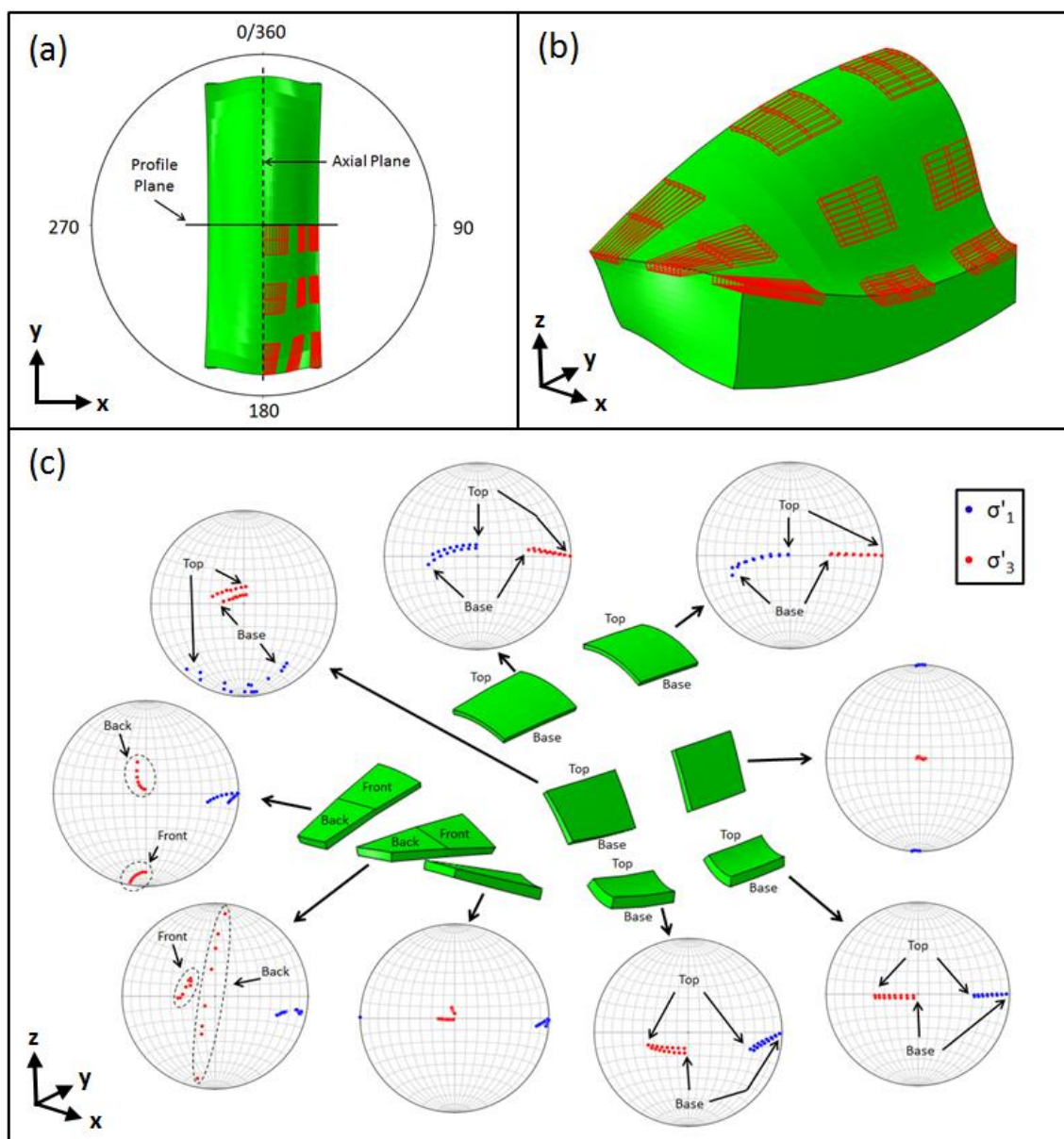
Figure 5.2. Stereographic projections applied to the pericline geometry. (a) Reference orientation of the pericline for stereographic projections. The y-direction is equivalent to the traditional north/south line and the x-direction is equivalent to the traditional east/west line. (b) 9 element sets from which the orientations of σ'_1 and σ'_3 are extracted to be plotted as lines on a stereonet. (c) Trend and plunge of σ'_1 and σ'_3 for the 9 element sets at the top of the folding layer. These orientations correspond to the σ'_1 and σ'_3 orientations after 50% shortening.

5.1. FRACTURES ASSOCIATED WITH BUCKLING

Fracture potential results indicate that the type and extent of fracturing in the hinge and limb during buckling is heavily dependent on the permeability of the folding layer, and the thickness of the overburden. Low permeability (10^{-21}m^2) folds develop significant amounts of overpressure during buckling, and thus the extent of fracturing becomes much more widespread; a condition that is further amplified for higher anisotropic permeability ratios. Conversely, a large overburden thickness results in a highly compressive state of stress, making fracturing in high permeability folds (10^{-15}m^2) impossible for overburden thicknesses greater than 500 meters. Both observations are consistent with the findings of Eckert et al. (2014). The remaining parameters have notable influences on the type and location of fractures that appear during buckling, but the extent of fracturing is not as heavily influenced by these parameters as it is for models with low permeabilities or high overburden thicknesses.

Eight fracture sets associated with buckling are identified based on the analysis of each parametric variation/rock strength combination (Fracture Sets A-H in Figures 5.3-5.10). It is important to note that Figures 5.3 -5.10 each depict a cumulative summation of the respective fracture sets observed for all buckling scenarios, and the geometry and fracture distributions shown are not representative of a unique buckling scenario.

5.1.1. Tensile Fractures. Fracture Set A comprises tensile fractures in the outer arc of the hinge that are perpendicular to the bedding planes, and parallel to the fold axis (Figures 5.3a-c). These fractures are identical to Fracture Set 1 presented in Cosgrove and Ameen's (1999) conceptual model (see Figure 5.1a), and are initiated during the mid to late-stages of buckling (>15% shortening; also observed by Eckert et al., 2014). The extent of observed fracturing can be seen in Figure 5.3b (blue outline). In general, the earliest fractures initiate in the outermost arc at the central portion, where the fold amplitude is the highest. Subsequent fractures progressively initiate along the outermost arc towards the end portion, as well as inwards toward the fold interior. Fracture Set A is observed in weak rocks for the cases of low permeability (10^{-21} m^2), or a high viscosity contrast ($R_\mu = 100$); intermediate strength rocks for all cases except for a low competence contrast ($R_\mu = 25$), greater than 500m of initial overburden, or less than 30% shortening; and strong rocks for only low permeability cases. The extent of fracturing is related to

permeability, with the most extensive fracturing being observed for low permeability folds, and significantly less extensive fracturing being observed for higher permeability folds ($> 10^{-21}$ m^2). This fracture set also features in other conceptual models (e.g., Stearns and Friedman, 1972; Twiss and Moores, 2007), and has been observed in numerous field studies of natural folds (e.g., Stearns, 1964; Bellahsen et al., 2006; Cooper et al., 2006).
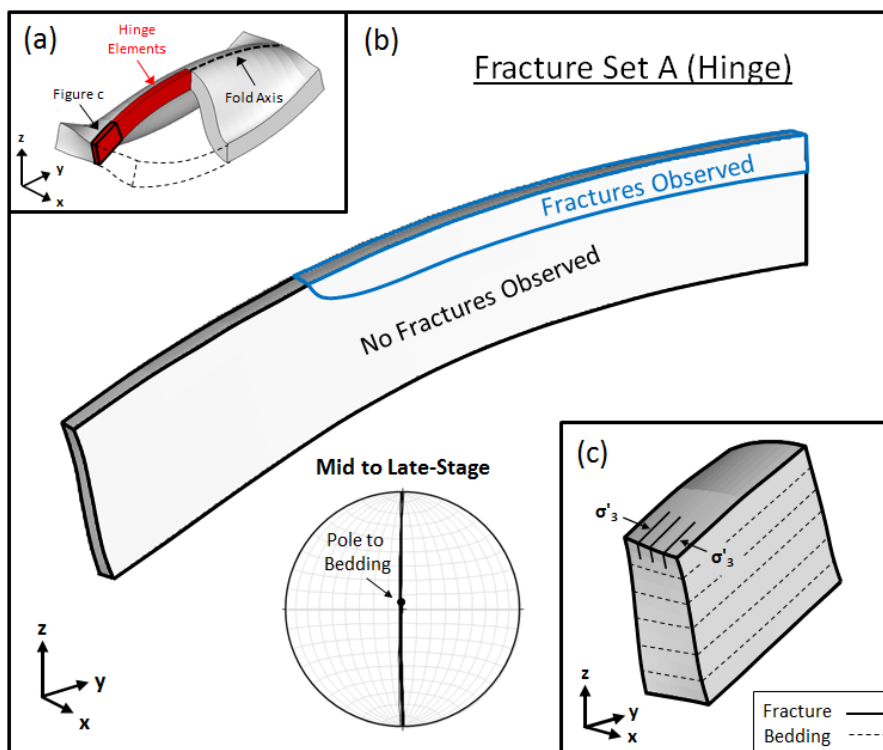

Figure 5.3. Depiction of the characteristics associated with Fracture Set A. (a) Location of hinge elements in the pericline. (b) Oblique view of the hinge elements showing the extent of fracturing from the central portion to over hallway along the hinge line (blue outline). The stereographic projection includes the average pole to the bedding planes in the fracture region during mid to late-stage buckling, and shows that the fractures strike parallel to the fold axis, and are normal the bedding planes. (c) Cut section from (a) used to present a conceptual illustration of the orientation of fracture planes with respect to the folding layer and bedding planes. This illustration is only meant to enhance conceptual understanding, and should not be used as an indicator for the true fracture location.

Fracture Set B comprises tensile fractures in the outer arc of the hinge that are perpendicular to the bedding planes, and perpendicular to the fold axis (Figures 5.4a-c).

These fractures are identical to Fracture Set 3 presented in Cosgrove and Ameen's (1999) conceptual model (see Figure 5.1a), and are initiated during the mid to late-stages of buckling (>15% shortening). Fracture initiation is observed along the back half of the outer arc, beginning nearly halfway along the hinge line, and progressively extending towards the end portion during later stages of folding (see Figure 5.4b; blue outline). Low permeability folds are capable of producing these fractures for weak, intermediate strength, and strong rocks. The only other scenario for which Fracture Set B is observed, is for the case of a weak rock combined with a high viscosity contrast ($R_\mu = 100$). Fracture Set B could not generally be explained using the 2D modeling approach presented by Eckert et al. (2014), but has been observed along the hinges of natural folds (e.g., McQuillan, 1974; Stephenson et al., 2007; Wennberg et al., 2007), and is classified as a commonly observed fracture set in the Stearns and Friedman (1972) conceptual model of fractures associated with a pericline.

     5.1.2. Shear Fractures. Fracture Set C comprises shear fractures in the outer arc of the hinge that strike parallel to the fold axis, and have dips of approximately 60 ° with respect to the bedding planes (Figures 5.5a-c). These fractures are equivalent to the outer arc normal faults in Cosgrove and Ameen's (1999) conceptual model (Fracture Set 7 in Figure 5.1c), and are observed during mid-stage buckling (15-30% shortening). Fracture initiation first occurs at the central portion, and continues along the outer arc towards the end portion, ultimately ceasing before reaching the halfway point along the hinge line (see Figure 5.5b; red outline). Fracturing is observed in weak rocks for every buckling scenario except for a low viscosity contrast ($R_\mu = 25$), greater than 500m of initial overburden, or less than 30% shortening; but is not observed in intermediate strength rocks, or strong rocks for any scenario. The maximum extent of fracturing is observed for high permeability folds (10^{-15} m^2) due to preferential initiation of tensile fractures (Set A) for low permeability folds (10^{-21} m^2). Fracture Set C also appears in Twiss and Moore's (2007) conceptual fold/fracture model, and has been commonly observed in the outer arc of natural folds (e.g., Coleman-Sadd, 1978; Cooper et al., 2006; Morley, 2007).
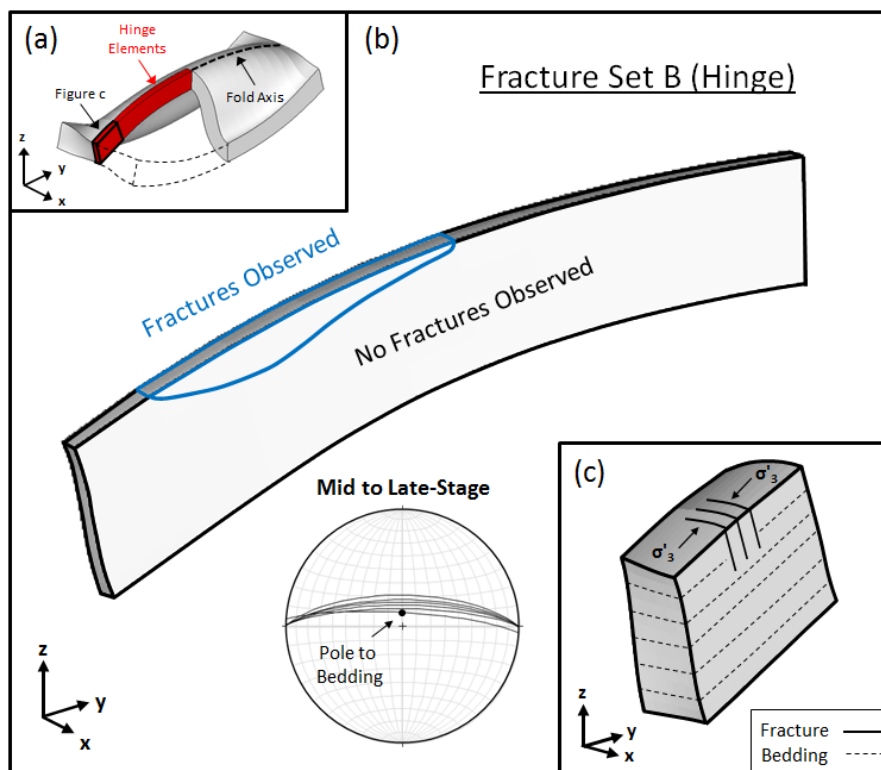
Figure 5.4. Depiction of the characteristics associated with Fracture Set B. (a) Location of hinge elements in the pericline. Fracturing is observed along the back half of the hinge (blue outline in b) with the stereographic projection showing that fractures strike perpendicular to the fold axis and are normal to the bedding planes (see conceptual illustration in c).

Fracture Set D comprises shear fractures in the hinge that strike generally parallel to the fold axis, and have dips of approximately 30 ° with respect to the bedding planes (Figures 5.6a-c). These fractures are equivalent to the inner arc thrusts in Cosgrove and Ameen's (1999) conceptual model (Fracture Set 8 in Figure 5.1c). Fractures initiate primarily during the early stages of shortening (< 15% shortening), but can be initiated during mid to late-stage shortening (> 15% shortening) in some instances near the end portion. It can be seen in Figure 5.6b (red outlines) that Fracture Set D is observed along the entire length of the inner arc, but is also observed near the end portion of the outer arc. The outer arc fractures are only initiated in weak rocks and intermediate strength strong rocks for the case of a low viscosity contrast ($R_\mu = 25$). Inner arc fractures initiate in weak rocks for every buckling scenario, except when the initial overburden thickness is greater than 500m; and in intermediate strength rocks for the cases of low permeability
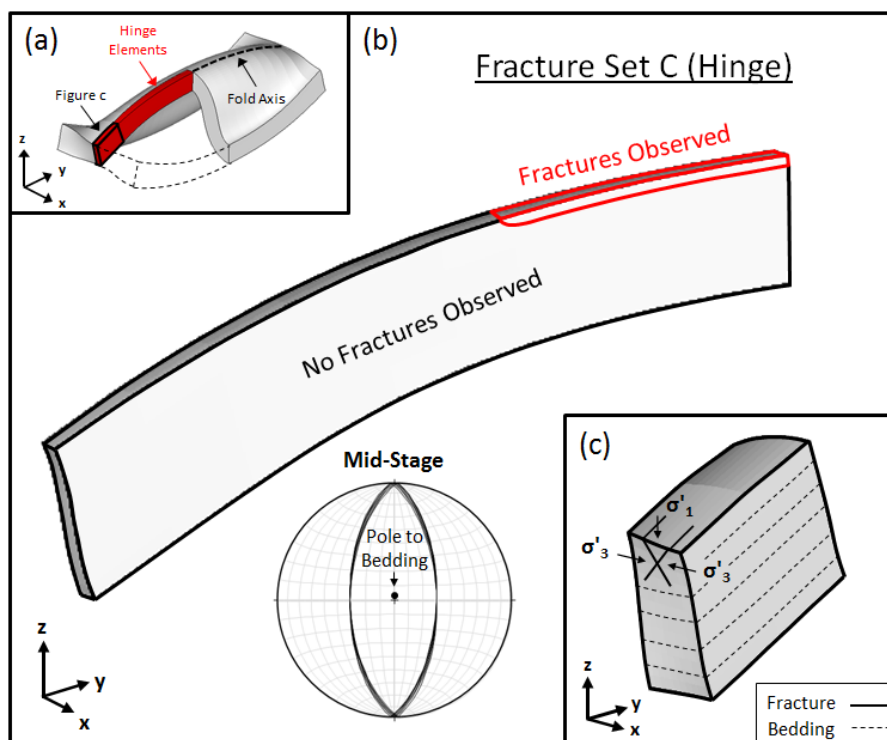
Figure 5.5. Depiction of the characteristics associated with Fracture Set C. (a) Location of hinge elements in the pericline. Fracturing is observed along the front half of the hinge (red outline in b), with the stereographic projection showing that fractures strike parallel to the fold axis, and have dips of approximately 60 ° with respect to the bedding planes (see conceptual illustration in c).

(10^{-21} m^2), a low viscosity contrast ($R_\mu = 25$), or a low aspect ratio (1:3). Set D does not initiate in strong rocks for any scenario. While fracture initiation along the entire length of the inner arc is possible for most scenarios involving weak rocks, the inward advance of fracture initiation towards the fold interior is much more pronounced for low permeability folds than for higher permeability folds ($>10^{-19} \text{ m}^2$). Fracture Set D also appears in the Twiss and Moores' (2007) conceptual model, and has been observed in the inner arc of many natural folds (e.g., Stearns, 1964; Narahara and Wiltschko, 1985; Mitra, 2002).

Fracture Sets E and F comprise mid to late-stage shear fractures in the end portion of the hinge that initiate with varying strikes and dips, which are reflective of different σ'_3 orientations and a constant orientation of σ'_1 normal to the axial plane. For Set E (Figures 5.7a-c), σ'_3 lies within the plane of the fold axis, and is nearly parallel to the bedding
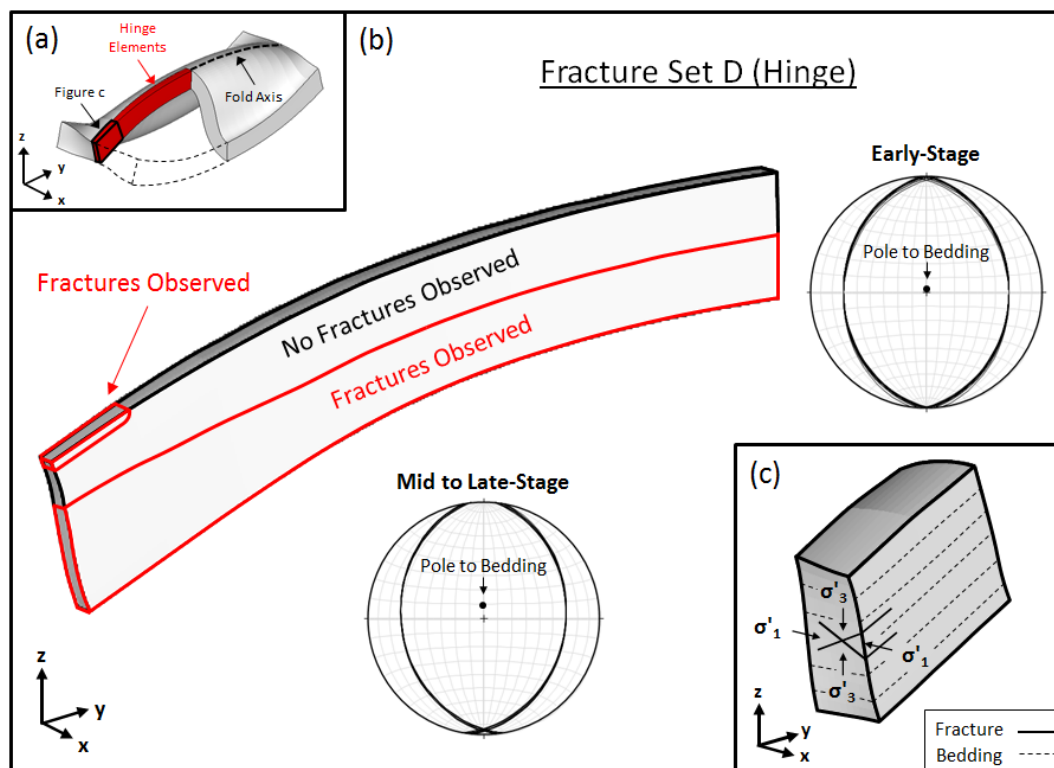
Figure 5.6. Depiction of the characteristics associated with Fracture Set D. (a) Location of hinge elements in the pericline. Fracturing spans the entire length of the inner arc of the hinge and is also observed near the end portion of the outer arc (red outlines in b). The stereographic projection shows that early stage fractures strike parallel to the fold axis, and mid to late-stage fractures strike nearly parallel to the fold axis. All fractures have dips of approximately 30 ° with respect to the bedding planes (see conceptual illustration in c).

planes. The resulting orientations of the fracture planes with respect to the folding layer and bedding planes are shown in Figure 5.7c (Notice that a 90 ° rotation of Set E about the x-axis results in Set D). For Set F (Figures 5.8a-c), σ'_3 exhibits rotation within the plane of the fold axis, resulting in transitional fractures that lie within the 90 ° rotation window between Set D and Set E (see Figure 5.8c). Set E is only observed near the outer arc of the end portion (see Figure 5.7b; red outline), and only initiates in weak rocks with low permeabilities (10^{-21} m^2) or a viscosity contrast of 75 or higher. Set F is observed throughout the entire fold thickness near the end portion (see Figure 5.8b; red outline), and initiates to some extent for all buckling scenarios involving weak rocks or intermediate strength rocks, except for cases involving a low viscosity contrast ($R_\mu = 25$),
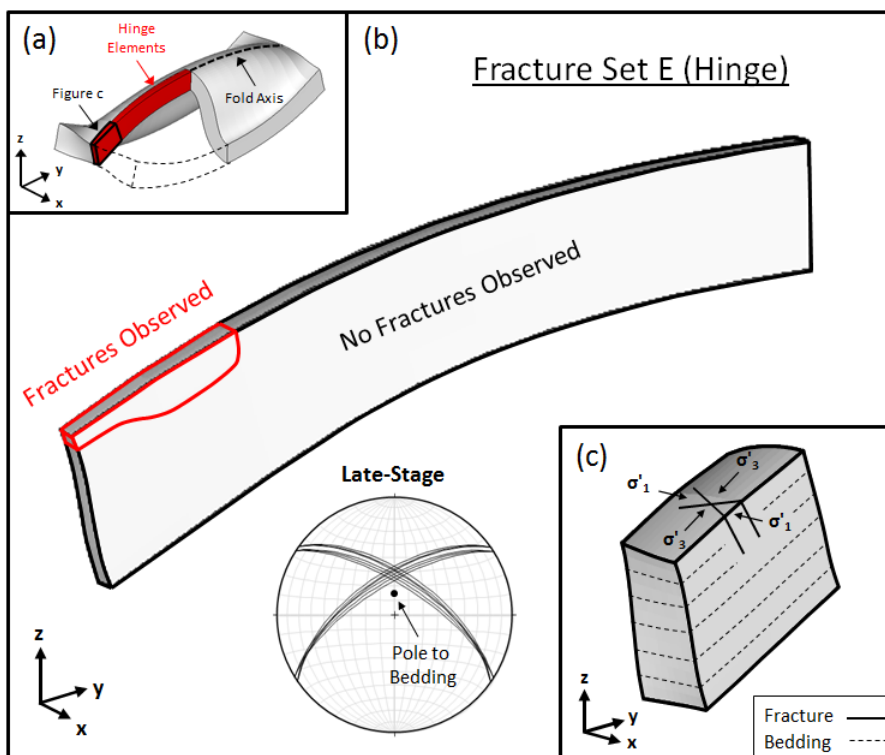
Figure 5.7. Depiction of the characteristics associated with Fracture Set E. (a) Location of hinge elements in the pericline. Fracturing is only observed near the end portion of the outer arc of the hinge (red outline in b). The stereographic projection shows that fractures exhibit strikes of approximately 237 ° and 305 °, with dips ranging from 60-70 °. Fracture orientation with respect to the folding layer and bedding planes can be seen in (c).

greater than 500m of initial overburden, or less than 50% shortening. Set F only initiates in strong rocks for the case of low permeability folds. The orientation of Set F is dependent on fracture location with respect to the inner and outer arcs. Fractures closer to the inner arc have orientation more similar to those of Fracture Set D, while fractures closer to the outer arc have orientations more similar to those of Fracture Set E. Neither Set E, nor Set F feature in Cosgrove and Ameen's (1999) conceptual model; however, Set E is considered a possible fracture set in periclines based on the conceptual model by Stearns and Friedman (1972), and has been observed in the hinges of large scale anticlines by Marshak et al. (1982), Hancock (1985), and Wenneberg et al. (2007).

Fracture Set G comprises shear fractures in the limb that strike generally parallel to the strike of the bedding planes, and have dips of approximately 30 ° with respect to the bedding planes (Figures 5.9a-c). These fractures are identical to Fracture Set 6 presented
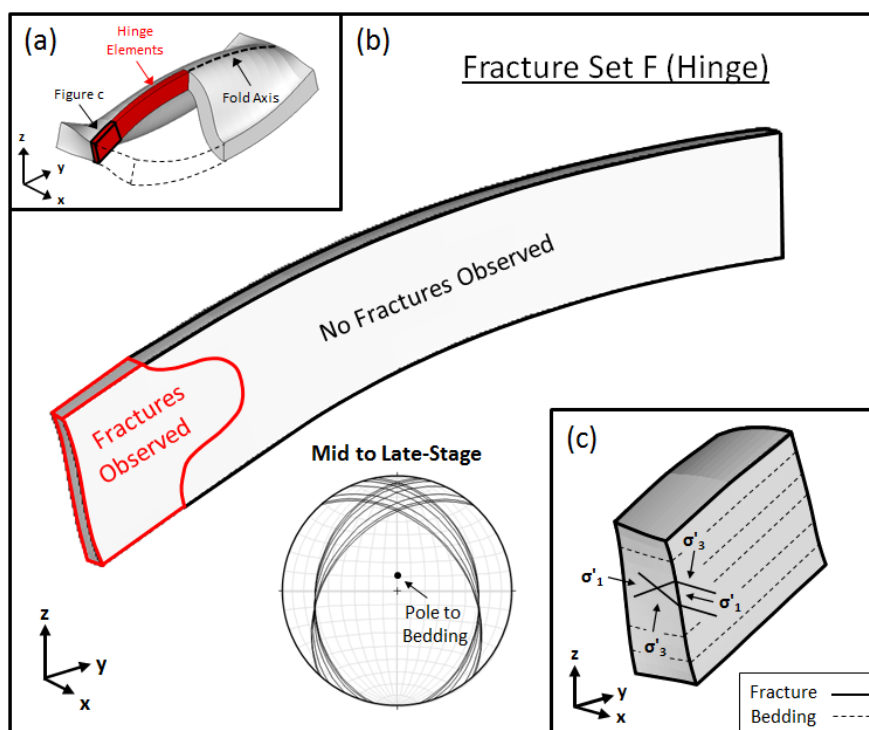
Figure 5.8. Depiction of the characteristics associated with Fracture Set F. (a) Location of hinge elements in the pericline. Fracturing is observed throughout the entire thickness of the folding layer at the end portion of the hinge (red outline in b). The stereographic projection shows that fractures exhibit variable strikes (190-220 ° and 320-350 °), with dips ranging from 30-45 °. Fracture orientation with respect to the folding layer and bedding planes can be seen in (c).

in Cosgrove and Ameen's (1999) conceptual model (see Figure 5.1b), and are initiated during the early stages of buckling (< 15% shortening). Fracture initiation is restricted to thin sections in the top and bottom of the limb near the end portion (see Figure 5.9b; red outlines), and furthermore is only observed in low permeability (10^{-21} m^2) weak rocks with anisotropic permeability ratios of 5 to 1 or higher. This limited observation could help explain why Fracture Set 6 in Cosgrove and Ameen's (1999) conceptual model is classified as a rarely occurring fracture set. Despite fractures in Set G being classified as rarely occurring, they have been observed in the limbs of the Teton Anticline in northwest Montana, USA (Stearns, 1964; 1967).

Fracture Set H comprises late stage shear fractures in the interior of the limb that strike parallel to the strike of the bedding planes (Figures 5.10a-c). At the time of initiation, σ'_1 is sub-vertical and σ'_3 is sub-horizontal, resulting in the relationship between
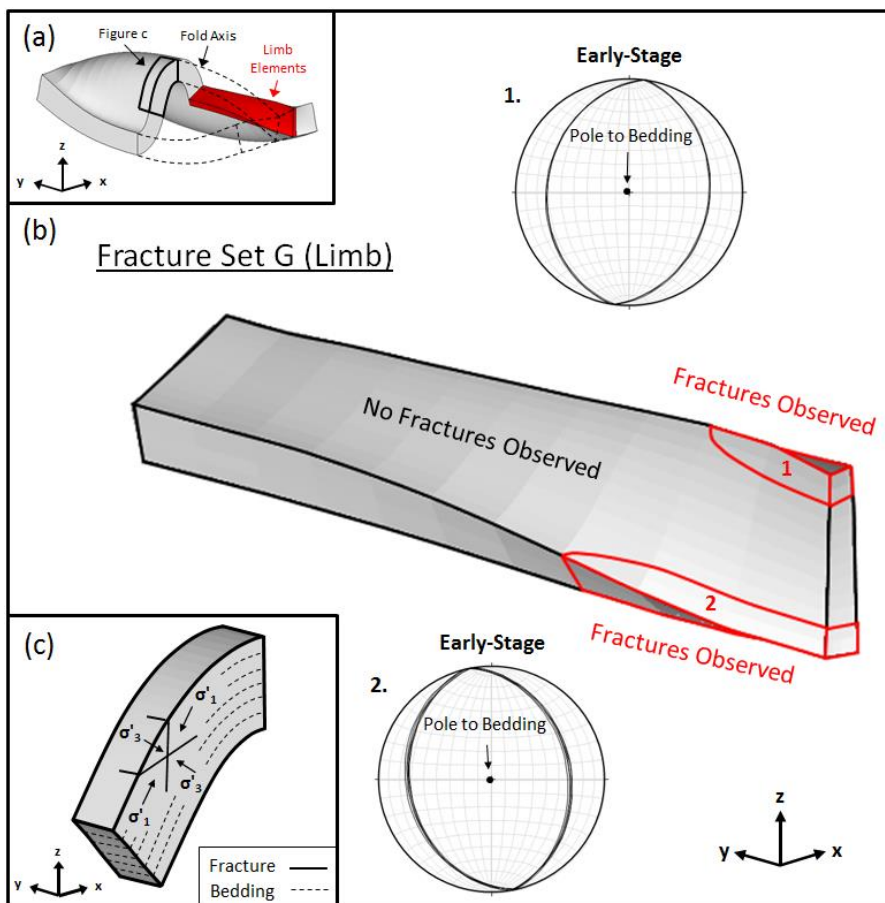
Figure 5.9. Depiction of the characteristics associated with Fracture Set G. (a) Location of limb elements in the pericline. Fracturing is observed in thin sections at the top and bottom of the limb near the end portion (red outlines in b), with the stereographic projection showing that fractures generally strike parallel to the strike of the bedding planes, and have dips of approximately 30 ° with respect to the bedding planes. (c) Conceptual illustration of fracture orientation with respect to the folding layer and bedding planes in the limb. It is important to note that the illustration in (c) is only meant to enhance conceptual understanding of the fracture orientations, and should not be used as an indicator of true fracture location or fold shape.

the fracture planes and folding layer given in Figure 5.10c. The stereographic projection in Figure 5.10b shows that one of the conjugate shear planes is nearly parallel to the bedding planes, while the other dips approximately 60 ° with respect to the bedding planes. These fractures are only observed in weak rocks with a low viscosity contrast (R_μ = 25), indicating that Set H might be a rarely occurring fracture set in natural buckle folds. Fracture Set H does not feature in Cosgrove and Ameen's (1999) conceptual
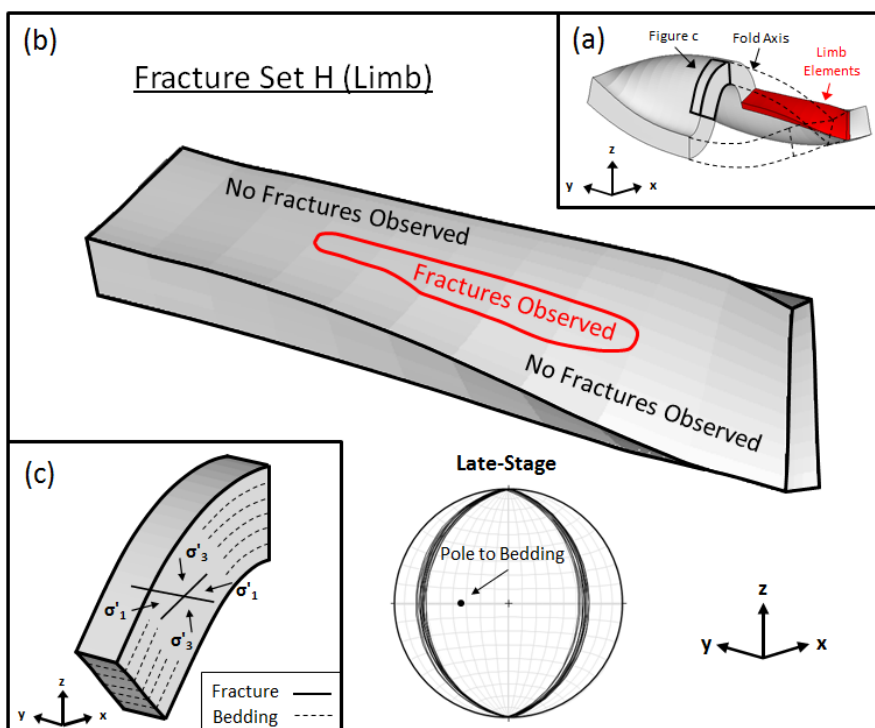
Figure 5.10. Depiction of the characteristics associated with Fracture Set H. (a) Location of limb elements in the pericline. Fracturing is observed in the interior of the folding layer, away from the central and end portions (red outline in b). The stereographic projection shows that fractures strike parallel to the bedding planes, with one fracture plane being nearly parallel to the bedding and the other dipping approximately 60° with respect to the bedding (see conceptual illustration in c).

model, and does not seem to appear in any field studies of natural buckle folds. It is interesting to note, however, that this fracture set has been generated in the limbs of experimentally produced forced folds above the equivalent of a normal basement fault (Ameen, 1990). Ameen (1990) also cites that the experimentally produced fractures analogous to Set H were mentioned by Stearns (1970) in a field study of the forced folds of Wyoming, USA.

5.2. FRACTURES ASSOCIATED WITH EROSIONAL UNLOADING

Nine fracture sets associated with erosional unloading are identified based on the analysis of each parametric variation/rock strength combination, with 6 of those sets being identical to fracture sets also associated with buckling (Figures 5.11 and 5.12) and

the remaining 3 sets being unique to erosional unloading (Fracture Sets I-K in Figures 5.13-5.15). In addition, a large group of diversely oriented shear fractures unique to erosional unloading is observed in the limb (Figure 5.16). It needs to be noted, that all erosion scenarios are for high permeability folds (10^{-15} m^2).

      5.2.1. Erosional Fractures Also Associated With Buckling. Tensile Fracture Sets A and B, which are observed in the hinge during buckling, are also observed in the hinge during erosional unloading. Set A (Figure 5.11a) initiates in weak, intermediate strength, and strong rocks for a combination of low initial overburden thickness (500m) and a 20-40% shortening period prior to erosional unloading. Initiation is also possible for a combination of low initial overburden thickness and a 50% shortening period prior to erosional unloading, but only in weak rocks. The observed extent of initiation for Set A begins at the central portion of the outer arc and terminates at a point over halfway along the hinge line in the direction of the end portion. Set B (Figure 5.11b) only initiates in a small region near the end portion of the outer arc for weak, intermediate strength, and strong rocks with a combination of low initial overburden thickness, an aspect ratio of 1:5 or higher, and a 50% shortening period prior to erosional unloading.

      Shear Fracture Sets C, D, E, and G, which are observed during buckling, are also observed during erosional unloading. Set C (Figure 5.12a) is observed along the front half of the outer arc of the hinge, and only initiates in weak rocks for a combination of low initial overburden thickness combined with 20-40% shortening prior to erosional unloading. Set D (Figure 5.12b) is observed along the entire length of the inner arc of the hinge, and throughout the entire thickness of the folding layer near the end portion. Despite the vast extent of observed Set D fracturing, initiation is only possible in weak rocks and intermediate strength rocks for a combination of low initial overburden thickness and 10-20% shortening prior to erosional unloading. Set E (Figure 5.12c) is observed throughout the entire thickness of the folding layer near the end portion of the hinge. Fracturing initiates in weak rocks for all erosion scenarios with at least 30% shortening prior to erosional unloading, while fracture initiation in intermediate strength rocks and strong rocks requires at least 50% shortening prior to erosional unloading. Set G (Figure 5.12d) is observed throughout the entire thickness of the back half of the limb,
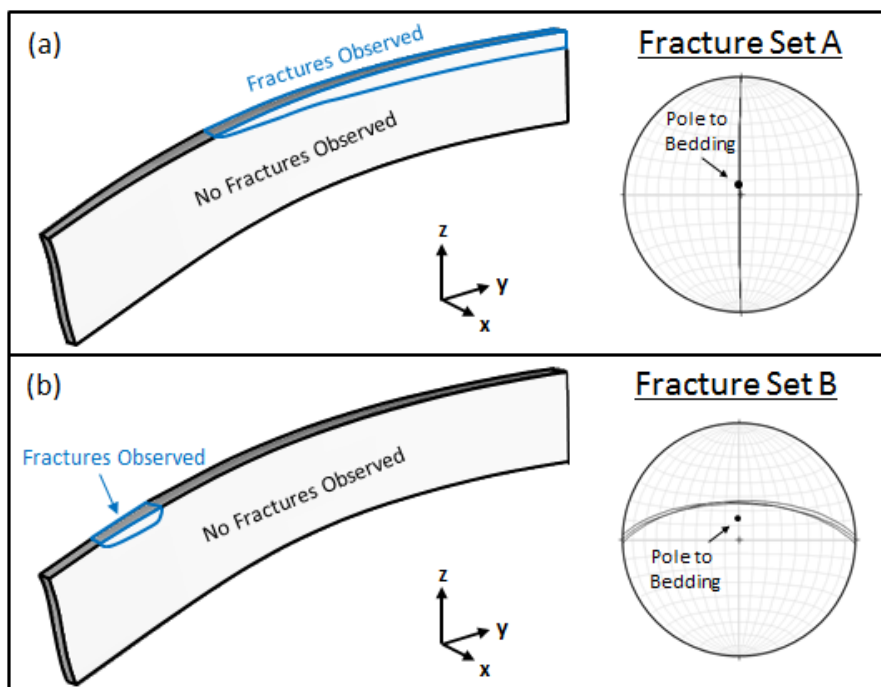
Figure 5.11. Tensile fracture sets observed in the hinge during erosional unloading that are identical to sets also observed during buckling. (a) Fracture Set A is observed along the outer arc from the central portion to a point over halfway along the hinge line. (b) Fracture Set B is only observed for a small region near the end portion of the outer arc.

and only initiates in weak rocks with a combination of low initial overburden thickness and 10-20% shortening prior to erosional unloading.

5.2.2. Tensile Fractures Unique to Erosional Unloading. Fracture Set I represents the only tensile fractures observed in this study that are unique to erosional unloading (Figures 5.13a-c). This set comprises fractures in the outer arc of the hinge that trend perpendicular to the fold axis, with dips of approximately 45 °with respect to the bedding planes. Initiation is confined to a small region near the outer arc of the end portion (see Figure 5.13b; blue outline), and only occurs for two scenarios: in an intermediate strength rock with an initial overburden thickness of 1000 meters, and in a strong rock with an initial overburden thickness of 1500 meters. Fracture Set I does not feature in Cosgrove and Ameen's (1999) conceptual model; however, tensile fractures with the same orientations relative to the fold axis and bedding planes have been observed at select locations near the end portions of large-scale anticlines in the Zagros Mountains of Iran (Lacombe et al., 2011).
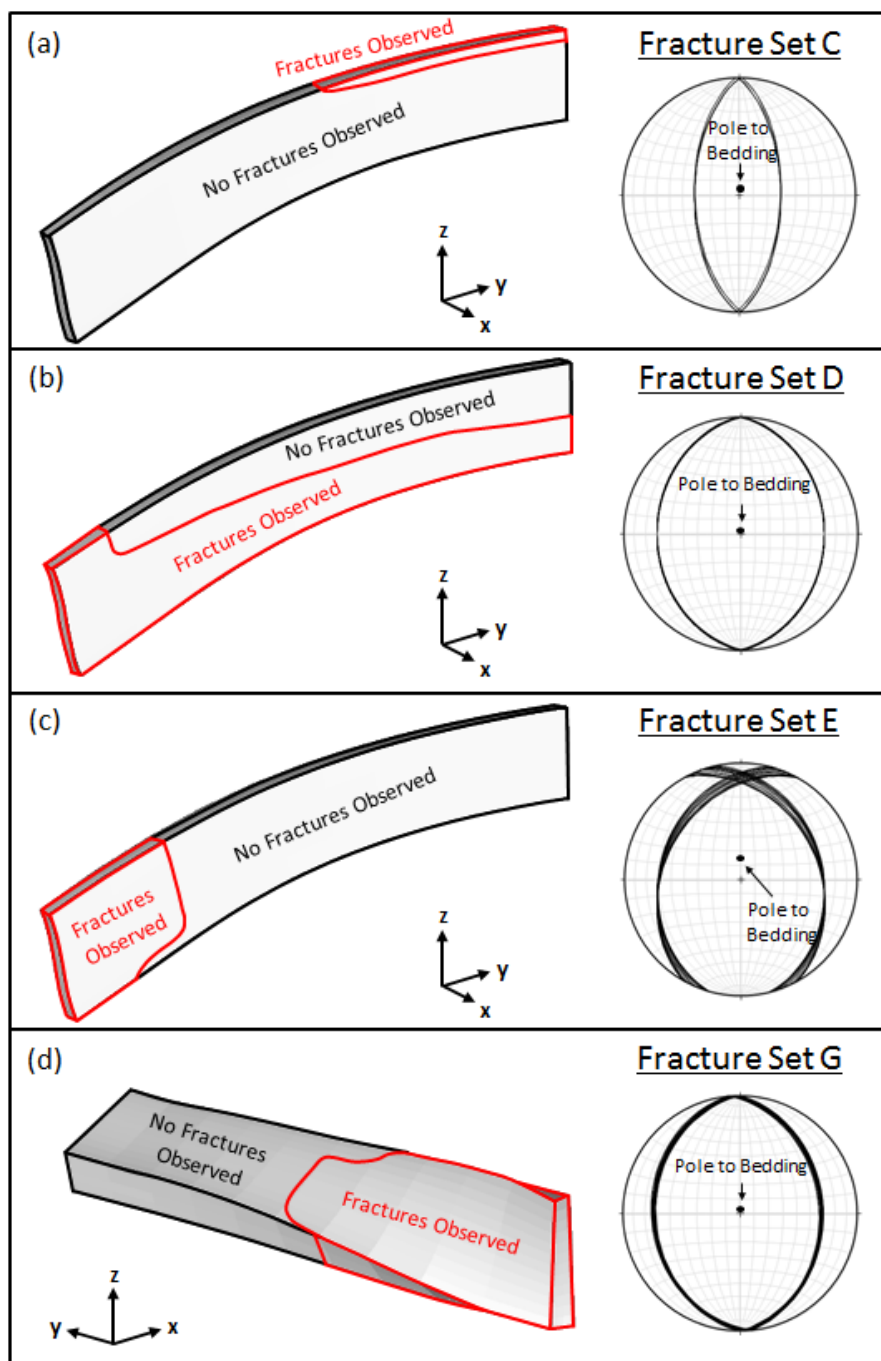
Figure 5.12. Shear fracture sets observed during erosional unloading that are identical to sets also observed during buckling. (a) Fracture Set C is observed in the hinge along the front half of the outer arc. (b) Fracture Set D is observed in the hinge along the entire length of the inner arc, and throughout the entire thickness of the folding layer near the end portion. (c) Fracture Set E is observed in the hinge throughout the entire thickness of the folding layer near the end portion. (d) Fracture Set G is observed throughout the entire thickness of the limb from the end portion to a point halfway between the central and end portions.
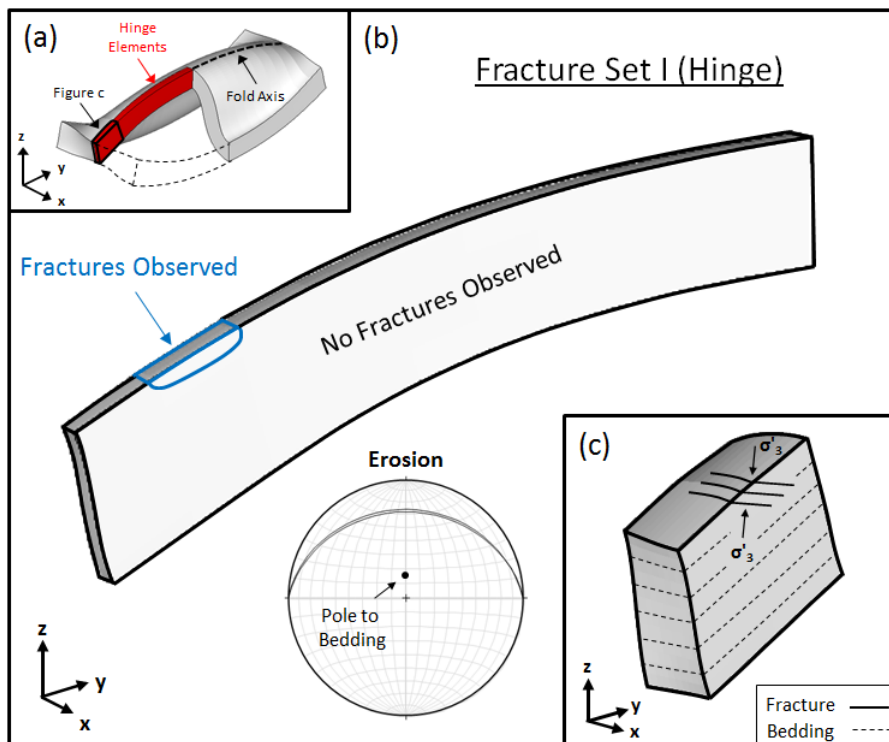
Figure 5.13. Depiction of the characteristics associated with Fracture Set I. (a) Location of hinge elements in the pericline. Fracturing is only observed in a small region near the end portion of the outer arc of the hinge (blue outline in b). The stereographic projection shows that fractures strike perpendicular to the fold axis, and have dips of approximately 45 ° with respect to the bedding planes (see conceptual illustration in c).

5.2.3. Shear Fractures Unique to Erosional Unloading. Fracture Set J comprises conjugate shears in the outer arc of the hinge that are vertical, with the fold axis bisecting the acute angles between the fracture planes (Figures 5.14a-c). These fractures are identical to Fracture Set 5 presented in Cosgrove and Ameen's (1999) conceptual model (see Figure 5.1b), where they are classified as infrequently occurring. Fracturing is confined to a small region of the outer arc near the central portion, and is only initiated in weak rocks for a combination of low initial overburden thickness (500m) and 40% shortening prior to erosional unloading. This highly selective scenario necessary to initiate Set J is consistent with Cosgrove and Ameen's (1999) classification of these fractures as being infrequently occurring. In spite of this classification, Fracture Set J features in other conceptual models (e.g., Stearns and Friedman, 1972; Twiss and
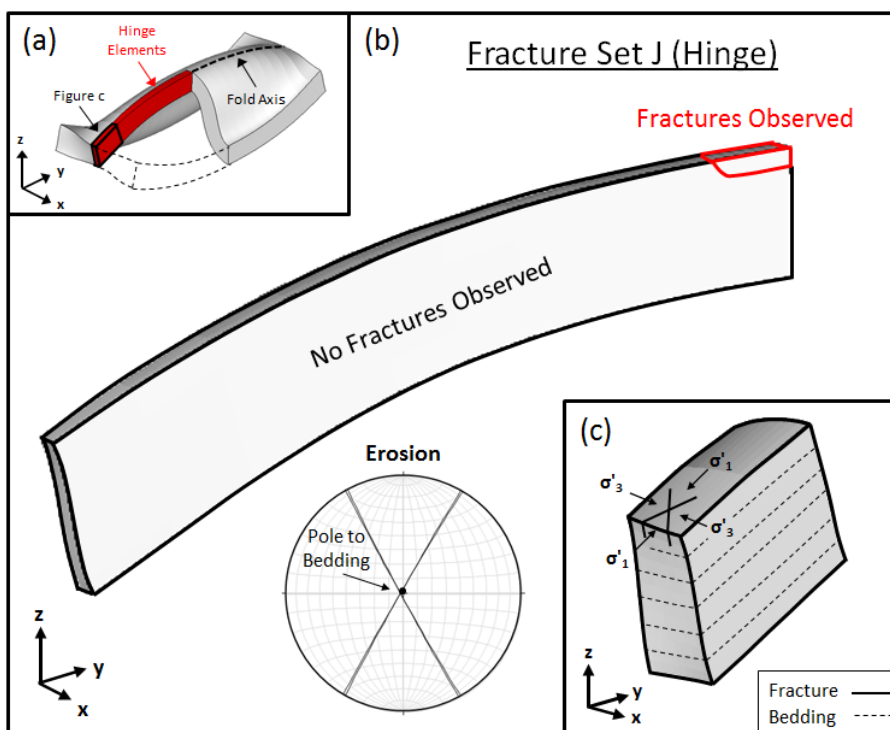
Figure 5.14. Depiction of the characteristics associated with Fracture Set J. (a) Location of hinge elements in the pericline. Fracturing is only observed in a small region near the central portion of the outer arc of the hinge (red outline in b). The stereographic projection shows that the fracture planes are vertical and normal to the bedding planes, with the fold axis bisecting the acute angle between the fracture planes (see conceptual illustration in c).

Moores, 2007), and is cited as an observed fracture set in numerous field studies (e.g., Stearns, 1964; Hancock, 1985, Vitale et al., 2012).

Fracture Set K comprises shear fractures in the outer arc of the hinge that strike perpendicular to the fold axis, and have varying dips with respect to the bedding planes that are dependent on the location along the hinge line (Figures 5.15a-c). All fractures observed in Figure 5.15b initiate with the same orientations of σ'_1 and σ'_3: σ'_1 is approximately parallel to the y-axis, and σ'_3 is sub-vertical. These orientations of σ'_1 and σ'_3 result in the acute angle between the fracture planes being bisected by the bedding planes near the central portion. Slight rotations in the dips of the fracture planes relative to the bedding are observed for locations farther along the hinge line towards the end portion, but the general relationship of the fracture planes with respect to the folding layer and bedding planes is approximate to that shown in Figure 5.15c. The extent of
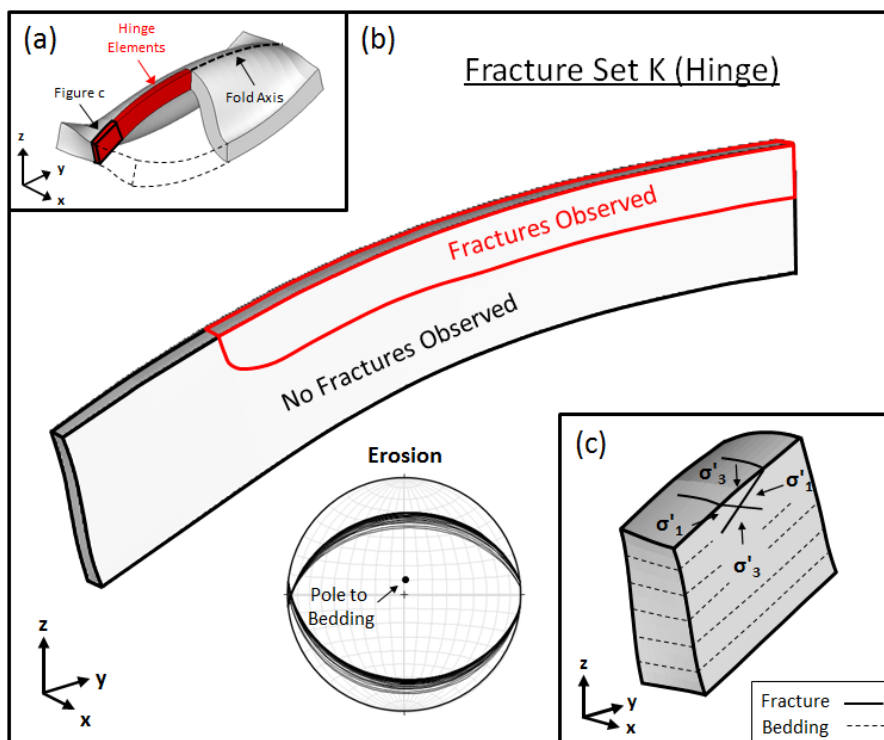
Figure 5.15. Depiction of the characteristics associated with Fracture Set K. (a) Location of hinge elements in the pericline. Fracturing is observed in the outer arc of the hinge beginning at the central portion, and ending at a point over halfway along the hinge line in the direction of the end portion (red outline in b). The stereographic projection shows that the fractures strike perpendicular to the fold axis, and have dips that range from 10-50 ° relative to the bedding planes (see conceptual illustration in c).

fracturing begins at the central portion, and ends at a point over halfway along the hinge line (see Figure 5.15b; red outline). Fracture initiation is observed in weak rocks and intermediate strength rocks for initial overburden thicknesses of 1500 meters or higher, but is only observed in strong rocks for the highest initial overburden thickness (2000m). Fracture Set K does not feature in Cosgrove and Ameen's (1999) conceptual model, and to the author's knowledge, is not cited as a common fracture set in other conceptual models; however, this set has been observed in select field studies (e.g., Hancock, 1985; Lacombe et al., 2011).

In addition to the fracture sets observed in the hinge that are unique to erosional unloading, shear fracturing unique to erosional unloading is observed in the limb (Figures 5.16a-d). These fractures exhibit a wide range of orientations, as can be seen in the

stereographic projection of cumulative fracture orientations in figure 5.15b, but it becomes apparent that fracture orientations are solely governed by the orientation of σ'_1. All fractures exhibit dips in the range of 20-40 ° with respect to the horizontal, indicating that σ'_3 is always sub-vertical, and that σ'_1 exists within the horizontal plane perpendicular to the z-axis. Furthermore, the ever changing strikes of the fracture planes show that σ'_1 not only lies within the horizontal plane, but is continuously rotated about the z-axis. Amongst these many fracture sets exist two end members, where the fracture planes strike perpendicular and parallel to the fold axis, respectively. The resultant orientations of the fracture planes for these two end members, relative to the folding layer and bedding planes, can be seen in Figures 5.16c and d. All other fractures represent transitional fractures that exist in the 90 ° rotational window, about the z-axis, between end members 1 and 2. This cumulative group of erosional fractures is observed throughout the entire thickness of the folding layer from the central portion to a point over halfway along the limb in the direction of the end portion (see Figure 5.16b; red outline). They initiate in weak rocks with a combination of at least 500 meters of initial overburden thickness, and 50% shortening prior to erosional unloading; and also initiate in intermediate strength rocks, and strong rocks, with initial overburden thicknesses of at least 1000 meters. Although none of these fracture sets feature in Cosgrove and Ameen's (1999) conceptual model, it should be noted that due to the nature of σ'_1 and σ'_3, fracture orientation with respect to the folding layer and bedding planes is highly dependent on the orientation of the limb at the time of fracturing.

5.3. FRACTURE SETS NOT OBSERVED

Four fracture sets presented in Cosgrove and Ameen's (1999) conceptual model cannot generally be explained by the modeling results: bedding perpendicular tensile fractures in the limb that strike parallel to the fold axis (Set 2 in Figure 5.1a); bedding perpendicular tensile fractures in the limb that strike perpendicular to the fold axis (Set 3 in Figure 5.1a); shear fractures in the limb that initiate with σ'_2 normal to the bedding, σ'_1 parallel to the dip of the bedding, and σ'_3 parallel to the strike of the bedding (Set 4 in
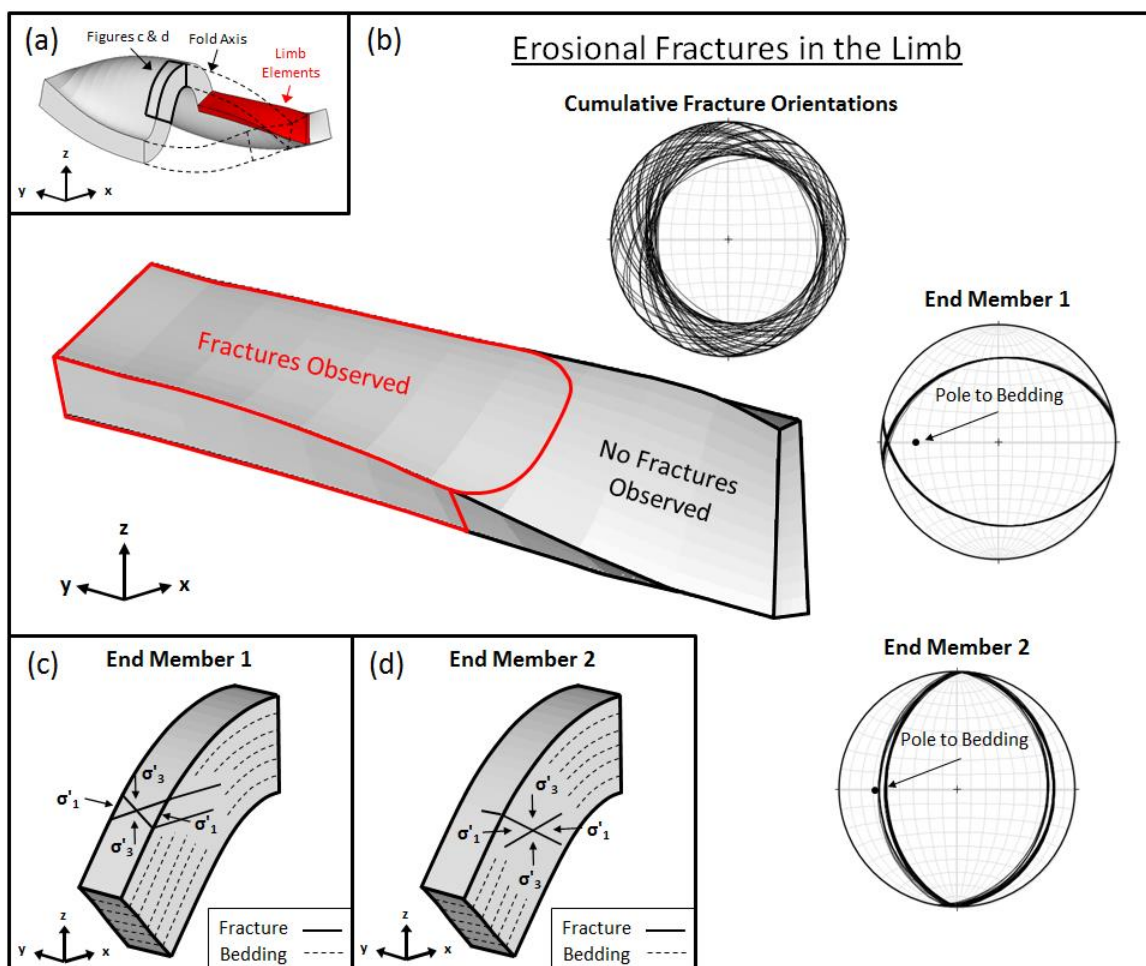
Figure 5.16. Depiction of the characteristics associated with shear fractures in the limb that are unique to erosional unloading. (a) Location of limb elements in the pericline. Fracturing is observed throughout the entire thickness of the limb from the central portion to over halfway along the limb in the direction of the end portion (red outline in b). The stereographic projection of cumulative fractures shows that fractures strike anywhere from 0-360 °, with dips that range from 20-40 °. Within these diversely oriented fracture sets exists two end members: one that strikes perpendicular to the fold axis (c), and one that strikes parallel to the fold axis (d).

figure 5.1b); and normal faults above the neutral surface, in the hinge and limb, that are generally perpendicular to the fold axis (Set 9 in Figure 5.1c).
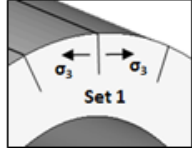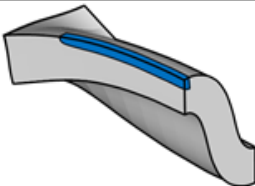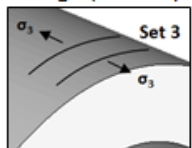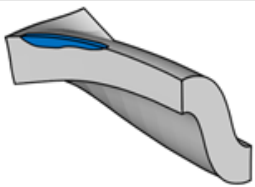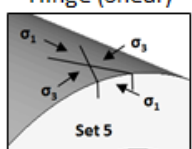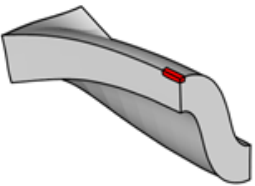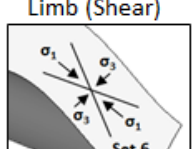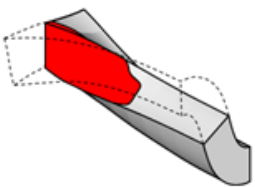
The inability of the modeling results to explain the occurrence of Set 2 is inconsistent with the results of Eckert et al. (2014), which indicate that Set 2 can be observed in the limbs of high permeability folds ($> 10^{-16}$ m^2) during erosional unloading. It should be noted, however, that the failure analysis used by Eckert et al. (2014) does not

include a shear failure criterion, and considers tensile fracturing a possibility for the case where $T = 0$ so as to avoid making assumptions regarding the rocks' tensile strength. In this study, tensile stresses are observed in the limbs during erosional unloading , but 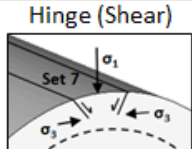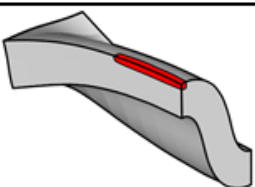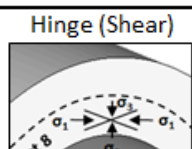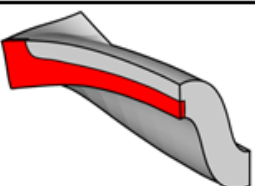the inclusion of a shear failure criterion, combined with the assumption of a minimum tensile strength of 3MPa, results in the conditions for shear fracture initiation being reached before $\sigma'_3 = -T$.

Fracture Sets 2 and 3 frequently appear in field studies of natural folds (e.g., Cooper et al., 2006; Stephenson et al., 2007; Al-Mahmoud et al., 2009), and Set 4 is classified as a common fracture set (Cosgrove and Ameen, 1999). Since all three of these sets are typically associated with folds, but none are observed during the buckling or erosional unloading procedures, an obvious possibility for their occurrence is that they are present pre-folding. Sets 2 and 3 are observed in field studies by Bergbauer and Pollard (2004) and Bellahsen et al. (2006), with both studies determining that the fractures were initially pre-folding joint sets. These bedding perpendicular joint sets are among the most abundant geologic structures (Davis et al., 2012), which could readily explain their common observance in natural folds. Set 4 may represent a pre-folding strike-slip fracture that initiates during a horizontal compression event prior to buckling. Set 9 is not as commonly observed as Sets 2-4, but could also have initiated pre-folding as a result of regional faulting prior to the onset of buckling (e.g., Cooper et al., 2006).
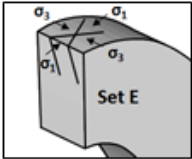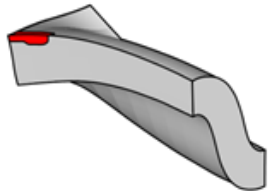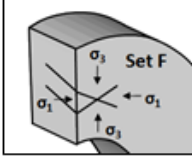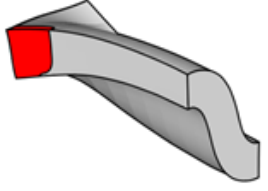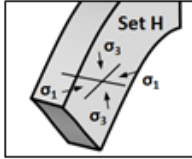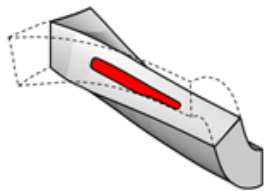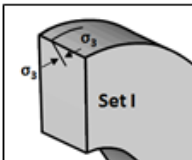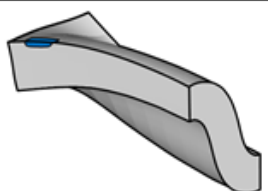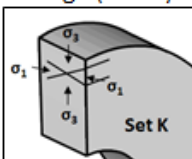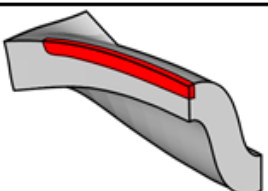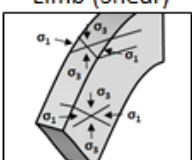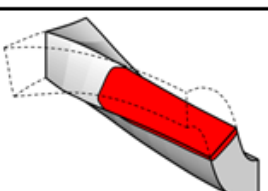
5.4. SYNOPSIS

A synopsis of the fracture sets observed during the numerical simulations is presented in Figures 5.17 and 5.18, and includes the following: fracture type and orientation, extent of observed fracturing, timing of fracture initiation, conditions required to initiate fractures, and any conceptual fold/fracture models or field studies that document the same fracture sets. The first group of fracture sets represents fractures that are identical to fracture sets that feature in Cosgrove and Ameen's (1999) conceptual model for fractures associated with buckle folds. The second group of fractures represents the remainder of the fracture sets observed during the numerical simulations; these fractures do not feature in Cosgrove and Ameen's (1999) conceptual model.

Fracture Sets (Cosgrove and Ameen, 1999; Figure 5.1)	Cumulative Spatial Extent (Blue = Tensile; Red = Shear)	Timing of Initiation	Conditions for Initiation	Other Conceptual Models and Field Studies
Hinge (Tensile) Set 1		Mid to Late-Stage Buckling	All conditions except: $R_\mu = 25$, OT > 500 m, or SP < 30%	Stearns and Friedman (1972), Twiss and Moores (2007), Stearns (1964), Bellahsen et al. (2006), Cooper et al. (2006)
		Post-Buckling	SP ≥ 20%, and OT ≤ 500m; combined with EU	
Hinge (Tensile) Set 3		Mid to Late-Stage Buckling	$k = 10^{-21}\,m^2$ or $R_\mu = 100$	Stearns and Friedman (1972), McQuillan (1974), Stephenson et al. (2007), Wennberg et al. (2007)
		Post-Buckling	SP = 50%, OT = 500m, and AR ≥ 1:5; combined with EU	
Hinge (Shear) Set 5		Post-Buckling	SP = 40%; combined with EU	Stearns and Friedman (1972), Twiss and Moores (2007), Stearns (1964), Hancock (1985), Vitale et al. (2012)
Limb (Shear) Set 6		Early-Stage Buckling	$k = 10^{-21}\,m^2$; combined with an APR ≥ 5:1	Stearns (1964), Stearns (1967)
		Post-Buckling	SP ≤ 20%; combined with EU	
Hinge (Shear) Set 7		Mid-Stage Buckling	All conditions except: $R_\mu = 25$, OT > 500 m, or SP < 30%	Twiss and Moores (2007), Coleman-Sadd (1978), Cooper et al. (2006), Morley (2007)
		Post-Buckling	20% ≤ SP ≤ 40%; combined with EU	
Hinge (Shear) Set 8		Early to Late-Stage Buckling	All conditions except for OT > 500m	Twiss and Moores (2007), Stearns (1964), Narahara and Wiltschko (1985), Mitra (2002)
		Post-Buckling	SP ≤ 30%; combined with EU	
k = permeability R_μ = viscosity contrast AR = aspect ratio OT = initial overburden thickness SP = shortening percentage EU = erosional unloading APR = anisotropic permeability ratio				

Figure 5.17. Fracture sets observed in the numerical simulations that are identical to fracture sets featured in Cosgrove and Ameen's (1999) conceptual model for fractures associated with buckle folds (see Figure 5.1). An explanation of the abbreviations used to describe the conditions for fracture initiation, are provided at the bottom of the figure.

Additional Fracture Sets	Cumulative Spatial Extent (Blue = Tensile; Red = Shear)	Timing of Initiation	Conditions for Initiation	Other Conceptual Models and Field Studies
Hinge (Shear) Set E		Late-Stage Buckling	$k = 10^{-21}\,m^2$ or $R_\mu \geq 75$	Stearns and Friedman (1972), Marshak et al. (1982), Hancock (1985), Wenneberg et al. (2007)
Hinge (Shear) Set F		Mid to Late-Stage Buckling	All conditions except: $R_\mu = 25$, OT > 500 m, or SP < 50%	N/A
		Post-Buckling	SP ≥ 30%, and OT ≥ 500m; combined with EU	
Limb (Shear) Set H		Late-Stage Buckling	$R_\mu = 25$	Ameen (1990; experimental study), Stearns (1970)
Hinge (Tensile) Set I		Post-Buckling	OT = 1000m, or OT = 1500m; combined with erosional unloading	Lacombe et al. (2011)
Hinge (Shear) Set K		Post-Buckling	OT ≥ 1500m; combined with EU	Hancock (1985), Lacombe et al. (2011)
Limb (Shear)		Post-Buckling	SP = 50% and OT ≥ 500m; combined with EU	N/A (Fracture orientation is highly dependent on the orientation of the limb at the time of fracture initiation)

k = permeability R_μ = viscosity contrast   AR = aspect ratio   OT = initial overburden thickness
SP = shortening percentage   EU = erosional unloading   APR = anisotropic permeability ratio

Figure 5.18. Fracture sets observed in the numerical simulations that do not feature in Cosgrove and Ameen's (1999) conceptual model for fractures associated with buckle folds. An explanation of the abbreviations used to describe the conditions for fracture initiation, are provided at the bottom of the figure.

5.5. LIMITATIONS

Although the 3D modeling approach presented in this study allows for the generation of realistic non-cylindrical fold geometries, and effectively alleviates restrictions to the out-of-plane principal stress orientation associated with cylindrical fold models (cited as a shortcoming to the 2D modeling approach by Eckert et al., 2014), there are still limitations that arise.

Considering that this study is primarily geared towards characterizing fracture initiation, one of the most important limitations is the inability of the viscoelastic material model to simulate plastic failure, consequently leading to an inadequate representation of the stress changes associated with failure. When fractures are initiated in rocks, the stresses near the fracture typically decrease rapidly (Jaeger et al. 2009); but the viscoelastic stresses in these models are allowed to continuously develop, even when the stress conditions required to initiate failure have been met. In order to provide a comprehensive characterization of fracture initiation, this limitation is counteracted using an assumption that does not allow fractures to propagate beyond the boundaries of an individual finite element (refer to Section 4.1.2). Although this is considered a major assumption, it is still deemed appropriate since the implementation of a plastic constitutive relationship is not feasible for this study.

Because a 3D modeling approach is utilized, a large number of finite elements are introduced for each model ($> 350,000$). A resulting set of over 380,000 equations must be solved by ABAQUS^{TM} for every specified time increment during the simulation. For the sake of executing practical run times for each model, both the number of time increments per simulation, and the output frequency of the unknown variables are reduced accordingly. The downside to reducing the runtime is a subsequent decline in the resolution of the stress evolution output, and by association, the fracture potential results. Models with higher resolution outputs can be readily acquired using ABAQUS^{TM}, but the required cumulative run time for such models goes beyond the time constraints for this particular study.

Additional limitations that do not directly influence the effectiveness of the post-processing analysis procedure (i.e., calculation of the fracture potential and the orientations of the fracture planes), include the following:

(1) Only a single, continuous layer-parallel shortening event is applied, and thus the influence of stress relaxation is not considered during buckling.

(2) An initial, isotropic pore pressure distribution is assumed throughout each model. These initial conditions restrict the inclusion of isolated overpressure zones, common in natural formations (Twiss and Moores, 2007), prior to the onset of shortening.

(3) Viscosity is the only material property that is heterogeneously distributed throughout the model. All other initial material properties are either assumed constant (i.e., specific gravity, Poisson Ratio), or are homogenously distributed in a depth dependent fashion throughout the model (i.e., porosity, permeability, Young's Modulus).

(4) Both buckling and erosional unloading are assumed to be isothermal processes, and thus thermal stresses are not included in this study.

(5) The failure criterion used only predicts the initiation of new fractures; consequently, the reactivation of optimally oriented, pre-existing fracture sets is not accounted for.

These five limitations represent a simplified geologic setting that may not be characteristic of most natural subsurface environments. The methodology presented is capable of being altered to simulate folding for more complex (i.e., realistic) geologic environments; however, the addition of more complex features is beyond the scope of this study, since the main purpose is to determine the relative impact of individual parameters on fracture initiation characteristics, and not to evaluate fracture initiation for a specific geologic environment.

6. CONCLUSIONS AND FUTURE WORK

6.1. CONCLUSIONS

The numerical modeling results presented in this study demonstrate the importance of utilizing a 3D approach when conducting an analysis of fracture initiation, based on effective stress evolution; especially when considering periclines, where the complex geometry has a significant influence on the state of stress. The 3D approach allows for the generation of periclinal fold geometries, which effectively mitigates any restrictions on principal stress orientations; a shortcoming that is associated with 2D cylindrical folding models. Moreover, the 3D approach permits the initiation of fracture sets that exist in nature, but cannot be explained using a cylindrical folding approach.

An extensive analysis of the fracture potential results reveals 11 unique fracture sets, and one large group of diversely oriented shear fractures in the fold limb, that are observed during the processes of buckling and erosional unloading. The fracture sets of primary interest are those that can be used to help explain the occurrence of fracture sets presented in Cosgrove and Ameen's (1999) conceptual model for fractures associated with buckle folds (see Figure 5.1). Six of the nine fracture sets that appear in Cosgrove and Ameen's (1999) conceptual model, are also observed during the numerical simulations (see Figure 5.17), and can be summarized as follows:

(1) Outer arc tensile fractures parallel to the fold axis (Set 1), outer arc normal faults striking parallel to the fold axis (Set 7), and inner arc thrusts striking parallel to the fold axis (Set 8) are observed for nearly every buckling scenario.

(2) Outer arc tensile fractures perpendicular to the fold axis (Set 3), and thrusts in the fold limb striking roughly parallel to the fold axis (Set 6) require more specific buckling scenarios involving low permeabilities (10^{-21} m^2) or high viscosity contrasts ($R_\mu = 100$).

(3) Fracture Sets 1, 3, 6, 7, and 8 can also be initiated for various scenarios involving erosional unloading.

(4) Vertical conjugate shears in the outer arc, where the fold axis bisects the acute angle between fracture planes (Set 5), are only observed for a single case involving erosional unloading.

Based on these observations, it is concluded that Sets 1, 7, and 8 are common fractures sets that should be observed in a majority of periclinal buckle folds. Sets 3 and 6 are less common fracture sets, but should still be initiated in most low permeability ($\leq 10^{-21}$ m^2) periclinal buckle folds. Set 5 is a rare fracture set that is not associated with buckling, and should only be observed in select periclinal buckle folds during or after erosional unloading. Additionally, based on the results presented in this study, it is concluded that the fracture sets in periclinal buckle folds exhibit the following hierarchical order of initiation:

(1) Early-Stage (0-15% Shortening) – Fracture Sets 6 and 8.

(2) Mid-Stage (15-30% Shortening) – Predominantly Fracture Sets 1 and 7, but also Fracture Sets 3 and 8.

(3) Late-Stage (> 30% Shortening) – Predominantly Fracture Set 3, but also Fracture Sets 1 and 8.

(4) Erosional Unloading – Fracture Sets 1, 3, 5, 6, 7, and 8 are all possible.

The five additional fracture sets, and large group of diversely oriented shear fractures in the fold limb, observed during the numerical simulations (see Figure 5.18) can be summarized as follows:

(1) Fracture Sets E (hinge; shear) and H (limb; shear) are late-stage fractures that are only observed for specific buckling scenarios.

(2) Fracture Set F (hinge; shear) are observed for nearly every buckling scenario, and can be initiated during mid to late-stage buckling, or during erosional unloading.

(3) Fracture Sets I (hinge; tensile) and K (hinge; shear) are only observed during erosional unloading when initial overburden thicknesses are greater than 500m.

(4) The large group of diversely oriented shear fractures in the fold limb, are observed for every scenario involving erosional unloading for folds that have experienced at least 50% shortening.

Based on these observations it is concluded that Set F is a common fracture set that should be observed in a majority of periclinal buckle folds, although this set is not documented in any known conceptual models or field studies. Sets E, H, I, and K are less common fracture sets that require more specific buckling or erosional unloading scenarios. Lastly, the erosional shear fractures in the fold limb are common fractures that should be observed in a majority of periclinal buckle folds after erosional unloading. The orientation of these erosional shear fractures in the limb, relative to the folding layer and bedding planes, are highly dependent on the orientation of the limb at the time of fracturing. This suggests that a large number of fracture sets in the limbs of periclinal buckle folds could be attributed to erosional unloading, even though the fracture sets observed in this study are not documented in any known conceptual model or field study.

All of these conclusions are drawn without any knowledge of pre-existing fracture sets that may be present prior to the onset of buckling.

6.2. FUTURE WORK

While this study has provided valuable insight into fracture initiation during the processes of subsurface buckle folding and erosional unloading, the results are still far from being able to completely explain fracture patterns associated with buckle folds. Additional 3D numerical studies could further contribute to the current body of knowledge on this subject, and can be divided into two categories: studies that serve as a continuation of this study, which do not require significant alterations to the presented methodology; and studies that introduce new geologic aspects, which require significant alterations to the presented methodology.

To the author's knowledge, this study is the first to simulate the effective stress evolution during non-cylindrical buckle folding, while including the influence of overburden stress, pore pressure, and a geologic strain rate. While this study is extensive in regards to the number of parameters considered, additional studies can still be conducted as an extension of this study. These include, but are not limited to:

- A re-examination of the most influential parameters for fracture initiation (i.e., permeability and initial overburden thickness combined with erosional

unloading), using a much finer mesh (i.e., more elements) to reduce the magnitude of the errors associated with using the finite element method, and including more time increments to increase the resolution of the stress evolution results. This will result in more precise predictions for the timing of fracture initiation and more reliable predictions for the spatial extent of fracturing than is observed in the current study.

- Inclusion of additional failure criteria in the post-processing stage. In this study, the likelihood of fracture initiation, and the fracture orientations, are both controlled by the shape of the combined Griffith/Navier-Coulomb failure envelope. The use of additional failure criteria could result in significantly different observations and conclusions with respect to fracture initiation than the ones presented in this study.

- Addition of a failure criterion that accounts for the reactivation of pre-existing fracture sets (i.e., $T = 0$; $C_0 = 0$). This addition could help explain the occurrence of fracture sets that cannot be explained by the current modeling results (see Section 5.3). Furthermore, if the unexplained fracture sets are observed while implementing a fracture reactivation criterion, it would further support the hypothesis that those fractures are present pre-folding.

For new studies on fracture prediction in 3D fold structures it is also necessary to introduce more complicated geologic aspects that are reflective of realistic folding scenarios. These aspects would help to mitigate some of the most important limitations in this study, but would require a new methodology and result in more complex simulations. New aspects to investigate include, but are not limited to the following:

- A plastic constitutive material model that is capable of simulating the initiation and propagation of fractures, as well as the associated stress changes. Finite element analysis codes exist that are capable of simulating plastic behavior, but it should be noted that simulations involving plasticity require much longer run times than a viscoelastic simulation using the same number of central processing units. This could make the incorporation of plasticity into a 3D model with a large number of finite elements very difficult.

- Inclusion of thermal stresses during buckling and erosional unloading. Significant increases in the temperature are expected during buckling, while significant decreases are expected during erosional unloading. These temperature changes may have a large impact on the pore pressure evolution and, as a result, the effective stresses will be impacted as well.

- The influence of multi-layer folding and the flexural slip mechanism. The periclines generated in this study represent a fold geometry that is commonly observed in nature. This geometry can be taken one step further to include alternating competent and incompetent layers, which would result in a multi-layer fold system that is commonly observed in nature. The addition of the flexural slip mechanism allows for the generation of even more realistic fold shapes, including chevron folds and box folds. These new folds generated by flexural slip have different strain distributions than the tangential longitudinal strain folds generated in this study and thus, the stress distributions and fracture characteristics could change as well.

Lastly it should be mentioned that this study, as well as the recommended future studies, are only meant to help explain the existence of various fracture sets that are commonly observed in buckle folds; the results from these studies should not be used as a direct indicator for fracture sets that will appear in a particular natural fold.

APPENDIX A

DERIVATION OF THE GOVERNING EQUATIONS

The three-dimensional (3D) numerical model is set up in an x-y-z coordinate system (the z axis is vertical). The model consists of a compressible material (rock) saturated with an incompressible pore fluid (water) and mass is conserved everywhere. The model has a viscoelastic Maxwell rheology and pore pressure is considered by utilizing effective stress analysis. The unknowns of the problem comprise the stress tensor components σ_{xx}, σ_{yy}, σ_{zz}, σ_{xy}, σ_{xz} and σ_{yz}, the pore pressure P_p, the material velocities in three directions v_x, v_y and v_z, and the material density ρ_m. For this set of 11 unknowns, 11 equations need to be defined to find a unique solution.

The first set of governing equations are obtained from the equilibrium equations using effective stresses [e.g. *Jaeger et.al*, 2007] and are given by:

$$\frac{\partial \sigma'_{xx}}{\partial x} + \frac{\partial \sigma_{yz}}{\partial y} + \frac{\partial \sigma_{xz}}{\partial z} + \rho_m F_x = 0 \tag{1}$$

$$\frac{\partial \sigma_{xy}}{\partial x} + \frac{\partial \sigma'_{yy}}{\partial y} + \frac{\partial \sigma_{yz}}{\partial z} + \rho_m F_y = 0 \tag{2}$$

$$\frac{\partial \sigma_{xz}}{\partial x} + \frac{\partial \sigma_{yz}}{\partial y} + \frac{\partial \sigma'_{zz}}{\partial z} + \rho_m F_z = 0 \tag{3}$$

where F_x, F_y and F_z represent the body force components along the x , y, and z axes, respectively. σ'_{xx}, σ'_{yy}, σ'_{zz}, σ_{xy}, σ_{xz} and σ_{yz} are the components of the effective stress tensor which is defined as:

$$\sigma'_{ij} = \sigma_{ij} - \alpha P_p \delta_{ij} \tag{4}$$

where the Biot coefficient α is defined by rock's bulk modulus K and solid grains bulk modulus K_S (e.g. Jaeger et.al, 2007):

$$\alpha = 1 - \frac{K}{K_s} \tag{5}$$

As gravity represents the body force in this study, equations (1) to (3) can be expressed using the total stress tensor components as:

$$\frac{\partial(\sigma_{xx} - \alpha P_p)}{\partial x} + \frac{\partial \sigma_{yz}}{\partial y} + \frac{\partial \sigma_{xz}}{\partial z} + \rho_m g_x = 0 \tag{6}$$

$$\frac{\partial(\sigma_{yy} - \alpha P_p)}{\partial y} + \frac{\partial \sigma_{xy}}{\partial x} + \frac{\partial \sigma_{yz}}{\partial z} + \rho_m g_y = 0 \tag{7}$$

$$\frac{\partial(\sigma_{zz} - \alpha P_p)}{\partial z} + \frac{\partial \sigma_{xz}}{\partial x} + \frac{\partial \sigma_{yz}}{\partial y} + \rho_m g_z = 0 \tag{8}$$

where σ_{xx}, σ_{yy}, σ_{zz}, σ_{xy}, σ_{xz} and σ_{yz} are the components of the of the total stress tensor. The pore pressure, P_p, is a function of time, t, and of the spatial coordinates x, y and z. g_x, g_y and g_z are the gravitational accelerations along the x, y, and z axes respectively with $g_x = g_y = 0$. The stress equilibrium equations are rewritten as:

$$\frac{\partial \sigma_{xx}}{\partial x} - \frac{\partial(\alpha P_p)}{\partial x} + \frac{\partial \sigma_{yz}}{\partial y} + \frac{\partial \sigma_{xz}}{\partial z} = 0 \tag{9}$$

$$\frac{\partial \sigma_{yy}}{\partial y} - \frac{\partial(\alpha P_p)}{\partial y} + \frac{\partial \sigma_{xy}}{\partial x} + \frac{\partial \sigma_{yz}}{\partial z} = 0 \tag{10}$$

$$\frac{\partial \sigma_{zz}}{\partial z} - \frac{\partial(\alpha P_p)}{\partial z} + \frac{\partial \sigma_{xz}}{\partial x} + \frac{\partial \sigma_{yz}}{\partial y} + \rho_m g_z = 0 \tag{11}$$

The constitutive equations are used to obtain the next set of governing equations for the viscoelastic material described by the Maxwell model. In this model the total stress σ, strain ε and strain rate ἐ are given as [*Turcotte and Schubert*, 2002]:

$$\sigma = \sigma^e = \sigma^f \tag{12}$$

$$\varepsilon = \varepsilon^e + \varepsilon^f \tag{13}$$

$$\dot{\varepsilon} = \dot{\varepsilon}^e + \dot{\varepsilon}^f \tag{14}$$

where the superscript "*e*" denotes the linear elastic part and the superscript "*f*" denotes the linear viscous part. The elastic strain ε_{ij}^e of a poro-viscoelastic material is given by:

$$\varepsilon_{ij}^e = \varepsilon_{ij}^{e,iso} + \varepsilon_{ij}^{e,dev} \tag{15}$$

$$\varepsilon_{ij}^{e,iso} = \frac{1}{3K}\sigma_{ij}^{iso}\delta_{ij} - \frac{\alpha}{3K}P_P\delta_{ij} \tag{16}$$

$$\varepsilon_{ij}^{e,dev} = \frac{1}{2G}\sigma_{ij}^{dev} \tag{17}$$

where the superscript "*iso*" denotes the isotropic part of the stress tensor and the superscript "*dev*" denotes the deviatoric part of the stress tensor. G is the shear modulus. Since G, K and α are constant, the elastic strain rate $\dot{\varepsilon}^e$ can be expressed as:

$$\dot{\varepsilon}_{ij}^e = \dot{\varepsilon}_{ij}^{e,iso} + \dot{\varepsilon}_{ij}^{e,dev} = \frac{1}{3K}\dot{\sigma}_{ij}^{iso}\delta_{ij} - \frac{\alpha}{3K}\dot{P}_P\delta_{ij} + \frac{1}{2G}\dot{\sigma}_{ij}^{dev} \tag{18}$$

which can be written explicitly in this 3-D model as:

$$\dot{\varepsilon}_{xx}^e = \frac{1}{3K}\dot{\sigma}_{xx}^{iso} - \frac{\alpha}{3K}\dot{P}_P + \frac{1}{2G}\dot{\sigma}_{xx}^{dev} \tag{19}$$

$$\dot{\varepsilon}_{yy}^e = \frac{1}{3K}\dot{\sigma}_{yy}^{iso} - \frac{\alpha}{3K}\dot{P}_P + \frac{1}{2G}\dot{\sigma}_{yy}^{dev} \tag{20}$$

$$\dot{\varepsilon}_{zz}^e = \frac{1}{3K}\dot{\sigma}_{zz}^{iso} - \frac{\alpha}{3K}\dot{P}_P + \frac{1}{2G}\dot{\sigma}_{zz}^{dev} \tag{21}$$

$$\dot{\varepsilon}_{xy}^e = \frac{1}{2G}\dot{\sigma}_{xy}^{dev} \tag{22}$$

$$\dot{\varepsilon}_{xz}^e = \frac{1}{2G}\dot{\sigma}_{xz}^{dev} \tag{23}$$

$$\dot{\varepsilon}_{yz}^e = \frac{1}{2G}\dot{\sigma}_{yz}^{dev} \tag{24}$$

The constitutive equation for a Newtonian viscous fluid depends on shear viscosity (μ) and the volumetric viscosity (λ) and is given as [*Ockendon*, 1995]:

$$\sigma_{ij}^{'} = \sigma^{iso}\delta_{ij} - P_p\delta_{ij} + \lambda\dot{\varepsilon}_{kk}^{f}\delta_{ij} + 2\mu\dot{\varepsilon}_{ij}^{f} \tag{25}$$

where $\sigma^{iso}\,\delta_{ij}$ is the isotropic part as would exist in an inviscid fluid. The bulk viscosity is not considered here since both the rock grains and the saturated in rock is considered as incompressible fluid. Thus, equation (25) can be expressed as:

$$\sigma_{ij}^{'} = \sigma^{iso}\delta_{ij} - P_p\delta_{ij} + 2\mu\dot{\varepsilon}_{ij}^{f} \tag{26}$$

Hence, in terms of the deviatoric and isotropic decompositions, the viscous part of the strain can be written explicitly in this 3-D model as:

$$\dot{\varepsilon}_{xx}^{f} = \frac{\sigma_{xx}^{dev}}{2\mu} \tag{27}$$

$$\dot{\varepsilon}_{yy}^{f} = \frac{\sigma_{yy}^{dev}}{2\mu} \tag{28}$$

$$\dot{\varepsilon}_{zz}^{f} = \frac{\sigma_{zz}^{dev}}{2\mu} \tag{29}$$

$$\dot{\varepsilon}_{xy}^{f} = \frac{\sigma_{xy}^{dev}}{2\mu} \tag{30}$$

$$\dot{\varepsilon}_{xz}^{f} = \frac{\sigma_{xz}^{dev}}{2\mu} \tag{31}$$

$$\dot{\varepsilon}_{yz}^{f} = \frac{\sigma_{yz}^{dev}}{2\mu} \tag{32}$$

Thus, the total strain rate for Maxwell model is expressed as:

$$\dot{\varepsilon}_{xx} = \dot{\varepsilon}_{xx}^{e} + \dot{\varepsilon}_{xx}^{f} = \frac{1}{3K}\dot{\sigma}_{xx}^{iso} - \frac{\alpha}{3K}\dot{P}_{P} + \frac{1}{2G}\dot{\sigma}_{xx}^{dev} + \frac{\sigma_{xx}^{dev}}{2\mu}$$

(33)

$$\dot{\varepsilon}_{yy} = \dot{\varepsilon}_{yy}^{e} + \dot{\varepsilon}_{yy}^{f} = \frac{1}{3K}\dot{\sigma}_{yy}^{iso} - \frac{\alpha}{3K}\dot{P}_{P} + \frac{1}{2G}\dot{\sigma}_{yy}^{dev} + \frac{\sigma_{yy}^{dev}}{2\mu}$$

(34)

$$\dot{\varepsilon}_{zz} = \dot{\varepsilon}_{zz}^{e} + \dot{\varepsilon}_{zz}^{f} = \frac{1}{3K}\dot{\sigma}_{zz}^{iso} - \frac{\alpha}{3K}\dot{P}_{P} + \frac{1}{2G}\dot{\sigma}_{zz}^{dev} + \frac{\sigma_{zz}^{dev}}{2\mu}$$

(35)

$$\dot{\varepsilon}_{xy} = \dot{\varepsilon}_{xy}^{e} + \dot{\varepsilon}_{xy}^{f} = \frac{1}{2G}\dot{\sigma}_{xy}^{dev} + \frac{\sigma_{xy}^{dev}}{2\mu}$$

(36)

$$\dot{\varepsilon}_{xz} = \dot{\varepsilon}_{xz}^{e} + \dot{\varepsilon}_{xz}^{f} = \frac{1}{2G}\dot{\sigma}_{xz}^{dev} + \frac{\sigma_{xz}^{dev}}{2\mu}$$

(37)

$$\dot{\varepsilon}_{yz} = \dot{\varepsilon}_{yz}^{e} + \dot{\varepsilon}_{yz}^{f} = \frac{1}{2G}\dot{\sigma}_{yz}^{dev} + \frac{\sigma_{yz}^{dev}}{2\mu}$$

(38)

The time derivatives of the time-depended effective stress tensor in the constitutive equations (33) to (38) are given by using the chain rule of differentiation:

$$\dot{\sigma}_{xx}^{iso} = \frac{D\sigma_{xx}^{iso}}{Dt} = \frac{\partial\sigma_{xx}^{iso}}{\partial t} + v_x\frac{\partial\sigma_{xx}^{iso}}{\partial x} + v_y\frac{\partial\sigma_{xx}^{iso}}{\partial y} + v_z\frac{\partial\sigma_{xx}^{iso}}{\partial z}$$

(39)

$$\dot{\sigma}_{xx}^{dev} = \frac{D\sigma_{xx}^{dev}}{Dt} = \frac{\partial\sigma_{xx}^{dev}}{\partial t} + v_x\frac{\partial\sigma_{xx}^{dev}}{\partial x} + v_y\frac{\partial\sigma_{xx}^{dev}}{\partial y} + v_z\frac{\partial\sigma_{xx}^{dev}}{\partial z}$$

(40)

$$\dot{\sigma}_{yy}^{iso} = \frac{D\sigma_{yy}^{iso}}{Dt} = \frac{\partial\sigma_{yy}^{iso}}{\partial t} + v_x\frac{\partial\sigma_{yy}^{iso}}{\partial x} + v_y\frac{\partial\sigma_{yy}^{iso}}{\partial y} + v_z\frac{\partial\sigma_{yy}^{iso}}{\partial z}$$

(41)

$$\dot{\sigma}_{yy}^{dev} = \frac{D\sigma_{yy}^{dev}}{Dt} = \frac{\partial\sigma_{yy}^{dev}}{\partial t} + v_x\frac{\partial\sigma_{yy}^{dev}}{\partial x} + v_y\frac{\partial\sigma_{yy}^{dev}}{\partial y} + v_z\frac{\partial\sigma_{yy}^{dev}}{\partial z}$$

(42)

$$\dot{\sigma}_{zz}^{iso} = \frac{D\sigma_{zz}^{iso}}{Dt} = \frac{\partial\sigma_{zz}^{iso}}{\partial t} + v_x\frac{\partial\sigma_{zz}^{iso}}{\partial x} + v_y\frac{\partial\sigma_{zz}^{iso}}{\partial y} + v_z\frac{\partial\sigma_{zz}^{iso}}{\partial z}$$

(43)

$$\dot{\sigma}_{zz}^{dev} = \frac{D\sigma_{zz}^{dev}}{Dt} = \frac{\partial\sigma_{zz}^{dev}}{\partial t} + v_x\frac{\partial\sigma_{zz}^{dev}}{\partial x} + v_y\frac{\partial\sigma_{zz}^{dev}}{\partial y} + v_z\frac{\partial\sigma_{zz}^{dev}}{\partial z}$$

(44)

$$\dot{P}_p = \frac{DP_p}{Dt} = \frac{\partial P_p}{\partial t} + v_x \frac{\partial P_p}{\partial x} + v_y \frac{\partial P_p}{\partial y} + v_z \frac{\partial P_p}{\partial z}$$

(45)

$$\dot{\sigma}_{xy}^{dev} = \frac{D\sigma_{xy}^{dev}}{Dt} = \frac{\partial \sigma_{xy}^{dev}}{\partial t} + v_x \frac{\partial \sigma_{xy}^{dev}}{\partial x} + v_y \frac{\partial \sigma_{xy}^{dev}}{\partial y} + v_z \frac{\partial \sigma_{xy}^{dev}}{\partial z}$$

(46)

$$\dot{\sigma}_{xz}^{dev} = \frac{D\sigma_{xz}^{dev}}{Dt} = \frac{\partial \sigma_{xz}^{dev}}{\partial t} + v_x \frac{\partial \sigma_{xz}^{dev}}{\partial x} + v_y \frac{\partial \sigma_{xz}^{dev}}{\partial y} + v_z \frac{\partial \sigma_{xz}^{dev}}{\partial z}$$

(47)

$$\dot{\sigma}_{yz}^{dev} = \frac{D\sigma_{yz}^{dev}}{Dt} = \frac{\partial \sigma_{yz}^{dev}}{\partial t} + v_x \frac{\partial \sigma_{yz}^{dev}}{\partial x} + v_y \frac{\partial \sigma_{yz}^{dev}}{\partial y} + v_z \frac{\partial \sigma_{yz}^{dev}}{\partial z}$$

(48)

Substituting equations (39) to (48) into equations (33) to (38), the constitutive equations can be expressed as:

$$\dot{\varepsilon}_{xx} = \frac{1}{3K}(\frac{\partial \sigma_{xx}^{iso}}{\partial t} + v_x \frac{\partial \sigma_{xx}^{iso}}{\partial x} + v_y \frac{\partial \sigma_{xx}^{iso}}{\partial y} + v_z \frac{\partial \sigma_{xx}^{iso}}{\partial z}) - \frac{\alpha}{3K}\left(\frac{\partial P_p}{\partial t} + v_x \frac{\partial P_p}{\partial x} + v_y \frac{\partial P_p}{\partial y} + v_z \frac{\partial P_p}{\partial z} \right)$$
$$+ \frac{1}{2G}\left(\frac{\partial \sigma_{xx}^{dev}}{\partial t} + v_x \frac{\partial \sigma_{xx}^{dev}}{\partial x} + v_y \frac{\partial \sigma_{xx}^{dev}}{\partial y} + v_z \frac{\partial \sigma_{xx}^{dev}}{\partial z} \right) + \frac{\sigma_{xx}^{dev}}{2\mu}$$

(49)

$$\dot{\varepsilon}_{yy} = \frac{1}{3K}(\frac{\partial \sigma_{xx}^{iso}}{\partial t} + v_x \frac{\partial \sigma_{xx}^{iso}}{\partial x} + v_y \frac{\partial \sigma_{xx}^{iso}}{\partial y} + v_z \frac{\partial \sigma_{xx}^{iso}}{\partial z}) - \frac{\alpha}{3K}\left(\frac{\partial P_p}{\partial t} + v_x \frac{\partial P_p}{\partial x} + v_y \frac{\partial P_p}{\partial y} + v_z \frac{\partial P_p}{\partial z} \right)$$
$$+ \frac{1}{2G}\left(\frac{\partial \sigma_{xx}^{dev}}{\partial t} + v_x \frac{\partial \sigma_{xx}^{dev}}{\partial x} + v_y \frac{\partial \sigma_{xx}^{dev}}{\partial y} + v_z \frac{\partial \sigma_{xx}^{dev}}{\partial z} \right) + \frac{\sigma_{yy}^{dev}}{2\mu}$$

(50)

$$\dot{\varepsilon}_{zz} = \frac{1}{3K}\left(\frac{\partial \sigma_{zz}^{iso}}{\partial t} + v_x \frac{\partial \sigma_{zz}^{iso}}{\partial x} + v_y \frac{\partial \sigma_{zz}^{iso}}{\partial y} + v_z \frac{\partial \sigma_{zz}^{iso}}{\partial z} \right) - \frac{\alpha}{3K}\left(\frac{\partial P_p}{\partial t} + v_x \frac{\partial P_p}{\partial x} + v_y \frac{\partial P_p}{\partial y} + v_z \frac{\partial P_p}{\partial z} \right)$$
$$+ \frac{1}{2G}\left(\frac{\partial \sigma_{zz}^{dev}}{\partial t} + v_x \frac{\partial \sigma_{zz}^{dev}}{\partial x} + v_y \frac{\partial \sigma_{zz}^{dev}}{\partial y} + v_z \frac{\partial \sigma_{zz}^{dev}}{\partial z} \right) + \frac{\sigma_{zz}^{dev}}{2\mu}$$

(51)

$$\dot{\varepsilon}_{xy} = \frac{1}{2G}\left(\frac{\partial \sigma_{xy}^{dev}}{\partial t} + v_x \frac{\partial \sigma_{xy}^{dev}}{\partial x} + v_y \frac{\partial \sigma_{xy}^{dev}}{\partial y} \right) + \frac{\sigma_{xy}^{dev}}{2\mu}$$

(52)

$$\dot{\varepsilon}_{xz} = \frac{1}{2G}\left(\frac{\partial \sigma_{xz}^{dev}}{\partial t} + v_z \frac{\partial \sigma_{xz}^{dev}}{\partial z} + v_x \frac{\partial \sigma_{xz}^{dev}}{\partial x} \right) + \frac{\sigma_{xz}^{dev}}{2\mu}$$

(53)

$$\dot{\varepsilon}_{yz} = \frac{1}{2G}\left(\frac{\partial \sigma_{yz}^{dev}}{\partial t} + v_z\frac{\partial \sigma_{yz}^{dev}}{\partial z} + v_y\frac{\partial \sigma_{yz}^{dev}}{\partial y}\right) + \frac{\sigma_{yz}^{dev}}{2\mu}$$

(54)

As ABAQUS^{TM} utilizes a Lagrangian analysis the time derivatives of the time-dependent effective stress tensor in the equations (39) to (48) can be rewritten as:

$$\dot{\sigma}_{xx}^{iso} = \frac{D\sigma_{xx}^{iso}}{Dt} = \frac{\partial \sigma_{xx}^{iso}}{\partial t}$$

(55)

$$\dot{\sigma}_{xx}^{dev} = \frac{D\sigma_{xx}^{dev}}{Dt} = \frac{\partial \sigma_{xx}^{dev}}{\partial t}$$

(56)

$$\dot{\sigma}_{yy}^{iso} = \frac{D\sigma_{yy}^{iso}}{Dt} = \frac{\partial \sigma_{yy}^{iso}}{\partial t}$$

(57)

$$\dot{\sigma}_{yy}^{dev} = \frac{D\sigma_{yy}^{dev}}{Dt} = \frac{\partial \sigma_{yy}^{dev}}{\partial t}$$

(58)

$$\dot{\sigma}_{zz}^{iso} = \frac{D\sigma_{zz}^{iso}}{Dt} = \frac{\partial \sigma_{zz}^{iso}}{\partial t}$$

(59)

$$\dot{\sigma}_{zz}^{dev} = \frac{D\sigma_{zz}^{dev}}{Dt} = \frac{\partial \sigma_{zz}^{dev}}{\partial t}$$

(60)

$$\dot{P}_p = \frac{DP_p}{Dt} = \frac{\partial P_p}{\partial t}$$

(61)

$$\dot{\sigma}_{xy}^{dev} = \frac{D\sigma_{xy}^{dev}}{Dt} = \frac{\partial \sigma_{xy}^{dev}}{\partial t}$$

(62)

$$\dot{\sigma}_{xz}^{dev} = \frac{D\sigma_{xz}^{dev}}{Dt} = \frac{\partial \sigma_{xz}^{dev}}{\partial t}$$

(63)

$$\dot{\sigma}_{xz}^{dev} = \frac{D\sigma_{yz}^{dev}}{Dt} = \frac{\partial \sigma_{yz}^{dev}}{\partial t}$$

(64)

Substituting equations (55) to (64) into equations (33) to (38), the constitutive equations can be expressed as:

$$\dot{\varepsilon}_{xx} = \frac{1}{3K}\frac{\partial \sigma_{xx}^{iso}}{\partial t} - \frac{\alpha}{3K}\frac{\partial P_p}{\partial t} + \frac{1}{2G}\frac{\partial \sigma_{xx}^{dev}}{\partial t} + \frac{\sigma_{xx}^{dev}}{2\mu}$$

(65)

$$\dot{\varepsilon}_{yy} = \frac{1}{3K}\frac{\partial \sigma_{yy}^{iso}}{\partial t} - \frac{\alpha}{3K}\frac{\partial P_p}{\partial t} + \frac{1}{2G}\frac{\partial \sigma_{yy}^{dev}}{\partial t} + \frac{\sigma_{yy}^{dev}}{2\mu}$$

(66)

$$\dot{\varepsilon}_{zz} = \frac{1}{3K}\frac{\partial \sigma_{zz}^{iso}}{\partial t} - \frac{\alpha}{3K}\frac{\partial P_p}{\partial t} + \frac{1}{2G}\frac{\partial \sigma_{zz}^{dev}}{\partial t} + \frac{\sigma_{zz}^{dev}}{2\mu}$$

(67)

$$\dot{\varepsilon}_{xy} = \frac{1}{2G}\frac{\partial \sigma_{xy}^{dev}}{\partial t} + \frac{\sigma_{xy}^{dev}}{2\mu}$$

(68)

$$\dot{\varepsilon}_{xz} = \frac{1}{2G}\frac{\partial \sigma_{xz}^{dev}}{\partial t} + \frac{\sigma_{xz}^{dev}}{2\mu}$$

(69)

$$\dot{\varepsilon}_{yz} = \frac{1}{2G}\frac{\partial \sigma_{yz}^{dev}}{\partial t} + \frac{\sigma_{yz}^{dev}}{2\mu}$$

(70)

The strain rate is defined as:

$$\dot{\varepsilon}_{xx} = \frac{\partial v_x}{\partial x}$$

(71)

$$\dot{\varepsilon}_{yy} = \frac{\partial v_y}{\partial y}$$

(72)

$$\dot{\varepsilon}_{zz} = \frac{\partial v_z}{\partial z}$$

(73)

$$\dot{\varepsilon}_{xy} = \frac{1}{2}\left(\frac{\partial v_x}{\partial x} + \frac{\partial v_y}{\partial y}\right)$$

(74)

$$\dot{\varepsilon}_{xz} = \frac{1}{2}\left(\frac{\partial v_x}{\partial x} + \frac{\partial v_z}{\partial z}\right)$$

(75)

$$\dot{\varepsilon}_{yz} = \frac{1}{2}\left(\frac{\partial v_y}{\partial y} + \frac{\partial v_z}{\partial z}\right)$$

(76)

Since the modeled rock is compressible, the conservation of mass is expressed by:

$$\frac{\partial \rho_r}{\partial t} + \nabla \cdot (\rho_r \vec{v}) = \frac{\partial \rho_r}{\partial t} + \rho_m \left(\frac{\partial v_x}{\partial x} + \frac{\partial v_y}{\partial y} + \frac{\partial v_z}{\partial z} \right) = 0 \tag{77}$$

where v_x, v_y and v_z are the unknown functions of the material velocities along the x, y, and z axes, respectively.

The remaining governing equations are obtained from the conservation of fluid mass that saturates the rock and Darcy's law. For an incompressible fluid (i.e. water here) the conservation of mass can be expressed as:

$$\frac{\partial \xi}{\partial t} + \nabla \bullet q = \frac{\partial \xi}{\partial t} + \frac{\partial q_x}{\partial x} + \frac{\partial q_y}{\partial y} + \frac{\partial q_z}{\partial z} = 0 \tag{78}$$

where ξ is the volumetric fluid content, $\mathbf{q}$ is the fluid flux vector, and q_x, q_y, and q_z are the fluid discharge velocities along the x, y, and z axes, respectively.

Fluid flow is described by Darcy's law. For this three-dimensional (3D) numerical model, q_x, q_y, and q_z can be expressed as [*Jaeger et al.*, 2007]:

$$q_x = -\frac{k_x}{\mu_f} \frac{\partial P_p}{\partial x} \tag{79}$$

$$q_y = -\frac{k_y}{\mu_f} \frac{\partial P_p}{\partial y} \tag{80}$$

$$q_z = -\frac{k_z}{\mu_f} \left(\frac{\partial P_p}{\partial z} - \rho_f g \right) \tag{81}$$

where k_x, k_y, and k_z are the permeabilities along the x, y, and z axes, respectively. μ_f represents the fluid viscosity. Substituting equations 79 to 81 into equation 78 yields the governing equation for the pore pressure:

$$\frac{\partial \xi}{\partial t} = \frac{k_x}{\mu_f}\frac{\partial^2 P_p}{\partial x^2} + \frac{k_y}{\mu_f}\frac{\partial^2 P_p}{\partial y^2} + \frac{k_z}{\mu_f}\frac{\partial^2 P_p}{\partial z^2}$$

(82)

The pore fluid pressure is related to the deformation of the solid matrix and the variation of the liquid content (ξ) using the Biot's modulus M:

$$P_p = M(\xi + \alpha\varepsilon_b)$$

(83)

where ε_b is the volumetric strain and is expressed as:

$$\varepsilon_b = \varepsilon_{xx} + \varepsilon_{yy} + \varepsilon_{zz}$$

(84)

Insertion of equation 84 into 83 yields:

$$\frac{\partial P_P}{\partial t} = \frac{Mk_x}{\mu_f}\frac{\partial^2 P_p}{\partial x^2} + \frac{Mk_y}{\mu_f}\frac{\partial^2 P_p}{\partial y^2} + \frac{Mk_z}{\mu_f}\frac{\partial^2 P_p}{\partial z^2} + \alpha M(\dot{\varepsilon}_{xx} + \dot{\varepsilon}_{yy} + \dot{\varepsilon}_{zz})$$

(85)

The diffusion equation for pore pressure can also be express by pressure as:

$$\frac{\partial P_P}{\partial t} = \frac{KBk_x}{\alpha\mu_f}\frac{\partial^2 P_p}{\partial x^2} + \frac{KBk_y}{\alpha\mu_f}\frac{\partial^2 P_p}{\partial y^2} + \frac{KBk_z}{\alpha\mu_f}\frac{\partial^2 P_p}{\partial z^2} + B\dot{\sigma}^{iso}$$

(86)

where B is the Skempton coefficient and can be expressed in terms of drained Poisson's ratio (v) and undrained Poisson's ratio (v_u):

$$B = \frac{3(v_u - v)}{\alpha(1-2v)(1+v_u)}$$

(87)

In the model discussed here it is assumed that the rock matrix and pore fluid are treated as incompressible, which is a reasonable approximation (e.g. *Jaeger et al.*, 2007). In this

case, the Biot coefficient (α) equals to 1 and the undrained Poisson ratio (v_u) equals to 0.5. The density of the fully saturated rock is determined by the porosity which is depended on the stresses due to the pore compressibility. The Skempton coefficient B then becomes:

$$B = \frac{3(v_u - v)}{\alpha(1-2v)(1+v_u)} = 1$$

(88)

The diffusion equation for pore pressure can then be rewritten as:

$$\frac{Kk_x}{\mu_f}\frac{\partial^2 P_p}{\partial x^2} + \frac{Kk_y}{\mu_f}\frac{\partial^2 P_p}{\partial y^2} + \frac{Kk_z}{\mu_f}\frac{\partial^2 P_p}{\partial z^2} - \frac{\partial P_P}{\partial t} + \dot{\sigma}^{iso} = 0$$

(89)

Thus, a closed system of eleven partial differential equations, (9), (10), (11), (65), (66), (67), (68), (69), (70), (77), and (89), is available to find a unique solution for the eleven unknown functions v_x, v_y, v_z, ρ_r, σ_{xx}, σ_{yy}, σ_{zz}, σ_{xy}, σ_{xz}, σ_{yz}, P_p.
From equation 89 it can be seen that the pore pressure response is coupled to the volumetric strain (and hence to the isotropic stress tensor). Fluid flow is then modeled as the result of strain related pore volume changes, whereby pore pressure is increased in regions of compressional strain (i.e. reduction in volume) and pore pressure is decreased in regions of extensional strain (i.e. increase in volume).

APPENDIX B

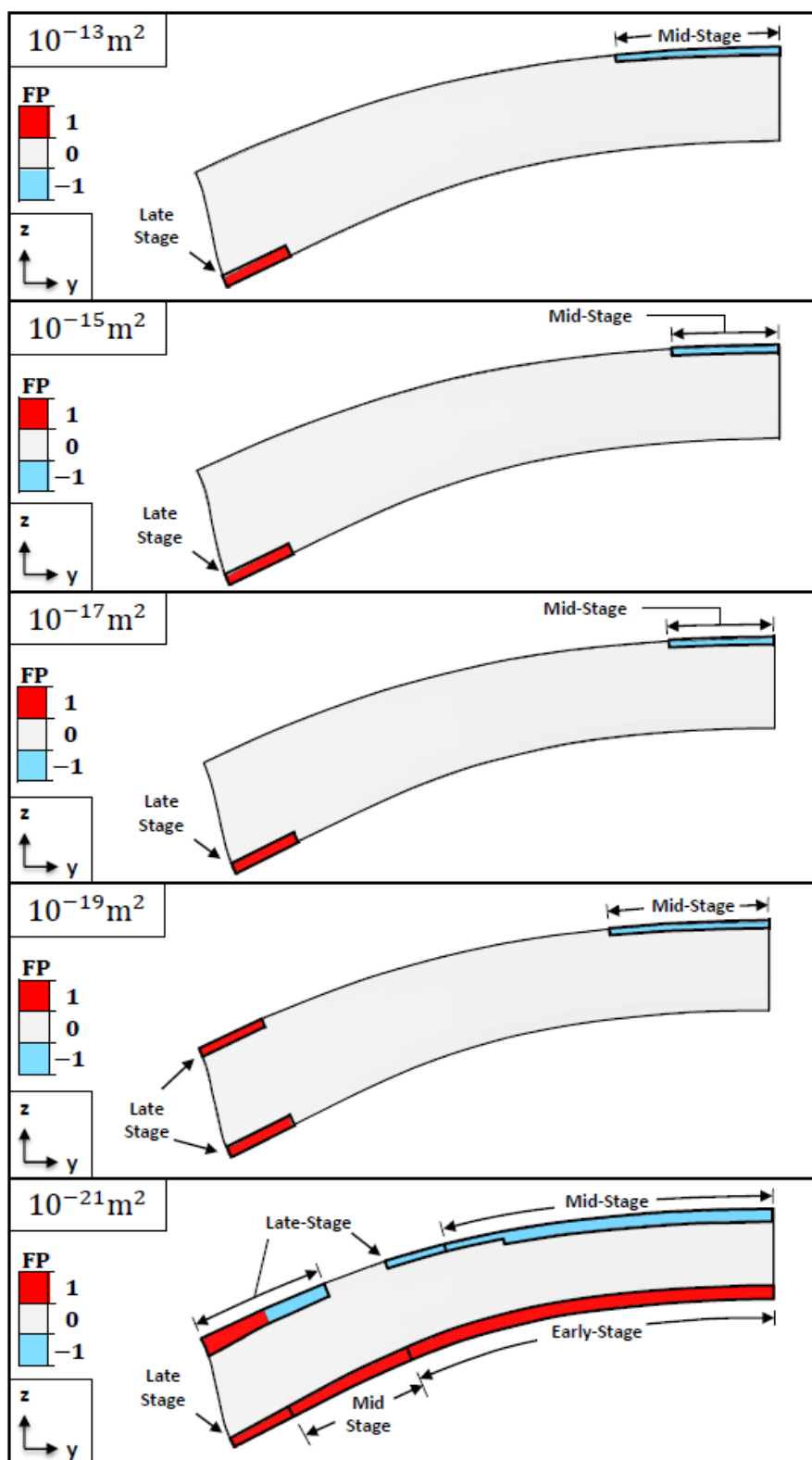ADDITIONAL FRACTURE POTENTIAL RESULTS FOR PERMEABILITY

MAGNITUDE ANALYSIS

Figure B.1. Fracture potential results in the hinge for an intermediate strength rock with varying permeability magnitudes. The final fold shape is approximately the same for each model.
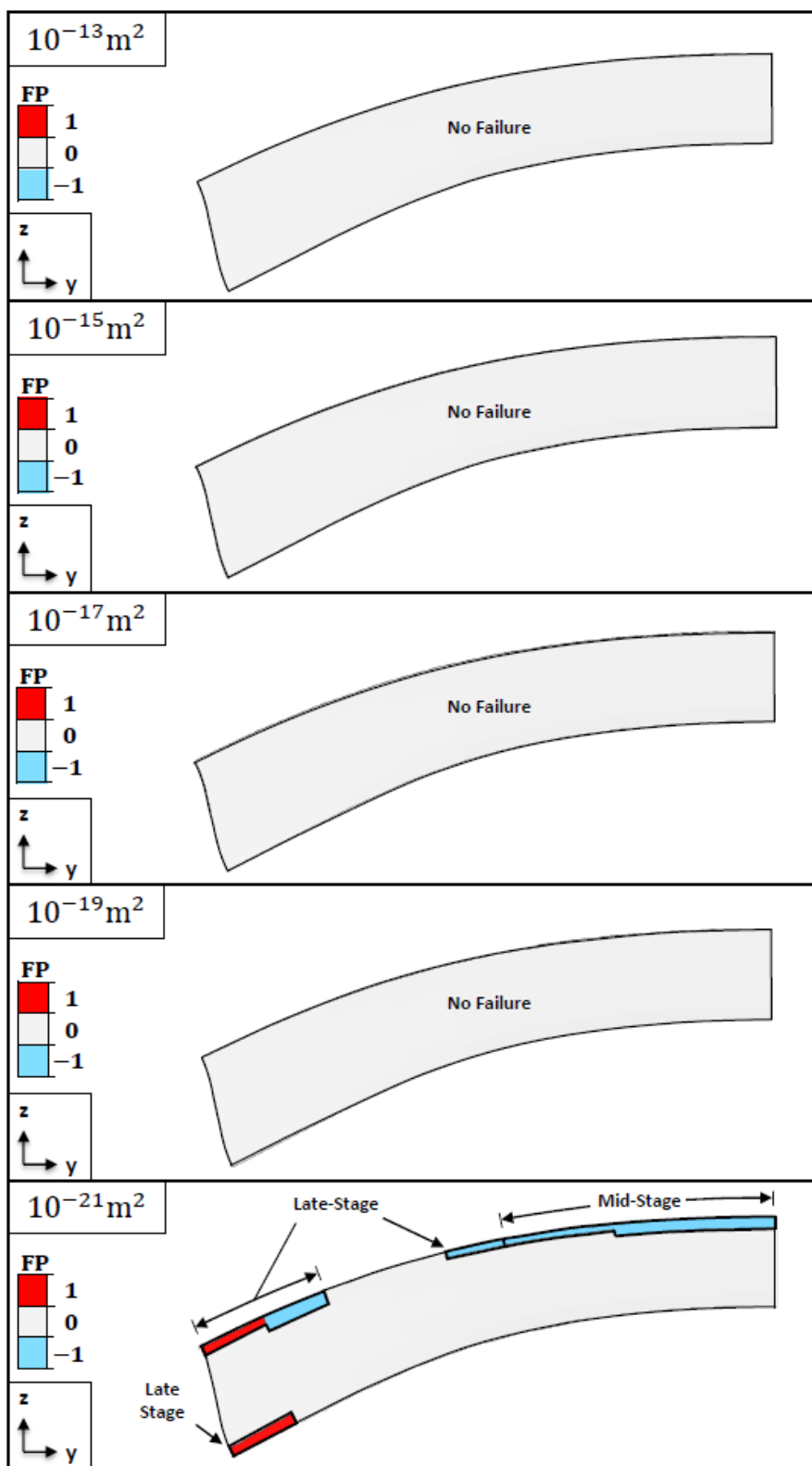
Figure B.2. Fracture potential results in the hinge for a strong rock with varying permeability magnitudes. The final fold shape is approximately the same for each model.

APPENDIX C

ADDITIONAL FRACTURE POTENTIAL RESULTS FOR ANISOTROPIC

PERMEABILITY ANALYSIS
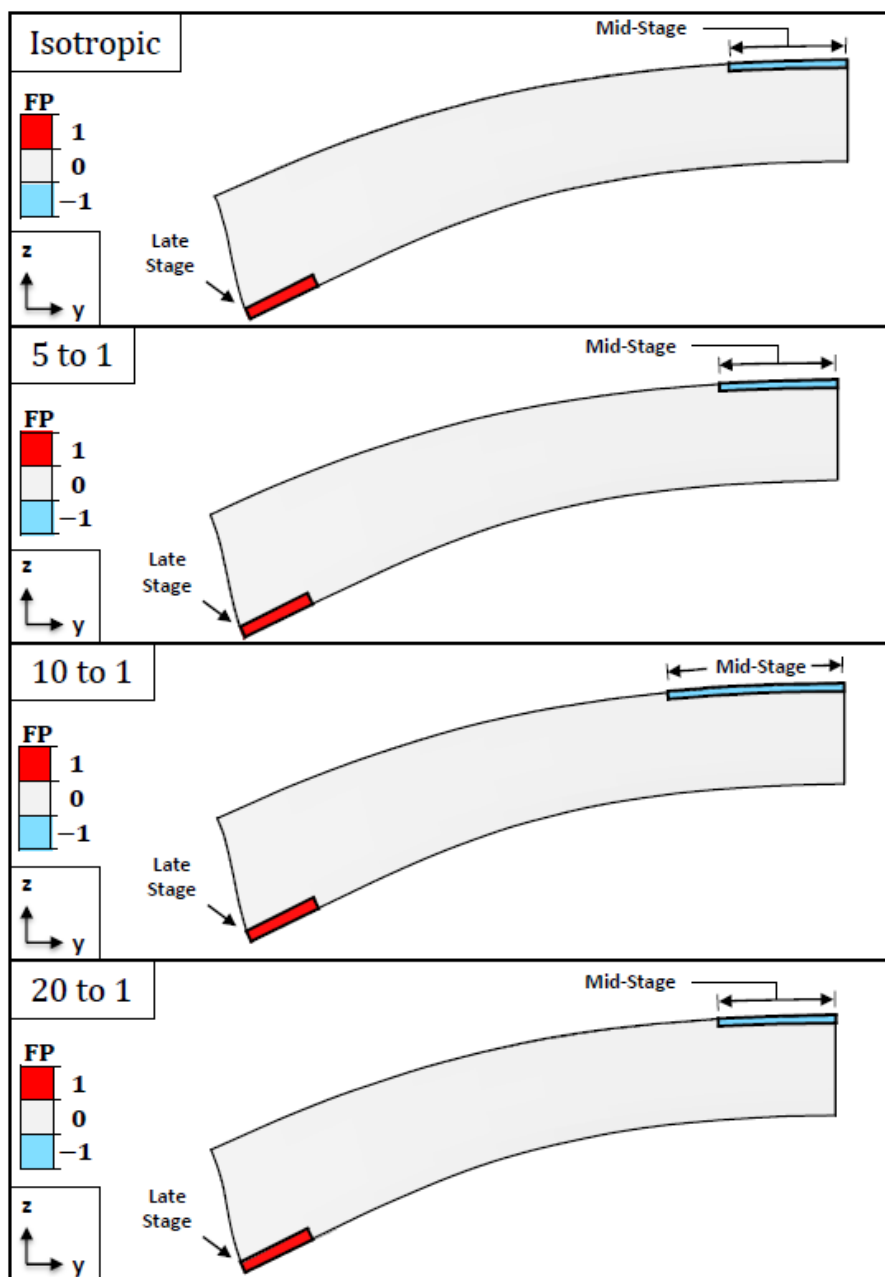
Figure C.1. Fracture potential results in the hinge for a high permeability (10^{-21} m^2) intermediate strength rock, with varying degrees of permeability anisotropy. The final fold shape is approximately the same for each model.
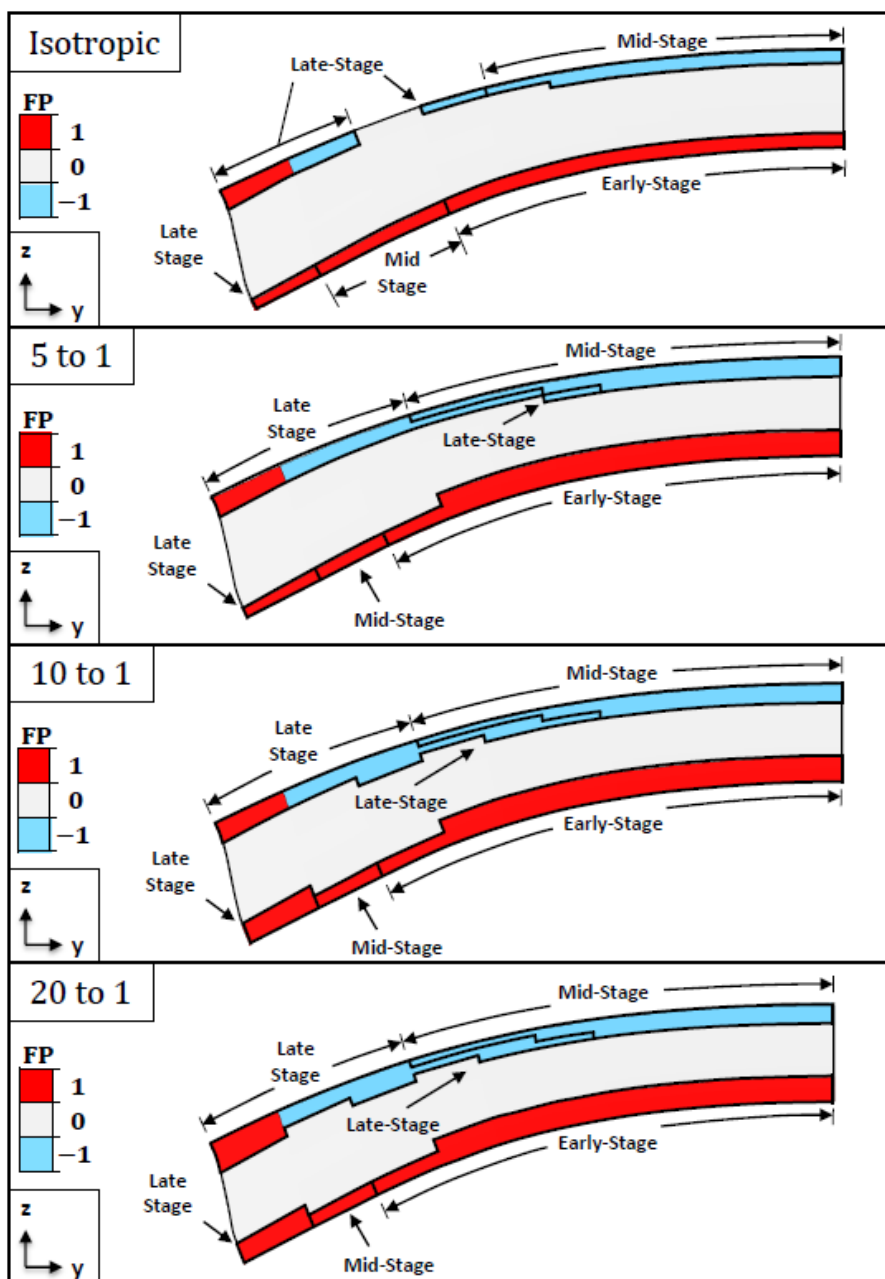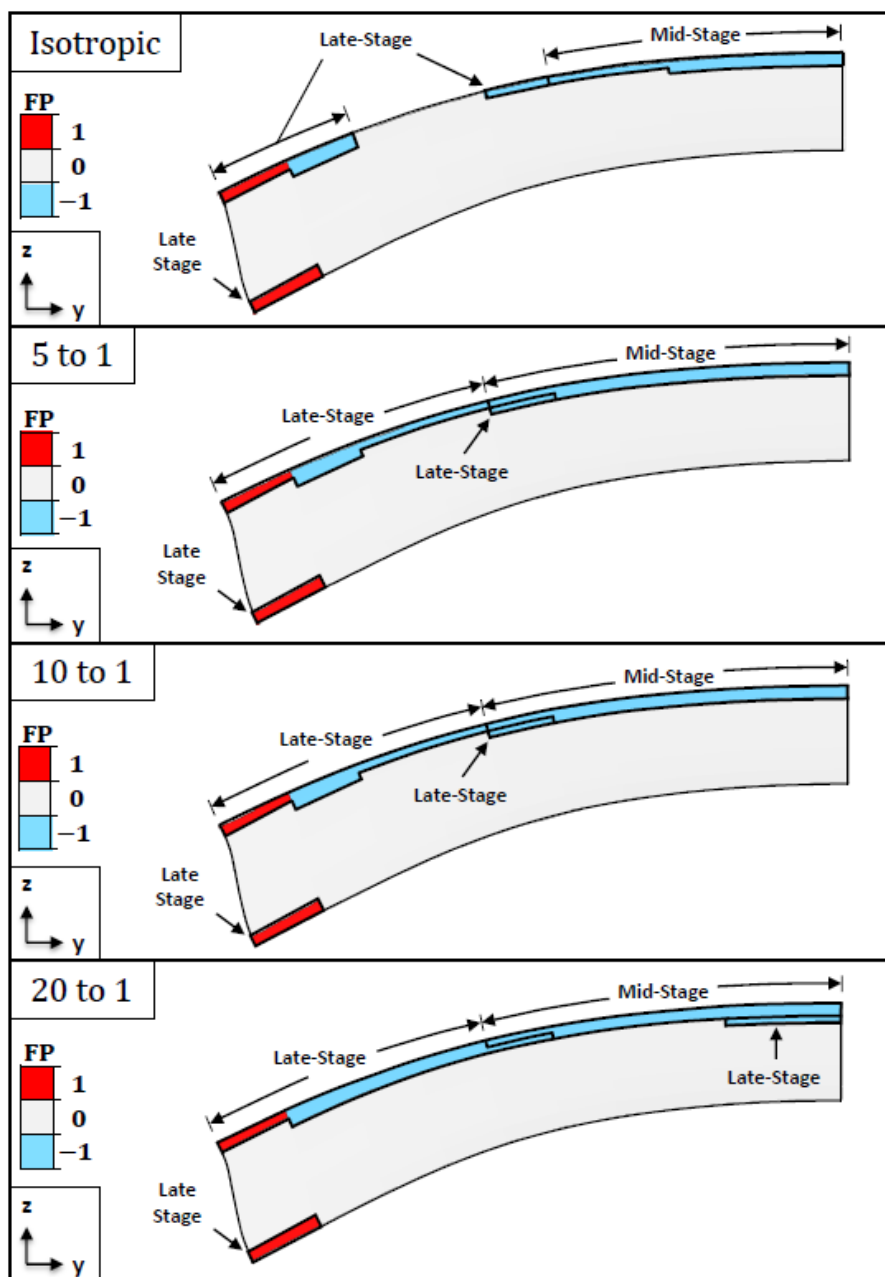
Figure C.2. Fracture potential results in the hinge for a low permeability (10^{-21} m^2) intermediate strength rock, with varying degrees of permeability anisotropy. The final fold shape is approximately the same for each model.

Figure C.3. Fracture potential results in the hinge for a low permeability (10^{-21} m^2) strong rock, with varying degrees of permeability anisotropy. The final fold shape is approximately the same for each model.
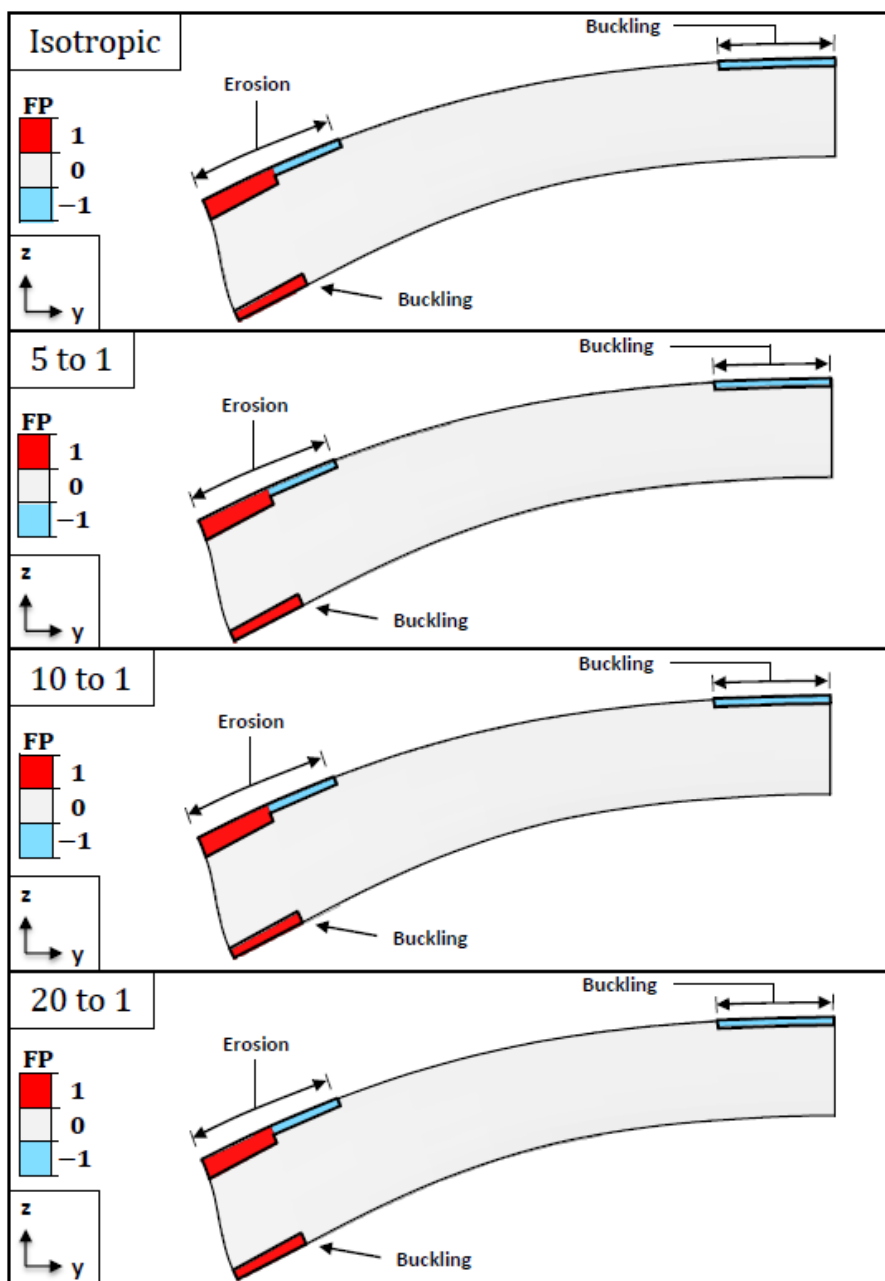
Figure C.4. Fracture potential results in the hinge for a high permeability (10^{-15} m^2) intermediate strength rock, with varying degrees of permeability anisotropy, after erosional unloading. The final fold shape is approximately the same for each model.
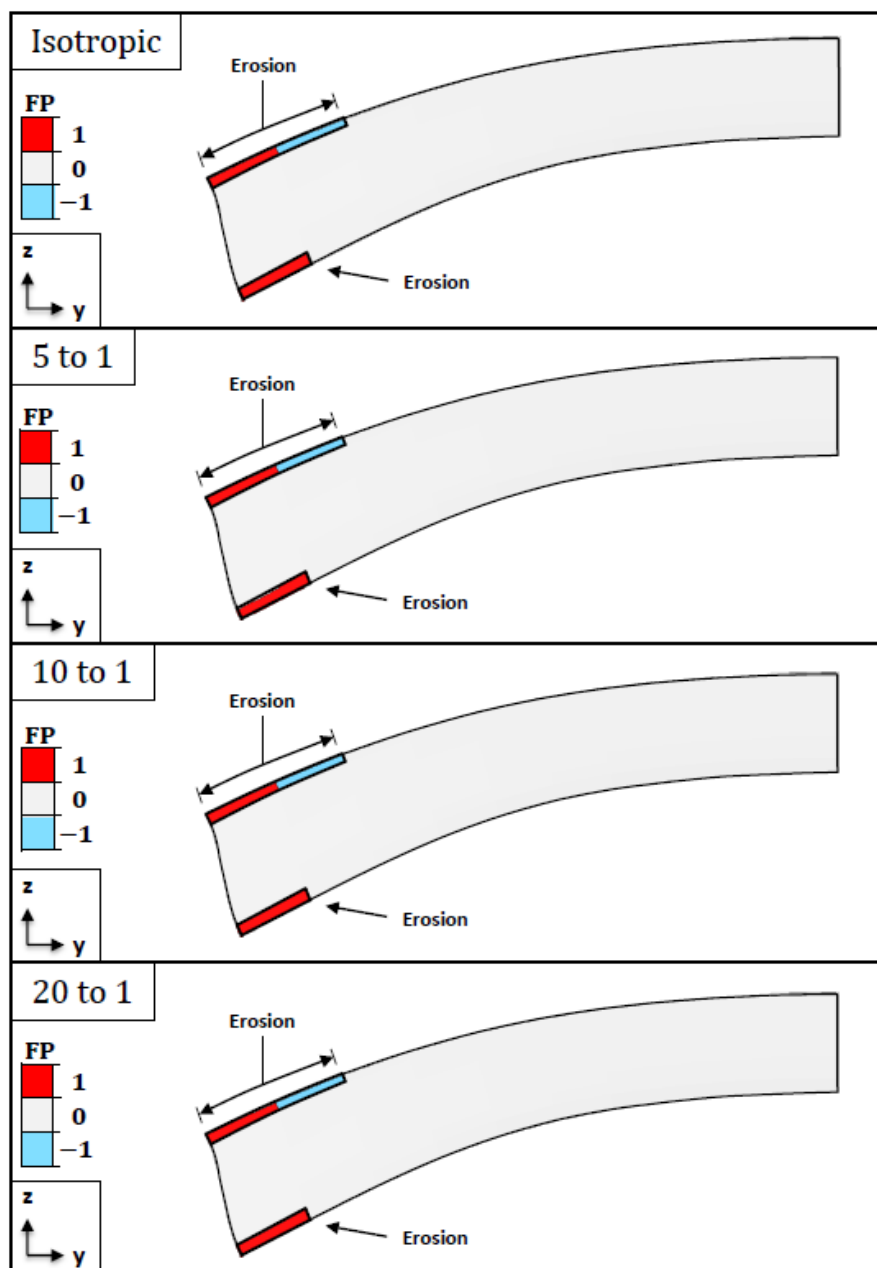
Figure C.5. Fracture potential results in the hinge for a high permeability (10^{-15} m^2) strong rock, with varying degrees of permeability anisotropy, after erosional unloading. The final fold shape is approximately the same for each model.

APPENDIX D

ADDITIONAL FRACTURE POTENTIAL RESULTS FOR VISCOSITY CONTRAST
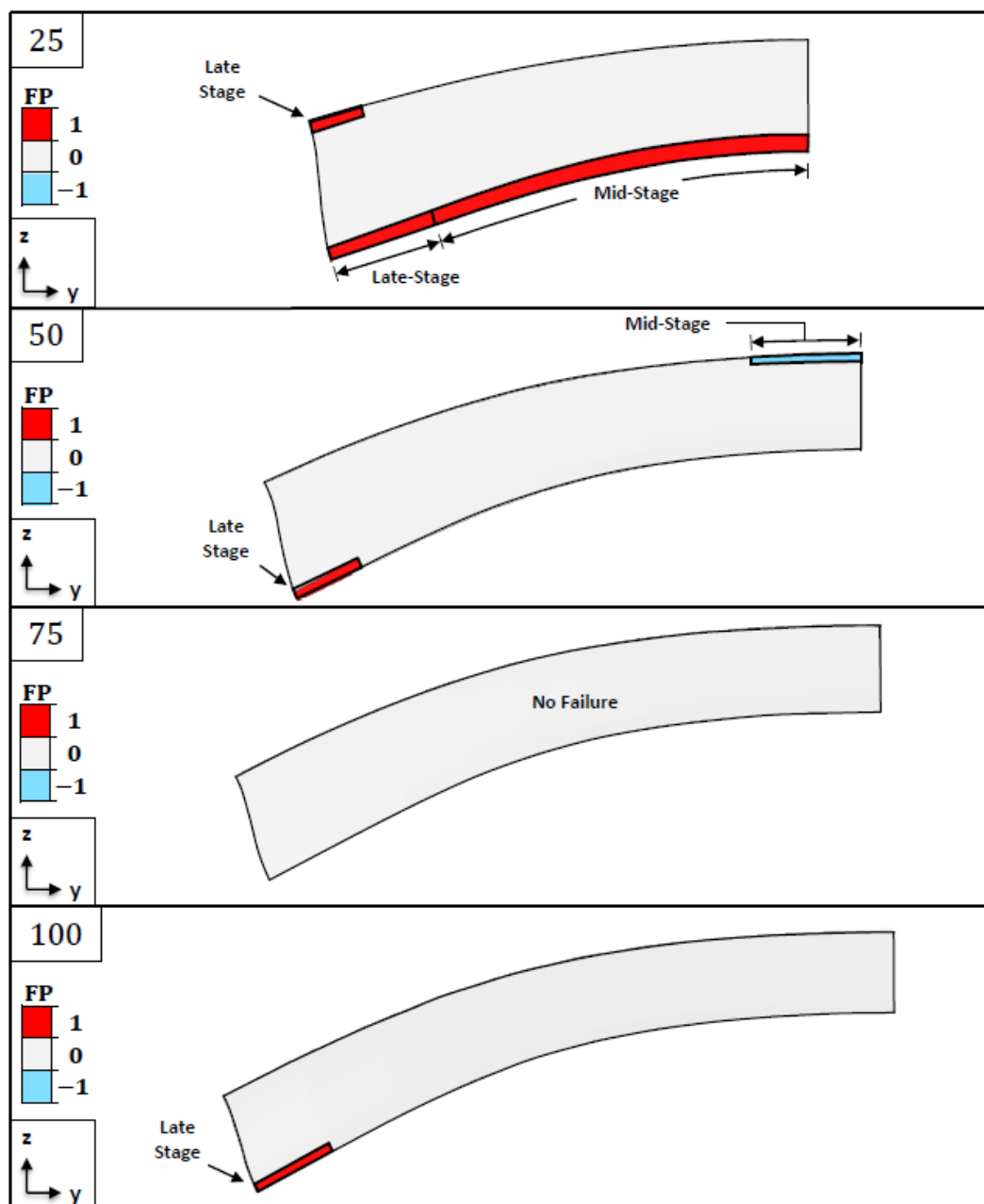
ANALYSIS

Figure D.1. Fracture potential results in the hinge for an intermediate strength rock with varying values of R_μ. Increasing the viscosity contrast will result in folds with larger wavelengths and hinge lengths, higher amplitudes, thinner folding layers, and steeper limb dips

Figure D.2. Fracture potential results in the hinge for a strong rock with varying values of R_μ. Increasing the viscosity contrast will result in folds with larger wavelengths and hinge lengths, higher amplitudes, thinner folding layers, and steeper limb dips
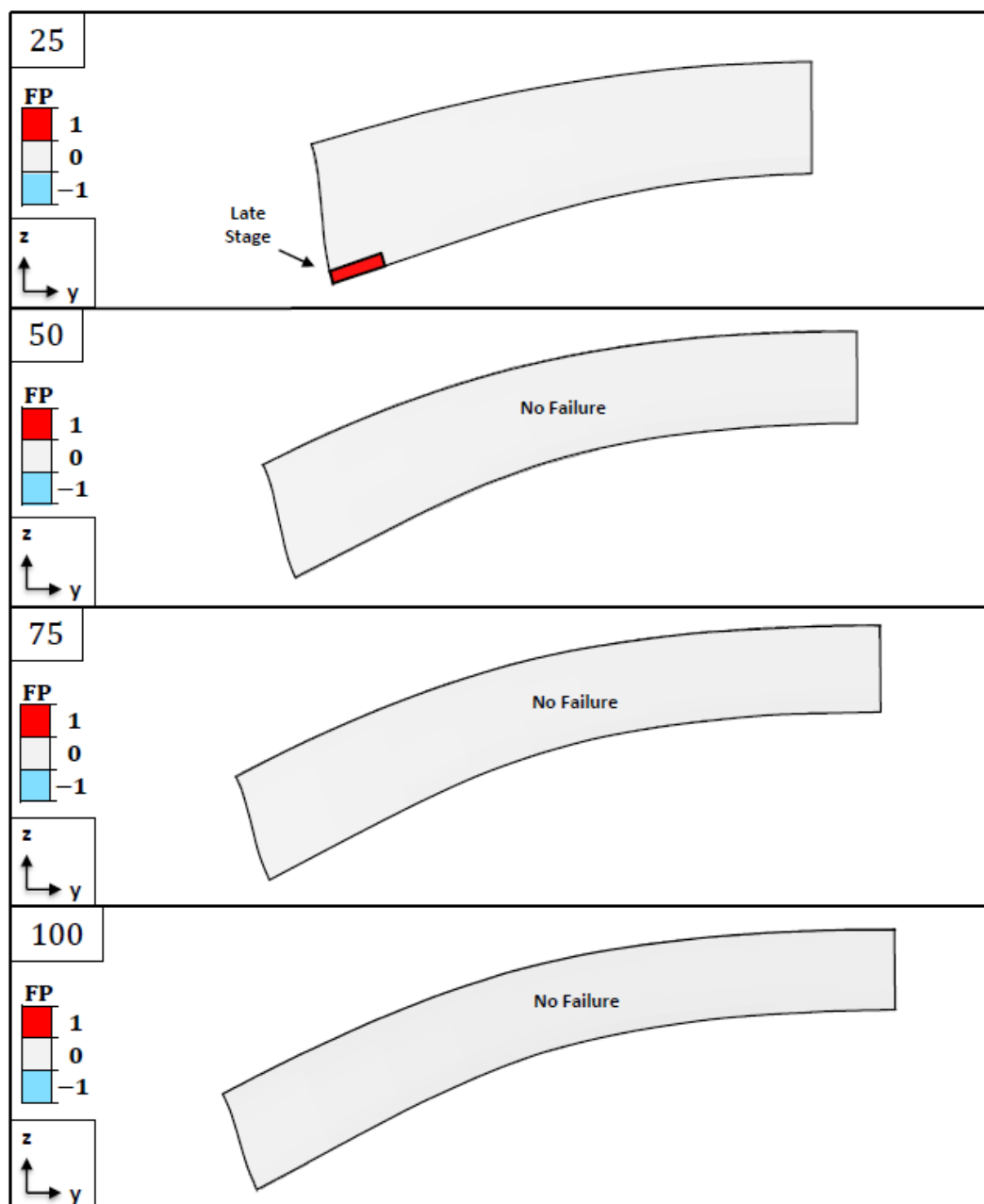
APPENDIX E

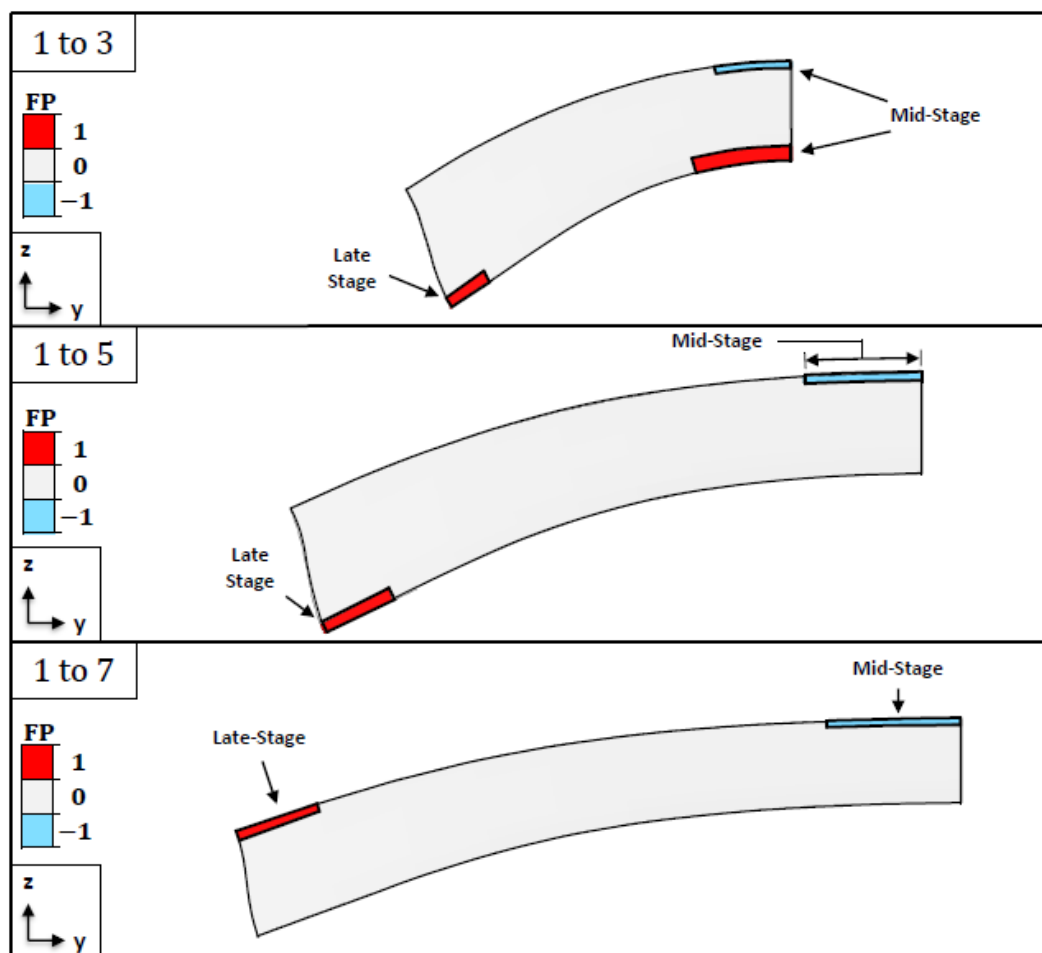ADDITIONAL FRACTURE POTENTIAL RESULTS FOR PERICLINE ASPECT

RATIO ANALYSIS

Figure E.1. Fracture potential results in the hinge for an intermediate strength rock with varying final aspect ratios. Increasing the aspect ratio will result in folds with longer hinge lengths.

Figure E.2. Fracture potential results in the hinge for an intermediate strength rock, with varying final aspect ratios, after erosional unloading. Differences in the final fold shape are a result of the different aspect ratios considered and not due to erosional unloading.
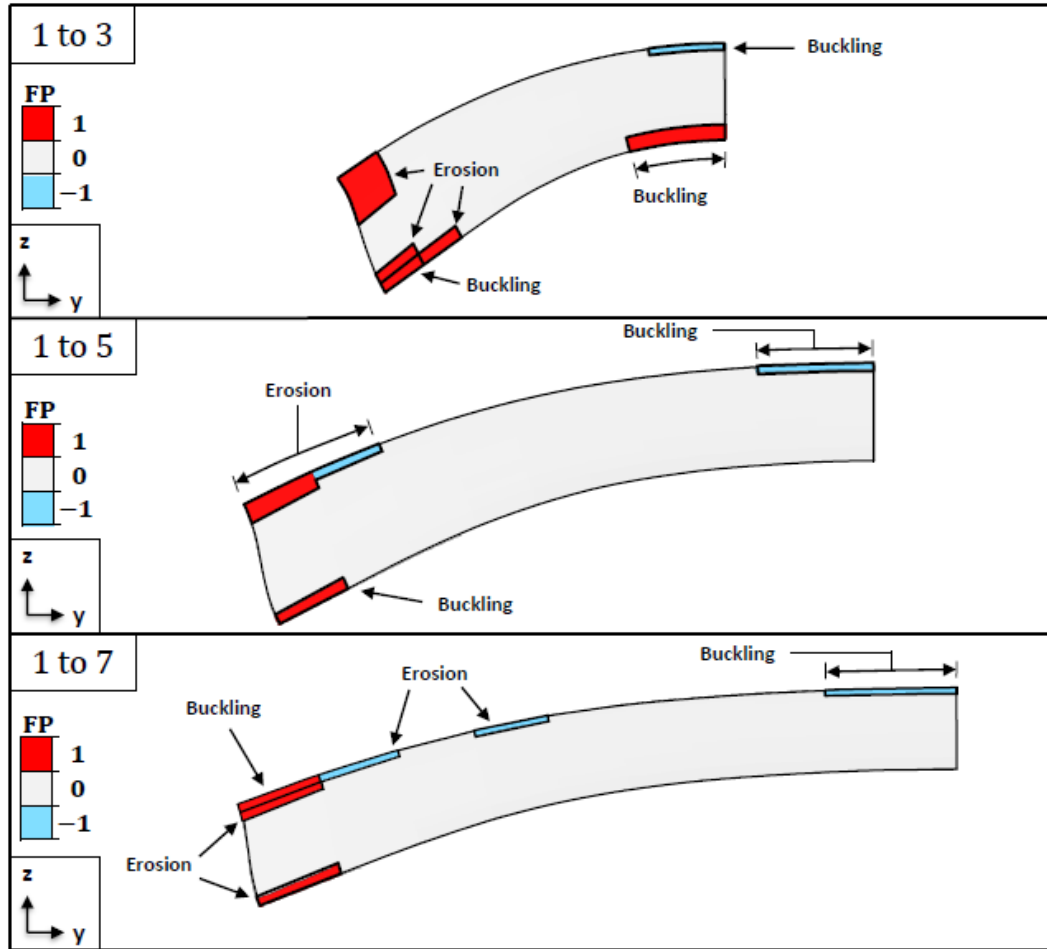
Figure E.3. Fracture potential results in the limb for an intermediate strength rock, with varying final aspect ratios, after erosional unloading. Differences in the final fold shape are a result of the different aspect ratios considered and not due to erosional unloading.

Figure E.4. Fracture potential results in the hinge for a strong rock, with varying final aspect ratios, after erosional unloading. Differences in the final fold shape are a result of the different aspect ratios considered and not due to erosional unloading.
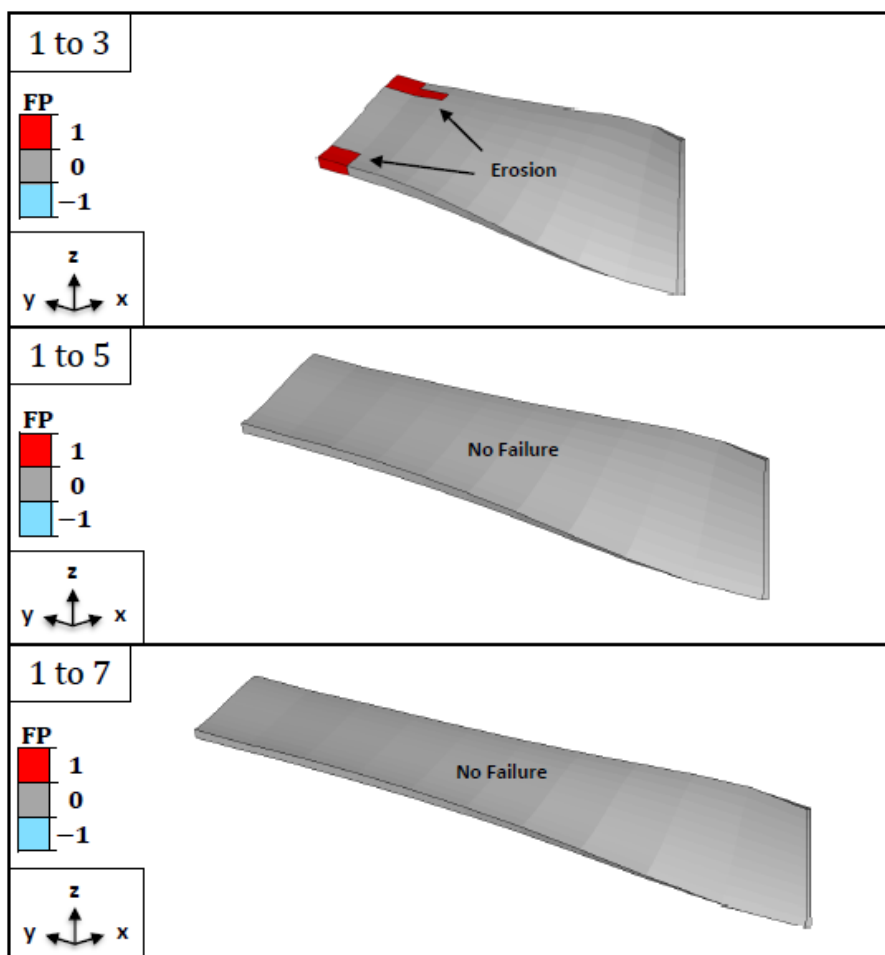
APPENDIX F

ADDITIONAL FRACTURE POTENTIAL RESULTS FOR SHORTENING

PERCENTAGE ANALYSIS

Figure F.1. Fracture potential results in the hinge for an intermediate strength rock with varying amounts of lateral shortening. Increasing the shortening percentage will result in folds with smaller wavelengths and hinge lengths, higher amplitudes, thicker folding layers, and steeper limb dips.

Figure F.2. Fracture potential results in the hinge for an intermediate strength rock, with varying amounts of lateral shortening, after erosional unloading. Differences in the final fold shape are a result of the differences in lateral shortening percentage and not due to erosional unloading.
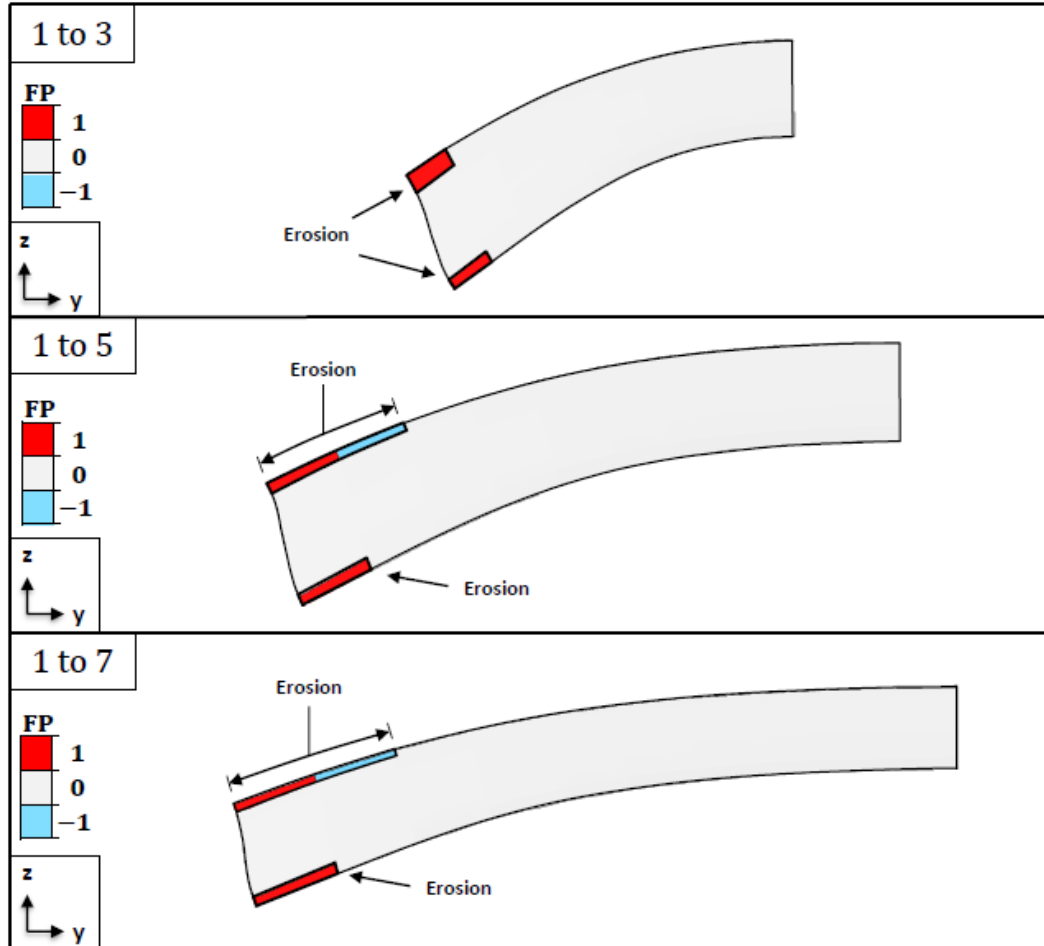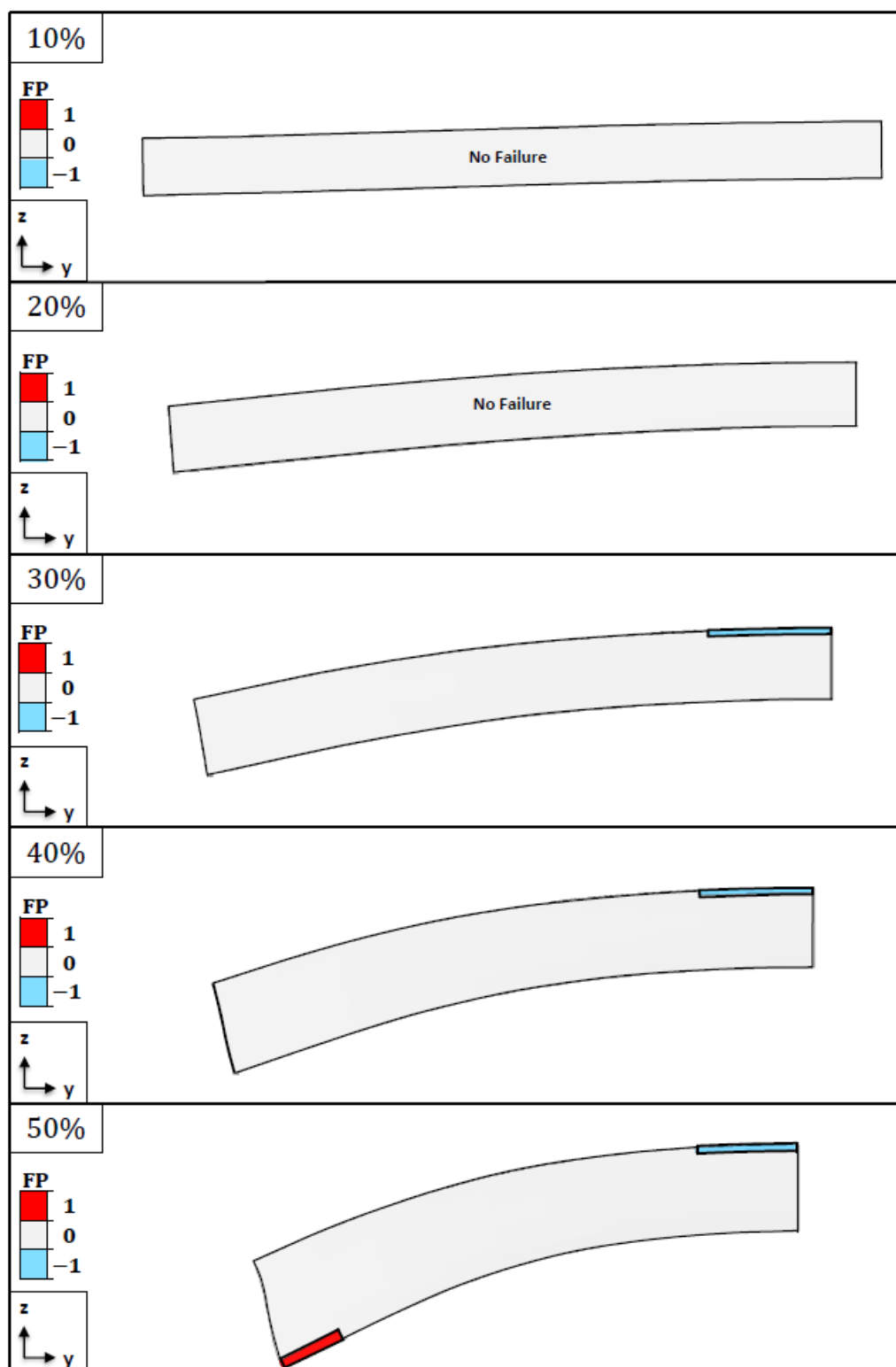
Figure F.3. Fracture potential results in the hinge for a strong rock, with varying amounts of lateral shortening, after erosional unloading. Differences in the final fold shape are a result of the differences in lateral shortening percentage and not due to erosional unloading.

APPENDIX G

ADDITIONAL FRACTURE POTENTIAL RESULTS FOR OVERBURDEN

PRESSURE ANALYSIS

Figure G.1. Fracture potential results in the hinge for an intermediate strength rock with varying amounts of overburden thickness. The final fold shape is approximately the same for each model.

Figure G.2. Fracture potential results in the hinge for an intermediate strength rock, with varying amounts of overburden thickness, after erosional unloading. The final fold shape is approximately the same for each model.
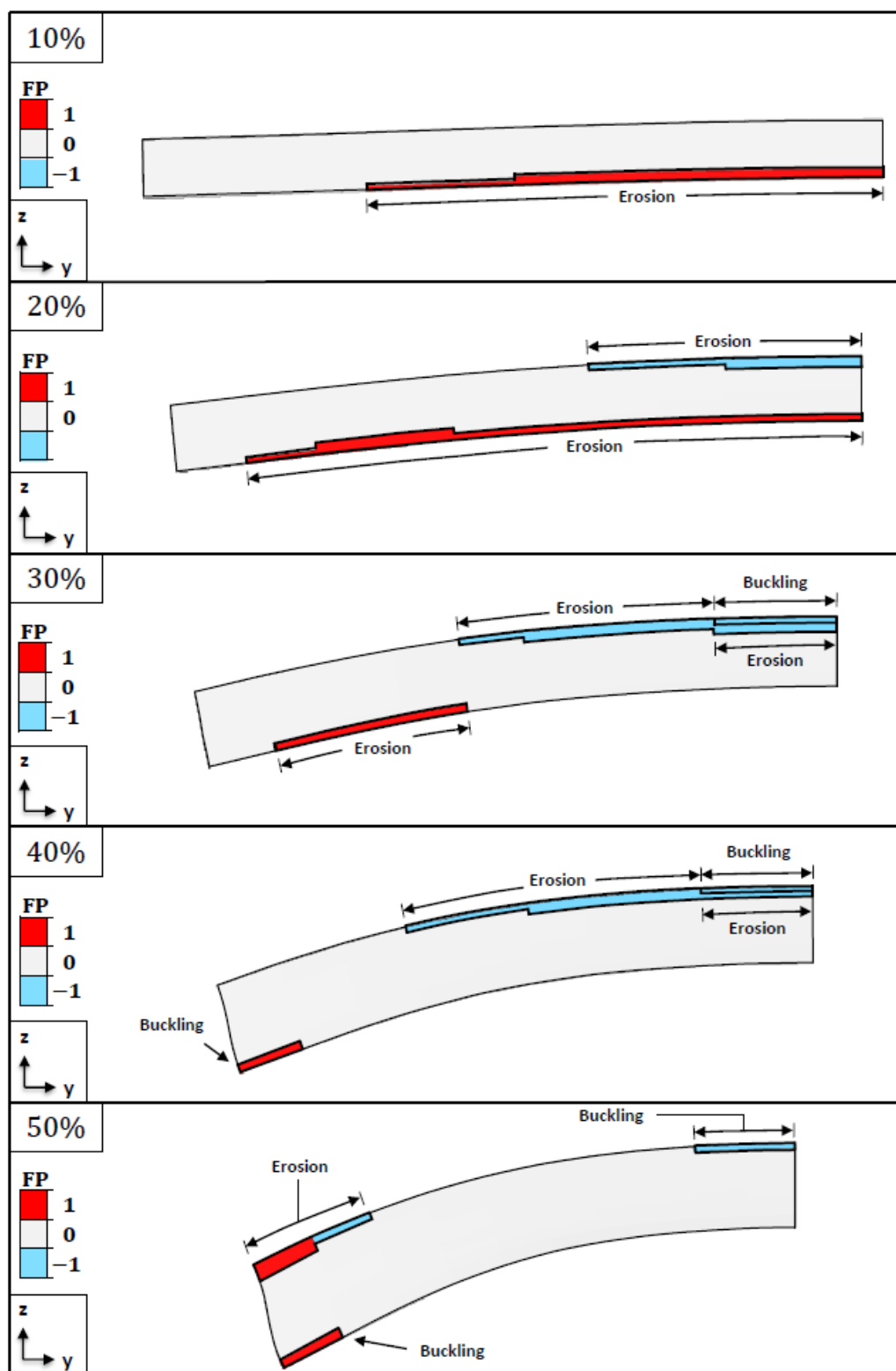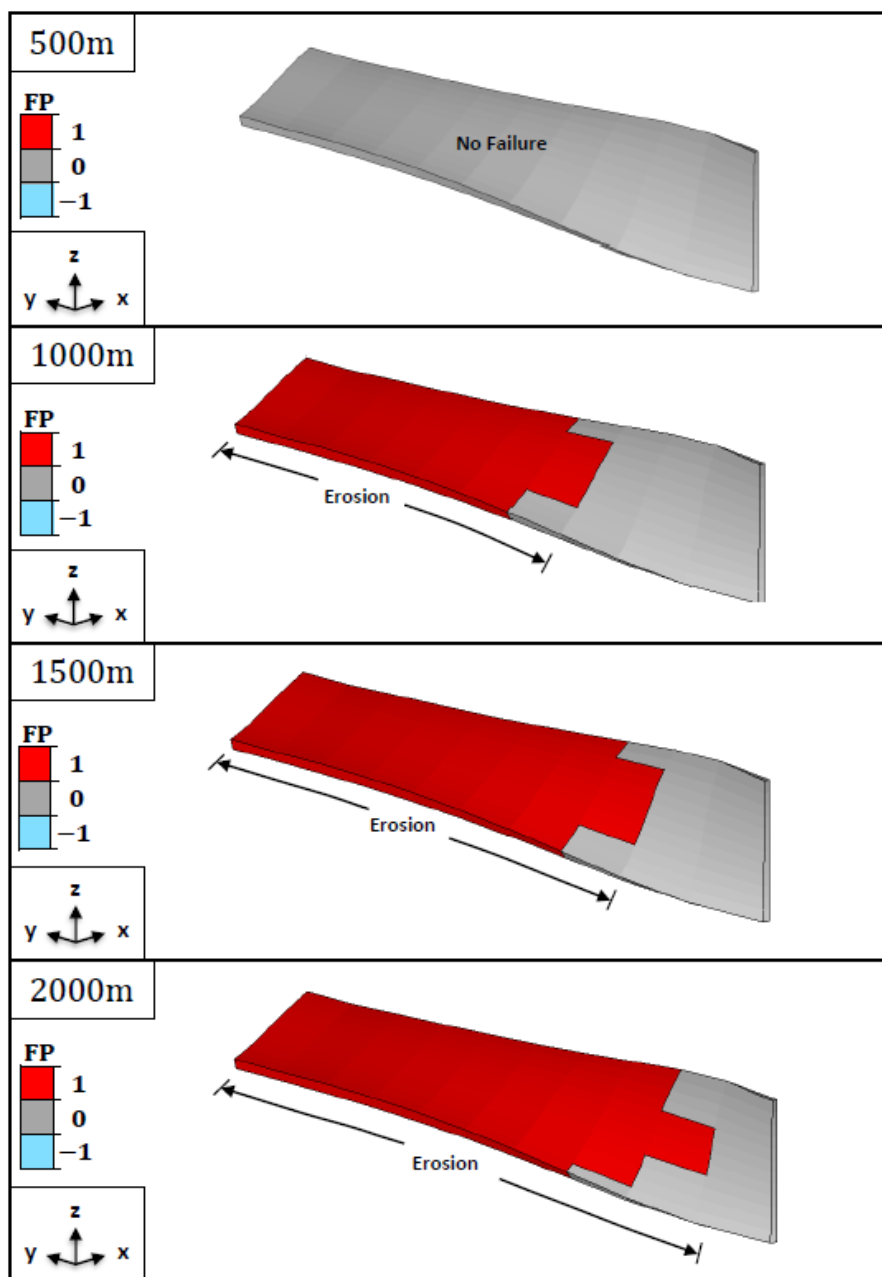
Figure G.3. Fracture potential results in the hinge for an intermediate strength rock, with varying amounts of overburden thickness, after erosional unloading. The final fold shape is approximately the same for each model.

Figure G.4. Fracture potential results in the hinge for a strong rock, with varying amounts of overburden thickness, after erosional unloading. The final fold shape is approximately the same for each model.
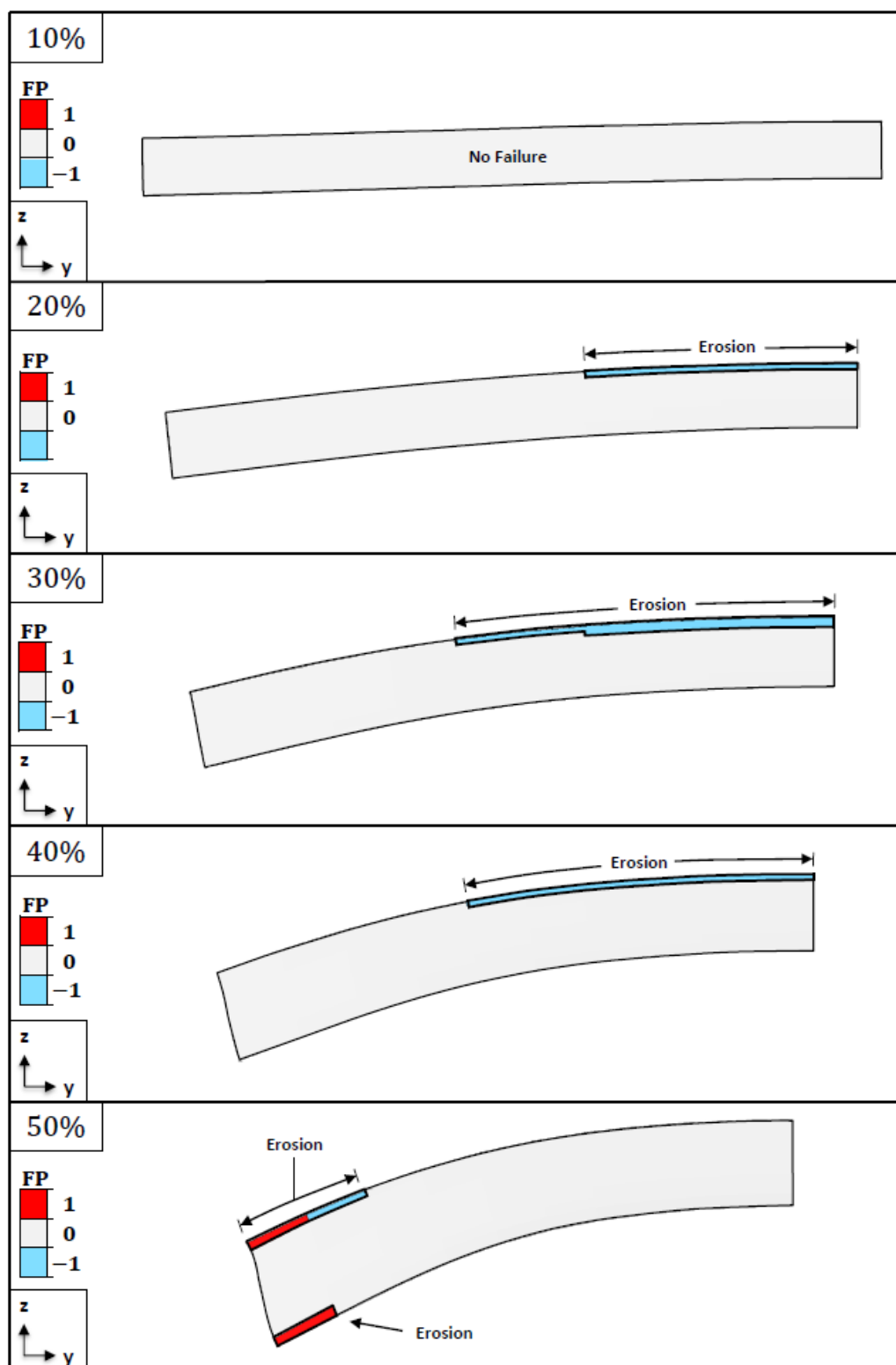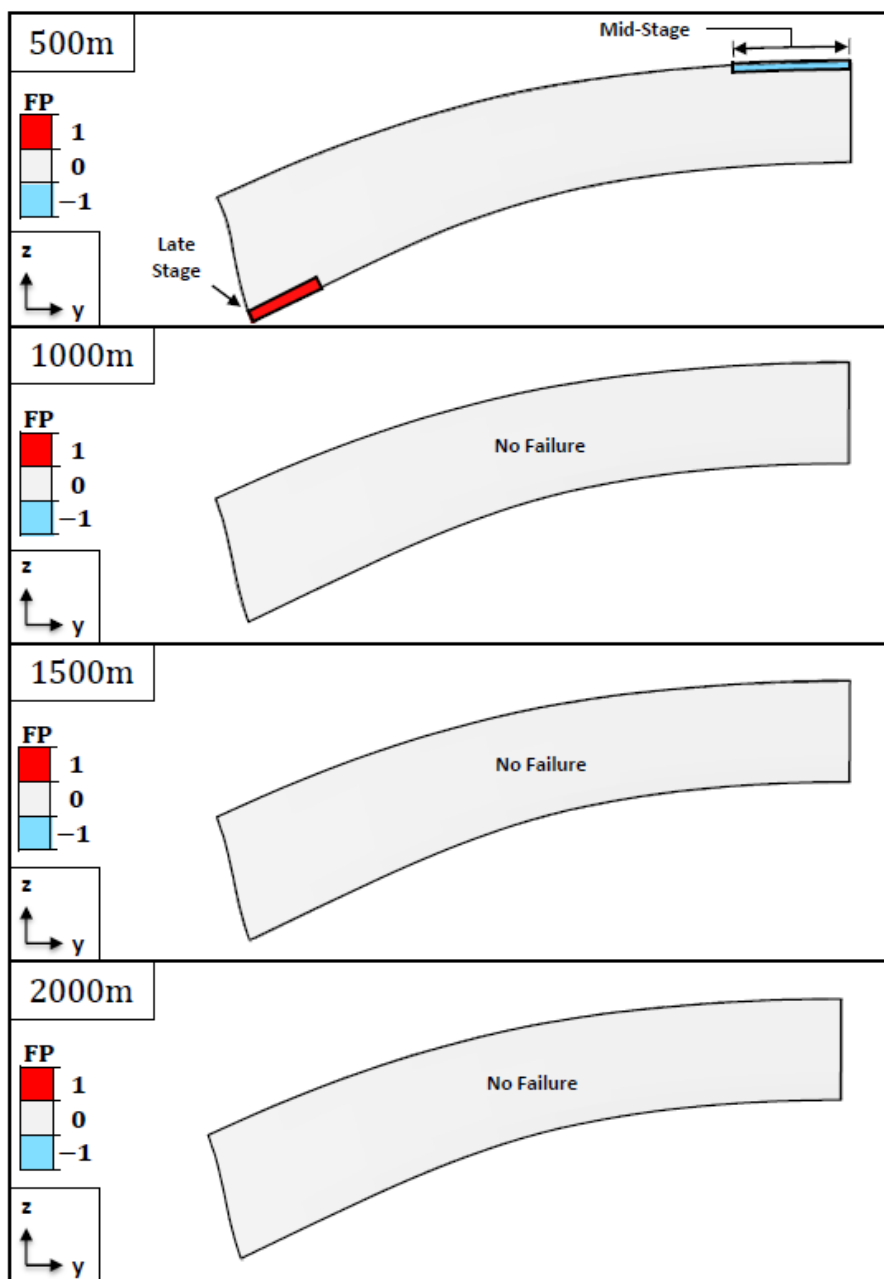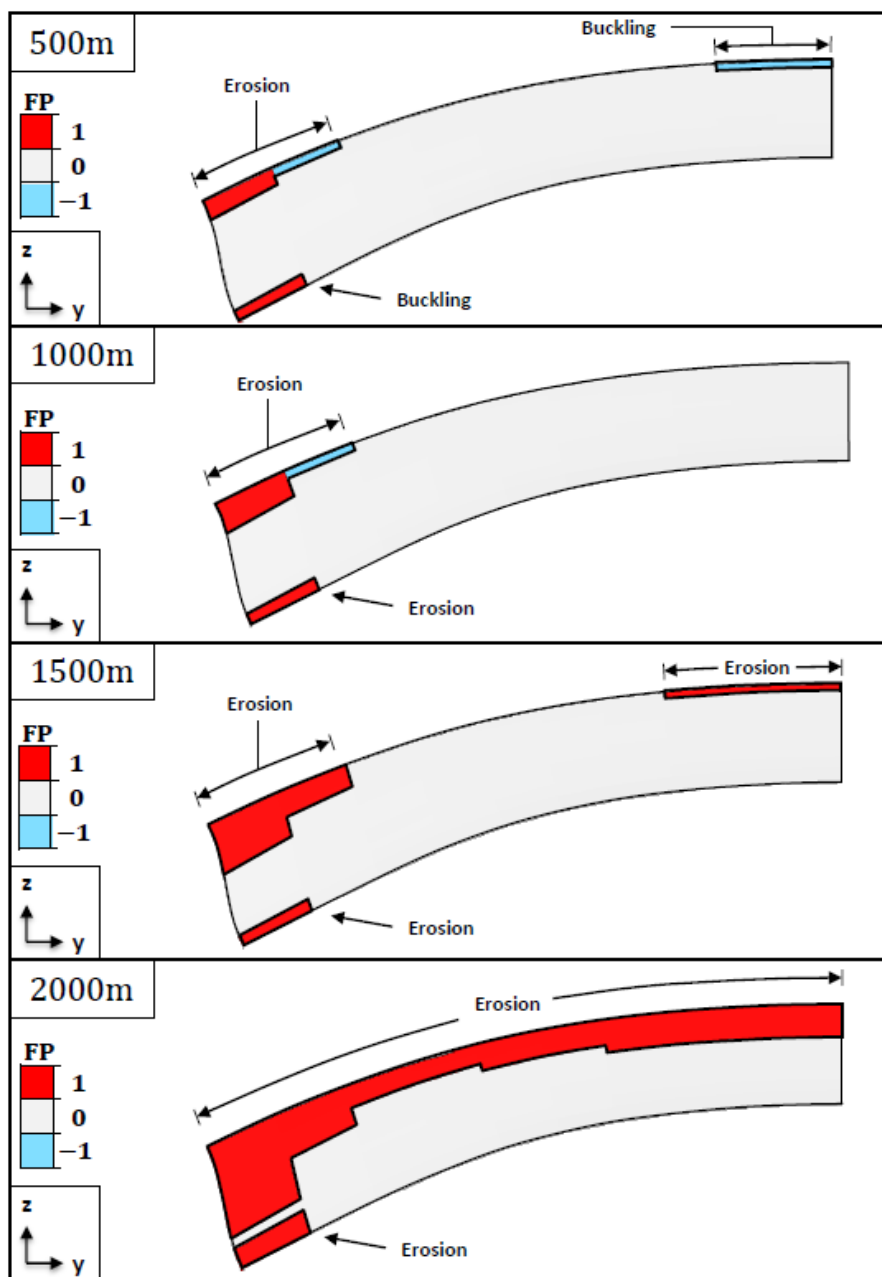
Figure G.5. Fracture potential results in the hinge for a strong rock, with varying amounts of overburden thickness, after erosional unloading. The final fold shape is approximately the same for each model.
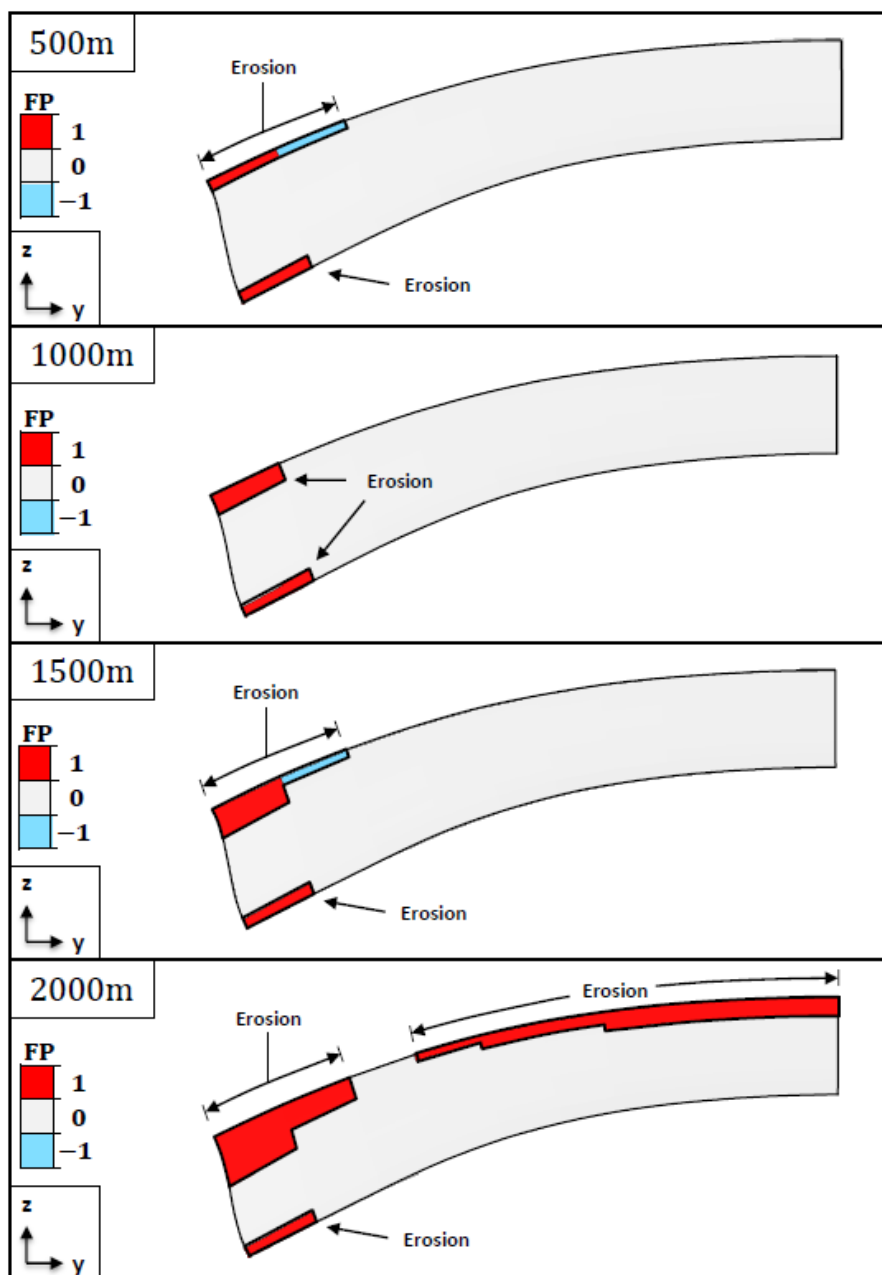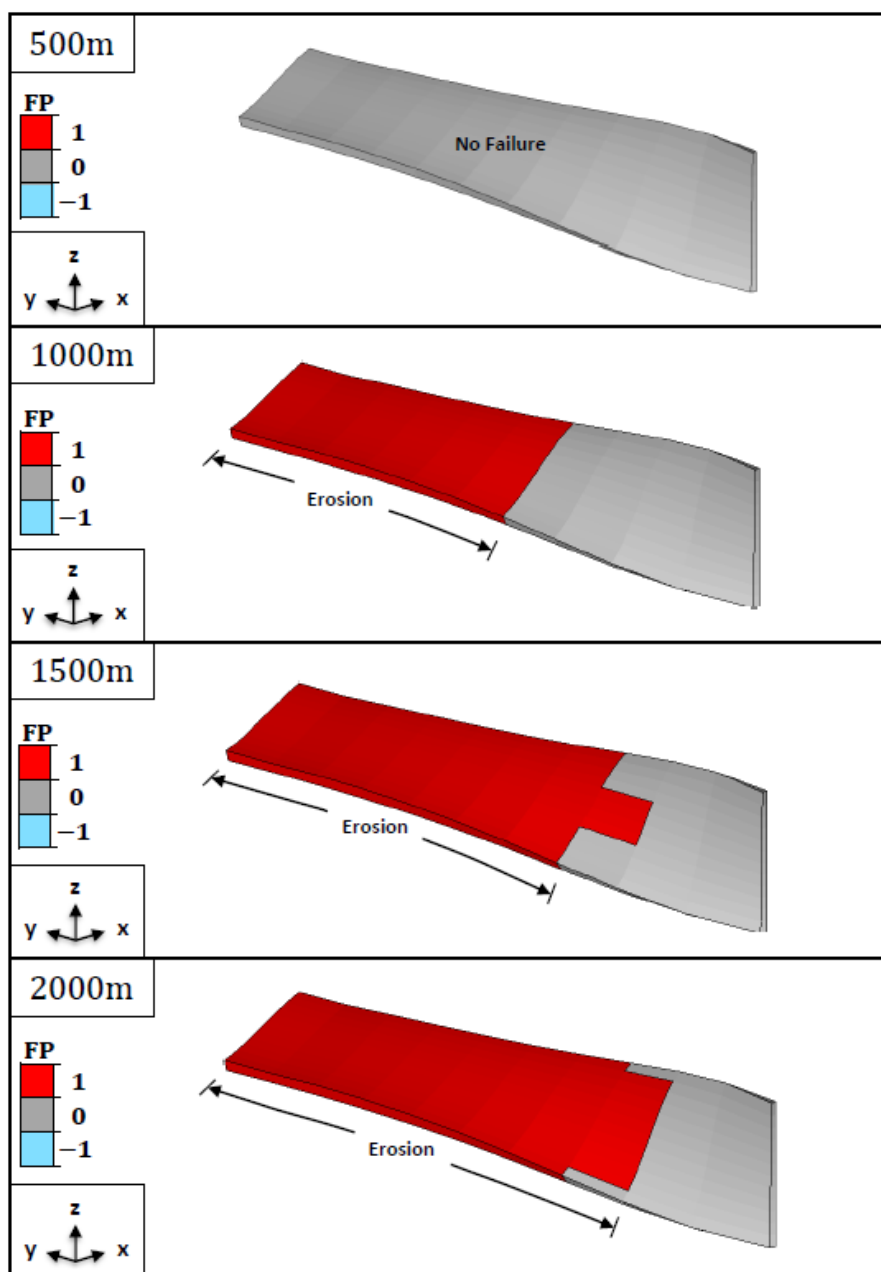
BIBLIOGRAPHY

Abaqus (2014) *ABAQUS Documentation*. Dassault Systèmes, Providence, RI, USA.

Al-Mahmoud, A. J., M. H. Khalil, and A. R. Moustafa (2009) The Jinadriyah anticlines: a surface model for oil fields in eastern Saudi Arabia. *Arabian Journal of Geosciences, 2*(3), 213-234.

Ameen, M. S. (1990) Macrofaulting in the Purbeck-Isle of Wight monocline. *Proceedings of the Geologists' Association, 101*(1), 31-46.

Barton, C. A. and M. D. Zoback (2002) Discrimination of natural fractures from drilling-induced wellbore failures in wellbore image data – Implications for reservoir permeability. *Society of Petroleum Engineering Reservoir Evaluation and Engineering, 5*(3), 249-254.

Bellahsen, N., P. Fiore, and D. D. Pollard (2006) The role of fractures in the structural interpretation of Sheep Mountain Anticline, Wyoming. *Journal of Structural Geology*, *28*(5), p. 850-867.

Bergbauer, S. and D. D. Pollard (2004) A new conceptual fold-fracture model including prefolding joints, based on field data from the Emigrant Gap anticline, Wyoming. *Geological Society of America Bulletin, 116*(3-4), 294-307.

Bieniawski, Z. T. (1984) *Rock Mechanics Design in Mining and Tunneling*. Balkema, Boston.

Biot, M. A. (1957) Folding instability of a layered viscoelastic medium under compression. In *Proceedings of the Royal Society of London A: Mathematical, Physical and Engineering Sciences, 242*(1231), 444-454.

Biot, M. A. (1959) On the instability of folding deformation of a layered viscoelastic medium in compression. *J. appl. Mech.*, 26, 393-400.

Biot, M. A. (1961) Theory of folding of stratified viscoelastic media and its implications in tectonics and orogenisis. *Geol. Soc. Am. Bull., 72*(11), 1595-1620.

Blanc, E. J. P., M. B. Allen, S. Inger, and H. Hassani (2003) Structural styles in the Zagros Simple Folded Zone, Iran. *Journal of the Geological Society, London, 160*(3), 401-412.

Blay, P., J. W. Cosgrove, and J. M. Summers (1977) An experimental investigation of the development of structures in multilayers under the influence of gravity. *J. Geol. Soc. Lond., 133*(4), 329-342.

Buchmann, T. J. and P. T. Connolly (2007) Contemporary kinematics of the Upper Rhine Graben: a 3D finite element approach. *Global and Planetary Change, 58*(1), 287-309.

Burbank, D. W. (2002) Rates of erosion and their implications for exhumation. *Mineralogical Magazine, 66*(1), 25-52.

Casciello, E., J. Vergés, E. Saura, G. Casini, N. Fernández, E. Blanc, S. Homke, and D. W. Hunt (2009) Fold patterns and multilayer rheology of the Lurestan Province, Zagros Simply Folded Belt (Iran). *Journal of the Geological Society, 166*(5), 947-959.

Chapman, R. E. (2000) *Petroleum Geology*. (Vol. 16). Elsevier.

Cloos, E. (1955) Experimental analysis of fracture patterns. *Geological Society of America Bulletin, 66*(3), 241-256.

Cooper, S. P., L. B. Goodwin, and J. C. Lorenz (2006) Fracture and fault patterns associated with basement-cored anticlines: The example of Teapot Dome, Wyoming. *AAPG Bull., 90*(12), 1903-1920.

Colman-Sadd, S. P. (1978) Fold development in Zagros simply folded belt, SW Iran, *American Association of Petroleum Geologists Bulletin, 62*(6), 984-1003.

Connolly, P. and J. Cosgrove (1999) Prediction of fracture-induced permeability and fluid flow in the crust using experimental stress data. *AAPG bulletin, 83*(5), 757-777.

Cosgrove, J. W. and M. S. Ameen (1999) A comparison of the geometry, spatial organization and fracture patterns associated with forced folds and buckle folds. *Geological Society, London, Special Publications, 169*(1), 7-21.

Davis, G. H., S. J. Reynolds, and C. F. Kluth (2012) *Structural Geology Of Rocks And Regions*. 3rd Edition. John Wiley and Sons, New York.

Dieterich, J. H. and N. L. Carter (1969) Stress-history of folding. *American Journal of Science, 267*(2), 129-154.

Dieterich, J.H. (1970) Computer experiments on mechanics of finite amplitude folds. *Canadian Jour. Earth Sci., 7*(2), 467-476.

Dietrich, R. V. and B. J. Skinner (1979) *Rocks and Rock Minerals*. John Wiley & Sons.

Dixon, J. M. and R. Turril (1991) Centrifuge modelling of fold-thrust structures in a tripartite stratigraphic succession. *J. Struct. Geol., 13*(1), 3-20.

Dubey, A. K. and P. R. Cobbold (1977) Noncylindrical flexural slip folds in nature and experiment. *Tectonophysics, 38*(3), 223-239.

Dyksterhuis, S., R. A. Albert, and R. D. Müller (2005) Finite-element modelling of contemporary and palaeo-intraplate stress using ABAQUS™. *Computers & Geosciences, 31*(3), 297-307.

Eckert, A. and P. Connolly (2004) 2D finite element modelling of regional and local fracture networks in the Eastern California Shear Zone and Coso Range, California USA. *GRC Transactions*, 28, 643-648.

Eckert, A., P. Connolly, and X. Liu (2014) Large-scale mechanical buckle fold development and the initiation of tensile fractures. *Geochem. Geophys. Geosyst., 15*(11), 4570-4587.

Eckert, A. and X. Liu (2014) An improved method for numerically modeling the minimum horizontal stress magnitude in extensional stress regimes. *International Journal of Rock Mechanics and Mining Sciences*, 70, 581-592.

Eckert, A., X. Liu, and P. Connolly (2015) Pore pressure evolution and fluid flow during visco-elastic single-layer buckle folding. *Geofluids*, doi: 10.1111/gfl.12145.

Engelder, T., M. R. Gross, and P. Pinkerton (1997) An analysis of joint development in thick sandstone beds of the Elk Basin Anticline, Montana-Wyoming. *Fractured Reservoirs: Characterization and Modeling: Rocky Mountain Association of Geologists Guidebook*, 1-18.

Far, M. E., C. M. Sayers, L. Thomsen, D. Han, and J. P. Castagna (2013) Seismic characterization of naturally fractured reservoirs using amplitude versus offset and azimuth analysis. *Geophysical Prospecting, 61*(2), 427-447.

Fischer, M. P. and M. S. Wilkerson (2000) Predicting the orientation of joints from fold shape: Results of pseudo-three-dimensional modeling and curvature analysis. *Geology, 28*(1), 15-18.

Fjar, E., R. M. Holt, A. M. Raaen, R. Risnes, and P. Horsrud (2008) *Petroleum Related Rock Mechanics*. (Vol. 53). Elsevier.

Fletcher, R.C. (1991) Three-dimensional folding of an embedded viscous layer in pure shear. *Journal of Structural Geology, 13*(1), 87-96.

Fletcher, R. C. (1995) 3-Dimensional folding and necking of a power-law layer: are folds cylindrical, and, if so, do we understand why? *Tectonophysics, 247*(1-4), 65-83.

Fossen, H. (2010) *Structural Geology*. Cambridge University Press.

Frehner, M. (2011) The neutral lines in buckle folds. *Journal of Structural Geology, 33*(10), 1501-1508.

Ghosh, S. K. and H. Ramberg (1968) Buckling experiments on intersecting fold patterns. *Tectonophysics, 5*(2), 89-105.

Ghosh, S. K. (1970) A theoretical study of intersecting fold patterns. *Tectonophysics, 9*(6), 559-569.

Ghosh, S. K., D. Khan, and S. Sengupta (1995) Interfering folds in constrictional deformation. *Journal of Structural Geology, 17*(10), 1361-1373.

Grasemann, B., G. Wiesmayr, E. Draganits, and F. Fusseis (2004) Classification of refold structures. *The Journal of Geology, 112*(1), 119-125.

Gray, D., S. Boerner, D. Todorovic-Maranic, and Y. Zheng (2003) Fractured Reservoir Characterization using AVAZ on the Pinedale Anticline. *CSEG Recorder, 28*(6), 40-46.

Griffith, A. A. (1997) The theory of rupture. *1st Int. Cong. Appl. Mech. Proc. Delft.*, 55-63.

Grujic, D. (1993) The influence of initial fold geometry on Type-1 and type-2 interference patterns – an experimental approach. *Journal of Structural Geology, 15*(3-5), 293-307.

Guterman, V.G. (1980) Model studies of gravitational gliding tectonics. *Tectonophysics, 65*(1), 111-126.

Hancock, P. L. (1985) Brittle microtectonics: principles and practice. *Journal of Structural Geology, 7*(3), 437-457.

Hennings, P. H. and J. E. Olson (1997) The relationship between bed curvature and fracture occurrence in a fault-propagation fold. In *Annual Meeting Abstracts-American Association of Petroleum Geologists Annual Convention. American Association of Petroleum Geologists and Society of Economic Paleontologists.*

Hudleston, P. J., S. H. Treagus, and L. Lan (1996) Flexural flow folding: Does it occur in nature? *Geology, 24*(3), 203-206.

Jaeger, J. C., N. G. Cook, and R. Zimmerman (2009) *Fundamentals of Rock Mechanics*. John Wiley & Sons.

Johns, M. K. and S. Mosher (1996) Physical models of regional fold superposition: the role of competence contrast. *Journal of Structural Geology, 18*(4), 475-492.

Kaus, B. J. P. and S. M. Schmalholz (2006) 3D finite amplitude folding: implications for stress evolution during crustal and lithospheric deformation. *Geophysical Research Letters, 33*(14).

Lacombe, O., N. Bellahsen, and F. Mouthereau (2011) Fracture patterns in the Zagros Simply Folded Belt (Fars, Iran): constraints on early collisional tectonic history and role of basement faults. *Geological Magazine, 148*(5-6), 940-963.

Lan, L. and P. J. Hudleston (1995) The effects of rheology on the strain distribution in single layer buckle folds. *Journal of Structural Geology, 17*(5), 727-738.

Lemiszki, P. J., J. D. Landes, and R. D. Hatcher (1994) Controls on hinge–parallel extension fracturing in single–layer tangential‐longitudinal strain folds. *Journal of Geophysical Research: Solid Earth (1978–2012), 99*(B11), 22027-22041.

Lisle, R. J. (1994) Detection of zones of abnormal strains in structures using Gaussian curvature analysis. *AAPG Bull., 78*(12), 1811-1819.

Lisle, R. J. and N. C. Toimil (2007) Defining folds on three-dimensional surfaces. *Geology, 35*(6), 519-522.

Lisle, R. J., J. Aller, F. Bastida, N. C. Bobillo-Ares, and N. C. Toimil (2009) Volumetric strains in neutral surface folding. *Terra Nova, 21*(1), 14-20.

Mancktelow, N. S. (1999) Finite-element modelling of single-layer folding in elasto-viscous materials: the effect of initial perturbation geometry. *Journal of Structural Geology, 21*(2), 161-177.

Marshak, S., P. A. Geiser, W. Alvarez, and T. Engelder (1982) Mesoscopic fault array of the northern Umbrian Apennine fold belt, Italy: Geometry of conjugate shear by pressure-solution slip. *Geological Society of America Bulletin, 93*(10), 1013-1022.

McClintock, F. A. and J. B. Walsh (1962) Friction on Griffith cracks in rocks under pressure. In *Proc. 4th US Nat. Congr. Appl. Mech.*, 2, 1015-1022.

McQuillan, H. (1974) Fracture patterns on Kuh-e Asmari anticline, southwest Iran. *AAPG Bulletin, 58*(2), 236-246.

Medina, C. R., J. A. Rupp, and D. A. Barnes (2011) Effects of reduction in porosity and permeability with depth on storage capacity and injectivity in deep saline aquifers: A case study from the Mount Simon Sandstone aquifer. *International Journal of Greenhouse Gas Control, 5*(1), 146-156.

Mitani, Y., F. Wang, A. C. Okeke, and W. Qi (2013) Dynamic Analysis of Earthquake Amplification Effect of Slopes in Different Topographic and Geological Conditions by Using ABAQUS. In *Progress of Geo-Disaster Mitigation Technology in Asia*, 469-490.

Mitra, S. (2002) Fold-accommodation faults. *AAPG Bulletin, 86*(4), 671-694.

Morley, C. K. (2007) Development of crestal normal faults associated with deepwater fold growth. *Journal of Structural Geology, 29*(7), 1148-1163.

Muhlhaus, H. B., H. Sakaguchi, and B. E. Hobbs (1998) Evolution of three-dimensional folds for a non-Newtonian plate in a viscous medium. *Proceedings of the Royal Society of London Series A-Mathematical Physical and Engineering Sciences, 454*(1980), 3121-3143.

Mynatt, I., S. Bergbauer, and D. D. Pollard (2007) Using differential geometry to describe 3-D folds. *Journal of Structural Geology, 29*(7), 1256-1266.

Narahara, D. K. and D. V. Wiltschko (1986) Deformation in the hinge region of a chevron fold, Valley and Ridge Province, central Pennsylvania. *Journal of Structural Geology, 8*(2), 157-168.

Nelson, R.A. (2001) *Geologic Analysis of Naturally Fractured Reservoirs*. 2nd Edition. Gulf Publishing, Houston.

Odling, N. E., P. Gillespie, B. Bourgine, C. Castaing, J-P. Chilès, N. P. Christensen, E. Fillion, A. Genter, C. Olsen, L. Thrane, R. Trice, E. Aarseth, J. J. Walsh, and J. Watterson (1999) Variations in fracture system geometry and their implications for fluid flow in fractured hydrocarbon reservoirs. *Pet. Geosci.,* 5, 373-384.

Odonne, F. and P. Vialon (1987) Hinge migration as a mechanism of superimposed folding. *Journal of Structural Geology, 9*(7), 835-844.

Parrish, D. K. (1973) A nonlinear finite element fold model. *American Journal of Science, 273*(4), 318-334.

Pollard, D. D. & Fletcher, R. C. (2005) *Fundamentals of Structural Geology*. Cambridge University Press.

Price, N. J. and J. W. Cosgrove (1990) *Analysis of Geological Structures*. Cambridge Univ. Press, U.K.

Ragan, D. M. (1973) *Structural Geology: An Introduction to Geometrical Techniques*. Wiley, New York.

Ramberg, H. (1959) Evolution of ptygmatic folding. *Norsk geol. Tidsskr.,* *39*(9), 99-151.

Ramberg, H. (1961) Contact strain and folding instability of a multi-layered body under compression. *Geol. Rdsch., 51*(2), 405-439.

Ramberg, H. (1963) Fluid dynamics of viscous buckling applicable to folding of layered rocks. *Bulletin of the American Association of Petroleum Geologists, 47*(3), 484-505.

Ramsay, J. G. (1967) *Folding and Fracturing of Rocks*. McGraw Hill, New York.

Sanz, P. F., D. D. Pollard, P. F. Allwardt, and R. I. Borja (2008) Mechanical models of fracture reactivation and slip on bedding surfaces during folding of the asymmetric anticline at Sheep Mountain, Wyoming. *J. Struct. Geol., 30*(9), 1177-1191.

Schmalholz, S. M. and Y. Podladchikov (1999) Buckling versus folding: importance of viscoelasticity. *Geophysical Research Letters, 26*(17), 2641-2644.

Schmalholz, S. M., Y. Y. Podladchikov, and D. W. Schmid (2001) A spectral/finite difference method for simulating large deformations of heterogeneous, viscoelastic materials. *Geophysical Journal International, 145*(1), 199-208.

Schmalholz, S. M., Y. Y. Podladchikov, and J. P. Burg (2002) Control of folding by gravity and matrix thickness: Implications for large-scale folding. *Journal of Geophysical Research: Solid Earth (1978–2012), 107*(B1).

Schmalholz, S. M. (2008) 3D numerical modeling of forward folding and reverse unfolding of a viscous single-layer: implications for the formation of folds and fold patterns. *Tectonophysics, 446*(1-4), 31-41.

Schmid, D. W., M. Dabrowski, and M. Krotkiewski (2008) Evolution of large amplitude 3D fold patterns: A FEM study. *Physics of the Earth and Planetary Interiors, 171*(1-4), 400-408.

Schoenberg M. and C. Sayers (1995) Seismic anisotropy of fractured rock. *Geophysics, 60*(1), 204-211.

Selley, R. C. and S. A. Sonnenberg (2014) *Elements of Petroleum Geology*. Academic Press.

Sibson, R. H. (2003) Brittle-failure controls on maximum sustainable overpressure in different tectonic regimes. *Am. Assoc. Petrol. Geol. Bull., 87*(6), 901-908.

Skjernaa, L. (1975) Experiments on superimposed buckle folding. *Tectonophysics, 27*(3), 255-270.

Smart, K. J., D. A. Ferrill, and A. P. Morris (2009) Impact of interlayer slip on fracture prediction from geomechanical models of fault-related folds. *AAPG Bull., 92*(11), 1447-1458.

Smart, K. J., G. I. Ofoegbu, K. Das, and D. Basu (2012) Geomechanical modeling of hydraulic fracture initiation and propagation in a mechanically stratified geologic system. In *46th US Rock Mechanics/Geomechanics Symposium*. American Rock Mechanics Association.

Stearns, D. W. (1964) Macrofracture patterns on Teton anticline, northwest Montana. *Transactions of the American Geophysical Union*, 45, 107-108.

Stearns, D. W. (1967) Certain aspects of fracture in naturally deformed rocks. In *Rock Mechanics Seminar,* 1, 97-118. R.E. Riecker, Bedford, Terrestrial Sciences Laboratory.

Stearns, D. W. (1970) Drape folds over uplifted basement blocks with emphasis on the Wyoming Province. Unpublished Ph.D. thesis, Texas A&M University, USA.

Stearns, D. W. and M. Friedman (1972) Reservoirs in fractured rock. In R. E. King, ed., Stratigraphic Oil and Gas Fields: Classification, Exploration Methods, and Case Histories: *AAPG Memoir 16/Society of Exploration Geophysicists Special Publication 10*, 82-106.

Stephenson, B. J., A. Koopman, H. Hillgartner, H. McQuillan, S. Bourne, J. J. Noad, and K. Rawnsley (2007) Structural and stratigraphic controls on fold-related fracturing in the Zagros Mountains, Iran: implications for reservoir development. Fractured Reservoirs. *Geological Society, London, Special Publications, 270*(1), 1-21.

Thiessen, R. L. and W. D. Means (1980) Classification of fold interference patterns – a reexamination. *Journal of Structural Geology, 2*(3), 311-316.

Tiab, D., and E. C. Donaldson (2015) *Petrophysics: Theory and Practice of Measuring Reservoir Rock and Fluid Transport Properties*. Gulf Professional Publishing.

Treagus, J. E. and S. H. Treagus (1981) Folds and the strain ellipsoid: a general model. *Journal of Structural Geology, 3*(1), 1-17.

Turcotte, D. L. and G. Schubert (2014) *Geodynamics*. Cambridge University Press.

Twiss, R. J. and E. M. Moores (2007) *Structural Geology*. 2nd Edition. W.H. Freeman and Company, New York.

Vidal-Gilbert, S., J. F. Nauroy, and E. Brosse (2009) 3D geomechanical modelling for CO 2 geologic storage in the Dogger carbonates of the Paris Basin. *International Journal of Greenhouse Gas Control, 3*(3), 288-299.

Vitale, S., F. Dati, S. Mazzoli, S. Ciarcia, V. Guerriero, and A. Iannace (2012) Modes and timing of fracture network development in poly-deformed carbonate reservoir analogues, Mt. Chianello, southern Italy. *Journal of Structural Geology, 37*, 223-235.

Wennberg, O. P., T. Svånå, M. Azizzadeh, A. M. M. Aqrawi, P. Brockbank, K. B. Lyslo, and S. Ogilvie (2007) Fracture intensity vs. mechanical stratigraphy in platform topcarbonates: the Aquitanian of the Asmari Formation, Khaviz Aniticline, Zagros, SW Iran. *Petroleum Geoscience, 12*(3), 235-245.

Wennberg, O. P., M. Azizzadeh, A. A. M. Aqrawi, E. Blanc, P. Brockbank, K. B. Lyslo, and T. Svånå (2007) The Khaviz Anticline: an outcrop analogue to giant fractured Asmari Formation reservoirs in SW Iran. *Geological society, London, special publications, 270*(1), 23-42.

Wicks, J. L., S. L. Dean, and B. R. Kulander (1999) Regional tectonics and fracture patterns in the Fall River Formation (Lower Cretaceous) around the Black Hills foreland uplift, western South Dakota and northeastern Wyoming. *Geological Society, London, Special Publications, 169*(1), 145-165.

Zemanek, J., E. E. Glenn, L. J. Norton, and R. L. Caldwell (1970) Formation evaluation by inspection with the borehole televiewer. *Geophysics, 355*, 254-269.

Zhang, Y., B. E. Hobbs, A. Ord, and H. B. Mühlhaus (1996) Computer simulation of single-layer buckling. *Journal of Structural Geology, 18*(5), 643-655.

Zienkiewicz, O. C., Z. R. L. Taylor, and J. Zhu (2005) *The Finite Element Method: Its Basis and Fundamentals*. Elsevier, UK.

Zulauf, J. and G. Zulauf (2005) Coeval folding and boudinage in four dimensions. *Journal of Structural Geology, 27*(6), 1061-1068.

VITA

Eli Jacob Steinbeck was born March 9, 1991 in Washington, Missouri, and grew up in rural Hermann, Missouri. In May 2014 he received his Bachelor of Science degree in Geological Engineering from Missouri University of Science and Technology. During his undergraduate career, Eli was a player on the men's varsity basketball team for four seasons. Immediately after earning his bachelor's degree, he enrolled in the Petroleum Engineering Master's program at the same university. During his time as a master's student, he held the position of graduate teaching assistant for the Department of Geosciences and Geological and Petroleum Engineering, and interned with the Missouri Department of Natural Resources and Devon Energy Corporation. Eli earned his Master of Science degree in Petroleum Engineering from Missouri University of Science and Technology in July 2016.